Geological Survey of Israel
Ministry of Energy

Mapping and Characterising Active Tectonic Sources in Israel and Adjacent Areas

Matty Sharon

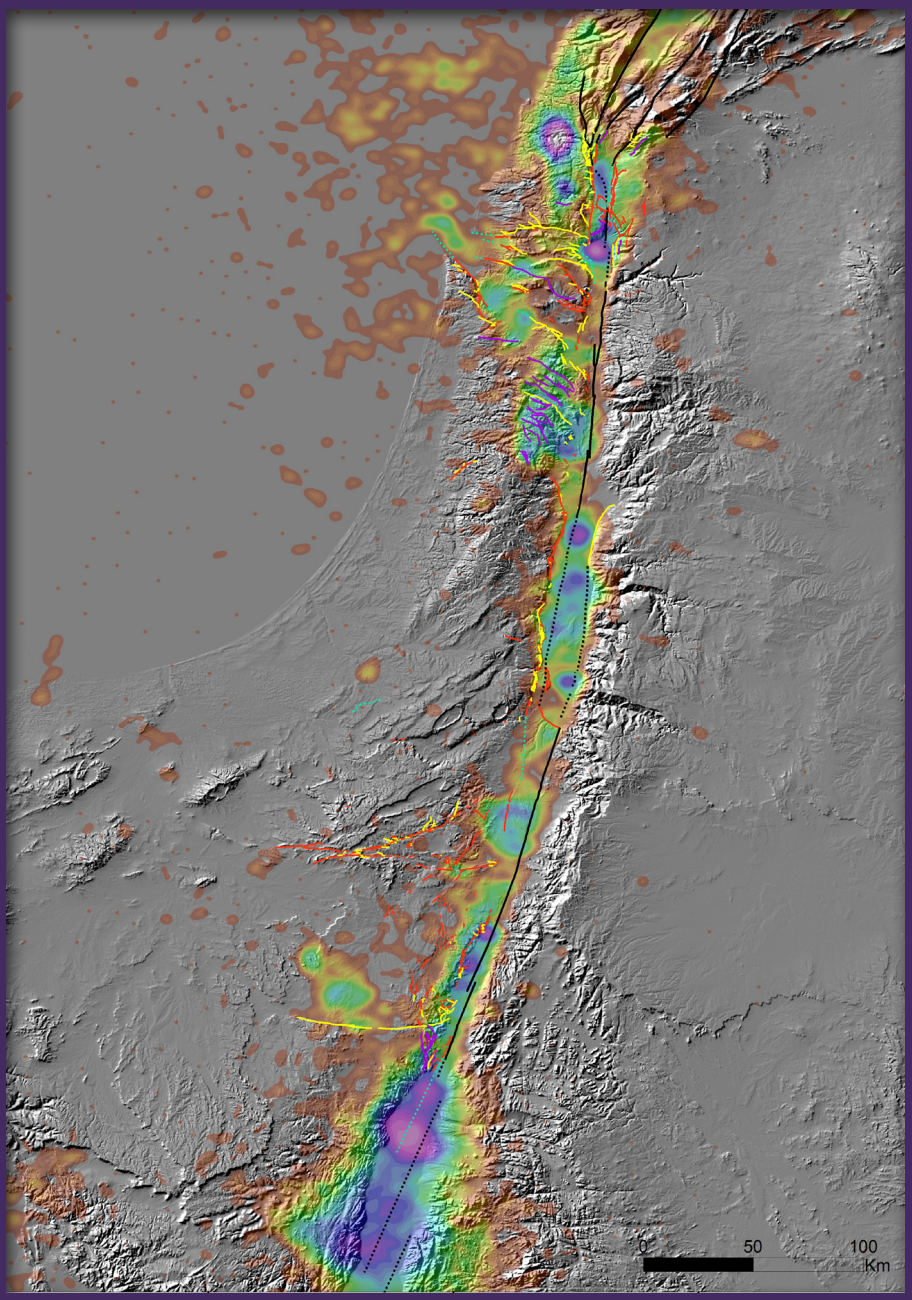

Report GSI/19/2020

Jerusalem, August 2020

32 Yeshayahu Leibowitz St. Jerusalem, 9692100 Israel

Cover:
Quaternary capable faults in Israel, as well as the main seismic sources in the region, superimposed on the spatial distribution of the earthquake kernel density

Cover design: Tirza Tzuberi

Geological Survey of Israel
Ministry of Energy

Mapping and Characterising Active Tectonic Sources in Israel and Adjacent Areas

Matty Sharon

Thesis submitted in partial fulfillment of the requirements for the degree of "Master of Science" in the Department of Geophysics and Planetary Sciences, Porter School of the Environment and Earth Sciences, Raymond and Beverly Sackler Faculty of Exact Sciences, Tel Aviv University

The study was carried out under the supervision of:

Dr. Ittai Kurzon, Dr. Amir Sagy, Geological Survey of Israel

Prof. Shmuel Marco, Prof. Zvi Ben-Avraham, Tel Aviv University

Report GSI/19/2020 Jerusalem, August 2020

Acknowledgments

I am deeply grateful for having the contribution of many people to this study.

First, I warmly thank my advisors for their dedicated guidance and support: to Ittai Kurzon and Amir Sagy for their caring, close guidance, and for offering me to work on this project; to Shmulik Marco for his devoted guidance and assistance wherever needed; and to Zvi Ben-Avraham for his important advices and encouraging spirit.

Secondly, many thanks to Marcelo Rosensaft for his collaboration in GIS analyses; and to Ronnie Kammai and Asaf Inbal for reviewing this work in detail, and for their constructive comments. I also thank the Israel Ministry of Energy for their funding.

On top of that, a very important assistance came from researchers associated with the Geological Mapping Division of the Geological Survey of Israel. Specifically, I wish to thank Yoav Avni, Amihai Sneh and Ezra Zilberman for introducing me to nuances of the Neogene-Quaternary stratigraphy of Israel, for helping me to achieve better understanding of the geological mapping in the region and for their assistance in recognising specific faults relevant to this study. In addition, I thank Rami Weinberger, Doron Mor, Hanan Ginat and Shimon Ilani for their assistance in achieving the most up-to-date age constraints of young formations; Yossi Bartov, Michael Beyth, Gideon Baer, Rani Calvo, Yehuda Eyal, Tsafrir Levi and Perach Nuriel for their aid in estimating age constraints of the activity of some faults; and Rivka Amit, Alex Borshevsky, Shmuel Hoyland, Chana Netzer-Cohen, Batsheva Cohen and Oksana Zarinsky for further assistance. I also thank Yael Sagy and Gal Hartman for supplying high-resolution subsurface fault locations. Many thanks to Zohar Gvirtzman, Amos Salamon, Yariv Hamiel and Rami Weinberger for reviewing part of this work and for their important comments.

For the seismological sections, I wish to thank Nadav Wetzler for his significant contribution to the analysis of the frequency-magnitude relation; to Avi Shapira for an important discussion about the network capability; to Rami Hofstetter for his comments on part of my work; and to Veronic Avirav, Andrey Polozov and Batya Reich of the Division of Seismology, the Geophysical Institute of Israel, for their assistance. I also thank Ronnie Kammai, Gony Biran and William Lettis for discussions and advices that contributed to the applicability of this study for seismic hazard estimations; and to Maryline Le Béon for providing updates and information regarding slip rates. I am also thankful to the faculty members of the Department of Geophysics, Tel Aviv University: Alon Ziv, Hillel Wust-Bloch, Moshe Reshef, Shmulik Marco and Lev Eppelbaum, for their effort in endowing vast scientific background essential to this study. In addition, I thank Zvi Garfunkel for several fruitful discussions; some of which were in late stage of my B.Sc. studies and prompted me to take part in research in the field of the current study.

For assistance, discussions and particularly good company, I thank my colleague graduate students Tzahi Lior, Guy Ben-Dor, Dorian Golriz, Yonatan Goren of blessed memory, Ran Issachar, Ariel Lellouch, Hila Navon, Netta Savin, Dan Elhanati, Yochai Magen, Shaked Engelberg, Niv Keren, Bar Oryan, Pavel Sinitsyn, Matan Shustak, Itai Sharabi, Omer Shamir and many others, also the postdoctoral fellows Lewis Schardong, Andy Eisermann in my department; and Evyatar Cohen, Jonathan Keinan, Ido Sirota and others in the GSI.

Last, but as important, I wish to thank my dear family and friends, here and overseas, for encouragement, assistance and interest in my work; and to many teachers, guides and kind people whom I have been fortunate to learn from and be accompanied with along the way, whose inspiration contributed to the accomplishment of this study.

Abstract

Recent earthquake-triggered disasters emphasise the necessity of seismic hazard-related research, especially where critical facilities are located. Products such as gridded seismicity and maps of hazardous faults are essential to evaluate ground motion and surface rupture hazards, for construction and siting purposes. Seismic hazard analyses in Israel are still based on a preliminary seismic zonation, and prior to this study, there are no fault maps of the whole country that adhere to international hazard standards for nuclear power plants. In this study, I endeavour to improve the seismo-tectonic understanding of the region, while aiming to produce essential products for hazard assessment, by: a) characterising the seismicity ; b) creating a database of mapped capable faults; c) defining and characterising seismogenic zones; d) developing a methodology that combines geological and seismological data for the benefit of the above objectives, and preferably can be applied in other regions as well. I utilise primarily the data sources of: 1) relocated earthquakes that were recorded between 1983 to 2017; 2) geological maps that cover all Israel (70 out of 79 sheets are in 1:50,000 scale). Complementary data are published works that constrain the latest activity of faults, aerial photography and slip rates of geodetic and geological sources.

A significant product of this work is a cascaded methodology that amalgamates the geological and seismological data in three steps: first, the region is characterised in gridded seismicity by the parameters: *earthquake density*, *seismic moment density* and *earthquake average depth*. They are achieved by statistics-based data processing that enables utilising large earthquake data that include spatial errors, and to use its large quantity as a benefit for circumventing the errors. The regional frequency-magnitude parameters are obtained, and used to calculate recurrence intervals of medium to strong earthquakes, based on the Gutenberg-Richter law. In the second step a database of mapped capable faults that show direct or indirect evidence for recent activity is created, by analysing geological maps and applying seismo-tectonic criteria, which are designed according to the local stratigraphy and tectonic configuration. The main seismic sources, which are likely to accommodate the largest shocks, are derived from the capable faults, through slip-rate-based criteria. Finally, seismogenic zones are delineated based on the achieved seismicity parameters and the associated fault system, and characterised by seismo-tectonic characteristics. Each step of the methodology contributes to surface rupture hazard and/or ground motion analysis.

Gridded seismicity maps are presented within the latitudes 28–34°N and longitudes 33–37°E (the whole investigated area). The *earthquake density* and the *seismic moment density*, mostly independent, complement one another for mapping the most active seismic sources and areas of the highest likelihood to nucleate the largest earthquakes. The seismicity is concentrated along the Dead Sea Transform fault system (DST) and its branches, particularly the Carmel-Gilboa-Tirza fault system (CGTF). It peaks in pull-apart basins, intersection zones with other faults, and some areas that have not been associated with surficial tectonic features. The *earthquake average depth* contributes to the understanding of the seismicity patterns. It varies between shallow depth of a few kilometres and up to 25-km or deeper, and correlates with former investigations.

A spatio-temporal analysis suggests that aftershocks in a poor-foreshock catalogue (like investigated here) affect the frequency-magnitude parameters in raising both the *b-value* and the *a-value*, and biasing the ensuing recurrence intervals towards short periods (and otherwise for the largest magnitudes). The *b-values* within the whole investigated area (0.99–1.19) are interpreted as biased by aftershocks. Accordingly, they yield recurrence intervals shorter than these revealed from 100 years of instrumental seismicity and 2000 years of geological and historical records. A relatively stable ~0.8 *b-value* is achieved within the seismic network coverage area, where the determination is more constrained, and aftershocks were scarce. The ensuing recurrence intervals consent with the longer time windows' records. Hence, it is suggested to represent the last ~35-year seismicity and possibly longer periods. The *b-value* is low in comparison to other strike-slip zones, possibly due to localised faulting along the DST. The suggested recurrence intervals are ~10, ~70 and ~450 years of $5.0 \leq M < 6.0$, $6.0 \leq M < 7.0$, and $7.0 \leq M < 8.0$ events, respectively, within the southern part of the DST (excluding the Gulf of Eilat).

Hierarchic tectonic criteria classify Quaternary capable faults by: 1) main strike-slip segments of the DST; 2) direct evidence for Quaternary faulting; 3) main branches of faults of the above criteria, and DST marginal faults; 4) association with instrumental seismicity; 5) subsurface faults. The map covers all Israel, with the extension of major faults beyond its borders and offshore. The rather homogenous distribution of faults of different criteria suggests that the criteria complement each other, and thus reinforces their design. The identified fault systems are: 1) DST strike-slip faults, main branches and marginal faults; 2) the CGTF; 3) faults parallel or sub-parallel to the Arava valley; 4) part of the Sinai – Negev shear belt (SNB); 5) ~NNW orientated faults in the Negev; 6) ~W to ~NW trending faults in the lower Galilee. The main seismic sources are classified by: 1) evidence for lateral slip rates $\geq$ 1 mm/a; 2) evaluated average slip rates of ~ 0.5–1.0 mm/a.

Seismogenic zones are located mainly along the DST, but some are mapped west of it, appear as branching off the main fault zone. Spatio-temporal variations of their characteristics, also within sub-zones, shed more light about the seismicity behaviour. The *b-values* and the ensuing recurrence intervals within zones are generally considered as not representative for long-term behaviour. In an opposite trend than the obtained intervals, the suggested long-term pattern is intense 'interseismic' seismicity in the basins and sparser seismicity in the long straight segments, which release more seismic moment in stronger events. Hence, a (quasi-?) 'characteristic' behaviour is suggested in these segments. The lack of $5.0 \leq M < 6.0$ events within them for almost a century is a reinforcement.

The seismicity maps reveal a gentle ~NW trend in straps or possible lineaments. The largest of them follows the CGTF and is the only one associated with significant surface expression. The predominant among the rest comprises the Eastern Sinai seismogenic zone. It is defined here as the Eilat-Bardawil lineament (EBL), suggested as a subsurface branch of the DST. The lineaments are parallel or sub-parallel to substantial extensional features, suggesting that they are a (mostly-) subtle reflection of a regional SW-NE extensional tectonic regime. It is supported by a few independent evidences. The relative absence of deformation along the SNB since the early Quaternary implies that the magnitude of the ~SE-NW axis of maximum horizontal compression has weaken and/or has shifted towards the north.

Table of contents

List of Figures

List of Tables

List of Appendices

Appendix 1: Details related to Chapter 3

Appendix 2: The frequency-magnitude relation analysis for seismogenic zones

1. Introduction

1.1 Background

Earthquakes have been the source for many fatalities and massive destruction of human-built structures throughout history (e.g. Ambraseys, 2009), including the destruction of the Fukushima nuclear power plant by tsunami waves triggered by the 2011 Tohoku-Oki earthquake. The global population growth and the establishment of different kind of facilities, varying from simple structures to very vulnerable facilities such as nuclear power plants, have been raising the risk to higher levels and entail the need for a profound understanding of the seismotectonics and for seismic hazard assessment.

Seismic hazard analysis is a process that includes a few stages. While initially, the seismic sources are defined and characterised, the hazard is finally being assessed by considering local or regional models. Such analysis involves complications and uncertainties, due to the complex nature of the earthquake phenomena, including the recurrence patterns and the relatively short time window of the instrumental record compared to the seismic cycle. The assessment of the seismic hazard of a given region is therefore a challenge that differs from one place to another, considering the data available of past earthquakes and the geological settings (i.e. lithology, tectonic configuration, fault geometry and slip rate). The hypothesis of the present study is that the incorporation of the analyses of two databases of independent sources, instrumental seismicity and geological maps, will produce a unified high-resolution picture of the present tectonic activity and essential products for a variety of seismic hazard estimations (particularly, ground motions and surface rupture hazards).

Seismological analysis provides fundamental tools for evaluating seismic hazard (e.g. Gutenberg and Richter, 1944; Reasenberg and Jones, 1989; Frankel, 1995; Kanamori et al., 1997; Harris, 1998; Yamanaka and Kikuchi, 2004; Stein and Liu, 2009). The first seismic stations in Israel have been in use since 1954, but the instrumental record has been relatively poor until the early 1980s, when the Israel Seismic Network began to operate, consisting of a wider distribution of stations. In addition, the pre-instrumental record of earthquakes in the region is vast, derived from historical documents (Ambraseys, 2009), archaeological and geological evidences (e.g., Agnon, 2014; Marco and Klinger, 2014).

A detailed geological investigation of faults can extend the necessary information for evaluating seismic hazards and improve it. In terms of seismic hazard perspective, faults that were active in the recent geological periods have more chances for future faulting, compared with other faults. Field relations between faults and geological units as revealed in geological maps can force constraints on the location, timing and the amount of offset of the relevant faults. The Quaternary era is selected here for the time reference for fault activity due to a variety of reasons: a) the regional stress field within this period represents the current stress field (Eyal and Reches, 1983; supported by Marco, 2007; Garfunkel, 2011; Palano et al., 2013); b) the local geological formations of the Quaternary are better age-constrained than other recent geological times; c) faults that were active within the Quaternary are often considered as ‘capable’ faults, which are used for seismic hazard estimation for nuclear power plants (e.g. Machette, 1978; 2000). Nonetheless, since the

most fundamental constrains for fault activity are restricted to intersection zones of faults and young formations, whose spatial distribution is limited, additional criteria are required for defining hazardous faults. More constraints on the timing and intensity of fault activity is achieved by combining geological information with geochronological methods, including paleoseismic investigations and the reconstruction of past landscape (e.g. Yeats et al., 1997).

The relationship between young faults and recent seismicity, however, cannot be easily understood. On a regional wide scale, according to plate tectonics (Wegener, 1966), concentration of earthquakes is expected along major active faults, representing deformation zones between plates. Yet, in a more detailed resolution, the width of these zones may differ along faults and fault systems (Otsuki, 1978; Sibson, 1986; Hull, 1988; Evans, 1990; Childs et al., 2009; Choi et al., 2016), depending on the local geology (e.g. lithology and older faults that can reactivate). In order to improve the seismo-tectonic understanding of a given region, it is essential to investigate the relation between the earthquake spatial distribution and mapped faults, especially young faults associated with the current tectonic regime.

One approach to integrate between faults and seismicity is the delineation of seismogenic zones. Although seismogenic zonation is traditionally based on a spatial distribution of epicentres (e.g. Turkelli et al., 2003), zones can be also depicted and/or characterised based on geostructural units (Radulian et al., 1996a); stress field (Radulian et al., 1996b; Gulia and Wiemer, 2010); geometrical and mechanical parameters (Heuret et al., 2011); geodetic measurements (Hashimoto et al., 2009); kinematic and structural analyses (Meletti et al., 2000) or a variety of combinations (Hamdache, 1998; Frankel, 1995; Markusic and Herak; 1999; Radulian et al., 2000; 2018; Shamir et al., 2001; Shapira and Hofstetter, 2002; Bus et al., 2009; Ashish et al., 2016). Seismogenic zonation commonly considers the parameters of the frequency-magnitude relation, particularly the *b-value*, an important hazard factor that reflects the proportion between small and large earthquakes. Furthermore, spatial variations of short-term seismicity can shed light on the issue of recurrence patterns of strong earthquakes in longer periods. This issue is rather important, as like other zone characteristics (e.g. maximum magnitude), it directly affects hazard assessment. It involves with the possibility that the frequency-magnitude relation deviates from the Gutenberg-Richter law (see section 2.3.2) in strong earthquakes. Instead, individual faults and fault segments may tend to generate earthquakes of a relatively narrow magnitude range near the possible maximum (a ‘characteristic’ behaviour; Schwartz and Coppersmith, 1984).

1.2. Objectives

The main objective is to generate databases that can be applied for seismo-tectonic and ground motion modelling and for surface rupture hazard. Particularly, these databases are aimed to be applicable for the siting and designing of vulnerable facilities, such as nuclear power plants and dams, in order to minimise the chances of surface rupture below the planned site. The structure design should be able to resist ground motions in a low

probability of the order of once in 10,000 or 100,000 years. For this purpose, I define and characterise the main tectonic sources in the area of Israel by combining seismological and geological databases. Therefore, a complementary essential task, or an additional objective of this study, is to develop a methodology that enables the integration between geological and seismological data, which are usually investigated separately.

Specifically, the objectives of this study are:

1. To characterise the seismicity in the region of Israel based on the most up-to-date data available, while aiming to achieve: a) spatial characterisation which will allow capturing active tectonic features in the region, based on either statistics and/or physical sizes; b) determination of the local and regional frequency-magnitude parameters; c) a better understanding of the recurrence pattern of strong earthquakes.

2. To create a database of faults that have been active in the recent geological past ('capable' faults), for evaluating surface rupture risks and regional seismic hazard, with an emphasis on sensitive facilities such as dams and nuclear power plants. Prior to this work, Bartov et al. (2002) published a map that is based on "potentially active" faults that offset Pliocene rocks or younger, utilising 1:200,000 scale geological maps (Sneh et al., 1998). Since then, more detailed studies that constrain the age activity of specific faults have been published, and most importantly, most of Israel area is covered by geological maps in the scale of 1:50,000 (currently, 70 of 79 map sheets are available). I aim to produce a capable fault map, based primarily on 1:50,000 geological maps, which differs from the previous map by: a) its resolution; b) the time reference of faulting; c) it considers the most up-to-date constraints of fault activity; d) its criteria, which also considers instrumental seismicity.

3. To define and characterise seismogenic zones in Israel. The last seismogenic zonation (Shamir et al., 2001) and its following study for determining the seismicity parameters (Shapira and Hofstetter, 2011) were based on the 1:200,000 scale mapped faults published by Bartov et al. (2000) and on limited recorded seismicity that was available at that time. Since then, more relatively high-quality seismic data has been recorded, and the geological data has dramatically improved. However, and although this seismic zonation (Shamir et al., 2001) was defined as preliminary, it is still in use for seismic hazard analyses. I aim to redefine seismogenic zones and to characterise them by seismo-tectonic parameters.

4. To develop a methodology that enables the integration of geological and seismological data. This goal is an outcome of objectives 2 and 3. The suggested methodology will be preferably applicable in other regions as well.

The above objectives are followed by the task of arranging and presenting the database in a platform that enables further analysis for different aims (e.g. seismotectonic models) in a user-friendly manner. This includes operating GIS platform that allows evaluation and updating of the database as well as analysis and graphical presentation of different maps and results. Since the objectives of this research are strongly related to the most recent tectonic regime, whose understanding further contributes to hazard aspects, an additional sub-goal is to improve its understanding.

1.3. Tectonic Settings

1.3.1. Geological background

The continental crust in the region of Israel was created as part of the Pan-African orogeny of Late Precambrian age (Garfunkel, 1988; 1998). Later, during the Paleozoic, it was subjected to alternating periods of sedimentation and erosion. Continental breakup occurred mainly during Triassic-Jurassic times, with the establishment of passive margins along the Tethys-Mediterranean coast of the Levant (Garfunkel, 1988; 1998; 2004). From the Cretaceous to mid-Eocene times, the unbroken African-Arabian plate was a carbonate platform dominated by widespread transgressions. Since the Upper Cretaceous, the region was subjected to WNW to NNW compression that triggered formation of the ~1,000 km long Syrian Arc system, deforming the sedimentary sequence into a series of asymmetric folds, reverse faults, and monoclines (Reches et al., 1981; Eyal and Reches, 1983; Flexer et al., 1984; Salamon, 1987; Garfunkel, 1981; 1988). Mid-Cenozoic rifting separated the previously-continuous African-Arabian plate to the plates of Africa and Arabia, forming the seafloor spreading centres of the Red Sea and the Gulf of Aden. In a later stage, a sub-plate of Israel-Sinai Peninsula was created between the two separated plates (Joffe and Garfunkel, 1987; Le Pichon and Gaulier, 1988; Garfunkel, 1998; Ben-Avraham et al., 2008).

1.3.2. Plate configuration and main tectonic features

The Israel-Sinai sub-plate may be considered as a splinter of the African plate on its north-eastern tip (Fig. 1.1; Ben-Menahem et al., 1976; Garfunkel, 1998; Salamon et al., 1996; 2003). The Suez rift borders between the two plates on the south-west of the Israel-Sinai sub-plate, but presently it does not seem to extend northwards into the Mediterranean (Garfunkel and Bartov, 1977; Nur and Ben-Avraham, 1978; Steckler and ten-Brink, 1986). In the Easternmost Mediterranean, the current plate border deformation is taking place along the convergent Cyprus Arc, where the Anatolian plate overrides the plates of Africa and Sinai, but left-lateral shear may be the dominant motion in its eastern part (Mckenzie, 1970; 1972; Dewey et al., 1973; Ben-Avraham et al., 1988; Kempler and Garfunkel, 1994; Garfunkel, 1998; Harrison et al., 2004; Wdowinski et al., 2006).

The eastern boundary of the Israel-Sinai sub-plate is the Dead Sea transform fault system (DST; also known as the Dead Sea fault or rift) that separates it from the Arabian plate (Fig. 1.1; Freund, 1965; Freund et al., 1970; Garfunkel, 1981; 2014). The rifts of Suez and of the Red Sea, and the DST were formed due to the mid-Cenozoic breakup of the once-continuous African-Arabian continent. However, the Suez rift has shown relatively minor signs of deformation since the end of the Miocene (Garfunkel and Bartov, 1977; Joffe and Garfunkel, 1987; Steckler et al., 1988). The three tectonic features meet near the southern tip of the Sinai peninsula, from which the DST extends northwards. It displays a major fracture zone along a distance of ~1,000 km through the gulf of Eilat (Aqaba), the Dead Sea basin, the Sea of Galilee and the Mt. Hermon - Anti-Lebanon structure, and finally to the continental collision zone of the Taurus Mountains, Turkey. Left-lateral strike-slip

motion has taken place along the DST since the mid-early Miocene, coincided with regional-scale uplifting and volcanism (Garfunkel, 1981; 1989; 2014; Walley, 1988; Garfunkel and Ben-Avraham, 2001).

The southern part of the DST (south of the Lebanon Restraining Bend; Fig. 1.1) is dominated by a sinistral motion of ~105 km (Quennell, 1959; Garfunkel, 1981; 2014). It is marked by a pronounced 5–20 km wide topographic valley, mostly with uplifted flanks, bordered by normal faults that extend along the valley margins. The lateral motion occurs on longitudinal left-stepping strike-slip and oblique-slip fault segments. They delimit a string of en-echelon arranged rhomb-shaped pull-apart basins whose dimensions are up to 150 km length and 20 km width, within the valley. These basins are associated with orthogonal separation of the transform flanks on the surface, which may well extend beneath the crust (Garfunkel, 1981; 2014; Garfunkel et al., 1981; Garfunkel and Ben-Avraham, 2001). The slip rates along the DST vary between different fault segments and time resolutions, but converges at around 4–5 mm/a, approximately the same values obtained by GPS measurements (Marco and Klinger, 2014 and references therein). Deep-crust seismicity is significant along the southern part of the DST, correlated with areas of low heat flow, particularly in the Dead Sea basin, and probably indicates a cool and brittle lower crust (Ben-Avraham et al., 1978; Eckstein and Simmons, 1978; Aldersons et al., 2003; Hofstetter et al., 2003; Shalev et al., 2007; 2013; Braeuer et al., 2012; Aldersons and Ben-Avraham, 2014; Oryan, 2016; Wetzler and Kurzon, 2016).

1.3.3. Further prominent fault zones

Several branches split off the main fault segments of the DST; the most prominent among them is the Carmel-Gilboa-Tirza fault system (CGTF; Fig. 1.1) that divides the Israel-Sinai sub-plate into two tectonic domains (Neev et al., 1976; Almagor and Hall, 1984; Ben-Gai and Ben-Avraham, 1995). It is also characterised by low heat flow and relatively deep seismicity (Hofstetter et al., 1996; Shalev et al., 2013). Fault scarps in this zone mainly indicate on normal component of slip. Yet, focal mechanisms show dominant left-lateral shear, accompanied by compression in the northwest, and more complex seismicity pattern in the southeast, with normal faulting that can be associated with local grabens (Hofstetter et al., 1996). Recent geodetic survey suggested both left-lateral and extension motions at coeval rates of ~0.7 mm/a and ~0.6 mm/a, respectively (Sadeh et al., 2012).

Another substantial fault system is the Sinai – Negev shear belt (SNB; Bartov, 1974). It comprises E-W to SW-NE trending faults (south to north: Thamed, Paran, Arif-Batur, Ramon, Sa'ad-Nafha, and perhaps Zin) that accommodate dextral motion of typically a few kilometres or less, accompanied with vertical displacements that can reach one kilometre (e.g. Vroman, 1956; Garfunkel, 1964; Bartov, 1974; Eidelman, 1979; Zilberman, 1981; 1983; 1985; Baer, 1989; Zilberman et al., 1996). Geological sources of evidence revealed different phases of activity throughout geological history, with earliest signs of deformation as early as Triassic times, and latest significant activity phase after the DST was formed, mainly in late-Miocene – Pliocene times (Garfunkel and Horowitz, 1966; Bartov, 1974 and references therein; Eidelman, 1979; Garfunkel, 1981; Calvo and Bartov,

2001). The present tectonic interaction between this ancient fault system and the DST is not entirely clear (Garfunkel, 2014).

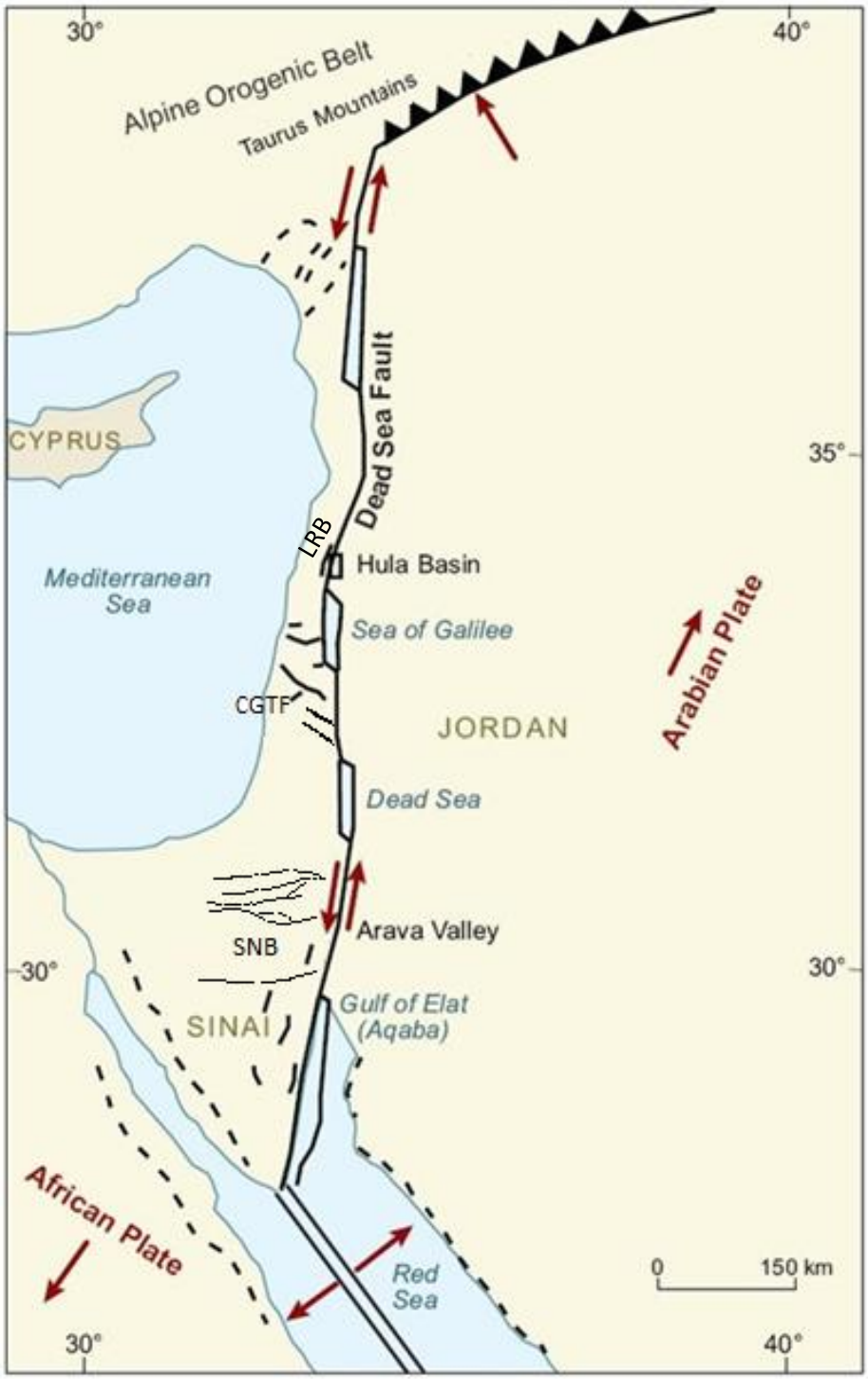

Fig. 1.1: Map of the DST showing relative plate motion (red arrows) from the Red Sea Rift in the south to the collision zone of the Taurus Mountains in the north. Strike-slip motion occurs between the Arabian plate and the Israel-Sinai sub-plate. The main pull-apart basins developed along the DST are shown. Abbreviations: CGTF - Carmel-Gilboa-Tirza fault system; LRB - Lebanon Restraining Bend; SNB - Sinai-Negev Shear belt. SNB faults from south to north: Thamed, Paran, Arif-Batur, Ramon, Sa'ad-Nafha. Modified from Ben-Avraham et al. (2008).

2. Regional characterisation by seismicity

2.1. Introduction

Many studies have contributed to the understating of the seismicity of Israel, in different aspects, including the distribution of earthquakes in relation to faults and regional tectonic settings, and the frequency-magnitude relation (e.g. Arieh, 1967; Ben-Menahem and Aboodi, 1981; Shapira and Feldman, 1987; Shapira and Shamir, 1994; Salamon et al., 1996; Shamir et al., 2001; Shapira and Hofstetter, 2002; Begin and Steinitz, 2005); stress field obtained from focal mechanism (e.g. Salamon et al., 2003; Hofstetter et al., 2007); source parameter analyses (e.g. Shapira and Hofstetter, 1993; Ataeva et al., 2014; Hofstetter et al., 2014; Meirova and Hofstetter, 2017); relocation of hypocentres (e.g. Wetzler and Kurzon, 2016); and seismic hazard analyses (e.g. Arieh and Rabinowitz, 1989; Shapira and van Eck, 1993; SI-413, 1995; Zaslavsky et al., 2012). The main differences between this work and previous studies are the larger amount of relatively high-quality data, and a new suggested methodology. The first part of the new methodology aims to characterise the recent recorded seismicity, in its most up-to-date dataset, by statistical and/or physical parameters, and to present them on regional maps.

2.2. Seismic dataset

The dataset is made of earthquakes that have been recorded by various networks between the period of 1.1.1983 – 31.8.2017, using a total of ~140 stations whose distribution has changed in time and space. The networks that supplied most of the data are the Israel Seismic Network (ISN), the Comprehensive Nuclear Test-Ban Treaty (CTBT), and the Cooperating National Facility (CNF), while much smaller percentage of the data was incorporated from other regional networks: GE, GEOFON global network of Deutsches GeoForschungsZentrum Potsdam (GFZ), JSO, Jordanian Seismic Observatory, and CQ, the seismic network of Cyprus. These earthquakes have been monitored by the Seismological Division of the Geophysical Institute of Israel (GII), composing a catalogue of 17,649 earthquakes that were recorded between 1.1.1981 – 31.8.2017.

These earthquakes have been relocated, generating a new catalogue with more precise locations of hypocentres (for further information on the specific method, see Wetzler and Kurzon (2016)). As part of the relocation process, 802 earthquakes were dismissed (half were recorded by less than 4 stations, and another half were recognised as poorly-constrained locations by the algorithm, including $M_d = 5.8$ 1993 event in the Gulf of Eilat). 16,847 events were left after the process. I further omit earthquakes that were recorded prior to 1983, when the locations supplied by the network were less reliable (Avi Shapira, personal communication), and events that were located far away from the seismic network and from the study area (i.e. outside the rectangular area within the latitudes $28°-34°N$ and the longitudes $33°-37°E$). Eventually, 16,725 earthquakes in the magnitude range of $0.1 \leq M \leq 7.2$ compose the earthquake catalogue used in this study (Fig. 2.1). Earthquakes with unknown magnitudes received a value of $M = 0.1$. The

magnitude and location of the $M_W = 7.2$ 1995 Nuweiba earthquake were fixed according to Hofstetter et al. (2003).

The seismic network coverage is defined in order to regard separately an area of better (lower) detection threshold and more constrained hypocentre locations and magnitudes. This area is defined here as the polygon that includes the least sides, so all the stations that recorded at least 350 arrivals are within it (Fig. 2.2). A completeness magnitude of $M_c = 2.0$ was suggested between the years 1984–1991 in an area that approximately overlaps the network coverage, in a probability of 90% (Shapira, 1992); and $M_c = 1.5$ between the years 2007–2014, in higher probability (Pinsky and Shapira, 2017).

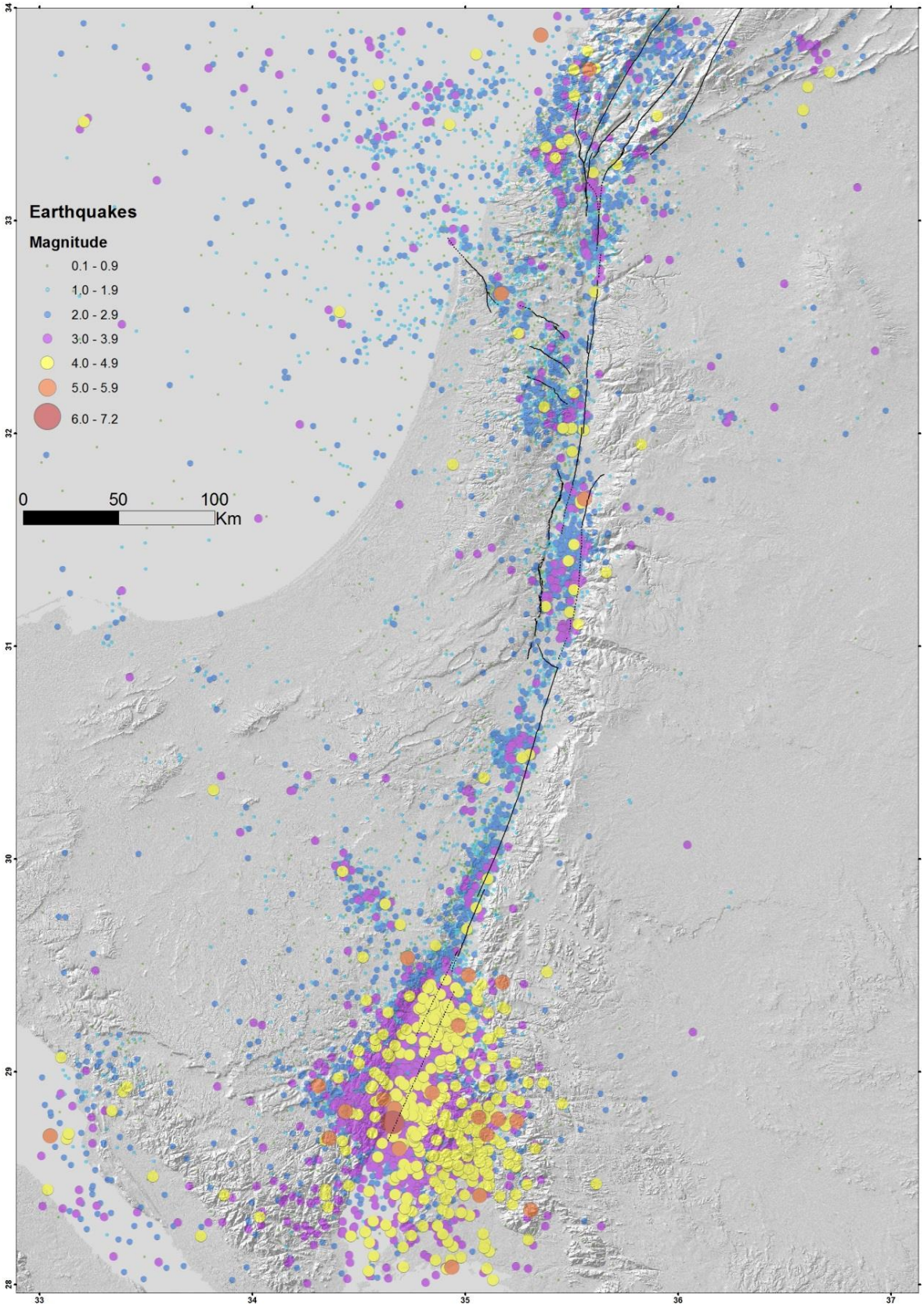

Fig. 2.1: Seismicity in Israel and surrounding areas between the years 1983–2017, based on the relocated earthquake catalogue used in this study. Circle size and colours indicate the magnitude. Black lines represent the main fault segments of the DST and the CGTF (see chapter 3). The background of the presented maps is based on the digital elevation model of the Earth (Farr et al., 2007).

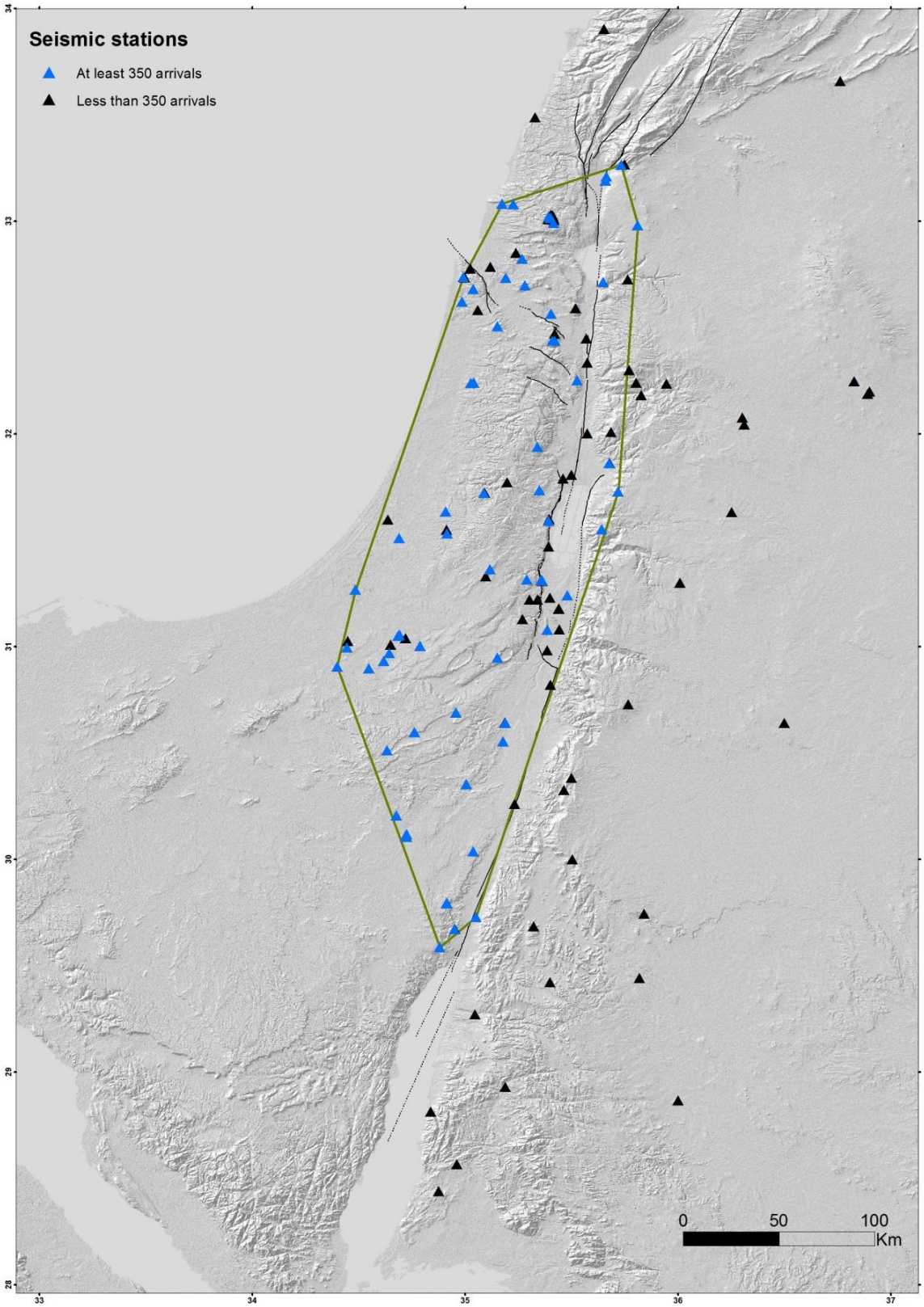

Fig. 2.2: All seismic stations utilised for recording the earthquakes of the examined catalogue, and the ensuing seismic network coverage area. The spatial distribution of the stations is temporal dependent. Station colours are according to the number of recorded arrivals. The green lines mark the borders of the seismic network coverage area. Black lines represent the main fault segments of the DST and the CGTF (see chapter 3).

2.3. Methods

2.3.1. Spatial data processing

I process the data in order to receive a quantitative perspective of the seismicity, utilising the entire investigated catalogue. The region is being scanned in a 0.5-km interval 2D grid, in the horizontal coordinates, latitudes and longitudes. At each grid point I consider all the events within 6-km, assuming point sources, and calculate three parameters: a) *earthquake kernel density*; b) *seismic moment* (M_0) *density*; c) *earthquake average depth*. The calculation is based on kernel density estimation. It allows to obtain the spatial distribution through a probability density function, using the distance of each event from a reference point (the circle centre) to weight the event, in this case by a Gaussian function (see Frankel, 1995; Fig. 2.3). The circle-shape weighting prevents any directional bias. The 6-km maximum distance is significantly higher than the horizontal median error (~1.2 km according to the relocation process, disregarding the depth). Hence, the weighting process significantly aids to statistically circumvent the location errors for achieving a more precise picture of the seismicity distribution.

The *earthquake kernel density*, ρ_{Nk}, is calculated by counting all the weighted events within a 6-km radius, dividing their sum by the area of the sampler (πr^2) and normalising by the duration of the earthquake recording:

$$\rho_{Nk} = \frac{\sum_{n=1}^{N} e^{-\frac{d(n)^2}{2\sigma^2}}}{T\pi r^2} \quad [events/km^2/years] \qquad \text{[Eq. 1]}$$

Where N is the total number of events within a radius r, $d(n)$ is the distance between an event n and the circle centre; σ is the standard deviation of the Gaussian function, and T is the duration of the earthquake recording.

The M_0 *kernel density*, ρ_{M0k}, is deduced by calculating the seismic moment released by each event separately, according to the empirical relation between M_0 and M_L obtained by Shapira and Hofstetter (1993):

$$log[M_0] = 10 + 1.3M_L \qquad \text{[Eq. 2]}$$

(after converting units from *dyne-cm* to *N-m*). Secondly, each amount of seismic moment is weighted according to the distance of the corresponding event from the circle centre (like the calculation of the *earthquake density*). Then, I sum the weighted-M_0 released from all the events within 6-km and divide the sum by the circle area (πr^2) and normalise it by the duration of the earthquake recording:

$$\rho_{M0k} = \frac{\sum_{n=1}^{N} M_0(n) e^{-\frac{d(n)^2}{2\sigma^2}}}{T\pi r^2} \quad [joule/km^2/years] \qquad \text{[Eq. 3]}$$

Where N is the total number of events within a radius r, $M_0(n)$ is the seismic moment released from an event n according to Eq. 2, $d(n)$ is the distance between an event n and the circle centre, σ is the standard deviation of the Gaussian function, and T is the duration of the earthquake recording.

The *earthquake* average *depth* parameter, $\tilde{Z}$, is calculated by summing the weighted depth from all the events within 6-km and dividing the sum by the overall weight:

$$\tilde{Z} = \frac{\sum_{n=1}^{N} Z(n) e^{-\frac{d(n)^2}{2\sigma^2}}}{\sum_{n=1}^{N} e^{-\frac{d(n)^2}{2\sigma^2}}} \quad [km] \qquad \text{[Eq. 4]}$$

Where *N* is the total number of events within a radius *r*, $z(n)$ is the depth of an event *n*, *d(n)* is the distance between an event *n* and the circle centre; σ is the standard deviation of the Gaussian function.

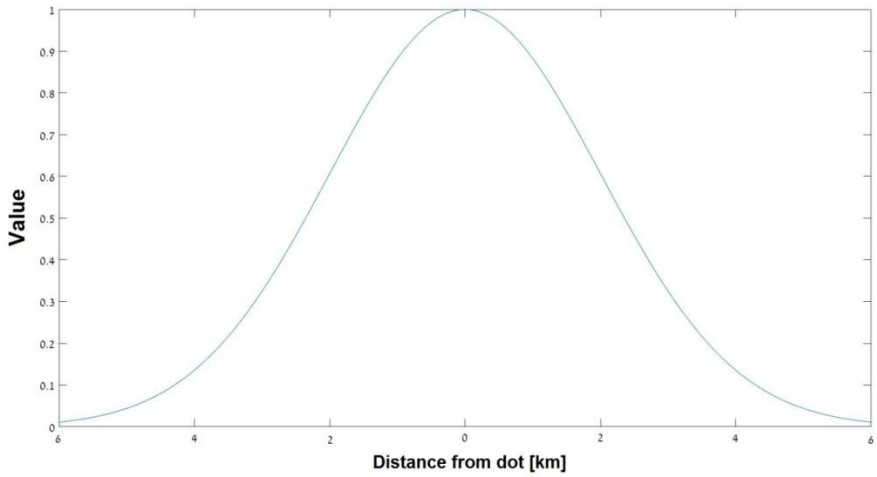

Fig. 2.3: Gaussian function with standard deviation of 2.0. The horizontal axis shows the distance of the earthquakes from the grid point; the vertical axis displays the weighted value each event receives according to its distance from the point.

2.3.2. The frequency-magnitude relation

The frequency-magnitude relation according to the Gutenberg-Richter empirical law follows:

$$log[N] = a - bM \qquad \text{[Eq. 5]}$$

where *N* is the cumulative number of earthquakes of at least a magnitude *M*; *a* and *b* are seismicity parameters, considered as constants that characterise the seismicity of an investigated zone. I calculate the *b-value* based on the Maximum Likelihood Estimation (MLE), using the equation (Marzocchi and Sandri, 2003; following Fisher, 1950; Utsu, 1966; and Bender, 1983):

$$b = \frac{1}{\ln[10][\bar{M} - (M_c - \Delta M/2)]} \qquad \text{[Eq. 6]}$$

where $\bar{M}$ is the sampling average of the magnitudes, M_c is the completeness (or the threshold) magnitude, and ΔM is the magnitude bin interval in which the data is being examined. The estimation of the *b-value* requires an input of the completeness magnitude of the catalogue. Although previous studies suggest that the catalogue is complete for $M \geq$ 2.0 (Shapira, 1992; Pinsky and Shapira, 2017), I analyse the data in order to obtain the completeness magnitude independently.

The main tool I use to determine the completeness magnitude is the Kolmogorov-Smirnov test (e.g. Goebel et al., 2017, for similar application of this test). According to this test, ideally, the goodness of fit between a function-model obtained from the calculated *b-value,* and the actual data, would converge to a best fit when potential-completeness magnitudes are being tested in a descending order, so the smallest magnitude that shows the best fit would be M_c. Practically, the magnitude that corresponds to the best fit is not necessarily the smallest within a series of magnitudes; the goodness of fit may improve or deteriorate when testing potential-completeness magnitudes in a descending order. Therefore, further conditions are applied in order to determine M_C.

The difference between the actual N and N according to the model-function is being calculated for each examined M_C, in a magnitude range of $M \geq M_C$ and a magnitude interval of $\Delta M = 0.1$. All data are normalised by the total number of events used for the *b-value* calculation. ΔS is defined as the largest difference between the actual data and the model-function, for a single examined M_C. The chosen M_C is the smallest magnitude in which the corresponding ΔS is smaller than a particular value (in the case of $\Delta S \leq 0.05$, a value that can be adopted for this study, there is at least 95% fit between the actual data and the model-function, based on $\Delta M = 0.1$ intervals). Nonetheless, when the ΔS lowest peaks (=best fits that suggest optional M_C) are made of approximately the same values, this approach assumes catalogue completeness for events of magnitudes lower than the highest M_C, an assumption that should not be made without visually examining the data or by using another tool. A different approach would opted for higher M_C. There are also other cases where the determination of M_C is not straightforward (e.g. the ΔS peaks are high; or the ensuing *b-value* implies incompleteness according to the Gutenberg-Richter law). Hence, the Kolmogorov-Smirnov test results were not accepted automatically, but rather examined so that more considerations can be added. The different *b-values* in relation to M_C are also presented in the Kolmogorov-Smirnov test; preferably, the *b-value* is relatively stable around M_c.

I stipulate two conditions for the *b-value* statistic-based calculation, which add crucial thresholds for achieving reliable values: 1) minimum magnitude difference of 2.0 between M_c and the largest observed magnitude; 2) at least 50 earthquakes in total. The two conditions enable to obtain minimum level of statistical significance for the seismicity parameters. The *a-value* is deduced after determining the *b-value*, when constraining Eq. 5 by the number of events of at least $M = M_c$. After deducing the *a* and *b* parameters, the recurrence intervals of earthquakes are obtained. For simplicity, I assume frequency-magnitude relation according to Gutenberg-Richter law also for large magnitudes. This approach enables to examine deviations from it when comparing to longer time periods (see discussion, section 5.2.2), and without estimating recurrence intervals based on different models (e.g. 'characteristic' models). The recurrence interval (*RI*) for the magnitude range of $M_a \leq M < M_b$ is calculated by the following equation, derived from Eq. 5:

$$RI = \frac{1}{10^{(a-bM_a)} - 10^{(a-bM_b)}} \ [years] \qquad \text{[Eq. 7]}$$

This equation is only applicable when the *a-value* is normalised by the duration (in years) of the earthquake recording. While previous studies regarded the issue of the maximum possible magnitude along the DST (e.g. Stevens and Avouac, 2017), in this work I assume a maximum magnitude of 8.0.

2.4. Results

2.4.1. Seismicity distribution maps

The results of the seismicity parameters are presented as distribution maps after a simple interpolation, applying the Inverse Distance Weighting (IDW) scheme.

2.4.1.1. Earthquake density

The *earthquake density* (Fig. 2.4) allows to capture the main active tectonic sources according to ~35 years of instrumental seismicity. As expected, most of the earthquakes are concentrated along the main fault zone of the DST, and to a lesser extent along the CGTF. Within the DST, the seismicity is pronounced within zones that are part of pull-apart basins (the Gulf of Eilat, the Dead Sea, The Sea of Galilee and Hula). Although the seismicity is generally sparser along the Jordan Valley and the Arava segments, the latter seem to accommodate descent portion of the earthquakes. In a higher resolution, the *earthquake density* emphasises smaller zones that may be interpreted as active seismic patches within faults. Another substantial zone of seismicity is captured west of the Roum fault, in Lebanon. Although there is no DST segment in proximity, it can be associated with either a SSE-NNW tectonic feature, parallel to the Roum fault, or to SE-NW parallel faults that traverse southern Lebanon (Meirova and Hofstetter, 2013).

The seismicity is discerned in different spots, mainly west of the DST, including near the Gulf of Suez, in the Mediterranean Sea and northwest of the Gulf of Eilat's northern tip (an area not associated with known surface tectonic features), showing an asymmetric distribution. The asymmetricity is also observed in proximity to the DST main segments (e.g. the Arava and the Jordan Valley) with patches of seismicity slightly west of these segments. East of the DST, there is hardly any apparent seismic activity. The seemingly asymmetric pattern of deformation (Figs. 2.1; 2.4; 2.5) is to some extent an artefact of the low detectability of the seismic network in the eastern side of the DST and further east, in areas that are far away from the seismic stations (Fig. 2.2). The International Seismological Centre catalogue reveals large portion of events recorded east of the DST as well (Palano et al., 2013). However, the asymmetricity is also possibly of tectonic origin, considering the CGTF that divides the Israel-Sinai plate into two distinct provinces, and the existence of faults along the passive continental margins in the easternmost Mediterranean Sea.

2.4.1.2. Seismic moment density

The *seismic moment density* parameter is presented on a logarithmic scale due to its high variations (Fig. 2.5). Its distribution emphasises the seismicity along the DST, with similarity to the *earthquake density* distribution (Fig. 2.4). The Gulf of Eilat includes the largest recorded event, the $M_W = 7.2$ 1995 Nuweiba earthquake, two order of magnitudes larger than the second-largest event of the catalogue ($M_d = 5.6$, occurred twice; one of these events can be interpreted as an aftershock of a $M_d = 5.8$ 1993 shock that was dismissed in the relocation process). In terms of *Mo density,* it is 15.7 compared with 13.7 of the $M_d = 5.6$ event, on the logarithmic scale. Since the seismic moment released by the $M_W = 7.2$ 1995 event is significantly higher comparing to the total cumulative seismic moment from all the other events in its area, it can be clearly seen as a white circle within the gulf. More than 16 other events in the magnitude range of $5.0 < M_d < 5.6$ were accommodated by the gulf and its surrounding flanks. While these events are hardly distinguishable in Fig. 2.5, other events in the same magnitude range are noticeable in less seismically-active zones. These include the $M_w = 5.1$ 2004 event in the Dead Sea, the $M_d = 5.3$ 1984 event near the Carmel fault, and two other events of $M_{\mathrm{d}} = 5.2$ and $M_{\mathrm{d}} = 5.5$ in the seismic patch southwest of the Roum fault, and offshore in the Mediterranean, respectively.

In contrast with the distribution of the *earthquake* density, the *Mo density* does not display spatial clusters significantly, unless they consist of high magnitude events. This contrast is predominant in the Sea of Galilee, which contains high density of events (to some extent, related to the 2013 swarm; Fig. 2.4) but is less significant in its *seismic moment density* (Fig. 2.5). Another example is the seemingly wide zone of deformation in the Gulf of Eilat according to the *Mo density* (Fig. 2.5), much wider than the relatively narrow gulf. This width is not observed in the same level according to the *earthquake density* (Fig. 2.4), thus it could be enhanced by poorly-constrained location of relatively strong events, far away from the network coverage (Fig. 2.2). A comparison of the two maps reveals that small to medium events ($3 < M_d < 5$, corresponding to $10.3 < \log [M_o\ kernel\ density] < 12.9$) are not necessarily accompanied by many micro-earthquakes in their proximity. Nonetheless, the seismic network is capable of detecting such events far away from the stations, where micro-earthquakes are below the detection threshold. Therefore, this statement is evident mainly within the seismic network (Fig. 2.2) and could not be ascribed to the Gulf of Eilat (apparent-) deformation zone edges, which are not accompanied by high values of *earthquake density*. In general, within areas of high detection, the *earthquake density* and the *seismic moment density,* which are mostly independent, seem to complement one another for mapping active tectonic sources.

2.4.1.3. Earthquake average depth

The reliability of the *earthquake average depth* is sensitive to a few factors. Since it is statistic-dependent, the higher the *earthquake density* is, the more reliable are its values. Another factor is the proximity to the seismic network, as hypocentres that are not spatially-bounded by seismic stations are doomed to have poor depth constraints. Thus, the reliability of this parameter is limited to earthquake-dense areas within the network coverage. Indeed, the *earthquake average depth* (Fig. 2.6) receives reasonable values in these areas, and sometimes unusual values in areas of sparse seismicity and/or beyond the network coverage. Within the reliability zones of this parameter, assuming that the weighting-based processing circumvents the error depth, patches of seismicity can be characterised by their average depth. Nevertheless, this kind of interpretation should be taken with a grain of salt, due to the lack of clarity of the depth distribution of the events. For instance, epicentres at the same location can represent more than one seismic patch within a fault.

Despite the aforementioned limitations, a few statements can be said according to the average depth distribution (Fig. 2.6.): 1) The Arava valley contains earthquakes, or seismic patches, within a variety of depths, from a few kilometres and up to ~25km or even deeper. 2) The average depth in the Dead Sea basin is relatively deep, with one patch at ~25km or deeper. 3) An area of shallow seismicity is captured in the area of the Nahal Tirza, in contrast to much deeper seismicity north of it towards the Gilboa fault. 4) The Sea of Galilee is characterised by shallow earthquakes, while north of it, towards the Hula basin and within it, hypocentres are deeper in average. In between the basins, deeper seismicity is apparent at the Jordan George segment. 5) Deeper seismicity appears northwest of the Sea of Galilee, while north of it, west of the Hula basin, the area is characterised once more by shallow seismicity. 6) The *earthquake average depth* variations along the DST approximately fit the seismogenic depth profile (Wetzler and Kurzon (2016), which is in agreement with the thermal profile (Shalev et al. (2013). More about the earthquake depth distribution is in Chapter 4.

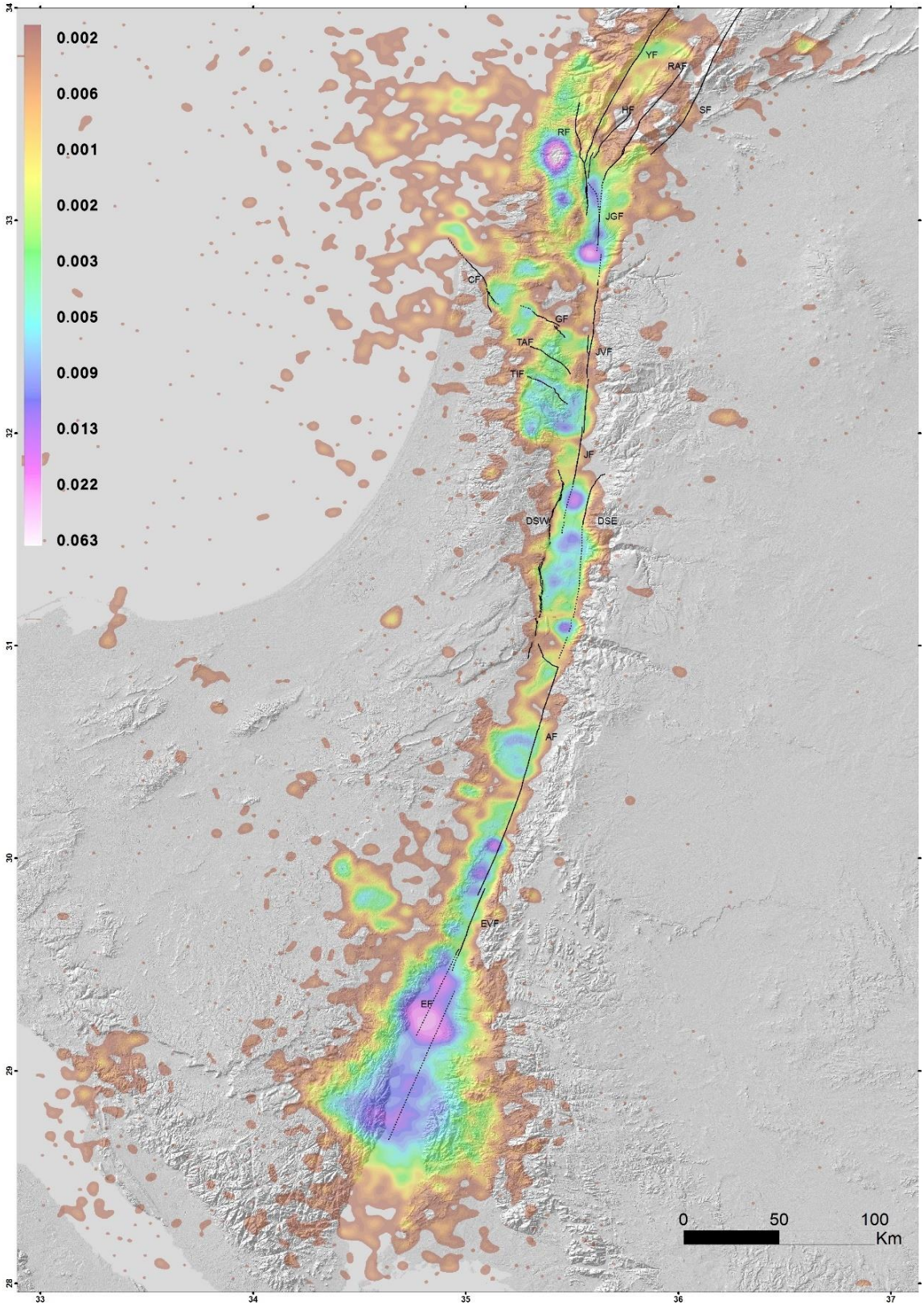

Fig. 2.4: The *earthquake density* distribution. Colours and corresponding numbers indicate the value in $[events/km^2/years]$. Black lines represent the main fault segments of the DST and the CGTF (see chapter 3). Abbreviations: AF - Arava fault; CF - Carmel fault; DSE - Dead Sea east marginal fault; DSW - Dead Sea west marginal fault; EF - Eilat fault; EVF - Evrona fault; GF - Gilboa fault; JF - Jericho fault; JGF - Jordan gorge fault; RAF – Rachaiya fault; RF - Roum fault; SF - Serghaiya fault; TAF - Tayasir fault; TIF - Tirza fault; YF - Yammuneh fault.

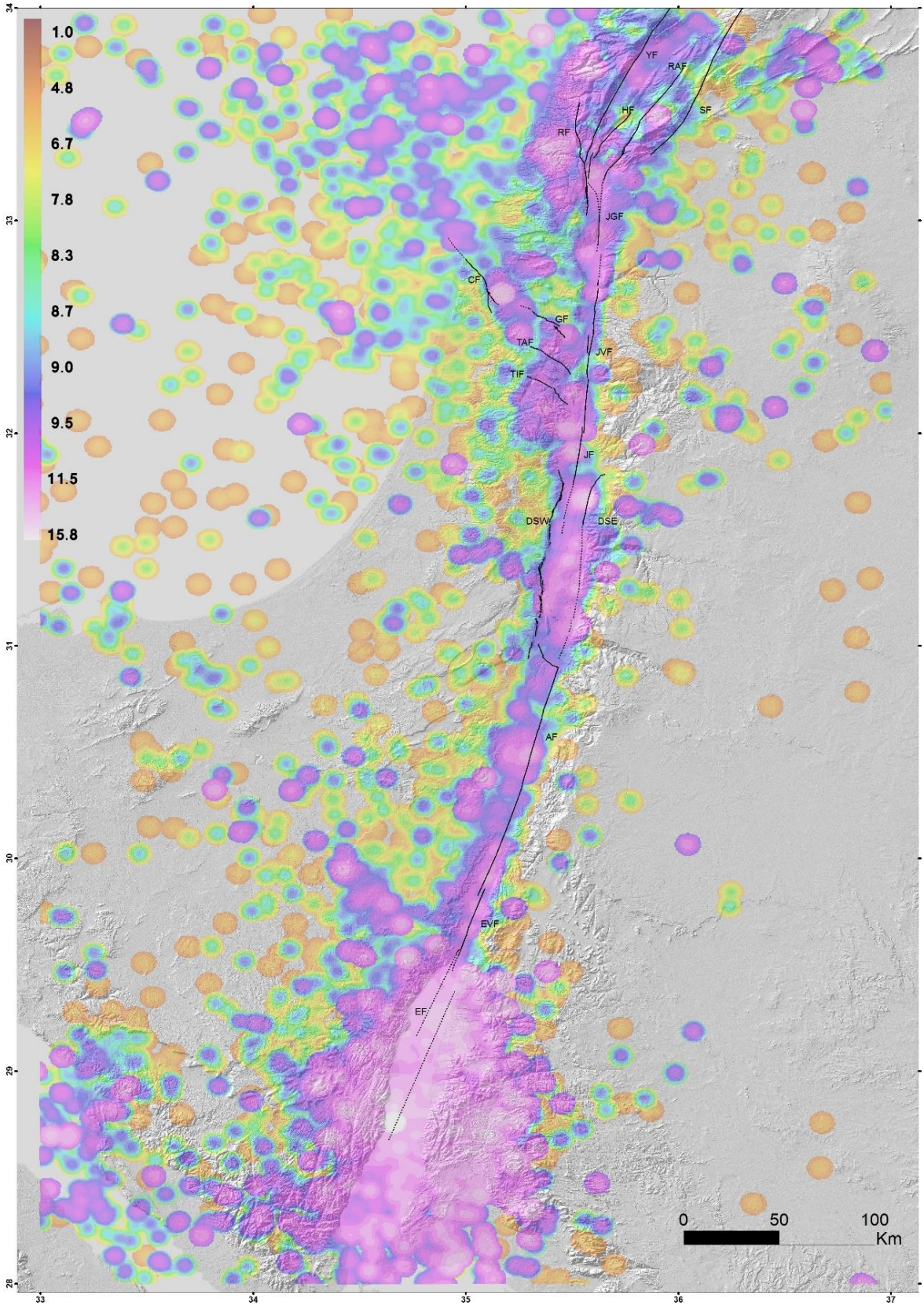

Fig. 2.5: The *seismic moment density* distribution. Colours and corresponding numbers indicate the value in log$[joule/km^2/years]$. Black lines represent the main fault segments of the DST and the CGTF (see chapter 3). See Fig. 2.4 for Abbreviations.

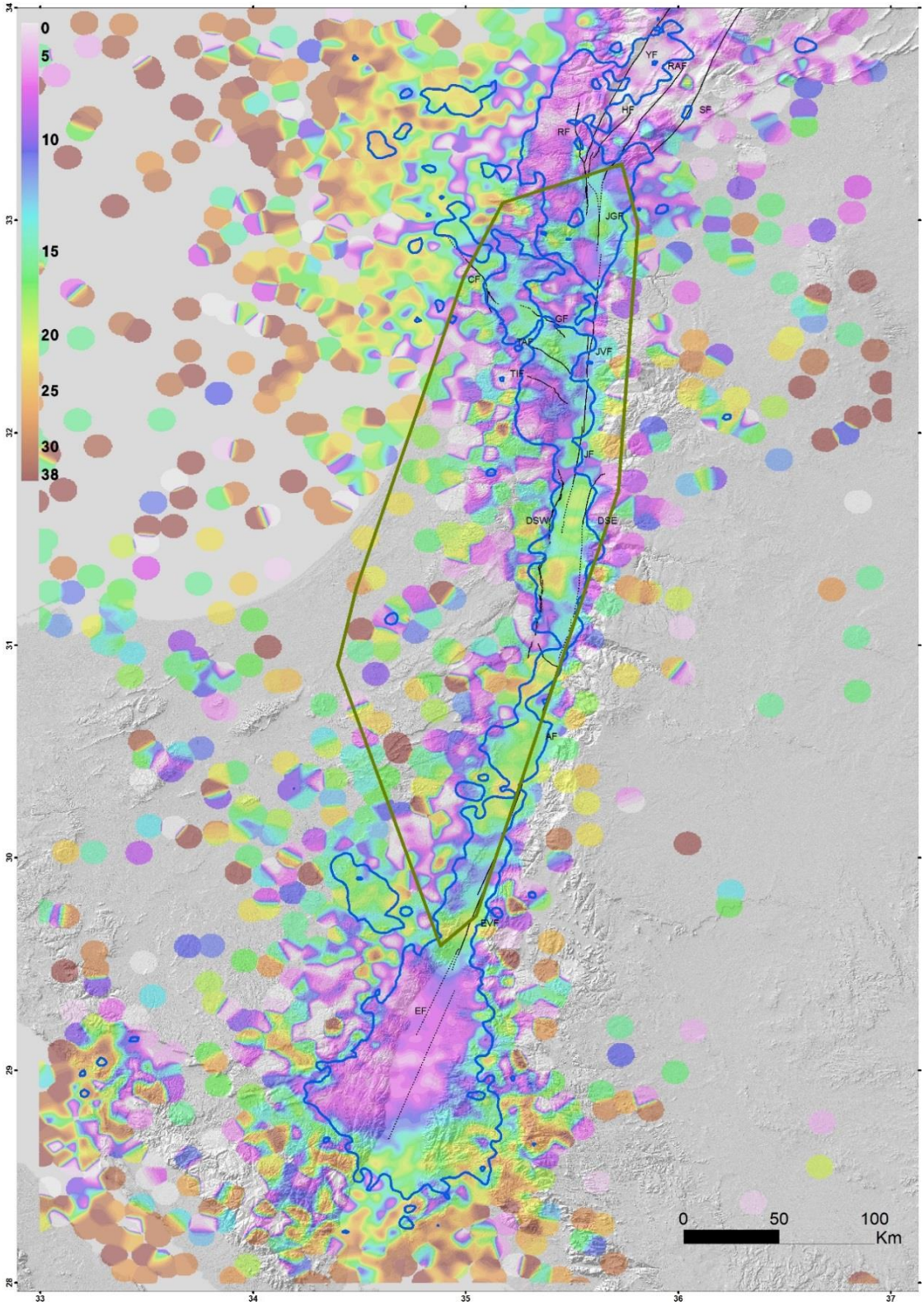

Fig. 2.6: The *earthquake average depth* distribution. Colours and corresponding numbers indicate the value in$[km]$. The circle-shape forms, where the seismicity is sparse, are due to the spatial processing of the data (see section 2.3). Green lines represent the spatial limits of the seismic network coverage area (as appear in Fig. 2.2), where the depth constraint is significantly better. Blue lines are contours of *earthquake density* value that corresponds to ten earthquakes in a distance of 3-km from a grid point. Above this value, meaning within the contour polygons, the results are much more reliable due to statistic considerations. Black lines represent the main fault segments of the DST and the CGTF (see chapter 3).

2.4.2. The frequency-magnitude relation

The frequency-magnitude parameters are deduced in four spatio-temporal frames, for their reliable determination: within two different areas: 1) on a wide regional scale, between the latitudes 28–34°N and the longitudes 33–37°E; 2) within the seismic coverage area (Fig. 2.2); and within the complete investigated time window (1983–2017) and the period of 2007–2017 separately. The year of 2007 is chosen as a reference point a in order to compare the analysis with a recently published paper (Pinsky and Shapira, 2017), and due to some upgrades in the ISN around this year (Andrey Polozov, personal communication).

2.4.2.1. Wide regional scale

2.4.2.1.1. Determining the completeness magnitude

The Kolmogorov-Smirnov test for the 1983–2017 data clearly shows that the best fit between the data and the model-function is reached at $M_c = 4.0$ (Fig. 2.7) with $\Delta S = 0.011$. Although it is a rather high magnitude for a detection threshold, it is reasonable since some earthquakes were recorded far from the network coverage. The smallest M_c that corresponds to a peak of $\Delta S < 0.05$, however, is reached at $M_c = 2.0$, with $\Delta S = 0.038$. The same test, when limiting the catalogue to 2007–2017 data, shows peaks at $M_c = 1.5, 2.0, 3.5$ (Fig. 2.8). Their goodness of fit is quite the same ($\Delta S = 0.036, 0.035, 0.039$, respectively). A comparison between the two tests, taken for the two periods, suggests that the potential M_c drop half a magnitude when the later period (2007–2017) is tested, with a new potential peak in between ($M_c = 2.0$). Considering the nearly-similar ΔS values of the 2007–2017 data, a 'conservative' approach would favour the higher M_c (i.e. without assuming better detection threshold and lower M_c). However, it is necessary to observe the fit of the corresponding linear fits to the data (Figs. 2.9; 2.10).

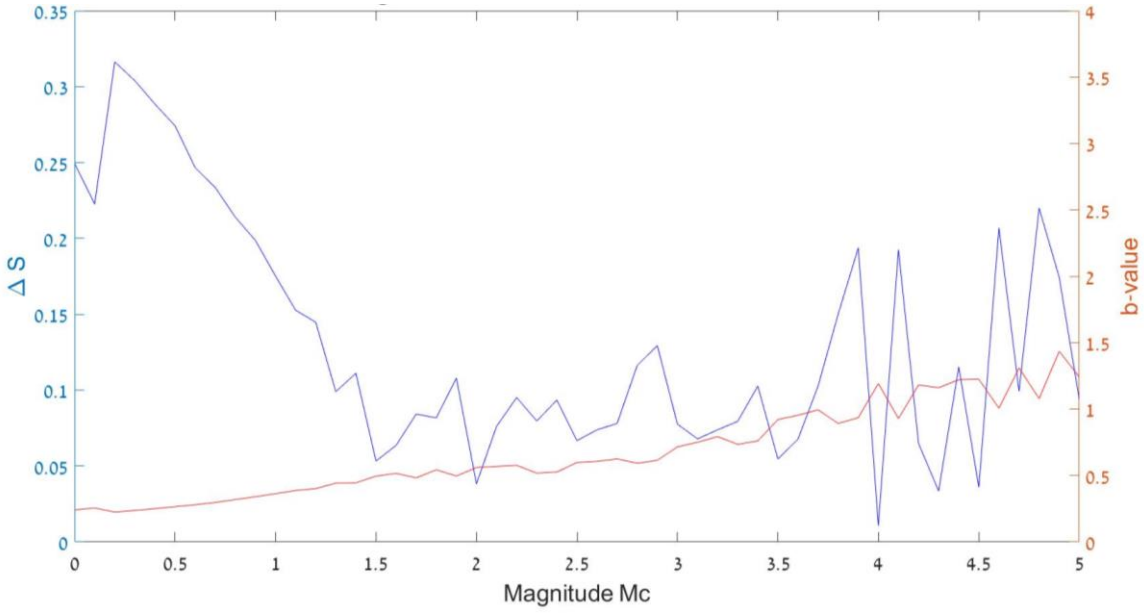

Fig. 2.7: The Kolmogorov-Smirnov test results for the 1983–2017 period, within the latitudes 28–34°N and longitudes 33–37°E.

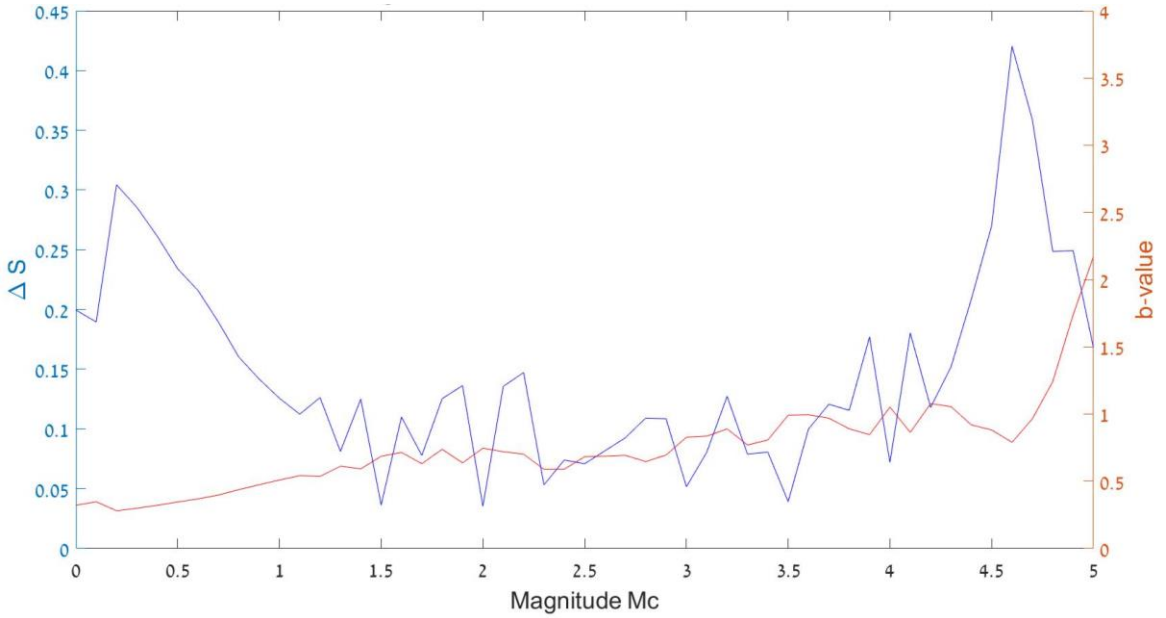

Fig. 2.8: The Kolmogorov-Smirnov test results for the 2007–2017 period, within the latitudes 28–34°N and longitudes 33–37°E.

2.4.2.1.2. Determining the *b-value*

A total of 6792 events are used for the 0.56 *b-value* deduction from the 1983–2017 data, where $M_c = 2.0$. Although the linear fit of the Gutenberg-Richter law concurs with the data for magnitudes below $M_d \cong 3.5$ or $M_d \cong 4.0$ (Fig. 2.9), the slope within $\sim 2 \geq M_d \geq \sim 5$ changes as a function of the magnitude and does not show a straight line. It highly suggests that the catalogue is incomplete for $M_d < 4.0$ so this linear fit does not represent the regional *b-value*. The linear fit for $M_c = 4.0$, however, is in tune with the data below $M_d \cong 5.5$ (Fig. 2.9). It is obtained from a 1.19 *b-value*, by utilising 418 events. The single $M_d > 5.6$ event (the 1995 $M_W = 7.2$ Nuweiba earthquake) flattens the $5.7 \geq M_d \geq 7.2$ data. The absence of $5.7 \geq M_d > 7.2$ events may trigger artefacts in the Kolmogorov-Smirnov test results, if ΔS is achieved from high misfits between the data and the model-function within this magnitude range. However, both the linear fits (Fig 2.9) and the Kolmogorov-Smirnov test (Fig. 2.7) clearly support a completeness magnitude of $M_c = 4.0$. This high completeness magnitude coincides with the intense seismic activity during 1983–2017 within the Gulf of Eilat, and to some extent in southern Lebanon, both are beyond the network coverage, in a distance of up to 150-km from the nearest station. Since the network performances were limited in the beginning of the 1983–2017 period, compared with the current state, a detection threshold of 4.0 is reasonable.

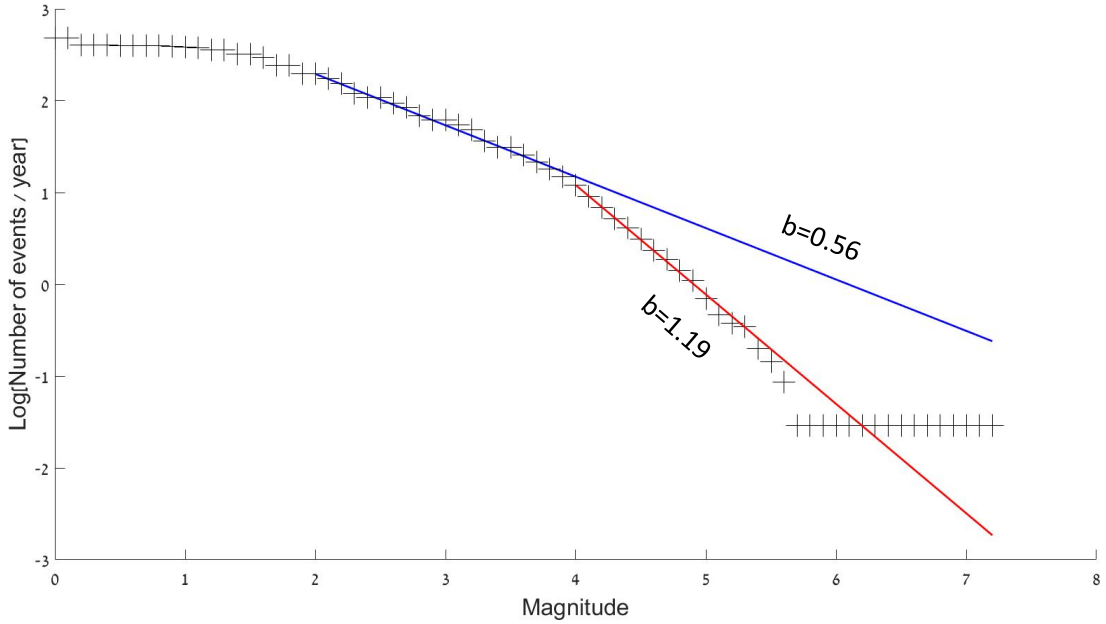

Fig. 2.9: The frequency-magnitude relation for all earthquakes recorded during the 1983–2017 period, within the latitudes 28–34°N and longitudes 33-37°E. Blue and red lines represent the Gutenberg-Richter linear fit for completeness magnitudes M_c of 2.0 and 4.0, respectively. In this figure and the followings, the length of the line corresponds to the magnitude range of the data used to calculate each line.

As for the 2007–2017 data, three linear fits are presented below, for the optional $M_c = 1.5$, 2.0, 3.5 (Fig. 2.10), suggested by the inconclusive Kolmogorov-Smirnov test results. 1970, 926, and 84 events are used for each case, with *b-values* of 0.69, 0.75 and 0.99, respectively (Table 2.1). The data show a better linear behaviour comparing to the 1983–2017 data (Figs. 2.9), emphasising the improvement of the network by the decrease of the detection threshold in the last 10 years of the catalogue. However, the scatter of the data in the later period is still somewhat curved in magnitudes lower than $M \cong 3.5$ (Fig. 2.10). This implies that a small portion of the $M < 3.5$ events were not recorded by the network. It is reinforced by Pinsky and Shapira (2017), whose analysis suggests a detection for $M_d \geq 2.0$ of perhaps 100% probability in most of the whole investigated area in this study, for the period of 2007–2014, but the southern ~half of the Gulf of Eilat is an exception, with probability that drops to lower percentages. Hence, $M_c = 3.5$ is suggested as the preferable option.

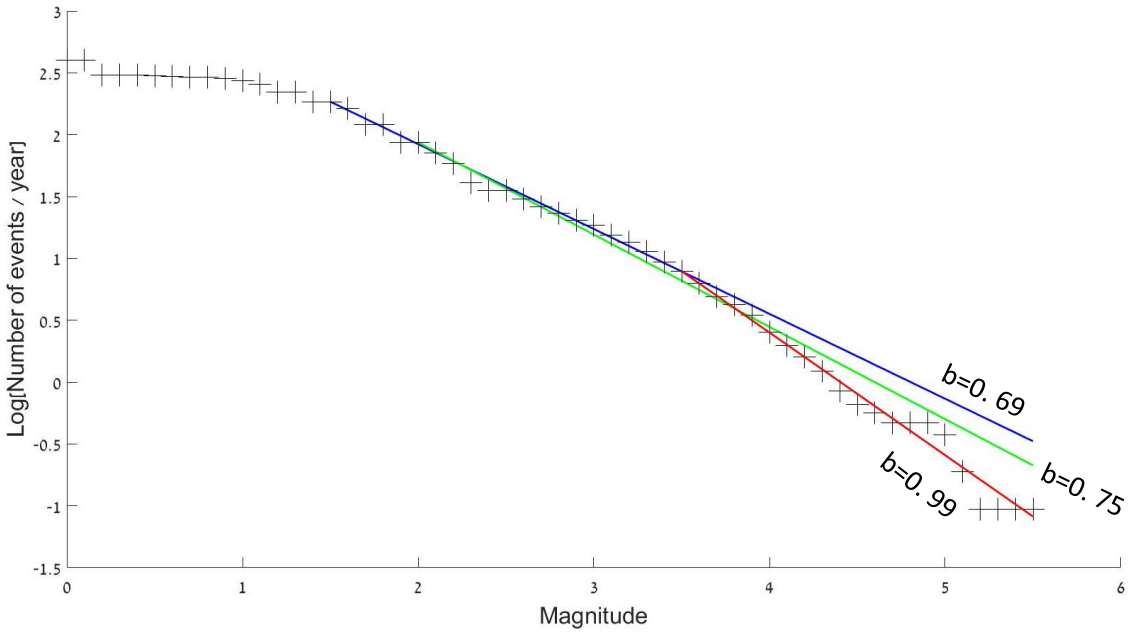

Fig. 2.10: The frequency-magnitude relation for all earthquakes recorded during the 2007–2017 period, within the latitudes 28–34°N and longitudes 33–37°E. Blue, Green and red lines represent the Gutenberg-Richter linear fit for completeness magnitudes $M_c = 1.5, 2,0, 3.5$, respectively.

The seismicity parameters obtained based on the two periods (1983–2017; 2007–2017), and pertinent data for the M_c determination, are presented in Table 2.1. In both periods, the obtained *b-value* is not quite stable around the suggested completeness magnitudes ($M_c = 4.0, 3.5$, respectively; Figs. 2.7; 2.8). Since these magnitudes are associated with positive peaks of the *b-value* (Fig. 2.7; 2.8), it implies that lower *b-values* might be better options (perhaps with lower completeness magnitudes). This contradiction perhaps indicates the disadvantages of the Kolmogorov-Smirnov test, which according to this study, is insufficient to determine the completeness magnitude without being manually examined, or by using an additional tool. The comparison between the two periods suggest a magnitude drop of ~0.5 in the detection threshold. This decrease is reasonable, considering the improvement of the network, on the one hand, but on the other hand the geographical barriers (seas and borders) that still limit the spatial distribution of the stations.

Period	**M_c**	**ΔS**	**Events (total)**	**Events of $M_d \geq M_c$**	***a-value***	***b-value***	**Max. observed magnitude**
1983–2017	2.0	0.038	16725	6792	3.41	0.56	7.2
1983–2017	**4.0**	**0.011**	**16725**	**418**	**5.85**	**1.19**	**7.2**
2007–2017	1.5	0.036	4293	1970	3.30	0.69	5.5
2007–2017	2.0	0.035	4293	926	3.43	0.75	5.5
2007–2017	**3.5**	**0.039**	**4293**	**84**	**4.37**	**0.99**	**5.5**

Table 2.1. Seismicity parameters obtained within the latitudes 28-34°N and the longitudes 33-37°E, in each case of optional completeness magnitudes. The *a* and *b* parameters, ΔS of the Kolmogorov-Smirnov test, the maximum observed magnitude, the number of earthquakes in total and those used for the *b-value* calculation were added too, in order to understand the goodness and limitations of the calculation. Rows that represent the preferable options are in bolded blue.

2.4.2.2. Within the seismic network coverage area

2.4.2.2.1. Determining the completeness magnitude

A completeness magnitude of $M_c = 2.0$ is inferred for the 1983–2017 period, when $\Delta S = 0.018$, reinforced by a relatively stable *b-value* (Fig. 2.11). The Kolmogorov-Smirnov test for the 2007–2017 period is even more unequivocal, with a peak at $M_c = 1.5$, $\Delta S = 0.032$ and a relatively stable *b-value* (Fig. 2.12).

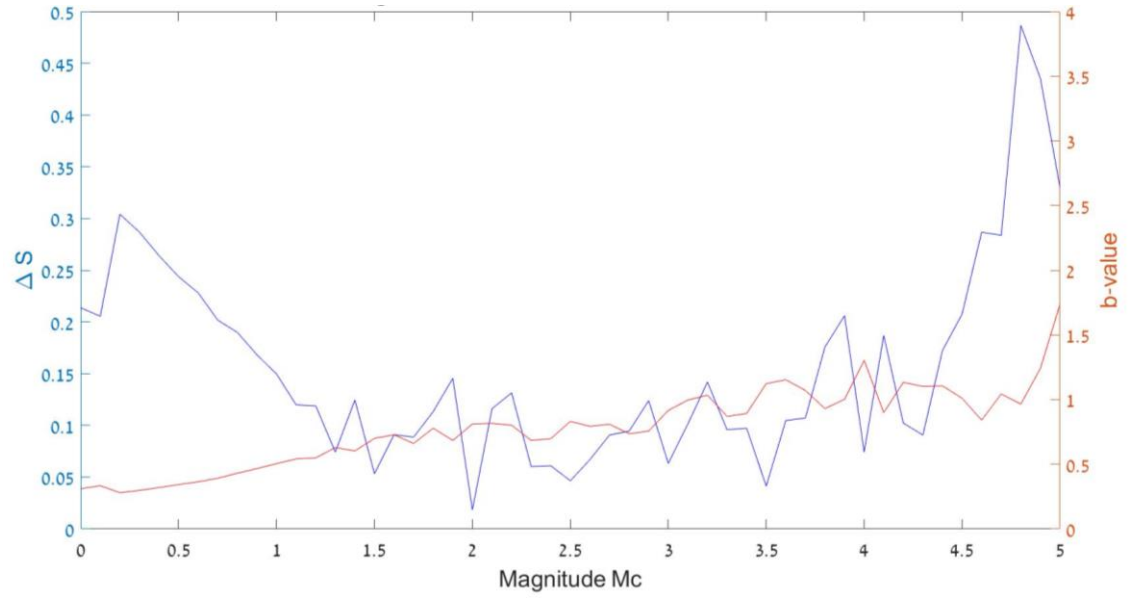

Fig. 2.11: The Kolmogorov-Smirnov test results for the 1983–2017 period, within the network coverage area.

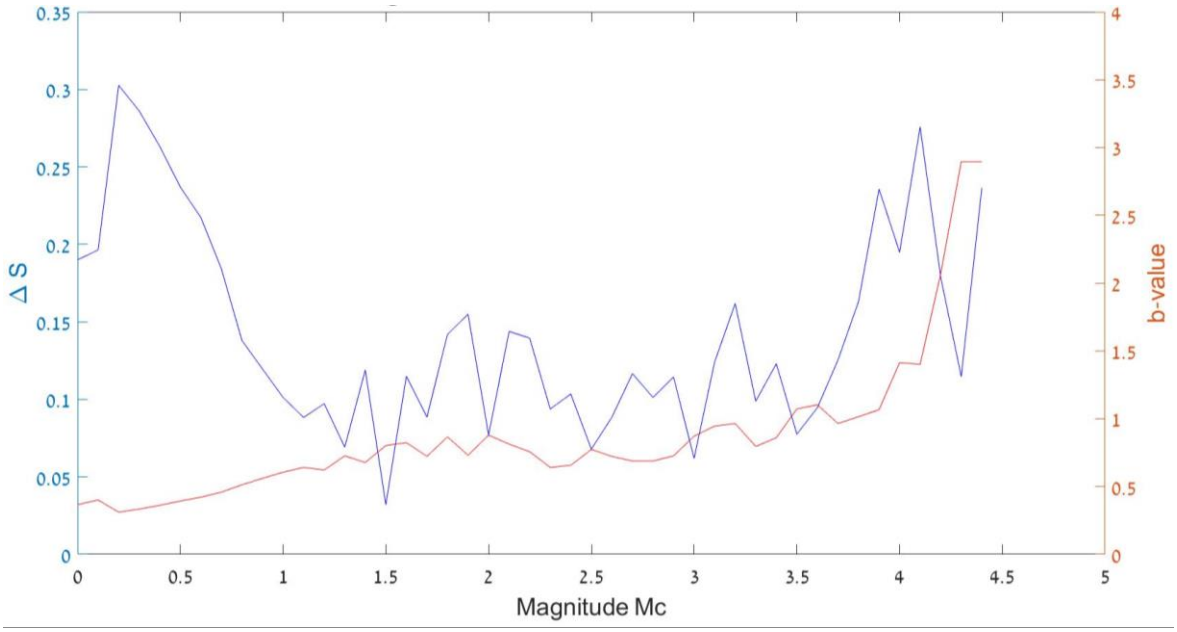

Fig. 2.12: The Kolmogorov-Smirnov test results for the 2007–2017 period, within the network coverage area.

2.4.4.2.2. Determining the *b-value*

A *b-value* of 0.81 is achieved when $M_c = 2.0$, by utilising 1221 events (Table 2.2). Linear fits are presented also for the less preferable peak in the Kolmogorov-Smirnov test, where $M_c = 3.5$ (Fig. 2.13). In this case, the goodness of fit is worse ($\Delta S = 0.041$ versus $\Delta S = 0.018$) and the *b-value* (1.16) is poorly constrained, deduced from 76 events. Thus, the most reliable *b-value* is achieved when $M_c = 2.0$. Furthermore, Shapira (1992) estimated independently that by very high probability, all $M \geq 2.0$ events were recorded in an area that approximately overlaps the network coverage defined in this study, during the years 1984–1991. Since then, the network detectability has only improved. If $M_c = 2.0$, the linear fit suggests that the data is slightly incomplete for the higher ($M > 4.0$) magnitudes (i.e. less earthquakes than expected from the Gutenberg-Richter law; Fig. 2.13). A synthetic increase of relatively-high magnitude events to the catalogue, reveals that seven or eight $4.5 \leq M_d \leq 5.3$ earthquakes are needed to compensate the incompleteness. The lack of these earthquakes is possibly circumstantial but may also imply a (quasi-?) 'characteristic' behaviour, which is characterised by a relative lack of events in the magnitude range that is slightly lower than the characteristic magnitude range.

Different completeness magnitudes in the range of $2.0 < M_c < 3.5$ are possible but are less likely to represent the data, since they are less supported by the Kolmogorov-Smirnov test (Fig. 2.11). However, the peaks suggested by the test, within this range, are also presented (M_c = 2.5 and *b-value* of 0.83, and M_c = 3.0 and *b-value* of 0.92). The analysis of Shapira (1992) and the only few 'missing' larger-magnitude events, suggest to negate the M_c = 3.0 option as well. Nonetheless, M_c = 2.5 is a plausible option. Both options of M_c = 2.0, 2.5 yield a similar *b-value* (0.81, 0.83), respectively. The M_c = 2.0 is chosen here as preferable, since it is supported by the Kolmogorov-Smirnov test and due to the independent analysis of Shapira (1992). However, despite his analysis, it is still possible that a few $2.0 \leq M < 2.5$ were not recorded. Thus, the optional M_c = 2.5 is considered here as an alternative.

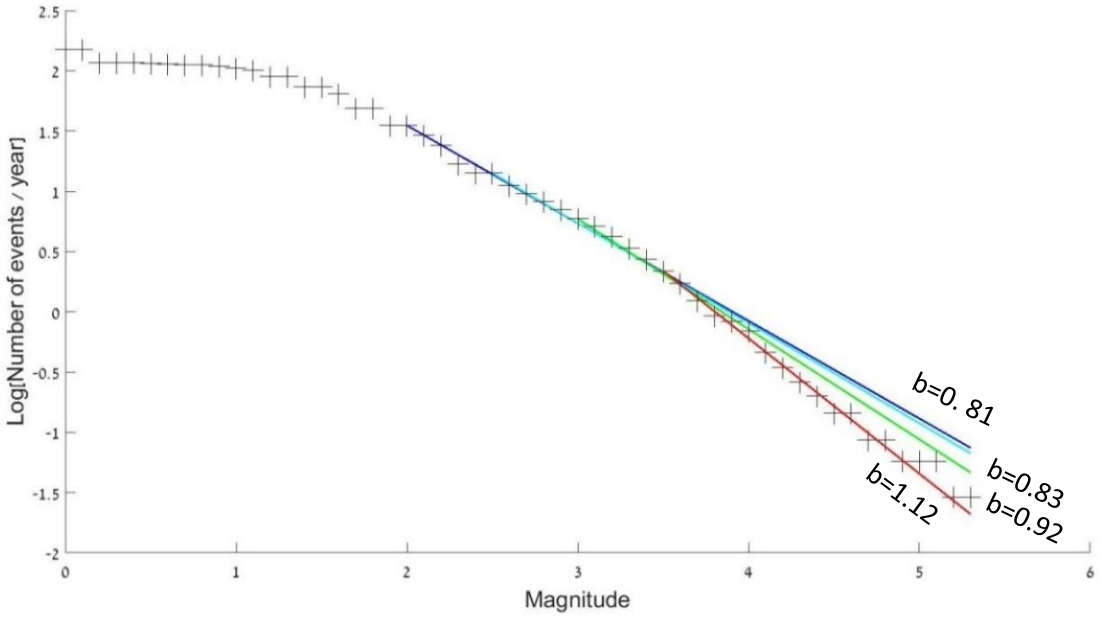

Fig. 2.13: The frequency-magnitude relation for all earthquakes recorded during the 1983–2017 period, within the network coverage area. Blue, pale blue, green and red lines represent the Gutenberg-Richter linear fit for completeness magnitudes $M_c = 2.0, 2.5, 3.0, 3.5$, respectively.

A *b-value* of 0.80 is obtained when $M_c = 1.5$ in the 2007–2017 period, utilising 731 events. The linear fit (Fig. 2.14) and the Kolmogorov-Smirnov test (Fig. 2.12) unambiguously agree that $M_c = 1.5$ is the detection threshold. Accordingly, Pinsky and Shapira (2017) revealed that during the period of 2007–2014, 100% of the $M_d \geq 1.5$ were recorded within the area defined here as the network coverage, and even beyond. Therefore, a well-constrained 0.80 *b-value* is deduced from the 2007–2017 period.

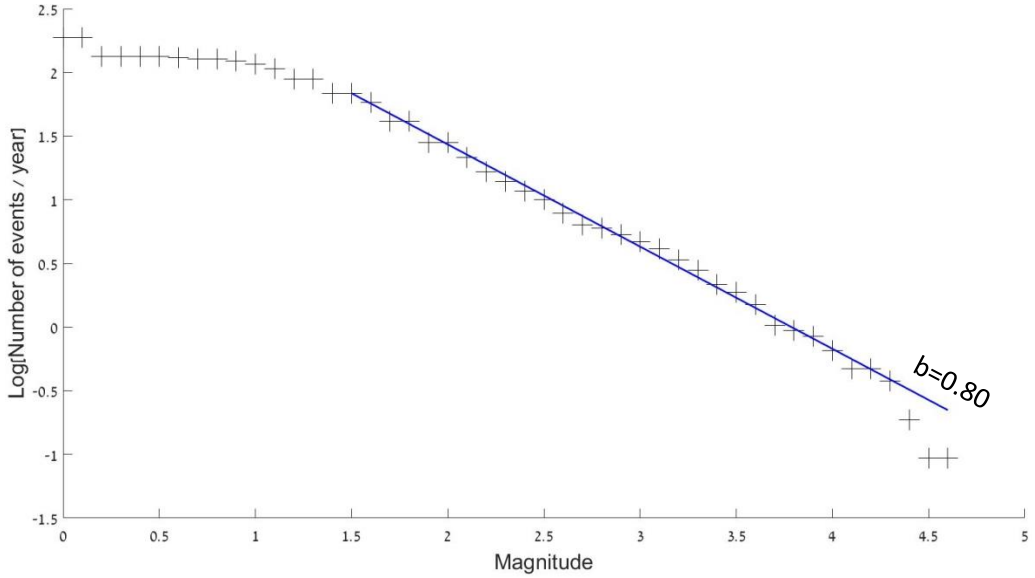

Fig. 2.14: The frequency-magnitude relation for the 2007–2017 period, within the network coverage area. Blue line represents the Gutenberg-Richter linear fit for $M_c = 1.5$.

Period	M_c	ΔS	Events (total)	Events of $M_d \geq M_c$	*a-value*	*b-value*	Max. observed magnitude
1983–2017	**2.0**	**0.018**	**5212**	**1221**	**3.17**	**0.81**	**5.3**
1983–2017	2.5 *	0.046	5212	492	3.23	0.83	5.3
1983–2017	3.0	0.063	5212	205	3.52	0.92	5.3
1983–2017	3.5	0.041	5212	76	4.27	1.12	5.3
2007–2017	**1.5**	**0.032**	**2003**	**731**	**3.04**	**0.80**	**4.6**

Table 2.2. Seismicity parameters within the network coverage area, in each case of an optional completeness magnitude: the *a* and *b* parameters, Δ*S* of the Kolmogorov-Smirnov test, the maximum observed magnitude, the number of earthquakes in total and those that were used for the *b-value* calculation were added too, in order to understand the goodness and limitations of the *b-value* calculation. Rows that represent the preferable options are in bolded blue. Asterisk denotes an alternative for the bolded line within the same time window.

2.4.2.3. The *b-value* and recurrence intervals

Table 2.3 summarises the seismicity parameters presented in Tables 2.1; 2.2. It includes the ensuing recurrence intervals of medium to strong earthquakes, and other seismicity parameters that contribute to the understanding of the goodness and the limitations of the *b-value* calculations.

The different spatio-temporal frames reveal recurrence intervals of the same magnitude range that highly differ, up to three orders of magnitudes, particularly when comparing to these yielded from the non-preferable M_c - *b-value* sets. The whole investigated area is expected to show higher frequency of earthquakes, within all ranges, since: a) it is larger than the seismic network coverage; b) it includes the two most seismically active areas: the Gulf of Eilat and within southern Lebanon. Although the recurrence intervals are indeed shorter than these obtained from the network coverage area, a comprehensive examination should be carried to determine if they accord with further details (e.g. the DST length in each frame). Moreover, the whole duration (1983–2017) within the larger area is the only frame that includes the 1993 $M_d = 5.8$ and the $M_W = 7.2$ 1995 Nuweiba earthquake and their aftershocks. These aftershocks may bias the *b-value* towards high values due to many events of a magnitude slightly above the detection threshold, and in turn, to bias the recurrence intervals. These issues are discussed in section 5.2.

Area	**Period**	**M_c**	**ΔS**	**Events total num.**	**Events of $M_d \geq M_c$**	***a-value***	***b-value***	**Max. observed Magnitude**	**Total *Mo* release [Joule]**	**Recurrence Interval [years]** $5.0 \leq M < 6.0$	**Recurrence Interval [years]** $6.0 \leq M < 7.0$	**Recurrence Interval [years]** $7.0 \leq M < 8.0$
Lat. 28-34°N and Lon. 33-37°E	1983 – 2017	2.0	0.038	16725	6792	3.41	0.56	7.2	2.72E+19	0.3	1	4
		4.0	**0.011**	**16725**	**418**	**5.85**	**1.19**	**7.2**	**2.72E+19**	**1.4**	**21**	**334**
	2007 – 2017	1.5	0.036	4293	1970	3.30	0.69	5.5	4.07E+17	2	8	40
		2.0	0.035	4293	926	3.43	0.75	5.5	4.07E+17	2	14	75
		3.5	**0.039**	**4293**	**84**	**4.37**	**0.99**	**5.5**	**4.07E+17**	**4**	**43**	**417**
Network coverage area	1983 – 2017	**2.0**	**0.018**	**5212**	**1221**	**3.17**	**0.81**	**5.3**	**2.70E+17**	**9**	**59**	**381**
		2.5 *	0.046	5212	492	3.23	0.83	5.3	2.70E+17	10	67	453
		3.0	0.063	5212	205	3.52	0.92	5.3	2.70E+17	13	107	884
		3.5	0.041	5212	76	4.27	1.12	5.3	2.70E+17	24	316	4192
	2007 – 2017	**1.5**	**0.032**	**2003**	**731**	**3.04**	**0.80**	**4.6**	**4.45E+16**	**11**	**71**	**451**

Table 2.3: Seismicity parameters and recurrence intervals of medium to large earthquakes, in each of the four spatio-temporal frames, and all optional completeness magnitudes as appear in tables 2.1; 2.2. Data from the later period (2007–2017) is filled in darker grey. The preferable completeness magnitudes and related data are in bolded blue, as also appear in tables 2.1; 2.2. Asterisk denotes that the results within the line are an alternative for the bolded line, within the same spatio-temporal frame.

2.4.2.4. Stability test for the *b-value*

The time-dependency of the *b-value* is further investigated in both areas, in time windows of 11 and 16 years within the period of the earthquake recordings (Figs. 2.15–2.18). The *b-value* is quite stable in the larger area when its determination is sufficiently constrained (Figs. 2.15; 2.16). The $M_d = 5.8$ 1993 and the $M_w = 7.2$ 1995 Nuweiba earthquakes were followed by many aftershocks, some of which are close or slightly above the catalogue detection threshold (i.e. M $\cong M_c = 4.0$), probably leading to biased high *b-values* (~1.2) within all the time-windows that include at least one of these events and their aftershocks. Although the post-1998 time-windows are not 'contaminated' by aftershocks, their *b-values* are very poorly constrained. The last 11-year time-window (2007–2017) yields approximately the same *b-value* (~1.0) when utilising 84 events of $M_d \geq 3.5$ (Table 2.3) instead of only 23 $M_d \geq 4.0$ earthquakes (Fig. 2.15). However, this *b-value* is still much less constrained comparing to these obtained within the network coverage (Table. 2.3; Figs. 2.17; 2.18) due to lower detection threshold of the latter.

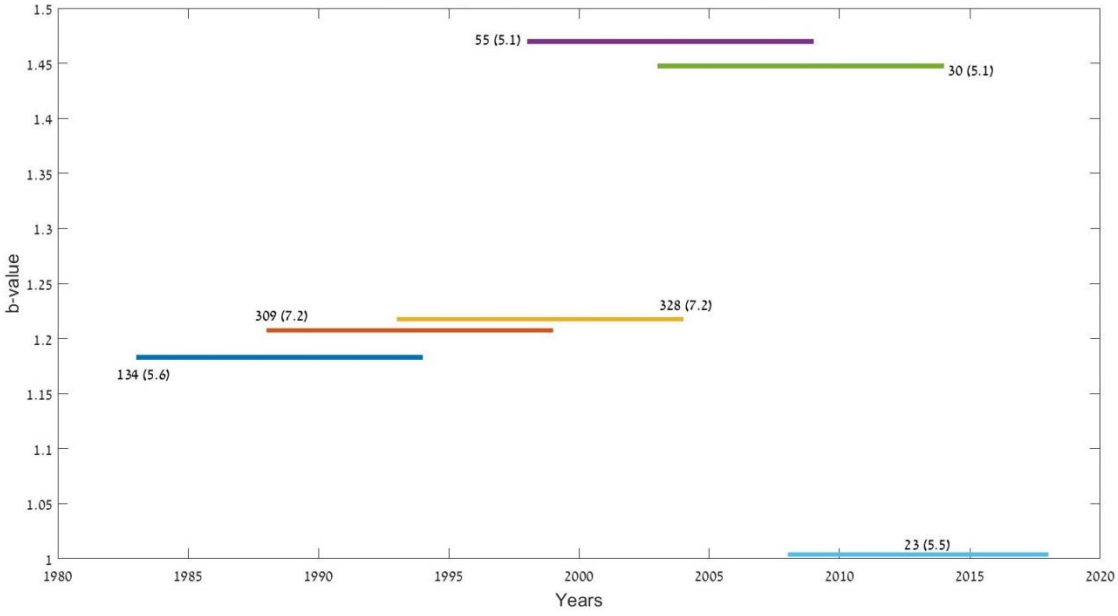

Fig. 2.15: The variation of the *b-value* in 11-year time windows, and time intervals of 5 years, in the whole investigated area. A completeness magnitude of $M_c = 4.0$ is assumed for all cases. The number of events of at least M_c and the maximum observed magnitude (in brackets), which were utilised for the *b-value* calculation, are mentioned next to each line.

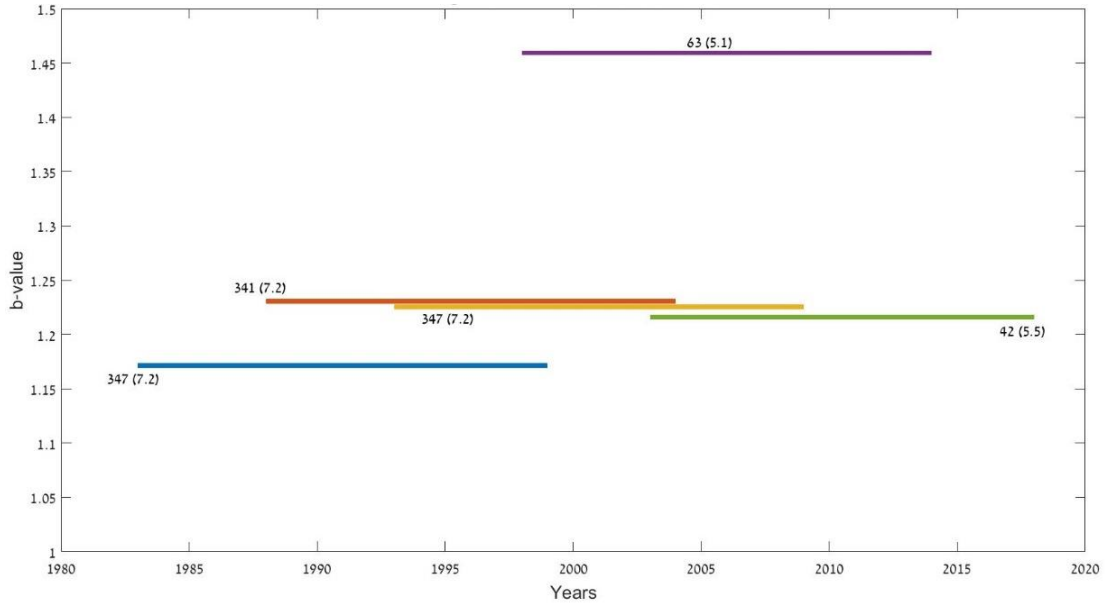

Fig. 2.16: The variation of the *b-value* in 16-year time windows, and time intervals of 5 years, in the whole investigated area. A completeness magnitude of $M_c = 4.0$ is assumed for all cases. The number of events of at least M_c and the maximum observed magnitude (in brackets), which were utilised for the *b-value* calculation, are mentioned next to each line.

A more robust determination of the *b-value* is achieved within the network coverage area, due to higher number of events utilised for the calculation, and higher magnitude differences between the completeness magnitude and the largest observed magnitude (Figs. 2.17–2.18 compared with Figs. 2.15–16), an outcome of the much lower completeness magnitude within the network coverage ($M_c = 2.0$ instead of 4.0 for the larger area). The variation of the *b-value* (~0.7 – ~0.9) is probably a reflection of changes of the seismicity pattern (e.g. the occurrence of aftershocks and swarms). These values reinforce the determination of a *b-value* of ~0.8, as deduced based on the episodes of 1983–2017, and 2007–2017 when $M_c = 1.5$, suggesting that over longer periods, the *b-value* is more stable within the network coverage, and receives a value approximately in the middle of the fluctuations' value.

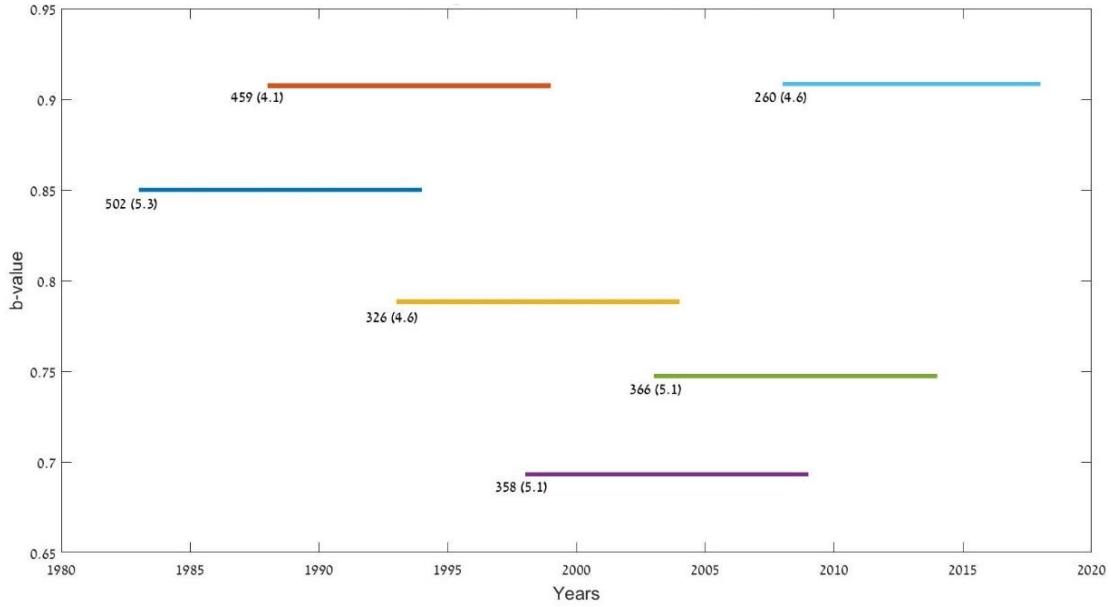

Fig 2.17: The variation of the *b-value* in 11-year time windows, and time intervals of 5 years, in the network coverage area. A completeness magnitude of $M_c = 2.0$ is assumed for all cases. The number of events of at least M_c and the maximum observed magnitude (in brackets), which were utilised for the *b-value* calculation, are mentioned next to each line.

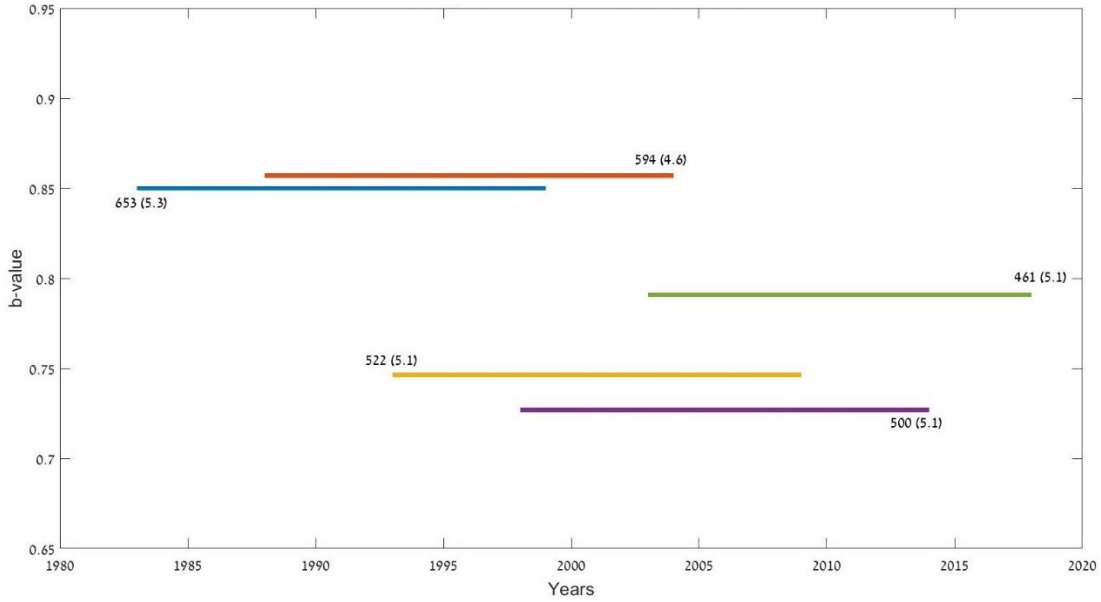

Fig. 2.18: The variation of the *b-value* in 16-year time windows, and time intervals of 5 years, in the network coverage area. A completeness magnitude of $M_c = 2.0$ is assumed for all cases. The number of events of at least M_c and the maximum observed magnitude (in brackets), which were utilised for the *b-value* calculation, are mentioned next to each line.

3. Quaternary faults: databases and maps

Criteria for faults that are relevant for earthquake resistant design of structures are primarily defined according to the specific seismic hazard (e.g. ground motion, surface rupture, tsunamis) and the specific designation of the structure. The criteria usually include the consideration of fault locations, the age of faulting, the relation to plate tectonics, fault lengths and slip rates. While the surface rupture hazard is more relevant for siting purposes, emphasising the importance of geological maps and their available resolution, ground motion predictions are highly dependent on the fault length and the slip rates, and/or the regional seismic activity. In this chapter, I focus on the mapping of faults for the surface rupture hazard for nuclear plants in Israel, and also highlight faults that have the highest likelihood to cause strong ground motions. Thus, the products of this chapter are also fundamental for other seismic-related hazards (e.g. surface shaking, landslides, and to some level - tsunamis).

The period of time between the latest activity of a fault and the present, for the fault to be classified as “capable” or “potentially active” for the siting purposes of nuclear power plants, usually varies between a few hundred thousand years to as early as the beginning of the Quaternary (~2.6Ma; e.g. Chapman et al., 2014). Faults that also may be considered as such, are those that have long-term slip rates of at least 0.02 mm/a, or that answer other criteria (e.g. geomorphologic expression; William Lettis, personal communication). As already discussed in Chapter 1, the Quaternary period in the Israel area samples well the present stress field (Eyal and Reches, 1983 for the Neogene-Quaternary stress field; supported by Marco, 2007; Garfunkel, 2011; Palano et al., 2013, specifically for the Quaternary). Thus, it is likely to assume that the probability of reactivation of faults, which were active during this period, is larger in comparison to other faults. Pragmatism has also played an important role, as the ability to separate faults of activity younger than a certain time limit is highly dependent of the stratigraphic configuration and the known age-constraints of young formations. In the case of fault activity < 0.5 Ma, this task is rather problematic in the Israel area, due to incomplete information for some of the Pleistocene formations. The Quaternary basis (~2.6 Ma), however, marks a better stratigraphic boundary so it is more useful to distinguish between geological formations that are younger or older than it. Therefore, it is adopted as the “base-time" for fault activity in this study. In other words, the decision to choose the Quaternary basis for this purpose is both pragmatic and scientific-based.

3.1. Previous works

There are limited works that were aimed to create databases of young mapped faults in Israel and its environs. Bartov et al. (2000) generated a catalogue and a map of faults, as a first step for creating a database of young faults. In the next step a database and a map of potentially active faults were presented (Bartov et al., 2002). This map was based on faults that offset Pliocene rocks or younger, while other criteria were implemented as well. This work was primarily based on the 1:200,000 scale geological map of Israel (Sneh et al.,

1998), and was later updated (Bartov et al., 2009). Sagy et al. (2012) published new criteria for mapping active and potentially active faults for the Israel Standard 413 "Design Provisions for Earthquake Resistance of Structures". The criteria and the associated map are being updated consistently (Sagy et al., 2013; 2016; 2017). Faults that show evidence of activity during the last 13ka are considered as active faults, while potentially active faults are defined according to the following criteria: 1) first and second order branches of active faults; 2) evidence of being branches of the DST; 3) evidence of surface rupture during the period of 35–13ka.

3.2. Geological database

I use geological maps of the Geological Survey of Israel (GSI) as the primary sources for mapping Quaternary faults. Seventy map sheets in the scale of 1:50,000 are available for this study (out of the 79 sheets required to cover the whole state of Israel; Appendix 1.1). As geological maps are updated with time, an effort has been made to analyse the most updated versions. The 1:200,000 scale geological map of Israel (Sneh et al., 1998) is utilised where 1:50,000 data are absent. In the area of Eilat, the 1:10,000 scale hazard map (Wieler et al., 2017) is used. I also included the fault map for the Israel Standard 413 in order to add a few “potentially active faults” (Sagy et al., 2017) as fault branches, in case they did not match any of the current criteria (see the criteria section below), and for more accurate fault locations. Further information that aids to constrain fault activity is supplied by published scientific papers and reports, and Ph.D. and M.Sc. theses (Appendix 1.3), including information about well-constrained subsurface faulting. Beyond the borders of Israel, as well as offshore and at the subsurface, the continuations of major faults are mapped, including faults with evidence of Quaternary faulting that are directly related to the DST, based on literature (Appendix 1.4) and aerial photography. In addition, I consider the recent instrumental seismicity by utilising the gridded seismicity achieved in this study (Chapter 2).

3.3. Methods

First, I create a database of Quaternary geological formations (Appendix 1.2) as a basic step that allows constraining fault activity according to field relationships between faults and these formations. The establishment of this database is a complicated issue, since well-defined geochronology for many of the formations has yet to be obtained. In simple cases, late-Quaternary formations can be easily picked from stratigraphy charts or published papers, while in more complicated cases the ages' uncertainties are not less than millions of years. Moreover, the Pleistocene-Pliocene (or Neogene-Quaternary) boundary was shifted in 2009, from ~1.8Ma to ~2.6Ma. Thus, some formations that had been associated with the Pliocene became associated with the Pleistocene. Therefore, Geological periods attributed to some formations, mentioned in pre-2009 published papers, might mislead. In addition, many of the stratigraphic charts of the pre-2009 geological maps were not updated, nor were the symbols of the geological formations (which reflect the age).

Furthermore, as recent research is involved with dating methods and/or advanced geological interpretations, it reveals better geochronological constraints. Hence, the most up-to-date information is required in order to select carefully formations that were formed during the Quaternary. As much of this information has not been officially published, personal communication (see acknowledgements) significantly aided to obtain the most up-to-date geochronological constraints of the young formations.

In the next part, faults are marked according to the criteria defined in this study. An ArcGIS algorithm aided to recognise many contacts between mapped faults and Quaternary mapping units. The suitability of every mapped fault to the criteria has been checked manually and classified accordingly. Some faults are classified as active during the Quaternary, since their last activity was constrained in published works (Appendix 3.1). Hence, literature review and the matching of faults in other works to these of the geological maps was part of the Quaternary faults' mapping. Subsurface and offshore faults were mapped based on other works. In certain areas, the information revealed from the geological maps was insufficient to decide whether the fault belongs to any of the criteria (e.g. faults that border the contact between Quaternary mapping units and older rocks; faults that were mapped in 1:200,000 scale; or that their matching to faults in literature could not be clearly determined). In these cases, personal communication (see acknowledgements) with geologists that have mapped the areas was important. Beyond the Israel area, published works and aerial photography were the basis for mapping major faults.

3.4. Criteria

3.4.1 Quaternary fault map

The criteria and sub-criteria for the Quaternary fault map (Fig. 3.1) are listed in a descending order of categorisation, meaning that faults are initially examined according to the first criterion, and only if they do not match it, they are examined according to the second criterion, and so on.

Primary criteria

1. Main strike-slip faults of the DST:

   faults of the DST that are identified based on previous research as main sources for intermediate to large earthquakes.

2. Faults with explicit evidence of Quaternary activity:

   Faults that have been mapped offsetting Quaternary formations or that have been interpreted as active at least once since the Quaternary basis by scientific peer-review publications. This criterion is mostly related to zones that are covered by Quaternary formations.

Secondary criteria

Faults that have no field relationship with Quaternary formations consequently show no direct evidence for Quaternary faulting. The secondary criteria are designed under the rationale that they expand the database with faults that can be reasonably assumed to have been active ever since the Quaternary basis.

3. First order branches and marginal faults of the DST:

   I) First order branches of faults that are mapped following the primary criteria. A fault branch is defined here as a fault that was mapped as splitting in an acute angle from a previously-marked fault. The similarity between the throw directions of the branch to that of the previously-marked fault was also taken into account.

   II) Faults that border the DST basins, separating Quaternary formations from older rocks and are associated with a sharp topographic boundary of at least a hundred of meters.

   III) Faults that emerge from Quaternary sediments that infill the DST valleys and are likely to be branches of the main DST segments.

4. Faults associated with recent seismicity:

   This criterion is based on the seismological analysis of this study (Chapter 2), on published scaling relations and on fault lengths according to the geological maps. I generated two polygons from the parameters of *earthquake density* and *Mo density* (Appendices 1.5; 1.6), by searching for a threshold value, so that each polygon is the smallest to cover the DST in the Israel area continuously (with the exception of the Bet She'an area, where the CGTF branches off the DST, the seismicity is sparse and creeping occurs (Hamiel et al., 2016)). Therefore, the overlap area of the two polygons (Fig. 3.1) consists at least minimum levels of both the released seismic moment and earthquake densities, along the DST in the Israel area.

   According to field observations and seismologic investigations, the majority of seismic surface ruptures of magnitudes 5.5–6.5 are above 6-km (Wells and Coppersmith, 1994; Stirling et al., 2002), in agreement with some model values for magnitude 6.0 (e.g. Mai and Beroza, 2000), considered as the minimum magnitude to cause surface rupture. The seismicity overlap area was correlated with mapped faults based on this scaling relation. I applied this criterion on mapped faults of at least 6-km surface trace within the overlap area. The assumption is that the surface trace associated with recent seismicity, is very likely to represent at least one event of surface rupture within the Quaternary.

5. Subsurface faults:

   While a rich research of the subsurface exists in the Israel area, the exact location and the activity age of inferred faults are usually not well constrained. Moreover, if the fault is not inferred in the shallow subsurface, its trace location on the ground is highly uncertain. Therefore, many subsurface inferred faults that exist in the literature are absent in Fig 3.2. Nevertheless, because of the importance of the DST faults to seismo-tectonic and ground motion maps, inferred continuations of the large DST strike-slip segments are marked

differently (Fig. 3.2) than other subsurface faults with published details for both their subsurface extension and their Quaternary activity (Appendix 1.4).

Faults that were mapped as concealed (mostly by alluvium) in the geological maps, and are the continuation of Quaternary fault surface traces, are marked here according to their criteria (in solid lines).

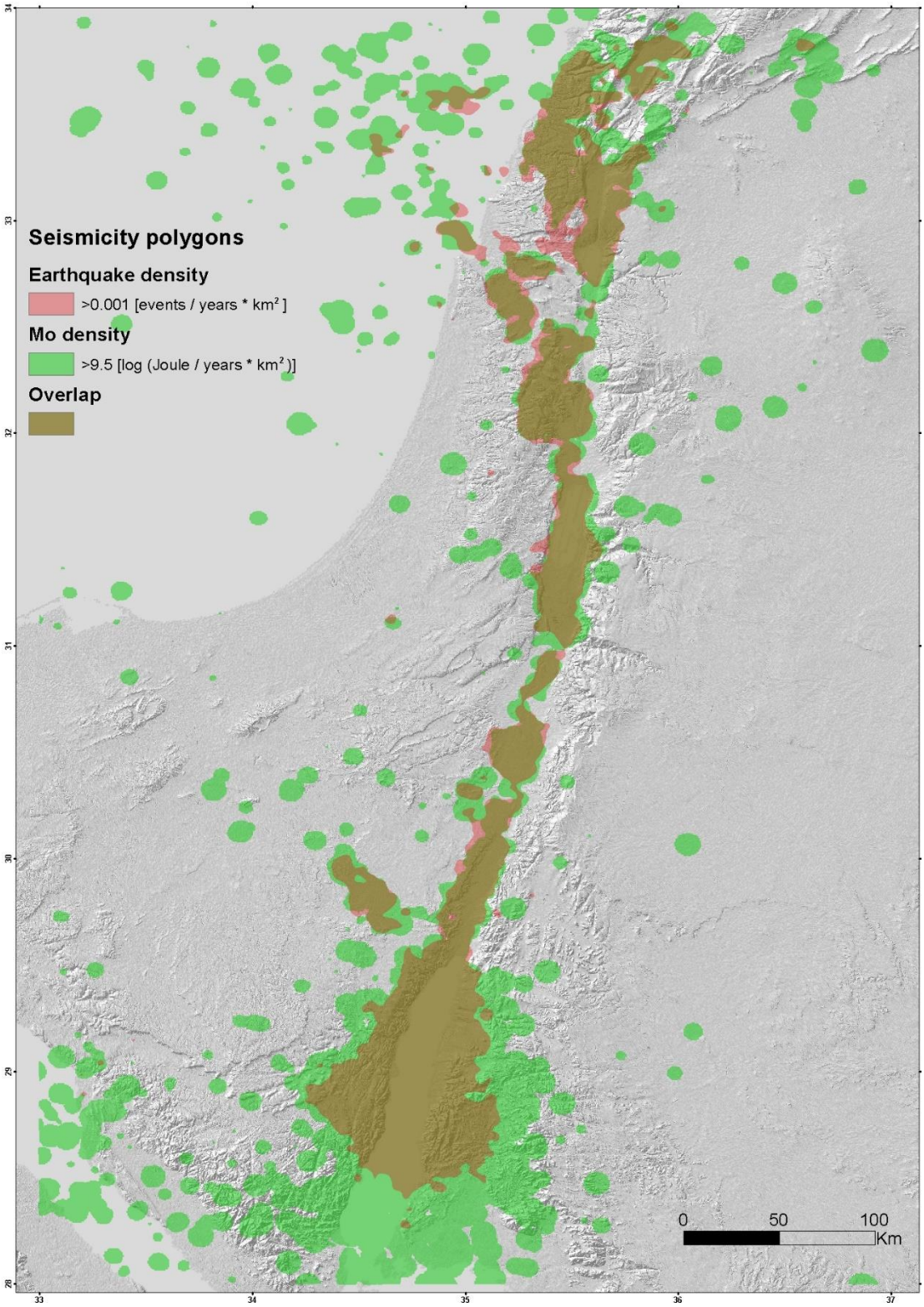

Fig. 3.1. The superimposition of the seismicity polygons: *earthquake density* of values > ~0.001 $events/Km^2 years$ and *Mo density* of values > ~9.5 log[$joules/Km^2\ years$]; the product is the overlap polygon (in brown).

3.4.2. Main seismic sources

Once the Quaternary fault map has been prepared, some faults are derived from it to form a smaller database and a map of the main seismic sources in the region (Fig. 3.3). The achievement of this map is by 'filtering' the Quaternary faults (Fig. 3.2.) according to primarily geodetic and field measurement slip rates. The criteria are:

1. Faults with evidence of strike-slip slip rates of at least 1 mm/a (Table 3.1).
2. Faults with evaluated average slip rates of at least ~0.5 mm/a (~10% of the slip rate along the DST; Table 3.2).

Table 3.1: Main strike-slip faults: average slip rate details

Fault	Lateral slip rate [mm/a]	Data	Period	Reference
Arava [AF]	4.9±0.5# 4.7±1.3# 4±2#	GPS Geology Geology	Recent ~15ka ~120ka	Masson et al., 2015 Niemi et al., 2001 Klinger et al., 2000
Evrona [EF]	5.0±0.8# 5.4±2.7#	GPS Geology	Recent Holocene	Hamiel et al., 2018a Le Béon et al., 2010
Gulf of Elat zone	4.5±0.3* (E 2.2±0.4)	GPS	Recent	Reilinger et al., 2006
Jericho [JF]	4.8±0.7#	GPS	Recent	Hamiel et al., 2018b
Jordan Valley [JVF] (south)	4.9±0.2#	Geology	~48ka	Ferry et al., 2007
Jordan Valley [JVF] (centre)	4.9±0.3#	Geology	~25ka	Ferry et al., 2011
Jordan Valley [JVF] (north)	4.1±0.6#&	GPS	Recent	Hamiel et al., 2016
Jordan Gorge [JGF]	4.1±0.8# ~4.1# ~2.6#	GPS Geology Archaeology	Recent 3.4ka ~3ka	Hamiel et al., 2016 Wechsler et al., 2018 Ellenblum et al., 2015
Lebanon Restraining Bend (LRB) zone	3.8±0.3* (C 1.6±0.4)	GPS	Recent	Gomez et al., 2007
Qiryat Shemona	3.9±0.3* (E 0.9±0.4)	GPS	Recent	Gomez et al., 2007
Roum [RF]	0.86–1.05#	Geology	Holocene	Nemer and Meghraoui, 2006
Serghaya [SF]	1.4±0.2#	Geology	Holocene	Gomez et al., 2003
Yammuneh [YF] (within LRB)	5.1±1.3#	Geology	~25ka	Daëron et al., 2004
Yammuneh [YF] (north of LRB)	6.9±0.1# 4.2±0.3*	Geology GPS	2ka Recent	Meghraoui et al., 2003 Gomez et al., 2007

Geodetic or geological measurements on a specific segment
* According to geodetic-based model
E, C extension and convergence, respectively, normal to the fault
[&] creeping from a depth of 1.5 ± 1.0 km to the surface at a rate of 2.5 ± 0.8 mm/a

Table 3.2. Marginal faults and branches with integrated slip or subsidence of ~ 0.5–1 mm/a

Fault	Slip rate [mm/a]	Data	Period	Reference
Dead Sea basin marginal faults	≥1 Based on basin subsidence rates	Geology Geophysics	Pleistocene-Holocene	Bartov and Sagy, 2004; Torfstein et al., 2009; ten Brink and Flores, 2012
Carmel	0.9±0.45 Total slip rate (0.7±0.45 lateral; 0.6±0.45 extension) < 0.5	GPS Geology	Recent 200ka	Sadeh et al., 2012 Zilberman et al., 2011
Hula western border	~0.4 Based on basin subsidence rates	Geology Geophysics	~1 Ma	Schattner and Weinberger, 2008
Elat	?	Geology	Holocene	Porat et al., 1996; Amit et al., 2002; Shaked et al., 2004

Notes

- Where faults split into a few parallel or sub-parallel segments with an unknown slip rate, the predominant segments (in terms of length and topographic expression) are mapped due to the uncertainty of how the slip rate is divided.
- Slip rates are selected according to their recency and their level of constraint
- Marginal fault belts are usually marked by representative fault traces.

3.5. Results

3.5.1. Quaternary fault map

Tectonically, most of the Quaternary faults (Fig. 3.2) are related to the DST, including the main strike-slip fault segments, sub-parallel segments, marginal faults and branches. In the Negev desert, a few fault systems can be distinguished: The DST main strike-slip segments follow the Arava valley from the Gulf of Eilat to the Dead Sea basin, generating several bends, marginal faults and subparallel segments (e.g. Garfunkel et al., 1981). Three among five (possibly six) of the of the SNB faults appear in this map, from south to north: Thamed, Paran and Arif-Batur. Most of the evidences for activity in these faults are from

the early Pleistocene (Zilberman, 1985; Zilberman et al., 1996; Avni, 1998; Calvo et al., 1998; Calvo, 2002). However, the Zin shear zone, which is located to the north and it is doubtful whether it belongs to this system, shows evidence of middle and late Pleistocene faulting, in a few nearby sites (e.g. Avni and Zilberman, 2007). There is a lack of evidence for Quaternary activity along the northern faults, Ramon and Sa'ad-Nafha (early-Pleistocene faulting is possible in their easternmost continuations but is not sufficiently constrained; Avni, 1998). South of the Arif-Batur fault trace and throughout the southern Negev, SSE-NNW orientated faults are evident to rupture Quaternary sediments, and a fault system of SW-NE to SSW-NNE trending faults (sub-parallel to the DST) is substantial. West of the Eilat city, some of these faults have accommodated both sinistral strike-slip and vertical motions that occurred in earlier period of the current tectonic phase (Garfunkel, 1970; Marco, 2007; Avni et al., 2012; Nuriel et al., 2017), and are part of the current map due to their association with recent seismicity, probably reflecting residual deformation near the DST. In the north-western Negev, the activity of two small near-surface faults was dated to the late-Quaternary (Eyal et al., 1992).

In centre Israel, the western marginal faults of the Dead Sea basin (Garfunkel, 1981; Sagy et al., 2003) are predominant. Further north, the Jericho - Jordan valley faults are the major DST segments between the Dead Sea basin and the Sea of Galilee. In the eastern Samaria, horsetail-shaped SW-NE to WSW-ENE orientated faults are predominant and considered as part of the CGTF. In the absence of direct evidence for rupture of Quaternary formations, most of these faults are included in the map based on recent seismicity, which is significant in this area (Figs. 2.1; 2.4; 2.5; 5.2). The Carmel fault and other related faults are mapped to the northwest. Ongoing seismic activity and geophysical observations suggest that the CGTF continues offshore to some distance (e.g. Ben-Avraham and Ginzburg, 1986; Hofstetter et al., 1996; Schattner and Ben-Avraham, 2007; Figs. 2.1; 2.4; 2.5 in the current study). North of the CGTF, E-W to SE-NW striking faults are common in the southern (lower) Galilee, including the ~E-W fault that borders the lower and upper Galilee along a sharp topographic boundary. However, the upper Galilee hardly accommodates faults with known evidence for Quaternary activity. Some faults show explicit evidence of Quaternary faulting in the southern Golan Heights, mainly in its slopes to the southwest, and near and within the Hula basin. The main DST segment north to the Sea of Galilee is the Jordan Gorge fault. North of the Hula basin, the DST splits into at least five different segments, in Lebanon and Syria.

3.5.2. The main seismic sources in the Israel area

The DST main segments are these that accommodate the highest slip rates, with values of approximately 4–5 mm/a, south of the Hula basin (Fig. 3.3). The slip-rate values increase from ~4 mm/a in the vicinity of the Sea of Galilee to ~5 mm/a in the area of the northern Dead Sea, and further south, probably due to the motion along the CGTF (Sadeh et al., 2012), particularly. Fault systems with evaluated slip rates of ~10% of the relative plate motion include the marginal faults of the DST main basins, and the main segments of the CGTF (Fig. 3.3). In the northwest of this system, the whole motion can be ascribed to the

Carmel fault. In the southeast, however, the division of the slip rates between parallel segments is unclear. Thus, the predominant faults are marked (Fig. 3.3).

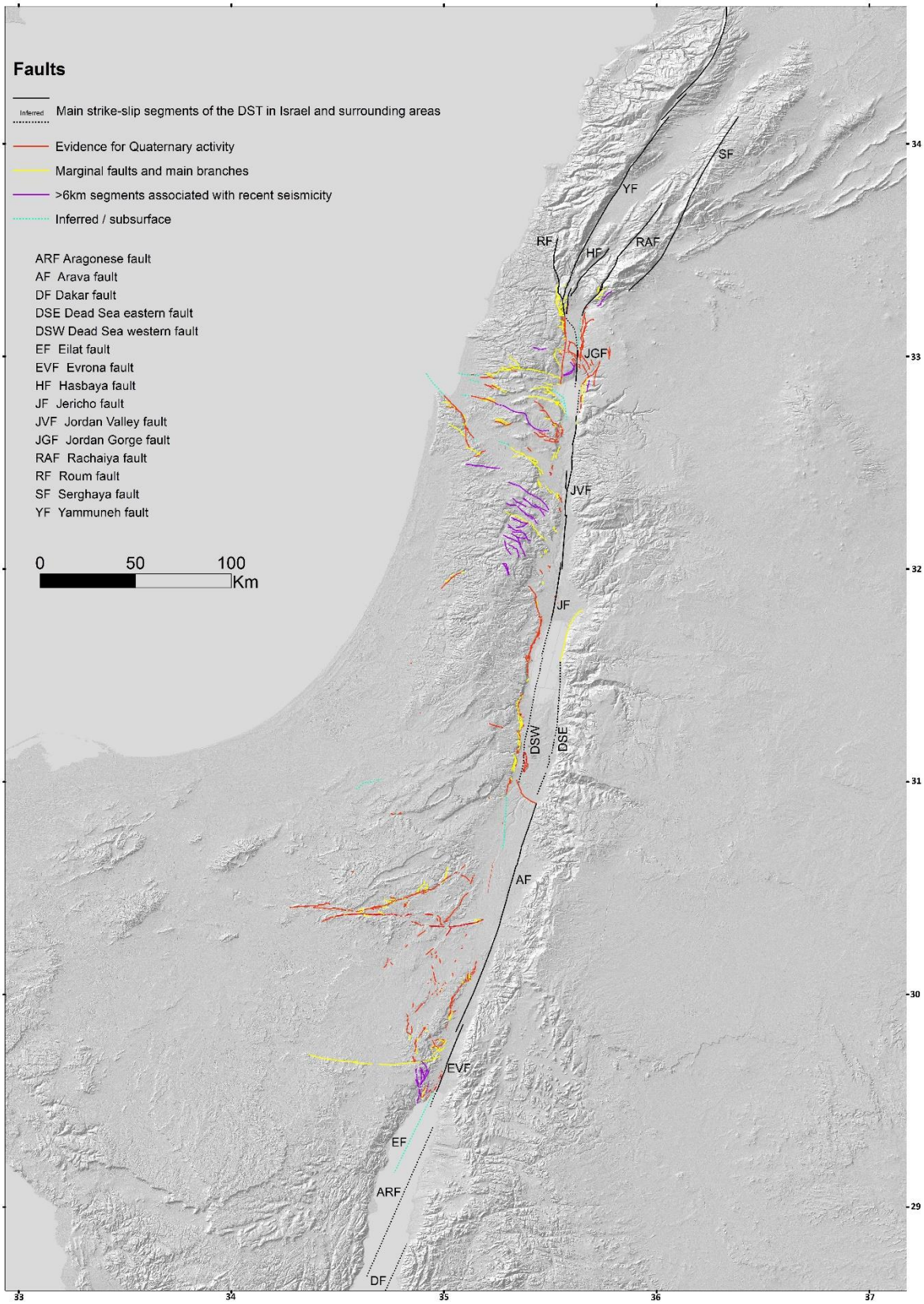

Fig. 3.2. Quaternary fault map of Israel. Colours indicate the faults according to the criteria. Subsurface faults are marked by dashed lines. Abbreviations are for the DST main strike-slip segments. Small faults are difficult to view in this figure due to the high resolution of the maps' data. A high-resolution version upon request. This map is also available at the GSI website, where it shall be updated with time (Sharon et al., 2018).

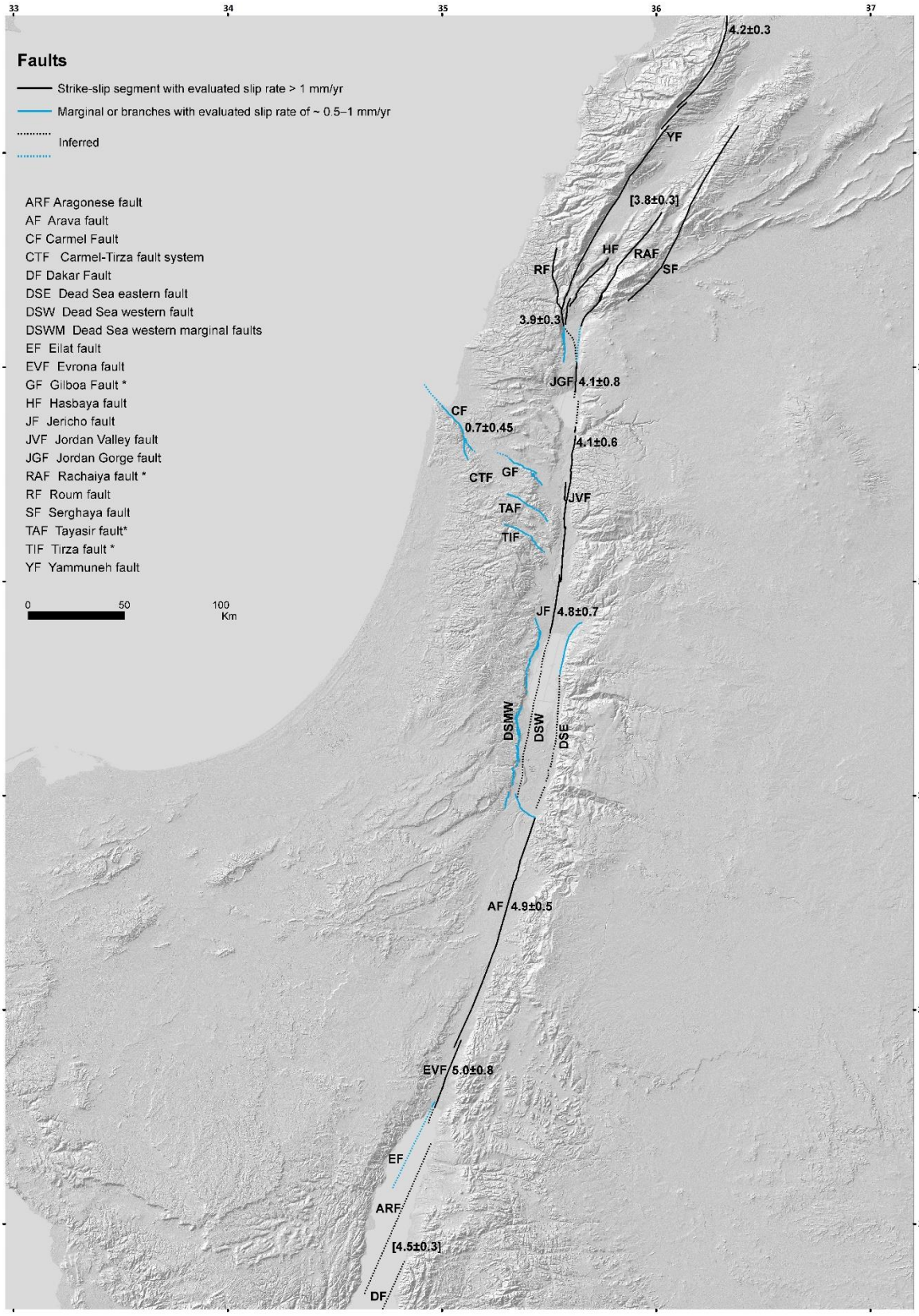

Fig. 3.3. The main seismic sources in Israel and adjacent areas. Colours indicate the faults according to the criteria. Subsurface faults are marked by dashed lines. Abbreviations are for the DST main strike-slip segments, its main branches and marginal faults. Numbers indicate geodetic slip rates [mm/a] of strike-slip components, according to recent studies (Tables 3.1; 3.2; see Appendix 1.8 for all slip rate locations, geological and geodetic origin). Brackets indicate slip rate accommodated by an entire fault zone. Asterisk denotes cases of unknown slip rate, where the fault splits into a few (sub-) parallel segments.

4. Seismogenic zones

A new seismogenic zonation is presented in this study, suggesting a new approach for the compilation of seismological and geological data sources, using the previous chapters' results as an input. Seismogenic zones and their characteristics, particularly the *a* and *b* parameters of the frequency-magnitude relation, are applicable for seismic hazard analysis (e.g. for probabilistic seismic hazard assessment; Pecker et al., 2017). The basic assumption in this kind of analysis is that the *a* and the *b* values are uniform in each zone (e.g. Frankel, 1995; Shapira and Hofstetter, 2002; Helmstetter et al., 2006; 2007; Deif, 2009; Ashish et al., 2016). In order to examine this assumption, these parameters are deduced also in sub-zones, within the primary zones.

4.1. Previous works

Seismogenic zonation in Israel has been presented in previous studies, showing a variety of resolutions: from basic zonations with only a few earthquake producing regions (e.g. Shapira, 1983; Rotstein, 1987), to more detailed zonations that included subdivisions to second and even third order zones (e.g. Arieh and Rabinowitz, 1989; Shapira and Shamir, 1994). The last zonation was suggested by Shamir et al. (2001), based on the integration of seismological and age-constrained geological data, followed by the analysis of the frequency-magnitude relation (Shapira and Hofstetter, 2002). Naturally, the resolution and accuracy of the suggested zonations improve with time, as more seismological data is compiled and the geological data resolution is improved, followed by up-to-date interpretations. Since the latest zonation, more seismic data has been recorded, and on a larger network, consisting more stations, and the resolution of the available geological maps has improved. It emphasises the necessity of an improved and more robust seismogenic zonation.

4.2. Methods

I use the spatial distribution of the seismicity parameters (Chapter 2) as the basis for delineating seismogenic zones. Initially, I determine a threshold value for the *earthquake density* contours. A regional observation of the epicentre distribution shows that the seismic activity focuses within zones designated by a contour of $0.00105\ events/km^2/years$ (Figs. 4.1; 4.2**)**. Areas that surround these initial zones from the outside (i.e. where the *earthquake density* values are slightly lower) are part of wider deformation zones that are excluded, at least initially. Zones that are small (a few kilometres length at most) and/or consist of less than hundred earthquakes were ignored. However, spaces of sparse seismicity inside seismogenic zones were included.

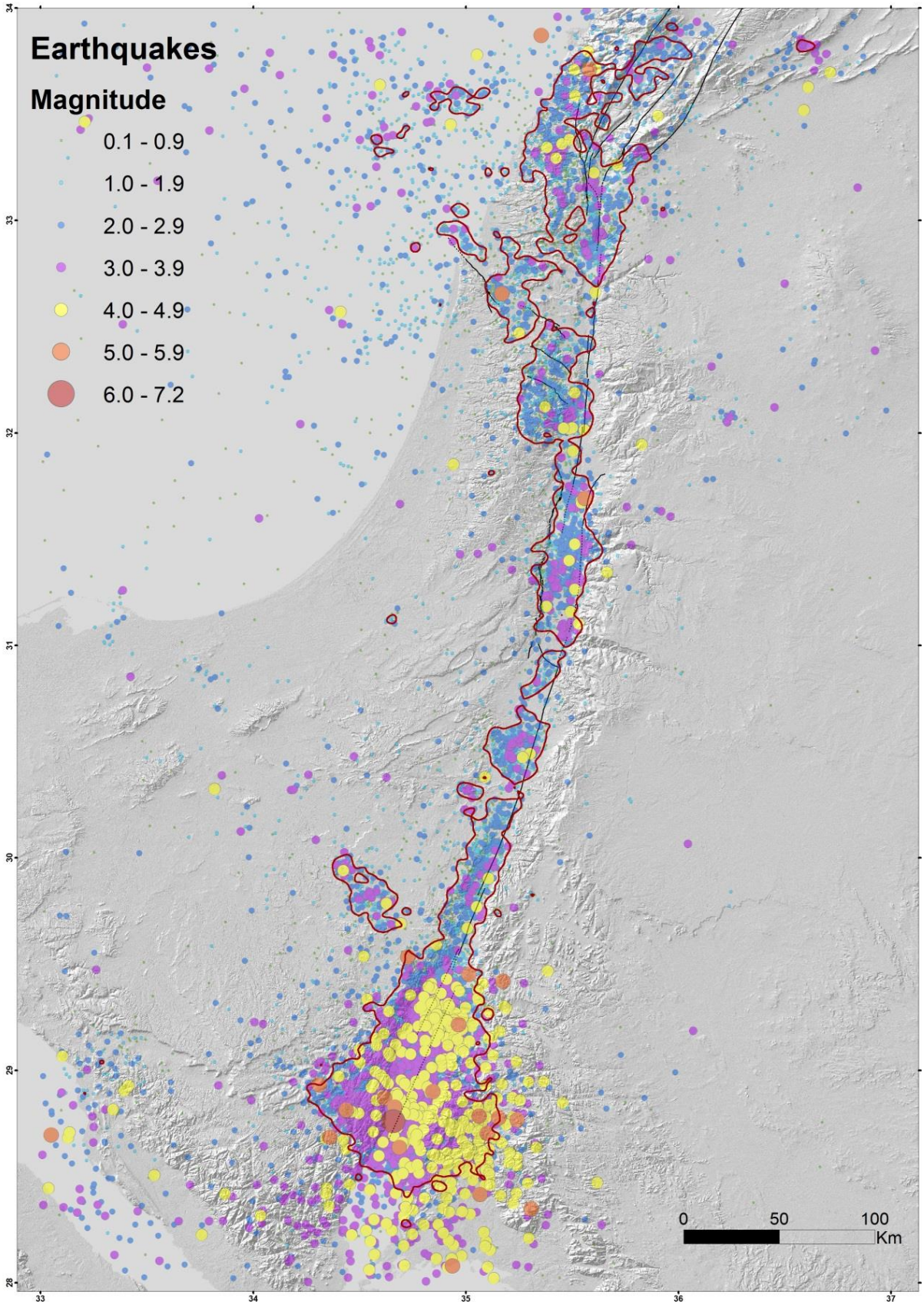

Fig. 4.1: Preliminary stage for delineating seismogenic zones. *Earthquake density* values of 0.00105 $events/km^2/years$ (dark-red contours), superimposed on the relocated epicentres (Fig. 2.1). Circle size and colour indicate the magnitude. Black lines represent the main fault segments of the DST and the CGTF (see chapter 3).

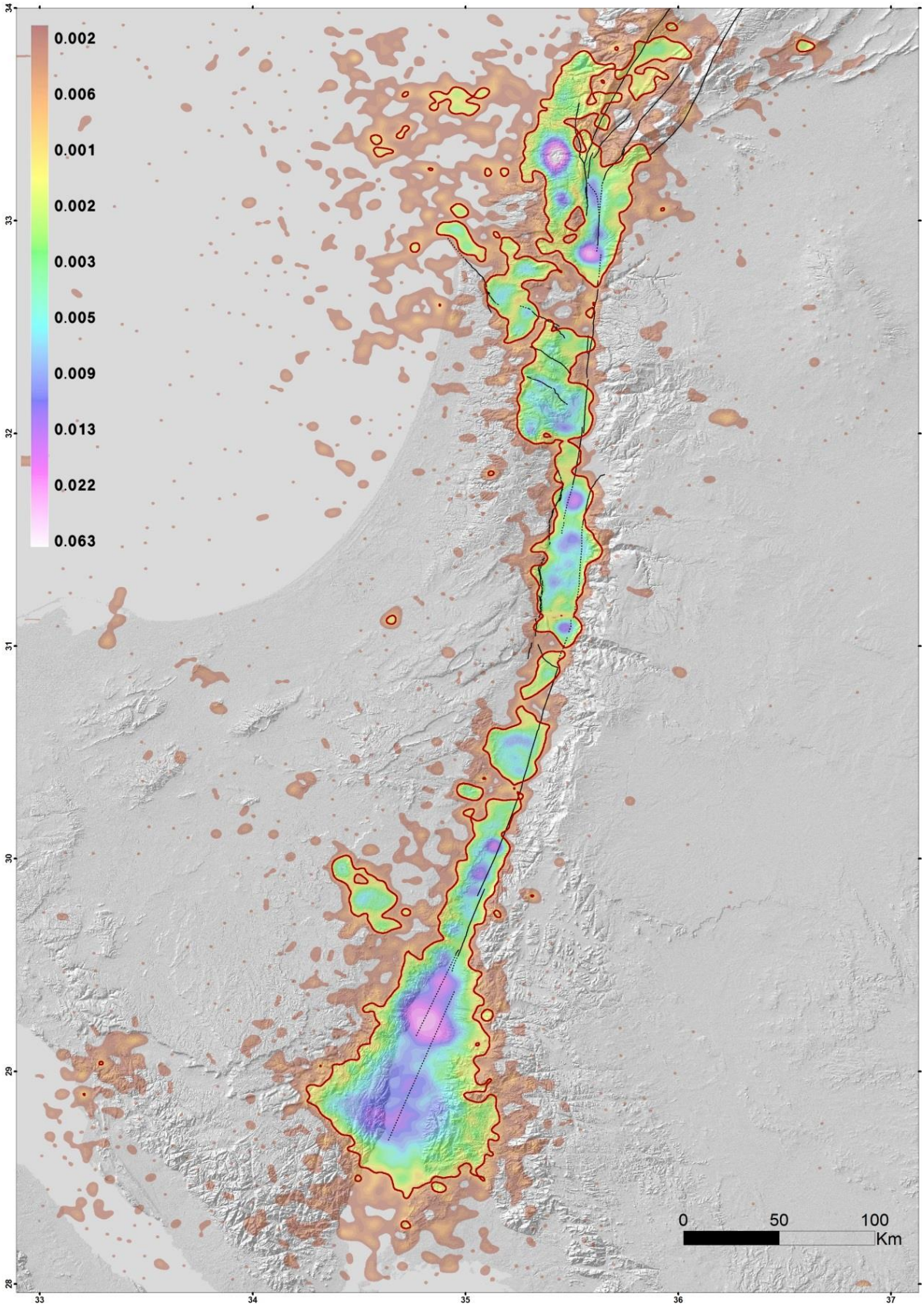

Fig. 4.2: First stage of delineating seismogenic zones. The contour of 0.00105 events/km^2/years (dark-red line) in the *earthquake density* distribution map (Fig. 2.4). Black lines represent the main fault segments of the DST and the CGTF (see chapter 3).

In the next stage the tectonic settings are considered, by examining the relation between the main seismic sources (Fig. 3.3) and the *earthquake density* distribution (Fig. 4.2). In order to match between the zones and the fault segments, I adjust the threshold value of the *earthquake density*'s contour. Each zone is now bordered by a contour value that may be lower or higher than $0.00105\ events/km^2/years$. The adjustment enables separating each zone if it includes different fault systems, or to expand zones so they will fit better to the associated fault system (Fig. 4.3). Consequently, zones defined by values lower than this are wider than the initial zones, and were cropped 'manually' so they would not overlap with other seismogenic zones, which are associated with different fault systems. The crops were done in the narrowest places possible within the zones. In other cases, the separation between the zones was based on the selection of minimum *earthquake density* contour values, keeping the zones separated, without cropping manually; for this purpose, I used a high-resolution 0.00001 interval between contours. The adjustment of the zones according to the major seismic sources allows the characterisation of zones also by fault lengths and the ensuing maximum potential magnitude (Table 4.1).

In the last stage, I utilise the *Mo density* distribution to enlarge pre-existing zones, so they include areas of *Mo density* $\geq 10^7 [\log\left(\frac{joule}{km^2 years}\right)]$ (Fig 4.3), a value that corresponds to a 4-km distance from a single $M = 4.0$ earthquake. This expansion is limited to cases of overlap between the M_0 *density* and the *earthquake density* polygons. The rationale is that stronger events are identified in more stations and therefore their location is more constrained, and in addition the energetic spatial distribution should be also considered, as it can be focused in tectonic features that may not be associated with micro-seismicity. The Gulf of Eilat is an exception due to its location beyond the network coverage, resulting in less reliable contours of the *Mo density* that show a fallible wide deformation zone (Fig 4.3). The northern edge of this seismogenic zone is slightly expanded, though, since the associated events are closer to the stations.

Second order zones, or sub-zones, are depicted within primary zones solely according to *earthquake density* contours. The contours are such that allow the separation of different peaks inside primary zones, without overlapping of the sub-zones.

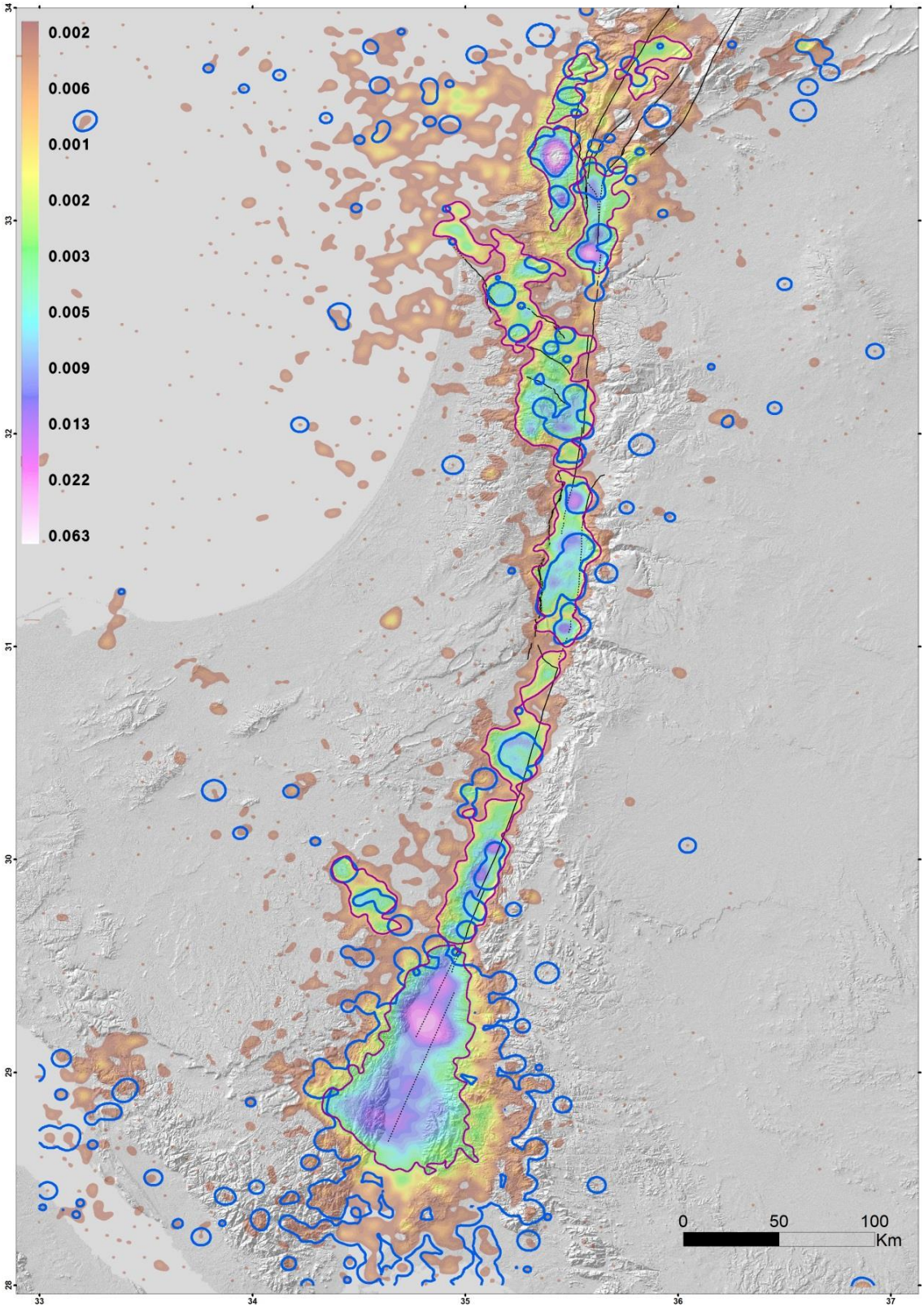

Fig. 4.3: Second and third stages for delineating seismogenic zones. Colours represent the *earthquake density* distribution (Fig. 2.4). Dark red lines represent the zones after adjusting the 0.00105 $events/km^2/year$ contour values (displayed before the adjustment in Fig. 4.2) so they fit to the main seismic sources. Blue lines are *Mo density* contours of $10^7[\log\left(\frac{joule}{km^2 years}\right)]$. Where the two different contours intersect, the pre-existing zones defined by the *earthquake density* are expanded according to the *Mo density* contour. Black lines represent the main fault segments of the DST and the CGTF (see chapter 3).

4.3. Results

4.3.1 First order zonation

Seismogenic zones and their characteristics are presented (Fig. 4.4; Fig. 4.5 after smoothing; Table 4.1; Appendix 2 for analyses of the frequency-magnitude relation). The Gulf of Eilat is the largest zone (Fig 4.4). It accommodated the highest number of recorded events, which occurred mainly during the 1983–2007 period, including the $M_W = 7.2$ 1995 Nuweiba earthquake that had almost reached the largest magnitude possible within this zone (Table 4.1). Accordingly, the zone accommodates the highest seismic moment release. It seems to include two out of the three pull-apart basins that constitute the Gulf of Eilat (Ben-Avraham, 1985). Its southern border probably represents poor detectability of the seismic network, rather than the actual deformation limit. The *b-value* drops significantly from ~1.3 to ~0.7–0.9, between the whole (1983–2017) and the latest (2007–2017) periods, respectively (Table 4.1). The ~1.3 *b-value* is probably biased by aftershocks of the 1993 and 1995 events (see chapter 2; section 5.2). However, the *b-value* variations are also subjected to the selection of M_c, and specifically in this zone, the frequency-magnitude parameters should be taken with a grain of salt due to the unclarity of the detectability threshold of the network.

Seismic activity concentrates in the central-eastern Sinai Peninsula with no associated mapped faults (Eyal et al., 1980), in a zone that is referred here as Eastern Sinai. The Thamed fault, however, crosses the zone's southern tip (Fig 4.7). The average earthquake depth here is the deepest within all zones (Table 4.1; Fig. 4.8), indicating seismic activity on deep sub-surface faults. The obtained recurrence intervals of $6.0 \leq \mathrm{M} < 7.0$ events, which usually cause surface rupture, are either 175 or ~1500 years, depending on the completeness magnitude (Table 4.1; details about the *b-value* at Appendix 2.2.3). Even when considering the longer interval, it is still surprising there are no mapped surface ruptures, as interplate earthquakes are related to plate motions and stress fields that change much slower than the earthquake cycle. Thus, the seismicity in this zone, with no reported evidence for surface rupture, is an enigma. This unusual phenomenon can be explained by a non-tectonic source. These events are probably not explosions since: a) explosions are not included in the earthquake catalogue supplied by the GII; b) a simple observation of the catalogue, within this zone, reveals an increasing in the seismicity rate following the 1995 Nuweiba earthquakes; c) the sources are too deep for explosions. Induced seismicity could explain these events, but evidence for possible triggers are currently absent, or at least were not found by the author. The zone may reflect local stresses on pre-existing faults in the intermediate-to-lower crust, or a very recent change in the stress field that trigger the formation of new faults (less plausible). Further discussion is in sections 5.3.2; 5.3.3.

Zone	Period	M_c	ΔS	Events total num.	Events of $M_d \geq M_c$	Focus Average Depth [Km]	*a-value*	*b-value*	Recurrence Interval [years] $5.0 \leq M < 6.0$	Recurrence Interval [years] $6.0 \leq M < 7.0$	Recurrence Interval [years] $7.0 \leq M < 8.0$	Max. observed Magnitude	Total *Mo* release [Joule]	Min. earthquake density $[events/km^2/years]$	Max. Zone length [Km]	Max. Fault Length [Km]	Max. Potential magnitude
Gulf of Eilat	1983 – 2017	4.0	0.021	6641	196	8.24	6.01	1.31	4	79	1622	7.2	2.48E+19				
	2007 – 2017	2.0 (3.5)	0.031 (0.181)	355	112 (23)	9.30	2.44 (3.08)	0.71 (0.88)	16 (23)	83 (174)	425 (1308)	5.5	1.59E+17	0.00270	124	84	7.3
Eastern Sinai	1983 – 2017	1.5 (3.0)	0.050 (0.077)	228	126 (23)	16.96	1.45 (2.54)	0.59 (0.94)	45 (166)	175 (1455)	689 (15590)	4.4	1.56E+16	0.001050	50		7.1
Arava Valley	1983 – 2017	2.0	0.019	1414	308	15.13	2.61	0.83	41	277	1872	4.6	4.46E+16				
	2007 – 2017	1.5	0.064	563	172	14.66	2.53	0.88	86	650	4932	4.6	1.70E+16	0.000980	160	125	7.5
Dead Sea Basin	1983 – 2017	2.0	0.032	1087	365	16.31	2.52	0.75	20	113	630	5.1	9.00E+16				
	2007 – 2017	1.5	0.068	287	176	16.34	2.22	0.67	17	78	362	4.5	2.21E+16	0.001210	92	100	7.4
Carmel – Gilboa – Tirza	1983 – 2017	1.5	0.050	1381	674	11.34	2.35	0.71	19	97	491	5.3	1.28E+17				
	2007 – 2017	1.5	0.035	476	189	12.01	2.56	0.88	76	572	4306	3.4	2.34E+15	0.000770	116 *	46	7.0
Kinnarot – Korazim – Hula	1983 – 2017	1.5	0.035	849	298	11.28	1.93	0.66	31	144	664	4.4	2.01E+16				
	2007 – 2017	1.0	0.048	462	245	11.44	2.06	0.70	33	165	819	4.0	6.82E+15	0.001920	75	40	7.0
Upper Galilee – Southern Lebanon	1983 – 2017	2.0	0.030	1121	300	6.74	2.65	0.86	49	355	2543	4.9	5.00E+16				
	2007 – 2017	2.0	0.047	1019	252	6.72	3.09	0.86	18	132	948	4.9	4.70E+16	0.001920	55		7.1
Roum fault	1983 – 2017	2.0	0.077	170	88	5.08	2.12	0.86	170	1225	8810	5.2	7.11E+16	0.001690	46		7.0
Lebanon Restraining Bend	1983 – 2017	2.0	0.080	131	55	2.52	2.36	1.08	1182	14156	169562	3.9	2.81E+15	0.001050	35	22	6.7

Table 4.1: Seismological and geological characteristics of seismogenic zones. Data from the later period (2007–2017) is filled in grey. The frequency-magnitude parameters are derived from analyses presented in Appendix 2. Numbers inside brackets indicate alternative option for *earthquake density* value defines the bordering contour of each zone. The maximum potential magnitudes are based on the scaling relation of Wells and Coppersmith (1994), assuming a strike-slip motion and a potential surface rupture as long as the longest fault associated with the zone. Where fault data is missing, the maximum length of the zone is used as an input. * The zone length is measured parallel to the Carmel fault, from the SE to NW distinct zone edges, passing through areas outside the zone due to the discontinuity of the seismic activity in relation to the faults (Fig. 4.4).

The Arava Valley zone contains long strike-slip segments of the DST and other Quaternary faults (Figs 4.4; 4.7). Although the obtained *b-values* are quite similar (0.83 and 0.88), the recurrence intervals obtained from the two time-windows are rather different (Table 4.1), probably reflect changes in the seismicity rate that affect the *a-value.* The Dead Sea Basin zone includes DST strike-slip and marginal faults (Fig. 4.4). The latter seem to border the zone rather than accommodate large portion of the seismicity, especially the western marginal fault. Like the Arava Valley zone, the drop in the completeness magnitudes in the latter period indicates the improvement of the network detectability. In both zones, the intervals yielded from the whole period seem more reliable (compared with the later period only), in accordance with their deduction from more recorded events, so they are less subjected to temporal changes of the seismicity pattern. The average earthquake depth within these zones is quite deep, especially in the Dead Sea Basin (Table 4.1).

The Carmel-Gilboa-Tirza zone contains the CGTF that branches off the DST and continues offshore (Figs 4.4; 4.7). Although the zone covers only a portion of the DST main strike-slip segments, its south-eastern part is considered as a zone of high strain accumulation and that may have accommodated some of the historical earthquakes of the region (e.g. Ben-Menahem and Aboodi, 1981). The Carmel fault's surface trace is mostly outside the seismogenic zone at its northwestern part (Fig. 4.4). However, the depth domain is neglected in this correlation, so some of the zone's seismicity might be associated with the fault (see discussion in sub-section 5.1.2). The proximity of the zone to the seismic stations is probably related to the low detection threshold ($M_c = 1.5$ for both periods). The zone is comprised of different seismic patches or sub-zones, covering the mapped traces of different faults (Fig. 4.7), so the temporal variations of the *b-value* (0.71–0.88; Table 4.1) might indicate non-uniform spatio-temporal seismicity pattern. Like the foregoing zones, this difference of the *a* and *b* parameters is reflected in the recurrence intervals, particularly of the strongest shocks ($7.0 \leq M < 8.0$). In this case, they differ in an order of magnitude.

The Kinnarot-Korazim-Hula zone, which contains the tectonic basins of the Sea of Galilee and the Hula valley, is associated with both strike-slip and marginal normal faults of the DST (Figs. 4.4; 4.7). The detection capability of the seismic network is the best within this zone, with $M_C = 1.5$ and 1.0 for the whole period and for the second period, respectively. The *b-value* is quite stable (0.66–0.70; Table 4.1); accordingly, the ensuing recurrence intervals are similar. The frequency-magnitude diagram for the 2007–2017 period (Appendix 2.6.4) shows that more $3.0 \leq \mathrm{M} < 3.6$ events were recorded than expected from the Gutenberg-Richter law, probably caused by the 2013 swarm in the Sea of Galilee.

The Upper-Galilee–Southern Lebanon zone exhibits a 0.86 *b-value* with no temporal change. However, the latter period is characterised by a higher M_O release rate and a higher *a-value*, so shorter recurrence intervals are yielded (Table 4.1). Its northern part consists of a sub-zone, possible a fault patch, of intense seismicity, previously suggested to be associated with either SSE-NNW orientated faults or with SE-NW parallel faults that traverse southern Lebanon (Meirova and Hofstetter, 2013). The earthquake average depth indicates shallow crust seismicity (Table 4.1). The southern part of this zone includes a smaller and less significant sub-zone in the Upper Galilee that can hardly be associated with Quaternary faults

(Fig. 4.7). The sub-zone contains previously-mapped faults that do not fit the seismicity criterion due to their length limitation (see criteria section 3.4).

The zones of the Roum Fault and of the Lebanon Restraining Bend are located merely beyond the Israel borders, and out of the network coverage area (Fig 2.2). Consequently, the seismicity parameters are less reliable, also because these zones accommodated relatively sparse seismicity, particularly the Lebanon Restraining Bend. The current analyses suggest that $M_c = 2.0$ for both zones (Appendices 2.8.1; 2.9.1), implying that the low detectability is probably not the main reason for the lack of recorded events. Although the DST splays into several strike-slip segments in this area, it is still surprising that the seismicity is so sparse along these faults that display a plate boundary, especially along the Yammuneh fault that accommodates most of the strike-slip motion within the Lebanon Restraining Bend (e.g. Gomez et al., 2007). A *b-value* of 0.86 is deduced in both the Roum Fault and the southern Upper Galilee - Southern Lebanon zones (Fig. 4.4), implying a possible physical connection or similarity between them.

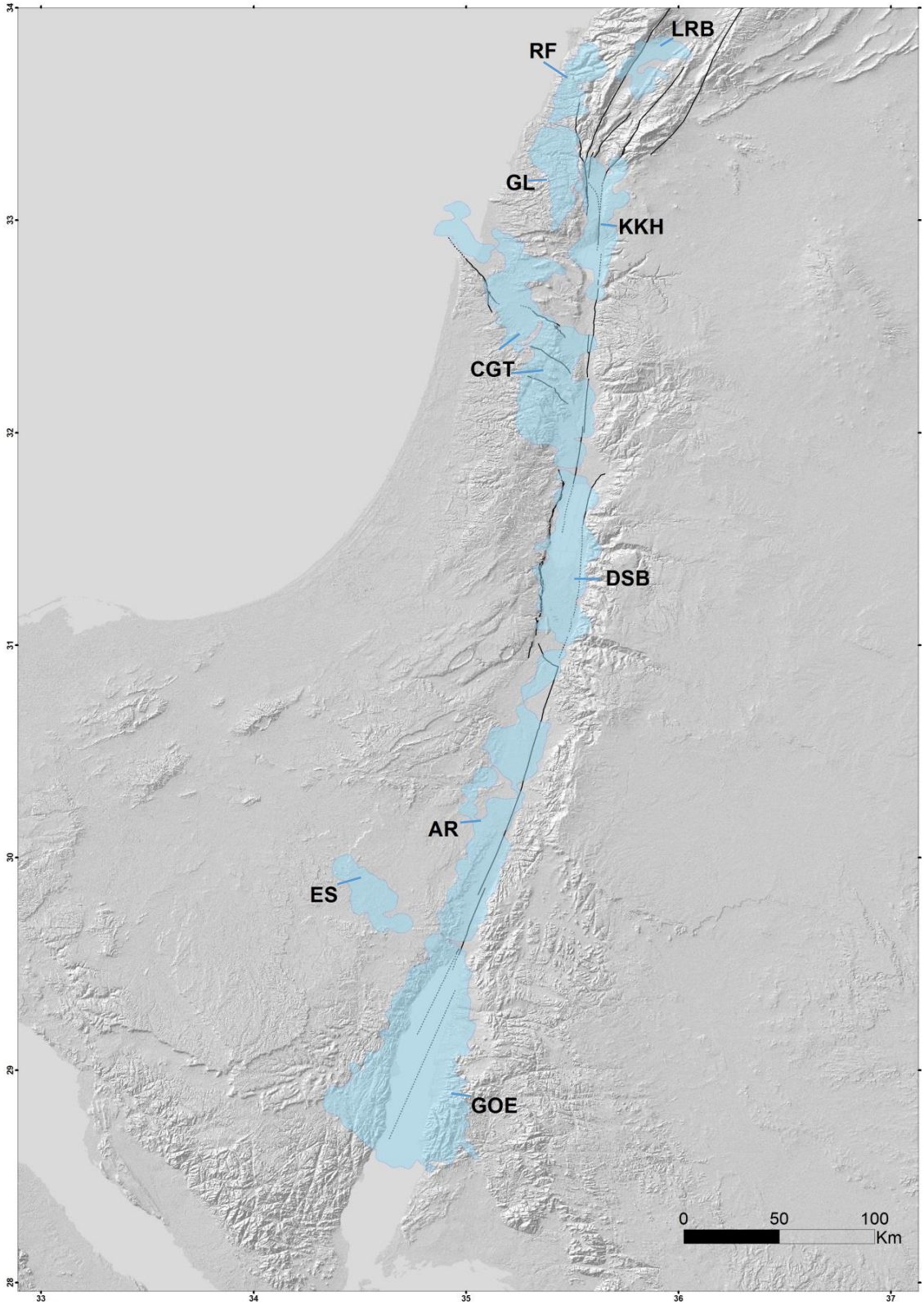

Fig. 4.4: Seismogenic zones. Abbreviations: GOE: Gulf of Eilat; ES: Eastern Sinai; AR - Arava Valley; DSB - Dead Sea Basin; CGT - Carmel-Gilboa-Tirza; KKH - Kinnarot-Korazim-Hula; GL - Upper Galilee-Southern Lebanon; RF - Roum fault; LRB - Lebanon restraining bend. Black lines represent the main fault segments of the DST and the CGTF (see chapter 3).

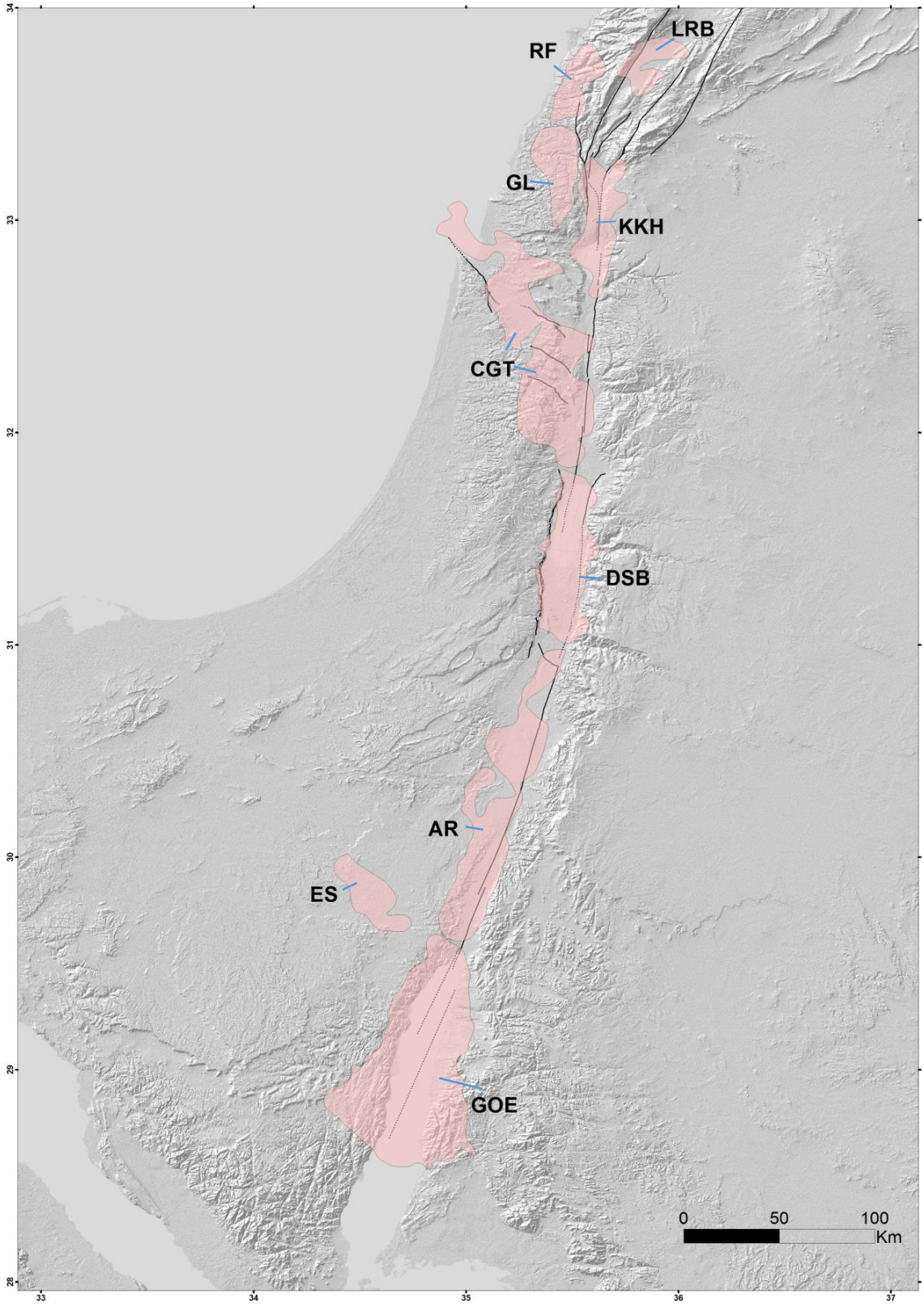

Fig. 4.5: Seismogenic zones after smoothing, made by the ArcGIS "Smooth Polygon" tool. Abbreviations: GOE: Gulf of Eilat; ES: Eastern Sinai; AR - Arava Valley; DSB - Dead Sea Basin; CGT - Carmel-Gilboa-Tirza; KKH: Kinnarot-Korazim-Hula; GL: Upper Galilee-Southern Lebanon; RF - Roum fault; LRB - Lebanon restraining bend. Black lines represent the main fault segments of the DST and the CGTF (see chapter 3).

4.3.2. The *a* and *b* values in second order zones

The second-order zones and their seismicity characteristics are presented (Figs. 4.6; 4.7; 4.8 Table 4.2) within the larger primary zones that consist of relatively high number of earthquakes. Since the seismogenic zones (Figs. 4.4; 4.5) are primarily based on the peaks of the *earthquake density* distribution (Fig. 4.2), it is possible or even expected that smaller similar zones, in some cases, represent seismicity along fault patches. The results show that within the Arava Valley and the Kinnarot-Korazim-Hula primary zones, the *a* and *b* parameters are not consistent in second-order zones (Table 4.2). However, both primary zones consist of sub-zones that are associated with different tectonic features (Fig. 4.7): the AR1 sub-zone follows the DST segments in the southern Arava valley and a wider deformation zone to the west, whereas the AR2 sub-zone probably reflects an interaction zone between the DST, sub-parallel faults and segments of the SNB; the KKH1 zone is associated with the Sea of Galilee, while the KKH2 zone is within a different pull-apart basin of the Hula valley. The three sub-zones that constitute the Dead Sea Basin exhibits a very similar *b-value* (0.70–0.72). Three sub-zones of the Carmel-Gilboa-Tirza zone show some similarity of the *b-value* (0.67–0.77) with poorly constrained deduction in sub-zone 2 (of the 0.77 *b-value*); the parameters within other sub-zones are very poorly constrained.

4.3.3. The depth distribution

The average depths within sub-zones, included by the same primary zone, are relatively close (Table 4.2), in accordance with the way the primary zones are depicted (so that each zone is associated with a single fault system). This implies a physical relation between sub-zones of the same primary zone. Seismogenic zones along the DST are associated with structural differences (e.g. long segments or restraining bends within pull-apart basins), and therefore also with lithological variations. Hence, seismic patches possibly tend to concentrate at similar depths associated with the lithological changes. Indeed, some second-order zones show rather uniform average depth, and therefore may reflect a single or a few seismic patches (the zones ES; DSB1; DSB3; CGT2; KK2; GL1; Fig. 4.8). Alternatively, the relatively-similar depths within sub-zones of the same primary zones may reflect thermal changes along the DST (Shalev et al., 2013; Wetzler and Kurzon, 2016). In addition, the temporal similarity of the average depth within primary zones (Table 4.1) probably indicates: 1) the statistic advantage achieved by averaging many events, resulting in an accurate average depth; 2) a lack of seismic migration between fault patches.

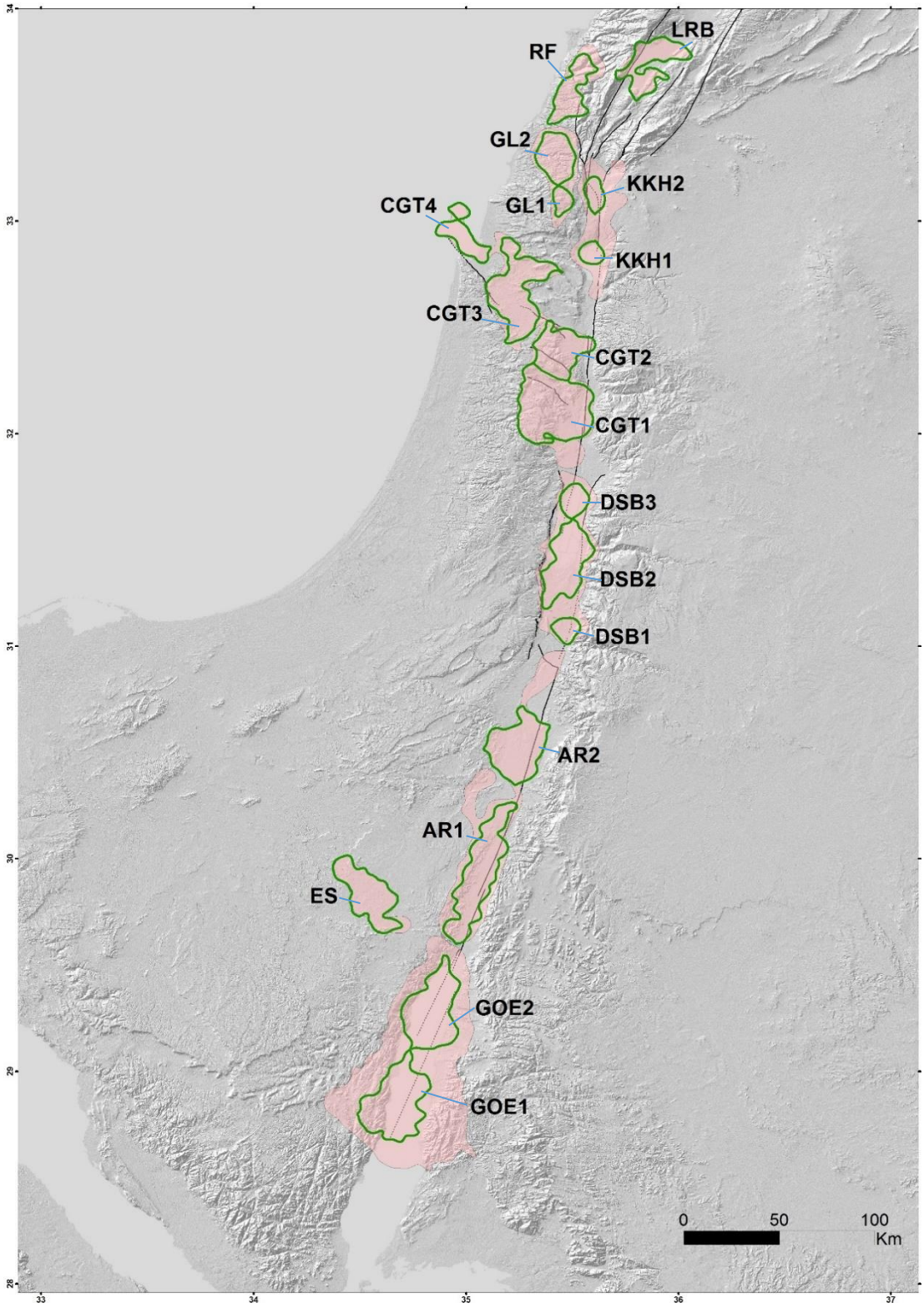

Fig. 4.6: Second-order seismogenic zones (delimited by green lines), and the smoothed-boundary primary seismogenic zones (in pink) presented (Fig. 4.5). The LRB, ES and RF primary zones are not divided; the green lines within the ES and RF represent their *earthquake density* contours (red lines in Fig. 4.3), without expanding the zones by high *Mo density* in proximity (blue lines in Fig. 4.3). Abbreviations: GOE1 - Gulf of Eilat; ES - Eastern Sinai; AR - Arava Valley; DSB - Dead Sea Basin; CGT - Carmel-Gilboa-Tirza; KKH - Kinnarot-Korazaim-Hula; GL - Upper Galilee - Southern Lebanon. Black lines represent the main fault segments of the DST and the CGTF (see chapter 3).

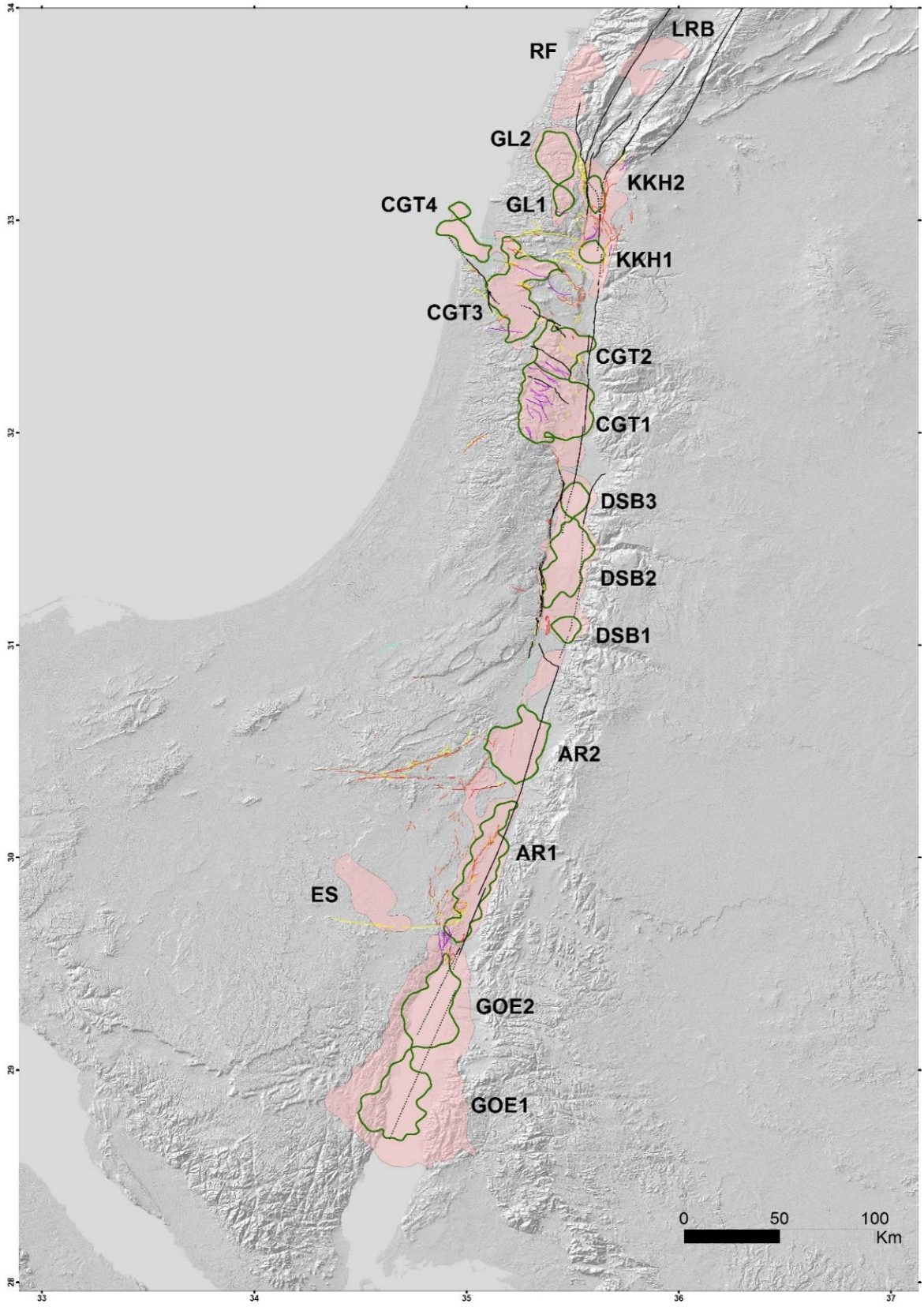

Fig. 4.7: Second-order seismogenic zones (in green lines), and the smoothed-boundary primary seismogenic zones (in pink) as presented as in Fig. 4.6, along with the Quaternary faults (Fig. 3.2). Abbreviations as in Fig. 4.6. Black lines represent the main fault segments of the DST and the CGTF (see chapter 3).

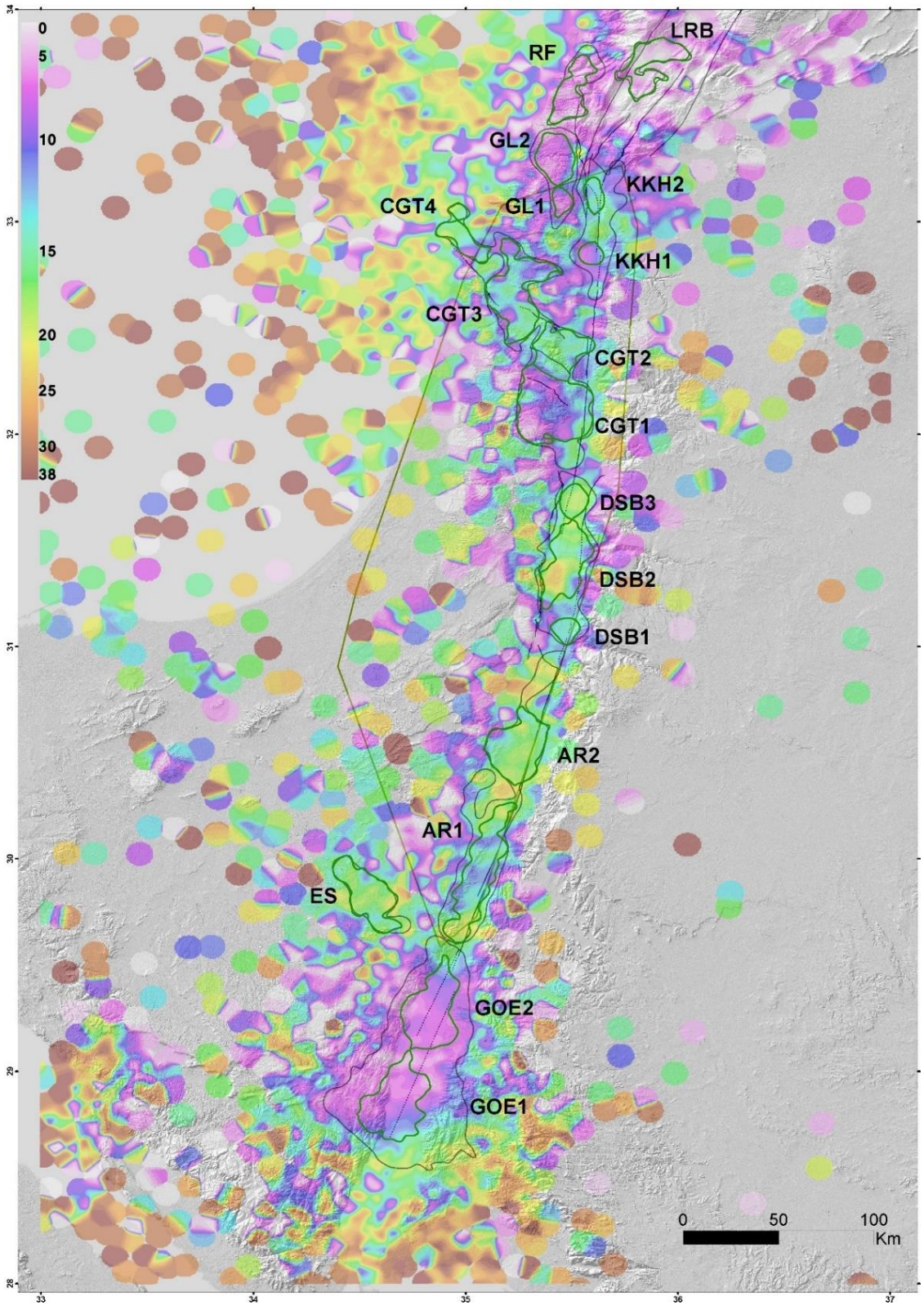

Fig. 4.8: Second-order seismogenic zones (delimited by green lines), and the smoothed-boundary primary seismogenic zones (delimited by brown lines) as presented in Fig. 4.6, superimposed on the *earthquake average depth* distribution (Fig. 2.6), whose reliability is assumed within the Grey lines of the network coverage area (Fig. 2.2) and within seismogenic zones; The ES and GL2 are probably an exception, located outside the network coverage but with a wide azimuthal coverage of the stations (Fig 2.2) and relatively high number of events to achieve reliable results. Abbreviations as in Fig. 4.6. Black lines represent the main fault segments of the DST and the CGTF (see chapter 3).

2nd order zone	M_c	Events total num.	Events of $M_d \geq M_c$	Focus Average Depth [Km]	*a-value*	*b-value*	Recurrence Interval [years] $5.0 \leq M < 6.0$	Recurrence Interval [years] $6.0 \leq M < 7.0$	Recurrence Interval [years] $7.0 \leq M < 8.0$	Max. observed Magnitude	Total *Mo* release [Joule]
Gulf of Eilat 1	4.0	1699	39	7.74	4.22	1.04	11	119	1309	7.2	2.35E+19
Gulf of Eilat 2	4.0	2392	53	7.34	6.88	1.67	32	1489	70300	4.9	3.34E+17
Arava Valley 1	2.0	800	144	14.17	2.54	0.96	208	1907	17473	4.3	1.30E+16
Arava Valley 2	2.0	415	108	16.45	2.06	0.78	87	527	3207	4.6	1.87E+16
Dead Sea Basin 1	2.0	132	65	13.38	1.68	0.70	86	432	2179	4.5	1.28E+16
Dead Sea Basin 2	2.0	596	198	16.94	2.20	0.72	32	169	892	4.4	2.47E+16
Dead Sea Basin 3	2.0	239	73	17.88	1.77	0.72	86	450	2371	5.1	5.20E+16
Carmel - Gilboa - Tirza 1	1.5	714	416	9.54	2.08	0.67	23	110	514	4.8	4.21E+16
Carmel - Gilboa - Tirza 2	1.5	190	76	14.50	1.50	0.77	275	1622	9576	3.9	3.25E+15
Carmel - Gilboa - Tirza 3	1.5	323	117	12.53	1.59	0.71	109	556	2825	5.3	8.21E+16
Carmel - Gilboa - Tirza 4	1.5	88	43	14.89	1.44	0.90	1260	9909	77925	3.4	9.03E+14
Kinnarot - Korazim - Hula 1	1.5	444	167	10.37	1.72	0.69	69	342	1688	4	8.30E+15
Kinnarot - Korazim - Hula 2	1.5	200	61	12.81	1.02	0.52	53	176	583	4.4	9.71E+15
Upper Galilee - Southern Lebanon 1	2.0	118	32	6.87	1.74	0.89	564	4326	33213	3.6	1.50E+15
Upper Galilee - Southern Lebanon 2	2.0	936	254	6.54	2.54	0.84	52	356	2444	4.9	4.82E+16

Table 4.2: Seismological characteristics of 2nd order seismogenic zones, based on 1983–2017 data. Red lines denote a *b-value* deduction that is very poorly constrained (less than 50 events and/or a magnitude interval of less than 2.0), and therefore it is not considered as reliable.

5. Discussion

5.1. Methodological aspects

5.1.1. Final products and their application for seismic hazard

The cascaded methodology (Fig. 5.1) that is implemented here, was developed as an integral part of this study, in the purpose of incorporating geological and seismological data, for seismic hazard evaluation. By utilising recorded seismicity solely and applying statistic-based data processing, the distribution of the density of earthquakes and of the seismic moment release are achieved (Figs. 2.4; 2.5). These two distribution maps are applicable for at least three different purposes: 1) a basis for ground motion prediction, using the *earthquake density* distribution as an input (Pecker et al., 2017), and possibly for other future models; 2) to mark young faults (Chapter 3; Figs. 3.1 3.2; 5.2); 3) for delineating seismogenic zones (Chapter 4; Figs. 4.1; 4.2; 4.3).

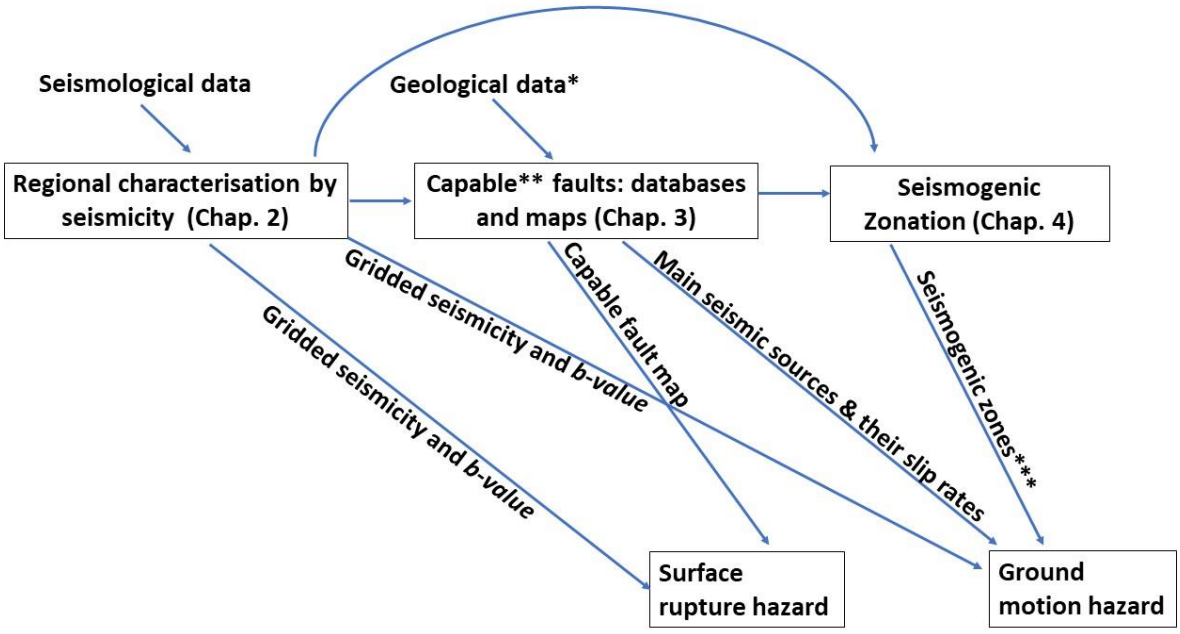

Fig. 5.1: A flowchart of the cascaded methodology suggested and implemented in this study. Seismological data is instrumental; the larger it is – the more ideal the method is. * Including information of slip rates (geodetic or paleoseismic source) to derive the main seismic sources from the capable fault map (see Chapter 3), for ground motion analysis. **In this case study, Quaternary faults are regarded as capable (see Chapter 3), but it is applicable for other recent geological periods that represent the current regional stress regime. *** Characterised by the *a* and *b* parameters of the frequency-magnitude relation. The hazard estimations of ground motion and surface rupture are subsequent steps that are not implemented in this work.

The main application of the Quaternary fault map is for surface rupture hazard rather than for ground motion analysis. The importance of this map is for siting and planning sensitive facilities. However, ground motion predictions can be analysed based on its derivative, the map of the main seismic sources. This map consists of the most significance faults in the region with the highest slip rates, so it is applicable for ground motion analysis.

The seismogenic zones, presented in the subsequent step of the methodology, are delineated based on the products of the previous chapters. They can be used as an input for ground motion predictions as well (Pecker et al., 2017), assuming a uniform seismicity pattern (constant *a* and *b* parameters). For each zone, the *b-value* can be either calculated based on its associated seismicity (like in the current work), or assumed as fixed regional value, especially when data is poor within zones (e.g. Ashish et al., 2016). Seismic hazard evaluation that is based on the suggested seismogenic zones can use either the local or the regional *b-value*, but the *a-values* presented here for each zone are only consistent with the local *b-values*. The regional *b-value* can be also an input for grid-based seismic hazard (e.g. Helmstetter el al., 2007). Hence, a few different approaches for seismic hazard estimation can be implemented based on the products of the current study (Fig. 5.1), and are not limited to these discussed here. On top of that, the cascaded methodology enables improving the understanding of the regional seismotectonics. Since each zone is depicted by an associated fault system, and it includes data of the maximum fault length, the *a* and *b* values, recurrence intervals of strong earthquakes, and slip rates for some of the faults (Fig. 3.3), the final results of this study, to some extent, can be also referred as a seismotectonic model.

One advantage of the suggested methodology is that some of its final products can be updated 'automatically' with time for a given region, by utilising an up-to-date earthquake catalogue, without 'manual' interference. These products include the gridded seismicity, i.e. the spatial distribution of the *earthquake density*, *seismic moment density*, and the *earthquake average depth*. However, the update of the 'capable' (in this study - Quaternary) fault map is based on future data from geological maps, and requires a detailed 'manual' work, apart from the implementation of the seismicity-based criterion. A catalogue of the same region that comprised of more earthquakes is expected to: a) reveal quite similar spatial seismicity distribution; b) raise the threshold values for the seismicity polygons (see chapter 3); c) adapt the polygon borders with (mostly-) minor changes. The delineation of seismogenic zones may require to reconsider the relation between the *earthquake density* distribution and other fault systems, if the distribution differs significantly in respect to earlier catalogues. The deduction of the frequency-magnitude parameters, at least through the method used here, also requires 'manual' considerations.

5.1.2. Reliability and Resolution of the Quaternary fault map

The seismological-based criterion of the Quaternary fault map is involved with a new approach, by amalgamating both data sources – instrumental seismicity and geological maps. The overlap polygons of this criterion and the Quaternary faults and superimposed in Fig 5.2. The spatial relation between the faults and the polygons can be an indicator of how successful this criterion is. Qualitatively, both features are distributed mostly in the same limited areas (Fig. 5.2). Moreover, the polygons cover mostly faults that enter the map based on geological criteria. In addition, by a simple observation, the majority of the latter are covered, either partially or to full extent, by the polygons. Hence, if there were no geological criteria, these faults would still enter the map based on the seismological-based criterion (ignoring its 6-km fault length limitation). This is a strong support for this criterion.

Despite the statistic approach for achieving reliable spatial distribution of the seismicity parameters (see Chapter 2), the accuracy of the seismic contours cannot compete with this of 1:50,000 mapped faults. Furthermore, the seismicity – faults correlation was based on the surface projection of the hypocentres and surface trace of faults without considering their structure and dip angle, so the depth domain was entirely neglected. The least successful correlation is expected to be achieved in the scenario of deep earthquakes that nucleate within low-angle faults, causing high misfit so the latter would not be marked; in addition, as an artefact, it may entail the marking of 'quiet' faults whose surface trace is closer to the epicentres. In such cases, the kernel weighting worsens the correlation since it gives a very little weight for events located away from a grid point for (Fig. 2.3). To a lesser extent, normal faults, which usually have higher dip angle, can also cause misfits in the correlation. The investigated region is characterised mainly by strike-slip faults, with some normal faults, and low-angle faults are rare. A more careful correlation shall consider the complexities of the depth domain, based on estimated dip angles and 3-D kernel-based spatial processing of hypocentres.

The seismicity distribution is based on high-resolution grid (500-m distance between grid points; see Chapter 2), as an attempt to improve the accuracy and the reliability of the results. A slight change of the 'overlap polygon' borders was observed when using a 1-km grid. However, a polygon derived from a 250-m grid was almost the same as the 500-m grid-based polygon that is implemented here.

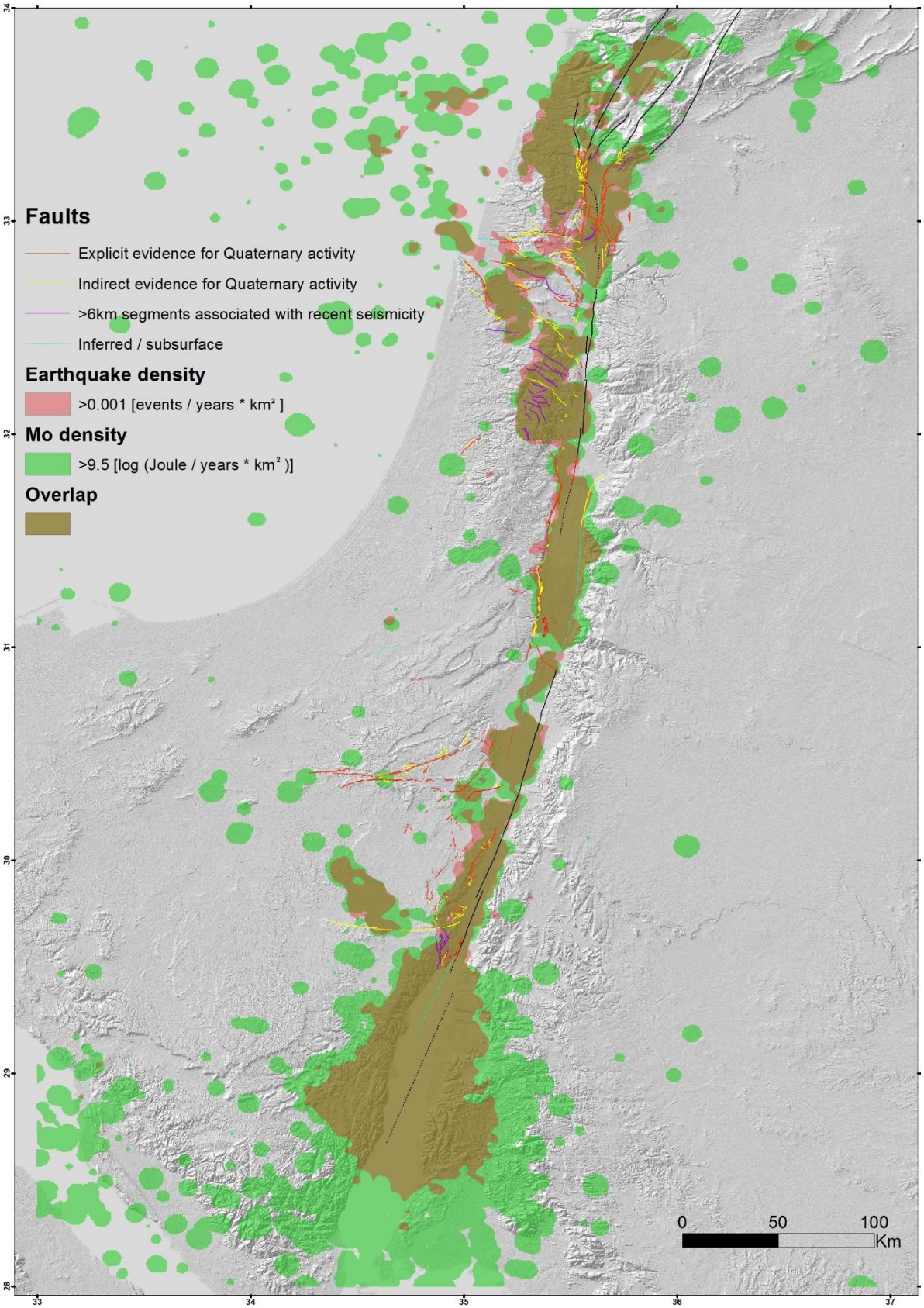

Fig. 5.2. The superimposition of the seismicity polygons: *earthquake density* of values > ~0.001 $events/Km^2/years$ and *Mo density* of values > ~9.5 log[$joules/Km^2$ $/years$]; the product is the overlap polygon (in brown; as in Fig. 3.1). The Quaternary faults are marked in different colours according to the criteria.

5.2. The frequency-magnitude relation

5.2.1. The *b-value*

5.2.1.1. Reliability

Several evidences from the current data support a correlation between the number of aftershocks and the *b-value*:

1) the *b-value* significantly drops from 1.19 to 0.99 in the whole investigated area, when examining the 1983–2017 and the 2007–2017 data (Table 2.3). The 1983–2007 data includes extremely high number of aftershocks (i.e. a few thousands), most of which followed the 1993 $M_d = 5.8$ and the 1995 $M_W = 7.2$ earthquakes. The 2007–2017 period contains very little aftershocks (probably a few hundreds, mainly these that followed a 2008 $M_d = 4.9$ event in southern Lebanon, within the Southern-Lebanon – Upper Galiliee sub-zone 2 (Fig. 4.6; Table 4.2), and the 2015 and 2016 $M_d = 5.5, 5.1$ shocks in the Gulf of Eilat, respectively). Potentially, a falsely-assumed drop in M_c can bias the *b-value* to lower values. This study shows that M_c drops from 1983–2017 to the 2007–2017 period in typically half a magnitude (4.0 vs 3.5 in the whole investigated area; 2.0 vs 1.5 in the seismic network coverage and in the zones of the Arava Valley the Dead Sea Basin; 1.5 vs 1.0 in the Kinnarot-Korazim-Hula zone; no change in the Carmel-Gilboa-Tirza zone; the 2007–2017 completeness magnitudes are unclear in zones that are mostly outside the network coverage). However, this drop is supported by the Kolmogorov-Smirnov test, corroborated visually according to the Gutenberg-Richter law (Figs. 2.7-2.14; Appendix 2), coincides with the ongoing improvements of the seismic network, particularly within the post-2007 period, and is not followed by a *b-value* drop in the network coverage area that hardly included aftershocks.

2) When focusing on the 11 and 16-year time windows within the whole investigated area (Figs. 2.15; 2.16), high *b-values* (~1.15–1.25) are obtained in the three time-windows that contain at least one of the two massive aftershocks sequences, which followed the 1993 and 1995 events. The same time windows within the network coverage area, which experienced very little aftershocks, yield much lower *b-values* (~0.75 – 0.9; Figs. 2.17; 2.18).

3) Accordingly, the *b-value* drops significantly from 1.19 or 0.99 (deduced from 1983–2017 and 2007–2017 data, respectively) in the whole investigated area, to 0.81 or 0.80 (1983–2017 or 2007–2017, respectively) in the network coverage area. The latter is poor of aftershocks, consists mainly a relatively short series that followed the 2001 $M_W = 5.1$ 2004 Dead Sea earthquake (Hofstetter et al., 2008); while the whole area includes very large number of aftershocks.

4) within seismogenic zones (Table 4.1), the *b-value* drops from 1.31 to 0.71–0.88 in the Gulf of Eilat, when examining data of 1983–2017 (which contains thousands of aftershocks) and 2007–2017 (which contains very little aftershocks in comparison, possibly tens), respectively; and from 0.75 to 0.67 in the Dead Sea Basin when examining the 1983–2017 and 2007–2017 data, respectively; only the first period contains the aftershocks of the 2004 $M_W = 5.1$ earthquake.

Several attempts were made to deduce the *b-value*, based on different datasets and time windows: Arieh (1967) achieved a 0.8 *b-value* within the latitudes 29–35°N and longitudes 33–37°E, based primarily on instrumental seismicity of the years 1919–1963. A *b-value* of 0.86 was obtained for the entire DST, based on two millennia of historical record and limited instrumental seismicity, and was used to describe the seismicity of a variety of zones (Ben-Menahem et al., 1977; Ben-Menahem, 1981), in agreement with two years of recorded data in a few zones (Ben-Menahem and Aboodi, 1981). Salamon et al. (1996) deduced a *b-value* of 1.0 for the DST from the 1900-1991 instrumental record, based on a limited magnitude range ($4.7 \leq M_L < 5.7$). Shapira and Hofstetter (2002) achieved a 0.96 *b-value* by combining regional historical and instrumental seismicity. Hamiel et al. (2009) integrated paleoseismic data of different time windows from the last 60,000 years, each consists of different frequencies, with instrumental and historical records. They yielded *b-values* in the range of 0.85–1.0 for the southern Arava valley, the Dead Sea Basin and the northern Jordan Valley, and 0.95 altogether.

The pre-instrumental record consists of macroseismicity and magnitudes that are less constrained. Thus, it is more ideal to compare the current results to a *b-value* that was deduced based on instrumental record only. Within the aforementioned studies, the study of Arieh (1967) is the only one based solely on the instrumental record that achieved a relatively constrained *b-value* (by a magnitude range of $4.5 \leq M < 6.25$). Arieh (1967) deduced a 0.8 *b-value*, and recurrence intervals of 36 years of $M \geq 6.0$ within an area that mostly overlaps the current investigated area. However, it includes parts of Cyprus and the eastern extension of the related convergence zone, an area of intense seismicity that may have affected the results due to a variety of reasons. On the other hand, it excludes the southern edge of the current area (i.e. parts of the Gulf of Eilat and the Suez rift). There are too many factors to figure how these changes affected the *b-value*. I assume that the different (but mostly overlapped) areas, of approximately the same size, can be compared for the frequency-magnitude parameters.

The current analysis yields recurrence intervals of ~60–70 years of $6.0 \leq M < 7.0$ earthquakes within the network coverage area, based on the investigation of 1983–2017 and 2007–2017 data (Table 2.3). These intervals are more stable than those obtained within the whole investigated area (21 and 43 years, based on 1983–2017 and 2007–2017 data, respectively) that suffers from the instability of the *b-value* (see Chapter 2). Assuming that $M \geq 6.0$ events occur only on the DST segments, an adjustment from the network coverage area to the whole investigated area can be made by considering the DST total length in each. Due to the poor detectability of the network in the Gulf of Eilat's southern section, I consider the latitude 28.5° as the southern limit (instead of 28.0°) of the investigated area. This reveals DST lengths of ~635-km in the whole area, and ~495-km in the network coverage area. Assuming similar seismicity pattern along the DST, the ~60-year interval within the network coverage area is adjusted to ~47–55 year interval within the whole investigated area. Considering also recurrence intervals of $M \geq 7.0$, the $M \geq 6.0$ intervals are of ~38-45 years in this analysis, nearly the same as ~36-year intervals of Arieh (1967). Since the *b-values* are also approximately the same, as expected, the *a-value* obtained here (3.17) is close to this achieved by Arieh (3.26 after normalising by the time window). Arieh (1967) utilised $4.5 \leq$

$M < 6.25$ events recorded during the 1919–1963 period. The high detectability threshold, due to poor network sensitivity, suggests that the *b-value* deduction was hardly affected by aftershocks. Hence, it reinforces a 0.8 regional *b-value* from a poor aftershock catalogue.

Shapira and Hofstetter (2002) calculated a 0.96 *b-value* by utilising instrumental and historic $2.2 \leq M < 7.3$ earthquakes. Their frequency-magnitude diagram shows that this *b-value* obeys the Gutenberg-Richter law, also for the $2.2 \leq M < 5.0$ events (i.e. exclusively instrumental seismicity). Their catalogue included a relatively small portion of the aftershocks of the 1995 $M_W = 7.2$ Nuweiba earthquake and thus their *b-value* was probably somewhat biased towards high values. The current analysis yields a *b-value* of 1.19 based on 1983–2017 data from the whole investigated area (Table 2.3), which includes many more aftershocks within the Gulf of Eilat. The further increasing of the *b-value* can be once again explained by aftershocks.

Based on geometric considerations, and reinforced by a probabilistic aspect, King (1983) suggested that aftershocks and foreshocks yield higher and lower *b-values*, respectively. Studies that were based on real data support this argument (e.g. Suyehiro, 1966; Suyehiro and Sekiya, 1972; Gibowicz, 1973; Papazachos, 1975; von Seggern et al., 1981). Consequently, a long-term *b-value* averages temporal and spatial earthquake distribution variations. Since aftershocks are more common than foreshocks (at least according to non-microseismic data; e.g. Shaw, 1993; Felzer el al., 2004), a *b-value* obtained from non-declustered catalogue is more likely to be affected from the aftershocks and thus is subjected to be biased towards higher values (for example, Helmstetter et al., 2006; the current results, based on a rich aftershock catalogue with very small number of foreshocks). However, it was demonstrated from a global earthquake data that a *b-value* of a unity is consistent with average ratios related to the occurrence of foreshocks and aftershocks (Felzer et al., 2004). A long-term *b-value* of a unity was also suggested for all fault systems, based on geometric consideration (King, 1983). These imply that catalogues that consist of many aftershocks but very small number of foreshocks (such as the catalogue investigated here) are likely to be biased towards high *b-values*, but different catalogues can be also biased otherwise, so a declustered catalogue would not necessarily yield a lower *b-value*.

The relative absence of aftershocks and the *b-value* stability within the network coverage area, suggest that ~0.8 is a stable value for the *b* parameter, at least within the examined period. If the suggested correlation between aftershocks and the *b-value* is correct, then a declustered catalogue that includes the area of the intense aftershocks (mainly, the Gulf of Eilat) may reveal a similar *b-value*. Studies that achieved values much higher (close to 1.0) that based primarily on the instrumental record, may have either used catalogues 'contaminated' by aftershocks; were based on poorly-constrained calculation (e.g. limited magnitude range and/or small number of events); or were based on spatio-temporal frames that are not representative. Extremely low or high values of *b* were obtained in previous studies that were focused on specific zones and/or limited time windows (e.g. El-Isa et al., 1984; Navon, 2012; Sharon et al., 2016). Generally, the smaller the investigated area is, the larger are the *b-value* variations, especially when being examined in limited time windows.

The foregoing discussion suggests that a complementary declustered catalogue will provide an alternative point of view, and might contribute to the determination a reliable *b-value*. This sub-section also postulates that a much longer time window, which spans more than the earthquake cycle, may reveal a *b-value* approximately similar to this that shall be obtained from a declustered catalogue of a much shorter time window, and perhaps, as supported by some studies (e.g. King, 1983; Felzer et al., 2004), a value close to a unity. This postulation assumes that a *b-value*, which is based on a very long time window, is not biased by either foreshocks or aftershocks because their total contribution balances the *b-value* in a long time window (Felzer et al., 2004), despite the relative abundance of aftershocks. The postulation has strings attached since: a) the ratio between foreshocks and aftershocks may vary between different regions; b) it neglects other spatio-temporal variations of the *b-value*, which are not necessarily related to aftershocks (see the next sub-section).

The analysis and the following discussion suggest that a ~0.8 *b-value* is best to represent the region, at least according to 1983–2017 data, considering its relative stability and constraints, and the very little, if any, bias due to aftershocks. Higher *b-values* (e.g. 0.95–0.96; Shapira and Hofstetter, 2002; Hamiel et al., 2009) that fit a combined instrumental and pre-instrumental data can be explained by either a 'contaminated' or poor instrumental data of the (mostly lower-) magnitudes, which may pretend to fit the long-term higher *b-value*. Regarding the pre-instrumental data, this sub-section leads to two primary options: 1) the high *b-value* reflects long-term seismicity behaviour, so the low ~0.8 *b-value* is temporarily. 2) the higher *b-value* does not reflect long-term seismicity behaviour, while the low ~0.8 *b-value* represents the region better also in longer periods. This option can be explained by the poorly-constrained magnitudes of the pre-instrumental record: a poor estimation (possibly - underestimation) of these magnitudes can bias the *b-value* towards higher values. Since every region has its own characteristics and subjected to local conditions (e.g. different structures, lithologies, differential stress; see the next sub-section), a *b-value* of a unity, like suggested by either data from other regions or theoretically (e.g. King, 1983; Felzer et al., 2004), does not necessarily represent a long time-window in every region. Possible explanations for both options are discussed in the next sub-section. However, the second option of a long-term 0.8 *b-value* is reinforced by the ensuing recurrence intervals (see section 5.2.2).

5.2.1.2. Implications

A few studies suggested that the *b-value* is inversely correlated to the differential stress (Scholz, 1968; 2015; Gibowicz, 1974; Henderson and Main, 1992; Amitrano, 2003; Spada et al., 2013), including a direct relation between the *b-value* and the style of faulting, and the subsequent tectonic environment (Schorlemmer et al., 2005; Gulia and Wiemer, 2010). The typical values are ~0.7 for areas governed by the highest stress (convergence zones characterised by thrust faults), ~0.9 for areas of lower stress (transforms or other strike-slip faults) and ~1.1 for areas of the lowest stress (e.g. rifting and other zones dominated by normal faulting). Thus, a 0.8 *b-value* is lower than typical zones dominated by strike-slip faults. Therefore, it may imply that the southern part of the DST is currently under a high differential stress in comparison to other strike-slip zones. Indeed, slip deficits in an order of

a few meters along the DST main segments (e.g. Sadeh et al., 2012; Lefevere et al., 2018) confirm that they accommodate a relatively high strain. In addition, asperities may be characterised by relatively low *b-values* as well (Wiemer and Wyss, 1997; Wyss et al., 2000; 2004; Wyss, 2001; Schrolemmer et al., 2004; Schorlemmer and Wiemer, 2005).

Other studies show an inverse correlation between the *b-value* and the earthquake depth through most of the brittle part of the earth' crust (Mori and Abercrombie, 1997; Gerstenberg et al., 2001; Amorese et al., 2010), including a negative correlation with the differential stress depth profile (Spada et al., 2013). Thus, the *b-value* is expected to generally decrease from near-surface to deeper areas of the brittle crust, until it reaches the intermediate crust. This suggests that rupture initiations have higher probability to grow in the intermediate crust compared with the shallow crust (Mori and Abercrombie, 1997). Deeper than the intermediate crust, the *b-value* is expected to increase towards the Moho. A careful analysis regarding the relation between the *b-value* and hypocentres with well-constrained depth could potentially point out whether the focus depths are an actual factor. Since the trend of the *b-value* with depth is suggested to alternate in the intermediate crust, following the brittle-ductile transition, the hypocentre depth accuracy is extremely important to supply highly-constrained depth profile. Moreover, this transition is expected to be correlated with the thermal profile, so thermal spatial variations should be also considered for estimating the trend of the *b-value* with depth. If the *b-value* can be used as a stress-meter, a spatial mapping of this parameter (e.g. Sharon et al. (2016), but with a more robust calculation and further considerations) have the potential to map areas of high stress and link them to the depth distribution and to young faults. This requires a comprehensive analysis that could not be achieved here. A rough examination between the *b-value* and the *earthquake average depth* in seismogenic zones does not suggest a clear correlation (not presented here).

Based on laboratory experiments, Goebel et al. (2017) suggested that the *b-value* increases with fault roughness and decreases with the localisation of the deformation, two relationships that accord with one another, presuming that faults become smoother as they evolve and accommodate slip (Sagy et al., 2007). The possible *b-value*–localisation inverse-correlation can be examined by the variations of the *b-value* between seismogenic zones, and the recent geological history of the associated fault system. If a *b-value* of ~0.8 characterises the investigated area as suggested in this study, then spatial variations of the seismogenic zones' *b-values*, in respect to the regional value, might reflect the level of the localisation of the associated fault system.

To a large extent, faulting along the DST became localised by the end of the Miocene (Marco, 2007), in agreement with the generally low *b-values*. Along much of the Arava valley, however, the deformation zone has undergone widening since the Plio-Pleistocene (Marco, 2007 and references therein; also notable in the Quaternary fault map, Fig. 3.2). If the *b-value* is correlative to fault roughness, then the Arava Valley seismogenic zone should be characterised by a relatively high *b-value*. Indeed, values are slightly higher than the suggested regional value (0.83 and 0.88, based on 1983–2017 and 2007–2017 data, respectively; Table 4.1). Accordingly, the *b-value* in zones where localisation has been taking place (the Dead Sea and the Hula basins; Marco, 2007 and references therein) are lower than

the regional *b-value* (0.75 within the Dead Sea Basin; 0.66 within the Kinnarot-Korazim-Hula zone; 0.52 within the Hula basin sub-zone, but it is poorly constrained; Tables 4.1; 4.2). Thus, the results of this study coincide with the low *b-value*–localised fault zones suggested correlation (Goebel et al., 2017). However, this agreement should be taken with a grain of salt as only three zones show this correlation (within other zones, the data is insufficient to examine). Furthermore, variations of the *b-value* are likely to be dependent on other suggested factors discussed earlier (e.g. earthquake depth profile; cumulative strain; and the number of foreshocks or aftershocks that can be significant in limited time-space frames).

There are multiple factors that may cause variations of the *b-value* among seismogenic zones. The possible effect of a single factor remains vague, also when attempting to explain the low ~0.8 regional *b-value*. The current high slip deficits along the DST support the possibility that this value is temporal, while the generally-localised faulting along the DST reinforces a long-term low *b-value.*

5.2.2. Recurrence intervals

The frequency-magnitude parameters are achieved based on ~35-year time window of recorded seismicity, a period that is much shorter than the seismic cycle. The purpose of this section is to determine the most reliable recurrence intervals of strong earthquakes in the region, within the optional frequency-magnitude parameters obtained here. The reliability is specifically important to assess carefully the regional *b-value*, with more clarity**,** and for the understanding of the long-term seismicity pattern. Hence, in this section I examine the fit of the achieved recurrence intervals to those that can be estimated in longer time windows and are relatively constrained in both intervals and magnitudes, compared with other historical and/or paleoseismic estimations.

5.2.2.1. The effect of biased high *a* and *b-values*: example from this data

In order to compare the recurrence intervals within different areas, I consider the spatio-temporal frequency of the events. First, the temporal frequency is the inversion of the recurrence intervals. Secondly, this inversion is divided by the DST total length in each area, under the assumptions of similar seismicity pattern, and that the largest events are only accommodated by the DST. Thus, the spatio-temporal frequency is achieved by $[recurrence\ interval \times fault\ length]^{-1}$. The obtained $7.0 \leq M < 8.0$ recurrence intervals are 334 and 381 years within the whole investigated area and the network coverage area, respectively (according to the 1983–2017 data; Table 2.3). Considering DST lengths of ~635-km and ~495-km (see section 5.2.1.1), respectively, average frequencies of $\sim 4.7 * 10^{-6}[year * km]^{-1}$ and $\sim 5.3 * 10^{-6}[year * km]^{-1}$ are yielded.

A higher spatio-temporal frequency within the whole area is expected, as unlike the network coverage area, it includes the most seismically active zones (the Gulf of Eilat and southern Lebanon). However, the frequency in the network coverage area is higher. The *b-value* of the whole region, probably biased towards high values, is suggested to bias the frequency to smaller values (=long recurrence intervals) in turn, when extrapolated to the largest

magnitudes. These long intervals are only slightly biased, probably because aftershocks also raise the *a-value*, and by that, the amount of bias is reduced. In the case of $6.0 \leq M < 7.0$ events, however, the whole area is characterised by a higher frequency as expected ($\sim 7.5 * 10^{-5}[year * km]^{-1}$ vs $\sim 3.4 * 10^{-5}[year * km]^{-1}$). The trend continues to $5.0 \leq M < 6.0$ frequencies, which are much higher in the whole area ($\sim 1.1 * 10^{-3}[year * km]^{-1}$ vs $\sim 2.2 * 10^{-4}[year * km]^{-1}$). Therefore, the effect of the high (biased) *b-value* on the recurrence intervals depends on the magnitude range. The same examination, but of the 2007–2017 data, shows a gentler picture of smaller differences, probably because the *b-value* (0.99) within the whole area is less biased by aftershocks.

When aftershocks bias the *b-value* towards higher values, it entails a raise of the *a-value* since it is defined as the intersection between the Gutenberg-Richter linear fit and the magnitude zero axis. Regardless, aftershocks also raise the *a-value* independently (i.e. for a given *b-value*), since they raise the number of the (mostly smaller-) events. Thus, aftershocks are suggested to: a) raise the *b-value*; b) raise the *a-value*, due to the high *b-value* but also independently; c) bias the recurrence intervals of the largest magnitude events towards long intervals, when extrapolating the Gutenberg-Richter law. This effect is somewhat reduced by the high *a-value;* d) 'bias' the recurrence intervals of the lower magnitude range towards short intervals, due to the combined effect of high *a* and *b* values. The latter is not an actual bias since the recurrence intervals reflect the examined time-window, when the data is not extrapolated to higher magnitudes. However, these intervals are not likely to reflect the frequency-magnitude relation in longer time periods, so in the context of such periods they should be regarded as biased.

The obtained spatio-temporal frequencies of $7.0 \leq M < 8.0$ are close to one another and therefore show consistency in the analysis, despite the very different *b-values* (0.80–1.19). This emphasises the importance of the *a-value*, which in some studies seems to be neglected, but is an essential parameter for estimating the recurrence intervals. The *b-value* of ~0.8 that was obtained within the network coverage area is more stable over the periods examined in this study, compared with the ~1.0 and ~1.2 values within the whole area (Table 2.3; reinforced by Figs. 2.15–2.18), and is considered here as reliable (see Chapter 2 and section 5.2.1.1). Hence, in the next sub-section, the recurrence intervals used for comparison are these yielded from data within the network coverage area, recorded in the whole period (1983–2017) which may be more representative due to larger data.

5.2.2.2. Comparison to a 100-year time-window of instrumental record

Earthquakes have been recorded by instruments for more than a century. Thus, it is worthwhile to exploit the relative accuracy in the magnitude determination, in respect to the pre-instrumental record, and to compare the intervals, assuming that a ~100-year time-window is more representative than a ~35-year time-window. Due to the limited instrumental detectability mainly in the first half of the 20th century, the catalogue is complete only for large earthquakes ($M \geq 6.0$) and possibly for $M \geq 5.0$ too. The frequency of earthquakes recorded in the last 100 years are compared to these obtained in the current study, in two magnitude ranges: $5.0 \leq M < 6.0$ and $6.0 \leq M < 7.0$.

The magnitude range of $5.0 \leq M < 6.0$ may be incomplete, and probably many of these events' magnitudes are not well-constrained. However, a comparison to the current results can lead to some insights. Within the whole investigated area, 33 earthquakes were recorded. The more-biased *b-value* (1.19) yields recurrence intervals of 1.4 years (i.e. 71 shocks in 100 years; Table 2.3). Even if the 100-year catalogue is somewhat incomplete for $5.0 \leq M < 6.0$ events, it is still not likely to accommodate that much events. Hence, the 1.4-year recurrence interval seems to be biased towards short periods. The less-biased *b-value* (0.99), however, deduces 4-year recurrence interval, i.e. 25 events in 100 years, slightly less than the recorded events (although the gap might be larger if some $5.0 \leq M < 6.0$ were not recorded). Nonetheless, 11 events from the 33 recorded earthquakes can be interpreted as aftershocks of the 1993 and 1995 shocks in the Gulf of Eilat. Thus, the 0.99 *b-value*, which is obtained from 2007–2017 data that did not include these aftershocks, is compatible with the 100-year catalogue when removing large portion of the aftershocks.

The results within the network coverage, as described in the last sub-section, are probably more accurate than these obtained for the whole area. The 9-year recurrence interval within the network coverage (Table 2.3) can be translated to ~7-year interval in the whole investigated area (assuming ~495-km and ~635-km DST lengths and similar seismicity pattern; see the above sub-section), i.e., ~14 events in a century. Since the whole investigated area is much wider in longitudes and includes areas far away from the DST, I omit 10 events that are probably not associated directly with the DST (except the 1984 $M_d = 5.3$ event in the area of the Carmel fault, because it is within the network coverage). That leaves 23 shocks located in the whole investigated area that are associated with the DST, and only 12 earthquakes that are also not aftershocks of the 1993 and 1995 events. Therefore, once again, there is a good agreement between the poor-aftershock data's results, and the actual record after removing large aftershock portion.

Although the $5.0 \leq M < 6.0$ event data may be incomplete and the magnitudes are not well-constrained, the comparison reveals that the recurrence intervals calculated from catalogue of relatively little aftershocks (2007–2017 in the whole area), or hardly any (1983–2017 within the network coverage), are in general agreement with non-or-poor aftershock record of events in a 100-year time-window. The rich aftershock catalogue (1983–2017 within the whole area), however, suggests many more earthquakes than actually recorded in a 100-time window, even when not omitting the recorded aftershocks. Therefore, it is probably biased towards short intervals.

Only a single $6.0 \leq M < 7.0$ event occurred in the past century in association to the DST within the investigated area (the 1927 $M_L = 6.2$ Jericho event; Ben-Menahem et al., 1976; Shapira, 1979). This event was located within the network coverage area, so it can be compared within it or in respect to the whole area, with the recurrence intervals obtained in this study. A ~60-year recurrence interval was obtained in this study (Table 2.3) within the network coverage area, in general agreement with this single event. The ~60-year recurrence interval can be adjusted to ~46-year interval in the whole investigated area (see the above sub-section). This implies that at least one $6.0 \leq M < 7.0$ earthquake is missing in the last century. The GII reports a $M_d = 6.0$ event in 1956 within southern Lebanon (in the

investigated area) that may be related to the Roum fault (Nemer and Meghraoui, 2006). However, a variety of estimations imply a magnitude lower than 6.0 (4.5 or 6.5 by the International Seismological Centre; $M_w = 5.3$ by the National Earthquake Information Center).

The flat scatter of the high-magnitude ($5.7 \leq M \leq 7.2$) regional data in the examined ~35-year time window (Fig. 2.9) emphasises that earthquakes as strong as the $M_w = 7.2$ 1995 earthquakes typically occur in much longer intervals than 35-year time window. This implies that the 1995 shock compensates the absence of $5.7 \leq M < 6.2$ events that were supposed to occur in the past ~35 years according to the Gutenberg-Richter law, or the absence of the latter is a consequence of the former. A 'characteristic' behaviour along the DST is also plausible, but the well-constrained magnitude record is too short to verify this. In general, the recurrence intervals obtained from the poor-aftershock data is in good agreement with the 100-year time-window of instrumental seismicity, for both $5.0 \leq M < 6.0$ (when removing aftershocks) and $6.0 \leq M < 7.0$ events. The possible absence of one or two $6.0 \leq M < 7.0$ events can be circumstantial.

The comparison of the recurrence intervals derived from the non-preferred *b-values* (Table 2.3) are also examined, to shed light on the reliability of the *b-value* - M_c sets. The recurrence intervals of $6.0 \leq M < 7.0$ shocks are either much lower (1, 8, 14 years) or higher (316 years). These intervals are far from matching the 100-year instrumental record. Hence, the comparison implies that the non-preferred b-*value* - M_c sets should be negated. Within the preferred sets, 21- and 43-year intervals are derived from the more-biased and less-biased *b-values,* respectively (1.19 and 0.99; Table 2.3). While the 43-year interval is almost the same as the preferred non-biased *b-value* (~46 years, after adjustment – see description above), the 21-year interval is closer to these yielded from the non-preferred *b-values*. In this case, the combined effect of aftershocks (see the above sub-section) is demonstrated. Both the *a-values* and the *b-values* are raised as a consequence of the aftershocks, mainly these of the 1993 and 1995 earthquakes in the Gulf of Eilat. Therefore, the deflection trend of the recurrence intervals is emphasised when they are yielded from the more-biased 1.19 *b-value,* obtained from 1983–2017 data. The same bias towards short period is achieved for the $5.0 \leq M < 6.0$ events. The more biased are the *a* and the *b* parameters, the shorter are the ensuing recurrence intervals. However, the largest magnitude recurrence intervals are deflected otherwise (see the above sub-section).

5.2.2.3. Comparison to a 2000-year time-window

The magnitudes of the pre-instrumental record are estimated by assumptions and therefore are less constrained than these of the instrumental era. About 25 historical earthquakes were documented in the past two millennia, estimated to rupture the southern DST segments north of the Gulf of Eilat (Agnon, 2014; Marco and Klinger, 2014; Lefevre et al., 2018). If most of these reported events are of at least a magnitude 6.0 (following Agnon, 2014), and more earthquakes occurred without any documentation (e.g. shocks nucleated in the Arava valley, where nearby population was sparse, and documentation was poor; Dead Sea Basin seismites that do not correlate with historical events – see Kagan et al., 2011; Agnon, 2014; and further

discussion below), it is reasonable to assume that at least 30 events of $M \geq 6.0$ occurred within the southern DST (excluding the Gulf of Eilat), during the last two millennia. The seismic network coverage area is comprised of the same DST segments. The frequency-magnitude relation within it, based on 1983–2017 data and 2007–2017 data, yields ~41 (or ~36 based on the alternative option; Table 2.3) and ~35 $M \geq 6.0$ earthquakes in two millennia, respectively. Therefore, the suggested recurrence intervals are in a general agreement with the reported historical record, with complementary paleoseismic evidences.

The similarity between the obtained recurrence intervals within the network coverage area, and these inferred from the pre-instrumental data, is further investigated considering a recent analysis of paleoseismic and historic data. Seismites that were correlated in three sites along ~50-km within the Dead Sea basin, revealed average intervals of ~200 years in the last two millennia (Kagan et al., 2011). It is reasonable to assume that the deformed sediments were triggered by $M \geq 6.0$ earthquakes in the vicinity of the sites or further in the Dead Sea basin, or by even larger events ($M \geq 7.0$) nucleated in a distance up to 100–200 kilometres away from the sites (following the magnitude-distance estimation by Kagan et al., 2011, based on historical data). Hence, it is plausible that $M \geq 6.0$ shocks along a ~150-km section can trigger the deformation resulted in the correlated seismites. This study suggests ~49-year (1983–2017 data; alternatively, ~56-year) or ~58-year (2007–2017 data) $M \geq 6.0$ recurrence intervals for a ~495-km section of the DST (within the network coverage), i.e., ~160- (or ~185-) ~190-year intervals for a ~150-km segment, assuming similar seismicity pattern along the DST. These intervals consent with these suggested by Kagan et al. (2011). Thus, the suggested regional recurrence intervals are reinforced by both historical and paleoseismic investigations, and by their combined analysis. This consent reinforces a regional *b-value* of ~0.8 (in the ranges of 0.80–0.83).

The nuances between the 1983–2017 and 2007–2017 data, within the network coverage, are probably circumstantial. Although the 2007–2017 data, which includes lower number of aftershocks, yields results that fit better to the 2000-year record, the results of the alternative option (1983–2017 data) are very similar. While the *b-values* are quite the same (0.80–0.83), the recurrence intervals are also *a-value* dependent, which is influenced by aftershocks too. However, the number of aftershocks in the 1983–2017 data is quite small, and the magnitudes of the pre-instrumental record are not constrained enough for a detailed comparison. Moreover, the extrapolation of the Gutenberg-Richter law from periods as short as decades to two-millennia naturally involves small inaccuracies.

The ~500- and ~150-km DST sections of the above comparisons are assumed here to have accommodated ~30 or slightly more, and ~10 $M \geq 6.0$ events, respectively, in the past two millennia. These two DST sections, respectively, are suggested by data from the whole investigated area to accommodate ~103 and ~31 $M \geq 6.0$ events in two millennia (based on 1983–2017 data); and ~54 and ~16 events (based on 2007–2017 data). Like the comparison to the 100-year of instrumental seismicity, the more-biased *b-value* (1.19) yields many more events than the actual record, while the less-biased *b-value* (0.99) suggests slightly more events than these suggested by the ~0.8 *b-values*. Since the numbers of $M \geq 6.0$ events obtained from the latter (35–41 and ~11–12) are already slightly higher than revealed from

the two millennia time record, a further increase implies inaccuracy obtained from the whole investigated area, especially from the 1983–2017 data, in agreement with the ongoing discussion.

In the methodological aspect, despite the lack of fit to the longer time-window records as discussed here, all the four (or five) *b-value* - M_C preferable sets (Chapter 2) yield recurrence intervals that are in better agreement to the 100 and 2000-year records, than the non-preferable sets (Table 2.3). This strengthens the selection of the preferable sets and support the claim (Chapter 2; partially, Appendix 2) that the Kolmogorov-Smirnov test is insufficient by its own for determining reliably the completeness magnitudes and the corresponding *b-value*. Nevertheless, when combining this test with additional analyses and considerations, reliable results can be achieved.

Although there are many assumptions regarding the pre-instrumental magnitude estimation and the comparison to the recurrence intervals obtained here (e.g. magnitude-distance relation estimation), the sets of ~0.8 *b-values* (particularly of 0.80 and 0.83) are in good agreement with the 2000-year record. This agreement reinforces a ~0.8 regional *b-value* that represents long-term seismicity and contradicts the possibility of a temporarily-low *b-value* (within decades or a few centuries) due to high tectonic stress (see section 5.2.1.2.).

5.2.2.4. Recurrence intervals within seismogenic zones

The obtained recurrence intervals within the Dead Sea Basin seismogenic zone is also regarded for the comparison to the correlated seismites (see the above section). The Gutenberg-Richter law yields recurrence intervals of ~95- and ~65-years of $M \geq 6.0$ events, according to the 1983–2017 and 2007–2017 data, respectively. Since all the seismite sites are within the seismogenic zone of a ~90-km length (Table 4.1), all of these earthquakes should be able to trigger the correlated seismites, following the aforementioned assumption that these shocks can cause the deformation along a ~150-km section. Thus, these recurrence intervals are too short to fit the study of Kagan et al. (2011). Accordingly, the $7.0 \leq M < 8.0$ intervals within the zone (~360 or 630 years; Table 4.1) are quite similar to the regional intervals (~380 or ~450 years within the network coverage; Table 2.3), about five times shorter than expected (considering DST lengths of ~495-km of the network coverage area and ~90-km within the zone, and assuming similar seismicity pattern along the DST). Hence, the recurrence intervals within the Dead Sea Basin seismogenic zone are too short and can be considered as unreliable.

With a zone length and associated fault maximum length of 75- and 40-km, respectively, the Kinnarot-Korazim-Hula seismicity yields $7.0 \leq M < 8.0$ recurrence intervals of ~660 and ~820 years (by 1983–2017 and 2007–2017 data, respectively), a few times shorter than expected when comparing to the network coverage area. Both zones, the Kinnarot-Korazim-Hula and the Dead Sea Basin, reflect predominant seismicity within pull-apart basins (e.g. Figs. 4.2; 4.3; 4.6). The Gulf of Eilat exhibits similar pattern, but here the recurrence intervals are not clear since the *b-value* is not well-determined. However, considering the zone length (~125-km), the longer ~1310-year obtained interval is more reasonable than the other option

of ~425 years (Table 4.1; based on the 2007–2017 that is not highly 'contaminated' by aftershocks), but it is still shorter than the interval expected by considering the regional recurrence interval (~1500–1800 years, yielded by assuming regional seismicity pattern and accepting the ~380 or ~450-year interval within the network coverage (Tables 2.3; 4.1)). Thus, the seismicity within seismogenic zones, which are dominant by pull-apart basins, derive recurrence intervals of the largest shocks that are shorter than expected.

This phenomenon binds recurrence intervals longer than expected, when assuming regional seismicity pattern, for other seismogenic zones. Within the others, the Arava Valley is the only zone that consists of non-parallel long straight strike-slip segments of the DST. The obtained $7.0 \leq M < 8.0$ intervals (~1870 or ~4930 years, yielded from 1983–2017 and 2007–2017 data, respectively) are indeed longer than expected (~1280 to 1400 ~years, calculated the same as shown for the Gulf of Eilat). A similar pattern of long intervals of strong earthquakes could have been probably achieved by investigating the Jordan River and the Jordan Gorge DST segments, but their associated seismicity is too sparse to yield the recurrence intervals reliably (suggesting the deflection would be even higher than in the Arava segment).

Therefore, it is suggested that the deflections of the recurrence intervals within zones, in comparison to the expected intervals, are associated with the tectonic structures: zones dominated by pull-apart basins and associated releasing bends are characterised by seemingly short recurrence intervals of strong shocks, whereas zones associated with long straight segments are characterised by seemingly longer recurrence intervals (i.e. low frequencies). The seismicity within the Lebanon Restraining Bend is much sparser than expected for a zone that contains the main DST segments, exhibiting extremely long recurrence intervals that should be considered as non-representative (Table 4.1). Assuming there were no detectability issues (with $M_c = 2.0$ and frequency-magnitude relation that follows the Gutenberg-Richer law; Appendix. 2.9.3), the seemingly recurrence intervals in zones dominated by restraining bends may be even longer than in the long straight segments.

The seemingly different recurrence intervals, when comparing zones of pull-apart basins and of long straight segments, are probably a consequence of the pronounced seismic activity in pull-apart basins (e.g. Fig. 2.4), which is suggested to bias the intervals of strong shocks towards short periods. The basins accommodate both strike-slip motion along the main DST segments and extension along marginal faults, but the slip rates of the latter are much lower (Tables 3.1; 3.2) and thus cannot explain the entire deflections (the enhanced seismicity in pull-apart basins is further discussed in section 5.3.1). The long straight segments, however, seem to be associated with sparse seismicity during the investigated time-window, within an interseismic period (e.g. Fig. 2.4; the southern Arava valley is an exception, but it is not certain whether the associated seismicity is related to the main segments or nearby faults). The sparser seismicity biases the obtained recurrence intervals to longer periods. Hence, assuming the investigated time-window represents an interseismic period, a 'characteristic' seismic behaviour seems plausible for the long straight segments. The combination of the different seismicity patterns, in association to structures, balances the regional recurrence

intervals, so they show good fitness to records of longer time windows (see the last sub-sections).

The zones of the Carmel-Gilboa-Tirza and the Roum Fault can be referred as branches that split off the main fault zone. By assuming they accommodate strike-slip rate components of respectively ~0.7 mm/a and ~0.95 mm/a, which are presumably reduced from the DST main fault zone (following Sadeh et al., 2012; Hamiel et al., 2016; 2018b; Nemer and Meghraoui, 2006), and zone lengths of ~115 and ~45 km, the expected intervals can be obtained by multiplying the regional intervals by the ratios of: 1) DST length – zone length; 2) DST average slip rate (~5.0 mm/a; Appendix. 1.5) – zone slip rate. By accepting the ~60 to ~70-year intervals within the network coverage area (Table 2.3), this yields expected $6.0 \leq M < 7.0$ intervals of ~1850–2150 and ~3500–4050 years within the Carmel-Gilboa-Tirza and the Roum Fault seismogenic zones, respectively. However, the obtained intervals are ~100 and ~570 years for the Carmel-Gilboa-Tirza (by 1983–2017 and 2007–2017 data, respectively) and ~1220 years for the Roum fault (Table 4.1). Hence, the obtained intervals are much shorter than expected for both zones. There might have been detectability issues within the Roum Fault zone (suggested by the frequency-magnitude relation, Appendix 2.8.3) that can explain the deflection from the expected intervals. However, the Carmel-Gilboa-Tirza zone is mostly within the network coverage area and its seismicity follows the Gutenberg-Richter law (Appendices 2.5.3; 2.5.4). While the deflection from the expected intervals should be partly compensated by extension rates normal to the CGTF (~0.6 mm/a; Sadeh et al., 2012), the large difference between the periods of 1983–2017 and 2007–2017 is probably related to temporal seismicity patterns that may not represent a longer time window (particularly the former period).

The results demonstrate the strong influence of temporal changes in the seismicity pattern on the obtained recurrence intervals, within seismogenic zones. As expected, this effect is significant when examining the frequency-magnitude parameters in small areas. The largest the area and the longer the time-window, the more stable are the parameters. The investigated time window (~35 years) is much smaller than the earthquake cycle. Therefore, it explains the general unreliability of the obtained recurrence intervals within zones. Notwithstanding, these intervals imply different seismic behaviours associated with tectonic structures. The tectonic role of the Upper Galilee – Southern Lebanon and the Eastern Sinai zones is not well understood (the latter is discussed in section 5.3). Hence, they are disregarded here.

5.3. Tectonic insights

5.3.1. The spatio-temporal seismicity distribution along the DST

In a glance, the seismicity of the last ~35 years (1983–2017) concentrates at the DST fault zone (Figs. 2.4; 2.5; 4.4; 4.7), but also peaks at junctions where Quaternary fault systems meet, mostly intersection zones of the DST and its branches (Fig. 4.7). A similar conclusion was based on ~two years (1976–1979) of microseismic monitoring (Ben-Menahem and Aboodi, 1981). The enhancement of seismic activity in interaction zones is not surprising due to the structural and lithological complications. These zones tend to accommodate more earthquakes and seismic moment release than the nearby parts of the DST, due to many M < 5.0 earthquakes. However, their potential to produce strong earthquakes ($M > 6.0$) depends on the associated fault length and the coeval slip rates, and is therefore limited.

Parts of the DST long straight strike-slip segments are associated with relatively poor seismicity, including the northern parts of the Arava segment, and particularly parts of the Jordan valley segment (e.g. Fig. 2.4). However, the main transform basins (the Dead Sea, the Sea of Galilee and the Hula) accommodate more earthquakes. The pronounced seismic activity is reflected in both relatively high seismic moment release (Figs. 2.5; 4.3) and (seemingly-) short recurrence intervals (Table 4.1; see discussion in section 5.2.2.4). The basins accommodate both horizontal and extension motions along the main DST segments and marginal faults, respectively, but the latter slip in much lower rates (Tables 3.1; 3.2) and thus can be neglected. This suggests that releasing bends within pull-apart basins affect the slip rate distribution in time, so that the M_0 release rate in the basins is higher during 'aseismic' periods (between strong earthquakes) in comparison to the long straight segments. The heterogenous (temporal-) spatial seismicity distribution can be explained by the tendency of stress to concentrate locally within releasing bends and to cause failure (e.g. Chester and Chester, 2000) so more spots along the main fault are doomed to fail and to produce micro and small (possibly medium) earthquakes more often. The long linear segments, on the other hand, can maintain higher strain accumulation, which tend to release in stronger earthquakes, so their associated seismicity is less affected by local stress concentrations. In addition, the straight geometry of the long segments, with limited barriers, enables the production of strong shocks (e.g. Nielsen and Knopoff, 1998).

In the southern part of the Jordan Valley segment, seismic activity is apparent but focused westwards along the SE-NW horsetail-shaped faults of the CGTF (Fig. 4.7). North of the intersection with the CGTF, the seismicity is even sparser. Recent evidence of creep of approximately half of the total plate motion (2.5 ± 0.8 mm/a; Hamiel et al., 2016) could explain the sparse seismicity, but this creep is restricted to shallow depths (1.5 ± 1.0 km to the surface). Most earthquakes nucleate at greater depths of the continental crust, so the relative absence of seismicity cannot be explained by this creeping. Geodetic analyses suggest that this section accommodates lower sinistral slip rates than the section south of the CGTF (based on regional GPS analysis: ~3.8 and ~4.9 mm/a, respectively; Sadeh et al., (2012), and on direct GPS measurements: ~4.1 and ~4.8 mm/a (Hamiel et al., 2016; 2018b)), with the slip difference being transferred to the CGTF (Sadeh et al., 2012; Hamiel et al., 2018b). The slip transfer, together with the shallow creep, can at least partially explain the

relative lack of earthquakes. The sparse seismicity coincides with an ongoing strain accumulation along this segment, manifested in an inferred slip deficit of 3.5–5 m, which can be compensated by a $M_W \cong 7.4$ earthquake (Ferry et al., 2007).

The hereby investigated seismicity suggests a regional time-space pattern of strong earthquakes that are likely to occur on the long straight segments, and mostly small to medium earthquakes in interaction zones of other fault systems with the DST, and along branches. The instrumental seismicity, together with paleoseismic and historical evidences (Marco and Agnon, 1995; Marco et al., 1996; Zilberman et al., 2000; Migowski et al., 2004; Begin et al., 2005; Agnon et al., 2006; Kagan et al., 2011) suggest that pull-apart basins combine both patterns. Despite the structural variations, the long-term M_0 release should be rather uniform along the DST, since it accommodates roughly the same lateral slip rates (neglecting spatial variations like the seismogenic depth and the lithology, and the extensional deformation in the basins).

5.3.2. The DST parallel branches and lineaments

The CGTF, approximately parallel to the Red Sea spreading centre and the Suez rift, accommodates the second-largest concentration of seismicity, after the DST (Figs. 2.1; 2.4; 2.5; 4.4; 4.7). Fig. 5.3. displays a possible seismic pattern of minor activity trend along more parallel features, lineaments or straps. Although most of the possible lineaments are very gentle, almost neglectable, two are well apparent: the predominant is associated with the CGTF, and also dominant is the lineament associated with the Eastern Sinai seismogenic zone (Chapter 4). The latter emerges from about the northern tip of the Gulf of Eilat and runs to the northwest with peak activity slightly northwest of the Thamed fault. It is possibly gently continuing to the northwest as seismicity becomes sparse through the topographic depression between the mountains of Helal and Yelleg, northern Sinai, and some earthquakes were still recorded further at the Bardawil lagoon (Fig. 5.3). Hence, it is referred here as the Eilat-Bardawil lineament (EBL), suggested as a branch of the DST.

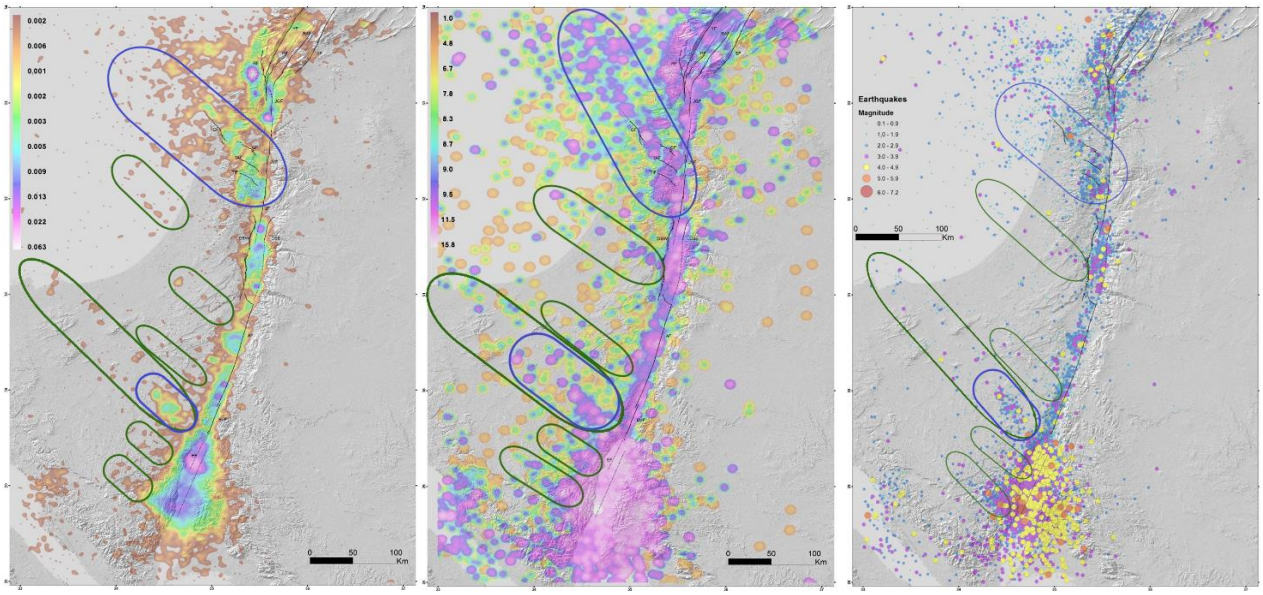

Fig. 5.3. ~NW trending seismicity lineaments or straps (Indigo: CGTF (north) and the EBL remarkable part (south); Green: possible lineaments). Backgrounds (Figs. 2.1; 2.4; 2.5): the epicentre distribution (left), *Earthquake density* (middle) and M_O *density* (right).

Some of the lineaments seem to emerge from structural transition within the DST: the EBL branches off the DST between the Gulf of Eilat, an extensional depression related to tectonic basins (Ben-Avraham et al., 1979; Ben-Avraham, 1985), and the Arava valley, a "structural and topographic saddle with hardly any 'rift valley' in its centre" (Garfunkel, 1981); the CGTF-associated seismicity strap emerges in proximity to the northern tip of the Dead Sea basin, another vast depression with extensional features (Garfunkel and Ben-Avraham, 1996). However, this case is different since the CGTF probably predates the DST (Segev et al., 2014). Other lineaments - structural relations are also possible (e.g. lineaments within the Gulf of Eilat that seem to emerge from transition zones between its basins).

5.3.3. Quaternary activity along the Sinai – Negev shear belt

The combined geological and seismological observations indicate that the SNB is mostly inactive in the context of large earthquakes, at least since the early Pleistocene: the Sa'ad-Nafha and the Ramon faults do not show direct evidence for Quaternary faulting (early-Pleistocene faulting is possible in their easternmost continuations but is not sufficiently constrained; Avni, 1998). If there have been vertical movements along these faults, they were probably minor (Yoav Avni, personal communication). With no other reported evidence for Quaternary activity, the Thamed fault is marked as Quaternary fault (Fig 3.2) only because it branches off the DST. Some sections of the Zin shear zone offset or tilted Quaternary sediments (Enzel et al., 1988; Avni and Zilberman, 2007; Yehouda Enzel, personal communication, for further deformation spots), but these displacements are limited to a few meters (at least in the Sede Zin region; Avni and Zilberman, 2007). The Paran and the Arif-Batur faults accommodated vertical offsets within the (probably early-) Quaternary up to a few meters and tens of meters, respectively (Bartov and Garfunkel, 1985; Zilberman, 1985; Zilberman et al., 1996; Avni, 1998; Calvo et al., 1998; Calvo, 2002). These displacements can be translated to very low average slip rates within the Quaternary, almost neglectable.

While the relative lack of activity of the SNB faults during the Pleistocene was known before this study (e.g. Garfunkel, 1988), less clear is their interaction with the DST (e.g. Garfunkel, 2014). The current results show that seismic activity along the DST peaks at the second-order zone AR2 (Fig. 4.7), located at a fault junction between the DST and N to NNE-trending Quaternary faults (Fig. 4.7; Avni et al., 2000 for faults' eastern extensions), bounded by the Paran and the Arif-Batur faults. Therefore, this sub-zone is probably the outcome of the interaction of these features. In addition, some epicentres were located along these fault lines. It may not be a coincidence that the only two SNB faults that show evidence for Quaternary activity (excluding the Zin shear zone), interact in a triple junction with the DST and accommodated more earthquakes in other parts during the instrumental period.

5.3.4. Regional and local stress fields

The regional stress field has been previously assessed based on a variety of considerations. Eyal and Reches (1983) suggested that mesostructures indicate the stress more accurately than macrostructures, since the latter are biased by the influence of older structures. They defined two regional stress fields, varied from a dominant maximum compression axis of W to WNW (the Syrian Arc stress (SAS)) governed in late-Cretaceous to Eocene times, to a younger, Neogene-Quaternary NNW to N (the Dead Sea stress (DSS)). The latter, however, is characterised by a predominant perpendicular extension. Nonetheless, a few evidences have brought Eyal and Reches (1983) to suggest a parallel occurrence of both stress regimes during the Neogene. It was corroborated by Eyal (1996) that analysed a variety of structures, which indicate a simultaneous formation of both SAS and DSS compatible structures since the mid-Miocene. However, the DSS stress prevails in the vicinity of the DST (Eyal and Reches, 1983). Nevertheless, the distinction between the two stress regimes may not be solid, as a more temporally-stable stress field, with principal axes that spread rather uniformly with mean ~NW maximum compression axis, is also possible (Flexer at al., 1984; Bahat and Grossman, 1988; Bahat, 1997). Based on macrostructures, Garfunkel (1981) inferred a ~NW maximum compression axis during the late Cretaceous to early Cenozoic, and a decrease in its magnitude since the late Cenozoic, resulting in predominant ~NE extension.

Analyses that ideally reflect the coeval state of stress consent with the above studies: the maximum horizontal compression axis, inferred from focal mechanism solutions, varies from WNW to NNW along the DST, while the latter varies between predominant compression and extension (Hofstetter et al., 2007); Geodetic data (Palano et al., 2013) suggest a spatial alternation between predominant NW to NNW compression along the DST and prevailing perpendicular extension in some distance away from it.

5.3.4.1. The context of ~SE-NW seismicity lineaments

Segev et al. (2011; 2014) concluded that Miocene rifting, probably related to the extensional regime associated with the Red Sea - Suez rifting, reactivated the CGTF and its eastern continuation beyond the DST (currently offset 90–100 km northward). The present extension along the CGTF (Sadeh et al., 2012) suggest that the possible seismicity lineaments (Fig.

5.3), all parallel or sub-parallel to these features, reflect a stress field of ~SW-NE extension (σ3, i.e. the minimum principal stress) and a vertical maximum compression (σ1, i.e. the maximum principal stress). It is reinforced by a variety of independent evidence: 1) the abundance of ~NW orientated faults in the Sinai Peninsula (Eyal et al., 1980), in Jordan and in Saudi Arabia (e.g. maps presented by Palano et al., 2013 and by Segev et al., 2014); 2) some of these faults seem to be associated with recent seismicity (Palano et al., 2013); 3) direct evidence of Quaternary faulting among ~NNW and ~NW to ~WNW trending faults in the western Negev and in the lower Galilee, respectively (Fig. 3. 2). 4) ~NE predominant coeval extension in the EBL by geodetic analysis (Palano et al., 2013); 5) a focal mechanism solution of a $M_d = 3.8$ event (Abdelazim et al., 2016) within the associated Eastern Sinai seismogenic zone suggests the same slip direction as accommodated by the CGTF (Sadeh et al., 2012).

The physical expression of the lineaments, possibly branches, is probably restricted to the sub-surface. Although the EBL follows the topographic separation between the mountains of Helal and Yelleg, both are related to anticlines of the Syrian Arc fold system (Moustafa, 2013 and references therein), so this separation currently brings no solid evidence for present SW-NE extension. The absence of mapped faults associated with the pronounced seismicity of the Eastern Sinai zone is surprising (see section 4.3.1). However, the lack of surface expression consent with the weak extensional stress inferred by the geodetic analysis (Palano et al., 2013) and the deep seismicity of the Eastern Sinai zone (Table 4.1; Fig. 4.8).

West of Eilat, some faults enter the Quaternary fault map due to their association with recent seismicity (Fig. 3.2), despite geological or structural-topographic evidence that in the recent geological past (i.e. Pliocene to present) they did not accommodate significant slip (Garfunkel, 1970; Marco, 2007; reinforced by Nuriel et al., 2017). In this case, seismicity is concentrated along pre-existing faults; in the case of the EBL and the other possible lineaments, the seismic sources are probably subsurface faults, which were reactivated or formed in the recent geological history as a response to stresses that sometimes accumulate in some distance away from the main fault zone. The extension-related stress probably concentrates locally along ~NW orientated features that mostly experienced a minor deformation in the recent geological history. The CGTF is an exception, with dominant surface features and topographic extension, which probably accommodates much of the deformation due to mechanical reasons (i.e. a weak zone) in relation to its geological history.

Since thermal changes can impose the type of the deep-crustal deformation (brittle or ductile), ductile lower-crust deformation may also occur elsewhere (e.g. along other parts of the EBL) and to reflect the same tectonic stress. The possible relation between the lineaments and structural transitions along the DST (see section 5.3.2.) implies that the lineaments reflect small tectonic movements associated with the DST structural variations. Subsurface analysis can confirm the existence of faults associated with the lineaments, and more focal mechanism solutions may support or negate an extension along the straps. Evidence for young activity of ~NW trending faults in Sinai, Jordan and Saudi Arabia is also essential to examine the suggested deformation pattern.

5.3.4.2. Insights from the activity along the Sinai – Negev shear belt

Field evidences indicate at least a single faulting phase of the SNB between the mid-Miocene to the early Pliocene, and another late-Pliocene - early Pleistocene phase (Garfunkel and Horowitz, 1966; Eidelman, 1979; Garfunkel, 1981; Zilberman et al., 1996; Avni et al., 2001; Calvo and Bartov, 2001). The post-Miocene regional tectonic phase is characterised by a tilt of the Negev highlands and surrounding areas towards the centre Arava valley, and since the early Quaternary, the main fault zone along the valley has undergone widening (Garfunkel and Horowitz, 1966; Avni et al., 2000; 2001; Ben-David et al., 2002; Marco, 2007; Guralnik et al., 2010). The current study emphasises that simultaneously, faulting along the SNB ceased, apart from minor movements.

The SNB faults have accommodated both vertical and right-lateral movements. Since these faults are trending E-W to WSW-ENE, the dextral motion is expected to be triggered by NW to WNW maximum compression axis. This motion is constrained by early-Miocene dykes, which were displaced by the total dextral slip where they apparent (Bartov, 1974). Hence, the relative lack of the Quaternary dextral displacement that postdates a faulting phase, suggests either a change in the direction of the regional ~NW maximum horizontal compression axis and/or a change in the magnitudes of the axes, resulting in a weak differential stress.

The post-Miocene trends of both regional tilt towards the DST, producing an extension-related morphological rift-valley (Garfunkel and Horowitz, 1966), and the decrease in the slip rates along the southern DST (Garfunkel, 2011), accord with the decrease of the magnitude of the ~NW compression, assuming a correlation between the amount of slip and the magnitude of maximum compression. The combination of these independent geological evidences and coeval predominant ~SW-NE extension in some distance away from the DST (by geodetic and seismological sources; see section 5.3.4.1) support a decrease in the ~NW compression of the regional stress field since the early Quaternary. The possibility of a weak differential stress due to a decreasing ~NE tectonic extension (i.e. higher $\sigma 3$) is less plausible due to the post-Miocene increasing extensional regime evident by the DST. However, a decrease of the ~NW maximum compression's magnitude does not contradict a shift of this axis towards the north, which also consent with the decrease of activity of the SNB.

The vertical motion along the SNB varies between normal and reverse faulting, with alternated throw directions within single faults, in both time and space (Bartov, 1974; Baer, 1981; Zilberman, 1981; 1983). While the spatial variations were ascribed to each fault's geometry (Bartov, 1974), the temporal variations are probably related to changes in the tectonic stress. The ~NW maximum compression axis is considered as the trigger for reverse motion along subsurface faults, including these of the SNB, associated with the rise of the Syrian Arc folds in the Negev and Sinai (Freund et al., 1975; Garfunkel, 1988). However, normal faulting occurred in the late Pliocene - early Pleistocene, accommodated by the Arif-Batur Fault, with vertical throw of at least 200m (Zilberman et al., 1996). A transition between oblique reverse-dextral to normal (-dextral?) faulting is likely to occur when the magnitude of the ~NW compressional principal axis decreases to a lower value than this of the vertical principal axis, so the latter becomes predominant. Nevertheless, the structural

relation between this normal faulting and other regional deformation (particularly, the central Negev uplifting) should be examined to draw conclusions.

The lack of both horizontal and vertical movements along the SNB implies that the ~NW compression reduced such that the ensuing differential stress is rather weak, insufficient to trigger significant motions. However, the SW-NE extension is sufficient to trigger small-scale deformation along ~SE-NW features (Quaternary faults in the Negev and in the Galilee (Fig. 3.2); the CGTF and possible seismicity lineaments (Fig. 5.3); see section 5.3.4.1.) This suggested change in the stress pattern can be explained by a recent tectonic phase accompanied by Euler pole shifting (Joffe and Garfunkel, 1987; Garfunkel, 2011). The possibility of the post-Miocene (early-Quaternary?) maximum compression axis shifting towards the north implies that the 'DSS'-recorded mesostructures analysed by Eyal and Reches (1983) are mostly younger than the Miocene (perhaps post early-Quaternary).

6. Conclusions

1) The cascaded methodology developed in this study amalgamates seismological and geological data, and generate essential products for seismic hazard assessment. The variety of products enables future hazard analyses to select a preferred analytical approach, or to combine or compare different approaches. The methodology enables the improvement of the tectonic understanding, and is suggested to be implemented elsewhere. It can be updated ongoingly and relatively easily with an up-to-date seismic catalogue.

2) The *earthquake density* and the *seismic moment density* reveal a more precise picture of the seismicity in the examined time window, compared with a simple observation of epicentres. The former enables capturing the main active seismic sources and to recognise zones that may reflect active patches within faults, while the latter highlights areas of the highest released energy, assuming point sources. These parameters, mostly independent, complement one another for mapping the most active tectonic sources and areas of highest likelihood to nucleate the largest shocks, based solely on instrumental seismicity. The *earthquake average depth* is reliable in limited areas but contributes to the understanding of the seismicity patterns and for characterising seismogenic zones, and consent with former seismological and thermal investigations. It varies along the DST between shallow depth of only a few kilometres and up to 25-km or deeper.

3) Within the past ~35-years, temporal variations of the *b-value* are interpreted to reflect changes in the seismicity pattern (e.g. aftershocks or swarms). A spatio-temporal analysis suggests that aftershocks enormously affect the frequency-magnitude parameters, by raising both the *a* and the *b values*. The ensuing recurrence intervals are interpreted here as biased towards short periods, except for the largest magnitude range that are biased otherwise.

4) A well-determined *b-value* of ~0.8 (0.80–0.83) is deduced within the network coverage area, where earthquake detectability is better, magnitudes are more constrained, and aftershocks were uncommon. It yields recurrence intervals of ~10, ~70 and ~450 years of $5 \leq M < 6$, $6 \leq M < 7$ and $7 \leq M < 8$ earthquakes, respectively, within the southern DST (excluding the Gulf of Eilat). These intervals fit well to much longer records of both 100- (instrumental) and 2,000-years (pre-instrumental). Thus, the ~0.8 *b-value* is suggested to represent the regional seismicity pattern, also in much longer periods than the investigated time window. The low *b-value* is possibly related to the generally-localised faulting along the DST. The good fit to the long-term recurrence intervals contradicts an alternative option that it is temporarily low due to high strain accumulation near the DST. In addition, the higher *b-values* (0.99–1.19), deduced within the whole investigated area that included many aftershocks, yield recurrence intervals that are too short to match the longer time-windows. Hence, it is further suggested that reliable frequency-magnitude parameters should be yielded from poor (or absent-) aftershock catalogues, at least in scarce-foreshock regions.

5) The DST-associated faults are predominant within the Quaternary faults, and consist of the main strike-slip segments, faults that are parallel to them including marginal faults, and faults that split off in an acute angle and can be classified as branches. The most significant among other Quaternary fault systems is the CGTF. Other systems are the SNB (partially), ~NNE and ~NNW orientated faults in the southern and central Negev and ~W to ~WNW trending

faults in the lower Galilee. There is a relative lack of evidences in the Upper Galilee. More faults with Quaternary activity are at the basins of the Sea of Galilee and the Hula, and in the Golan heights.

6) The relatively-uniform distribution of faults that entered the Quaternary fault map based on different criteria reinforces the designed criteria, especially the seismological-based criterion that is innovated here. The criteria can be the basis for further study of Quaternary faulting in the region. Since the Quaternary period samples well the current stress field, this map is significant for both Quaternary research and hazard evaluation purposes. It is essential for surface rupture hazard, for the planning of infrastructures and constructions, particularly for facilities of high vulnerability to this hazard. The Quaternary fault database shall be updated with the ongoing research and resolution improvement of geological mapping.

7) The main seismic sources, which are likely to produce the largest shocks in the region, can be derived from the Quaternary fault database by applying criteria that are based on slip rates (mostly geodetic-based). It consists of the most significant faults that accommodate the highest slip rate, and therefore is especially important for seismo-tectonic modelling and eventually for ground motion predictions.

8) Seismogenic zones are suggested to be defined and mapped according to the seismicity parameters' distribution and the associated fault systems. The peaks of the seismic activity mostly consent with the separation between major tectonic structures. Some sub-zones may represent seismically-active patches along faults. The delineation of the zones is based on the most up-to-date high-resolution geological data and statistically-processed seismological data. Hence, the location of the zones upon the surface is perhaps as precise as possible in respect to the associated seismic sources, whilst neglecting the depth domain.

9) The Gulf of Eilat is the most active seismogenic zone in the past ~35 years. The frequency-magnitude parameters within zones are highly dependent on the sampled time window and thus are generally not reliable. Although the catalogue is too poor to properly examine the uniformity of these parameters within zones, the *b-value* is rather uniform within the Dead Sea Basin, and possibly within the Carmel-Gilboa-Tirza zones. The average depth in sub-zones of the same primary zone is mostly similar, implying a physical connection that may be ascribed to either thermal or lithological variations related to tectonic structures. The deepest seismicity is within the Dead Sea Basin, the Eastern Sinai zone and to a lesser extent, in the Arava valley. The lack of temporal dependency of the average depth in primary zones may indicate a lack of migration of the seismic activity within faults.

10) The seismic activity is concentrated along the DST and to a lesser extent along the CGTF. In addition, it tends to concentrate at intersection zones of Quaternary fault systems, including the fault junctions of the DST with the CGTF, the SNB, ~NNE striking faults in the Arava valley, with possible branches of the Roum fault, and the Eastern Sinai zone. The interaction zones, probably related to structural and lithological complications, accommodate many $M < 5.0$ earthquakes, but their potential to produce stronger shocks depends on each zone's characteristics. The sparsest seismicity along the DST is accommodated by the northern part of the Jordan River segment. It is interpreted as a result of the slip transfer to the CGTF and possibly the shallow creeping.

11) The seismicity pattern along the southern DST in the examined time window is enhanced activity in the pull-apart basins and reduced activity in the long straight segments. The difference is reflected in high densities of earthquakes and seismic moment release, and seemingly short recurrence intervals of medium to strong earthquakes within the basins (and vice versa in the long segments). It is suggested that the ~35-year period is too short to represent the spatial variability of the frequency-magnitude relation between different structures along the DST. The suggested pattern is locked long segments that can accommodate high strain, which is released in strong earthquakes with high seismic moment release, and releasing bends that tend to fail more often and to produce more micro to medium earthquakes during the 'interseismic' period. Hence, it implies a long-term 'characteristic' behaviour within the long segments. It is reinforced by the absence of $5 \leq M < 6$ earthquakes within them, for perhaps nearly a century (the GII catalogue). The agreement of the regional recurrence intervals with records of the last two millennia implies that the intense seismicity within the basins balances the (quasi-?) 'characteristic' pattern, so the regional frequency-magnitude relation follows the Gutenberg-Richter law also for strong shocks.

12) The seismicity distribution maps reveal a possibility of ~NW trending seismicity lineaments or straps in the region. The most substantial follows the CGFT. The rest could not be simply associated with surface deformation. The predominant among them emerges from near the northern tip of the Gulf of Eilat and runs to the northwest, following the pronounced seismicity northwest of the Thamed fault (the Eastern Sinai zone). It might run further towards the Mediterranean Sea, and thus is referred here as the Eilat-Bardawil lineament (EBL), suggested as a subsurface branch of the DST. The other lineaments are very gently seen or neglectable. Since they are sub-parallel to broad regional extensional features, they are suggested as a (mostly-) gentle expression of a ~SW-NE predominant extensional stress field, perhaps in relation to structural variations along the DST. The suggested extensional pattern is supported by independent geological, seismological and geodetic evidences.

13) The SNB faults are long enough to generate strong earthquakes, but the combined geological and seismological observations suggest that they are mainly inactive in this term. Considering the regional ~NE extension and the geological history of the DST, their relative inactivity since the early Quaternary implies that the regional ~NW maximum horizontal compression axis decreased and/or shifted towards the north since the early Quaternary, perhaps earlier.

14) The methodology aids to examine the hypothesis of this study. The hypothesis is generally supported by the compatibility between peaks of the seismic activity and the main tectonic structures or fault systems, including the internal structure of the DST, the CGTF and fault junctions. It is reinforced by the general agreement of the maximum magnitude estimation within seismogenic zones and actual records. However, the seismicity is not always associated with mapped faults (e.g. the Eastern Sinai zone; although not mapped in 1:50,000 scale). Principally, the integration of geological and seismological database enables producing a vast platform for a variety of seismic hazards' estimations, and receive a high-resolution picture of the current tectonics, mostly unified by the two databases.

7. Bibliography

Abdelazim, M., Samir, A., El-Nader, I. A., Badawy, A., Hussein, H., 2016. Seismicity and focal mechanisms of earthquakes in Egypt from 2004 to 2011. NRIAG Journal of Astronomy and Geophysics, 5(2), 393-402.

Agnon, A., Migowski, C., Marco, S., 2006. Interclast breccias in laminated sequences reviewed: recorders of paleo-earthquakes. In Y. Enzel, A. Agnon, M. Stein (eds.)., New frontiers in the Dead Sea paleoenvironmental research: Geological Society of America Special Paper, 401, 195-213.

Agnon, A., 2014. Pre-instrumental earthquakes along the Dead Sea Rift. In Z. Garfunkel, Z. Ben-Avraham, E. J. Kagan (Eds.), The Dead Sea Transform Fault System: Reviews. Springer, Dordrecht, the Netherlands, pp. 207-262.

Aldersons, F., Ben-Avraham, Z., Hofstetter, A., Kissling, E., Al-Yazjeen, T., 2003. Lower-crustal strength under the Dead Sea basin from local earthquake data and rheological modeling. Earth and Planetary Science Letters, 214, 129-142.

Aldersons, F., Ben-Avraham, Z., 2014. The seismogenic thickness in the Dead Sea Area. In Z. Garfunkel, Z. Ben-Avraham, E. J. Kagan (Eds.), The Dead Sea Transform Fault System: Reviews. Springer, Dordrecht, the Netherlands, pp. 109–150.

Almagor, G., Hall, J. K., 1984. Morphology and the Mediterranean continental margin of Israel. Geo. Surv. Isr. Bull. 77, 1–31.

Ambraseys, N., 2009. Earthquakes in the Mediterranean and Middle East: a multidisciplinary study of seismicity up to 1900. Cambridge University Press, New York.

Amit, R., Harrison, J. B. J., Enzel, Y., 1995. Use of soils and colluvial deposits in analyzing tectonic events—the southern Arava rift, Israel. Geomorphology, 12, 91–107.

Amit, R., Zilberman, E., Porat, N., Enzel, Y., 1999. Relief inversion in the Avrona playa as evidence of large-magnitude historical earthquakes, southern Arava Valley, Dead Sea rift. Quat. Res., 52, 76–91.

Amit, R., Zilberman, E., Enzel, Y., Porat, N., 2002. Paleoseismic evidence for time dependency of seismic response on a fault system in the southern Arava Valley, Dead Sea rift, Israel, 114(2), 192–206.

Amitrano, D., 2003. Brittle-ductile transition and associated seismicity: experimental and numerical studies and relationship with the *b* value, Journal of Geophysical Research, 108(B1), 2044, doi:10.1029/2001JB000680.

Amorese, D., Grasso, J.-R. Rydelek, P. A., 2010. On varying b-values with depth: results from computer-intensive tests for Southern California. Geophysical Journal International, 180(1), 347–360, doi:10.1111/j.1365-246X.2009.04414.x.

Arieh, E., 1967. Seismicity of Israel and adjacent areas. Ministry of Development, Geol. Surv. Isr., Bull., 43, 1–14.

Arieh, E., Rabinowitz, N., 1989. Probabilistic assessment of earthquake hazard in Israel.

Tectonophysics, 167, 223–233.

Ashish, Lindholm, C., Parvez, I. A., Kuhn, D., 2016. Probabilistic earthquake hazard assessment for Peninsular India. Journal of Seismology, 20, 629-653.

Ataeva, G., Shapira, A., Hofstetter, A., 2014. Determination of source parameters for local and regional earthquakes in Israel. J Seismol DOI 10.1007/s10950-014-9472-x

Avni, Y., 1998. Paleogeography and tectonics of the Central Negev and the Dead Sea Rift western margin during the late Neogene and Quaternary. Geological Survey of Israel Report No. GSI/24/98. Ph.D. thesis, Hebrew University of Jerusalem, 231 pp. (In Hebrew, English abstract).

Avni, Y., Bartov, Y., Garfunkel, Z., 2000. Evolution of the Paran drainage basin and its relation to the Plio-Pleistocene history of the Arava Rift western margin. Israel. Isr. J. Earth Sci., 49, 215–238.

Avni, Y., Bartov, Y., Garfunkel, Z., Ginat, H., 2001. The Arava Formation—A Pliocene sequence in the Arava Valley and its western margin, southern Israel. Isr. J. Earth Sci., 50, 101–120.

Avni, Y., Zilberman, E., 2007. Landscape evolution triggered by neotectonics in the Sede Zin region, central Negev, Israel. Isr. J. Earth Sci., 55, 189–208.

Avni, Y., Segev, A. and Ginat, H., 2012. Oligocene regional denudation of the northern Afar dome: Pre-and syn-breakup stages of the Afro-Arabian plate. Bulletin, 124(11-12), pp.1871-1897.

Baer, G., 1981. The geology of the Arif-Batur lineament Ma'ale Hameshar area. Geological Survey of Israel Report No. GSI/5/81. MS.c. thesis, Hebrew University of Jerusalem, 63 pp. (In Hebrew, English abstract).

Baer, G., 1989. Igneous intrusions in Makhtesh Ramon, Israel: Mechanics of emplacement and structural implications. Geological Survey of Israel Report No. GSI/48/90. Ph.D. thesis, Hebrew University of Jerusalem, 88 pp. (In Hebrew, English abstract).

Bahat, D., 1997. Comment on “Stress field fluctuations along the Dead Sea rift since the middle Miocene” by Yehuda Eyal. Tectonics, 16(6), 1006–1008.

Bahat, D., Grossmann, N. F., 1988. Regional jointing and paleostresses in Eocene chalks around Beer Sheva. Israel journal of Earth Sciences, 37(4), 181–191.

Bartov, Y., 1974. A Structural and paleogeographical study of the central Sinai faults and domes. Ph.D. thesis, Hebrew University of Jerusalem, 143 pp. (In Hebrew, English abstract).

Bartov, Y., Garfunkel, Z., 1985. Field trip to the Karkom graben. Israel. Geological. Society, Annual Meeting. Yotvata, pp. 152–153.

Bartov, Y., Sagy, A., 2004. Late Pleistocene extension and strike-slip in the Dead Sea Basin. Geological Magazine, 141(5), 565–572.

Bartov, Y., Agnon, A., Enzel, Y., Stein, M., 2006. Late Quaternary faulting and subsidence in

the central Dead Sea basin. Israel J. Earth Sci., 55, 17–32.

Bartov, Y., Sneh, A. and Rosensaft, M., 2009. Potentially active faults in Israel (1 map). Isr. Geol. Surv., Jerusalem.

Bartov, Y., A. Sneh, L. Fleischer, V. Arad, Rosensaft, M., 2000. Map and catalogue of young faults in Israel. Geological Survey of Israel Report GSI/23/2000, 81 p. (in Hebrew, English absract).

Bartov, Y., Sneh, A., Fleischer, L., Arad, V. and Rosensaft, M., 2002. Potentially active faults in Israel stage B. Isr. Geol. Surv., Rep. GSI \29\2002, 8 p. (in Hebrew).

Begin, Z. B., Steinberg, D.M., Ichinose, G.A. and Marco, S., 2005. A 40,000 years unchanging seismic regime in the Dead Sea Rift. Geology, 33(4), 257–260.

Begin, Z. B. and Steinitz, G. 2005. Temporal and spatial variations of icroearthquake activity along the Dead Sea Fault, 1984–2004. Isr. J. Earth Sci., 54, 1–14.

Ben-Avraham, Z., 1985. Structural framework of the Gulf of Elat (Aqaba), Northern Red Sea. J. Geophys. Res., 90(B1), 703–726.

Ben-Avraham, Z., Hanel, R., Villinger, H., 1978. Heat flow through the Dead Sea rift. Mar. Geol, 28, 253–269.

Ben-Avraham, Z., Almagor, G., Garfunkel, Z., 1979. Sediments and structure of the Gulf of Elat (Aqaba)—northern Red Sea. Sedimentary Geology, 23(1-4), 239-267.

Ben-Avraham, Z., Ginzburg, A., 1986. Magnetic anomalies over the central Levant continental margin. Marine and Petroleum Geology, 3(3), 220-233.

Ben-Avraham, Z., Kempler, D., Ginzburg., A., 1988. Plate convergence in the Cyprean Arc. Tectonophysics, 146, 231–240.

Ben-Avraham, Z., Schubert, G., 2006. Deep “drop down” basin in the southern Dead Sea. Earth and Planetary research letters, 251, 254-263.

Ben-Avraham, Z., Garfunkel, Z., Lazar, M., 2008. Geology and Evolution of the Southern Dead Sea Fault with Emphasis on Subsurface Structure. Annual Review of Earth and Planetary Sciences, 36, 357–87.

Ben-David, R., Eyal, Y., Zilberman, E., Bowman, D., 2002. Fluvial systems response to rift margin tectonics: Makhtesh Ramon area, southern Israel. Geomorphology, 45(1-2), 147-163.

Ben-Gai, Y., Ben-Avraham, Z., 1996. Tectonic processes in offshore northern Israel and the evolution of the Carmel structure. Marine and petroleum Geology, 12(5), 533–548.

Bender, B., 1983. Maximum likelihood estimation of b values for magnitude grouped data, Bull. Seismol. Soc. Am., 73(3), 831–851.

Ben-Menahem, A., 1981. Variation of slip and creep along the Levant rift over the past 4500 years. In R. Freund, Z. Garfunkel (Eds.), The Dead Sea Rift. Tectonophysics, 80,183-197.

Ben-Menahem, A., Nur, A., Vered, M., 1976. Tectonics, Seismicity and structures of the Afro-Eurasian junction – the breaking of an incoherent plate. Physics of the Earth and planetary interiors, 12, 1–50.

Ben-Menahem, A., Aboodi, E., Vered, M., Kovach, R., 1977. Rate of seismicity of the Dead Sea region over the past 4000 years. Physics of the Earth and Planetary Intererios, 14, 17–27.

Ben-Menahem, A. and Aboodi, E., 1981. Micro- and macroseismicity of the Dead Sea rift and off-coast eastern Mediterranean. In R. Freund, Z. Garfunkel (Eds.), The Dead Sea Rift. Tectonophysics, 80, 199–233.

Bentor, Y. K, Vroman, A. J., 1960. The geological map of Israel, 1:100,000, Sheet 16: Mount Sdom, with explanatory text. Geological Survey of Israel, Jerusalem, 117 p.

Braeuer, B., Asch, G., Hofsetter, R., Haberland, Ch., Jaser, D., El-Kelani, R., Weber, M., 2010. Microseismicity distribution in the southern Dead Sea basin and its implications on the structure of the basin. Geophysical Journal International, 188, 873–878.

Buchbinder, B., & Sneh, A., 1984. Marine sandstones and terrestrial conglomerates and mudstones of Neogene – Pleistocene age in the Modi'im area: a re-evaluation. Geological Survey of Israel Current Research, 1983–84, 65–69.

Bus, Z., Grenerczy, Gy, Tóth, L., Mónus, P., 2009. Active crustal deformation in two seismogenic zones of the Pannonian region - GPS versus seismological observations. Tectonophysics, 474, 343–352.

Calvo, R., Bartov, Y. Avni, Y. Garfunkel, Z. Frislander, U., 1998. Geological field trip to the Karkom graben: The Hazeva Fm. and its relation to the structure. The Israel Geological Society, Annu. Mtg. Field Trips Guidebook, pp. 47–62 (in Hebrew).

Calvo, R., Bartov, Y., 2001. Hazeva Group, southern Israel: New observations, and their implications for its stratigraphy, paleogeography, and tectono-sedimentary regime. Isr. J. Earth Sci. 50, 71–99.

Calvo, R., 2002. Stratigraphy and petrology of the Hazeva Formation in the Arava and the Negev: Implications for the development of sedimentary basins and the morphotectonics of the Dead Sea Rift Valley. Geological Survey of Israel Report No. GSI/22/02. PhD thesis, Hebrew University of Jerusalem (In Hebrew, English abstract), 264 pp.

Chapman, N., Berryman, K., Villamor, P., Epstein, W., Cluff, L., Kawamura, H., 2014. Active Faults and Nuclear Power Plants. Eos, Trans. Am. Geophys. Union, 95(4), 33–34, doi:10.1002/2014EO040001.

Chester, F. M., Chester, J. S., 2000. Stress and deformation along wavy frictional faults. Journal of Geophysical Research: Solid Earth, 105(B10), 23421-23430.

Choi, J.-H., Edwards, P., Ko, K., Kim, Y.-S., 2016. Definition and classification of fault damage zones: A review and a new methodological approach. Earth-Science Reviews, 152, 70–87.

Childs., C., Manzocchi, T., Walsh, J. J., Bonson, C. G., Nicol, A., Schöpfer, M. P. J., 2009.

A geometrical model of fault zone and fault rock thickness variations. Journal of Structural Geology, 31, 117–127.

Daëron, M., Benedetti, L., Tapponnier, P., Sursock, A. Finkel, R. C., 2004. Constraints on the post ~25-ka slip rate of the Yammoûneh fault (Lebanon) using in situ cosmogenic ^{36}Cl dating of offset limestone-clast fans. Earth and Planetary Science Letters, 227(1–2), 105–119.

Deif, A., Elenean, K. A., El Hadidy, M., Tealeb, A., Mohamed, A., 2009. Probabilistic seismic hazard maps for Sinai Peninsula, Egypt. Journal of Geophysics and Engineering, 6(3), 288.

Dewey, J. F., Pitman III, W. C., Ryan, W. B. F., Bonnin, J., 1973. Plate tectonics and the evolution of the Alpine system. Geological Society of America Bulletin, 84, 3137–3180.

Eckstein, Y., Simmons, G., 1978. Measurements and interpretation of terrestrial heat flow in Israel. Geothermics, 6, 117–142.

Eidelman, A., 1979. The geology of the Arava rift margin in the Ein Yahav region. Geological Survey of Israel Report No. GSI/10/79. MS.c. thesis, Hebrew University of Jerusalem, 66 pp. (In Hebrew, English abstract).

Ehrhardt, A., Hübscher, C., Ben-Avraham, Z., Gajewski, D., 2005. Seismic study of pull-apartinduced sedimentation and deformation in the Northern Gulf of Aqaba (Elat). Tectonophysics, 396(1), 59-79.

El-Isa, Z. H., Merghelani, H. M., Bazzari, M. A., 1984. The gulf of Aqaba earthquake swarm of 1983 January – April. Geophysical Journal of the Royal Astronimical Society, 78, 711-722.

Ellenblum, R., Marco, S., Kool, R., Davidovitch, U., Porat, R., Agnon, A., 2015. Archaeological record of earthquake ruptures in Tell Ateret, the Dead Sea Fault. Tectonics, 34, 2105–2117, doi:10.1002/2014TC003815.

Enzel, Y., Saliv, G., Kaplan, M., 1988. The tectonic deformation along the Zin Lineament. Nuclear Power Plant - Shivta Site: preliminary safety analysis Report. Appendix 2.5E: Late Cenozoic Geology in the Site area. Israel Electric Corporation Ltd.

Enzel, Y., Kadan, G., Eyal, Y., 2000. Holocene earthquakes inferred from a Fan-Delta sequence in The Dead Sea Graben. Quaternary Res., 53, 34–48.

Eppelbaum, L., Ben-Avraham, Z., Katz, Y., 2007. Structure of the Sea of Galilee and Kinarot Valley derived from combined geological-geophysical analysis. First Break, 25(1), 21-28.

Eyal, Y., 1996. Stress field fluctuations along the Dead Sea rift since the middle Miocene. Tectonics, 15(1), 157–170.

Eyal, M., Bartov, Y., Shimron, A. E., Bentor, Y. K., 1980. Sinai – Geological Map: scale 1:500,000. Tel Aviv: Survey of Israel.

Eyal, Y., Reches, Z., 1983. Tectonic analysis of the Dead Sea rift region since the late-

Cretaceous based on mesostructures. Tectonics, 2(2), 167-185.

Eyal, Y., Kaufman, A., Bar-Matthews, M., 1992. Use of ^{230}Th/U ages of striated Carnotites for dating fault displacements. Geology, 20, 829 – 832.

Farr, T. G., et al., 2007. The Shuttle Radar Topography Mission, Rev. Geophys., 45, RG2004, doi:10.1029/2005RG000183.

Felzer, K. R., Abercrombie, R. E., Ekström, G., 2004. A common origin for aftershocks, foreshocks, and multiplets. Bulletin of the Seismological Society of America, 94(1), 88-98.

Evans, J. P., 1990. Thickness-displacement relationship for fault zones. Journal of Structural Geology, 12(8), 1061-1065.

Ferry, M., Meghraoui, M., Abou Karaki, N., Al-Taj, M., Amoush, H., Al-Dhaisat, S., Barjous, M., 2007. A 48-kyr-long slip rate history for the Jordan Valley segment of the Dead Sea Fault. Earth and Planetary Science Letters, 260, 394-406.

Ferry, M., Meghraoui, M., Abou Karaki, N,. Al-Taj, M., Khalil, L., 2011. Episodic Behavior of the Jordan Valley Section of the Dead Sea Fault Inferred from a 14-ka-Long Integrated Catalog of Large Earthquakes. Bulletin of the Seismological Society of America, 101(1), 39–67, February 2011, doi: 10.1785/0120100097.

Fisher, R. A., 1950. Contribution to Mathematical Statistics. New York: John Wiley and Sons.

Flexer, A., Dimant, E., Polishook, B., Livnat, A., 1984. Relation of joints in the Avedat Group (Eocene) to the tectonic pattern of Israel. Israel journal of Earth Sciences, 33(1-2), 12–25.

Frankel, A., 1995. Mapping seismic hazard in the central and eastern United States. Seismological Research Letters, 66(4), 8 – 21.

Freund, R., 1965. A model for the development of Israel and adjacent areas since the Upper Cretaceous times. Geological Magazine, 102(3), 189–205.

Freund, R., Garfunkel, Z., Zak, I., Goldberg, M., Weissbrod, T., Derin, B., 1970. The shear along the Dead Sea Rift. Phil. Trans. Ray. Soc. Land. A., 267, 107–130.

Freund, R., Goldberg, M., Weissbrod, T., Druckman,Y., Derin, B., The Triassic-Jurassic structure of Israel and its relation to the origin of the eastern Mediterranean. Geol. Surv. Isr. Bull., 65, 26 pp., 1975.

Frieslander, U., 2000. The structure of the Dead Sea Transform emphasizing the Arava using new geophysical data. Ph.D. thesis, Hebrew University of Jerusalem. 101 pp. (in Hebrew, English abstract).

Gardosh, M., Reches, Z., 1990. Holocene tectonic deformation along the western margins of the Dead Sea. Tectonophysics, 180, 123-137.

Garfunkel, Z., 1964. Tectonic problems along the Ramon lineament. MS.c. thesis, Hebrew University of Jerusalem, 111 pp. (In Hebrew, English abstract).

Garfunkel, Z., 1970. The tectonics of the western margin of the southern Arava. Ph.D. thesis. Hebrew University of Jerusalem, 204 pp. (in Hebrew, English abst.).

Garfunkel, Z., 1981. Internal structure of the Dead Sea leaky transform (rift) in relation to plate kinematics. In R. Freund, Z. Garfunkel (Eds.), The Dead Sea Rift. Tectonophysics, 80, 81–108.

Garfunkel, Z., 1988. The pre-Quaternary geology of Israel. In Z. Yom-Tov, E. Tchernov, E. (Eds.)., the zoogeography of Israel. Dr W. Junk Publishers, Dordrecht, the Netherlands, pp. 7–34.

Garfunkel, Z., 1989. Tectonic setting of Phanerozoic magmatism in Israel. Israel Journal of Earth Sciences, 38, 51–74.

Garfunkel, Z., 1998. Constrains on the origin and history of the Eastern Mediterranean basin. Tectonophysics, 298, 5–35.

Garfunkel, Z., 2004. Origin of the Eastern Miditerranean basin: a reevalulation. Tectonophysics, 391, 11 – 34.

Garfunkel, Z., 2011. The long- and short-term lateral slip and seismicity along the Dead Sea Transform: An interim evaluation. Israel Journal of Earth Sciences, 58(3), 217–235. https://doi.org/10.1560/IJES.58.3-4.217

Garfunkel, Z., 2014. Lateral motion and deformation along the Dead Sea transform. In Z. Garfunkel, Z. Ben-Avraham, E. J. Kagan (Eds.), The Dead Sea Transform Fault System: Reviews. Springer, Dordrecht, the Netherlands, pp. 109–150.

Garfunkel, Z., Bartov, Y., 1977. The tectonics of the Suez rift. Geo. Surv. Isr. Bull. 71, 1-44.

Garfunkel, Z., Zak, I., Freund, R., 1981. Active faulting in the Dead Sea rift. In R. Freund, Z. Garfunkel (Eds.), The Dead Sea Rift. Tectonophysics, 80, 1-26.

Garfunkel, Z., Ben-Avraham, Z., 1996. The structure of the Dead Sea basin. Tectonophysics, 266(1-4), 155-176.

Garfunkel, Z., Ben-Avraham., Z., 2001. Basins along the Dead Sea transform. In P. A. Ziegler, w. Cavazza, A.H.F. Robertson, S. Crasquin-Soleau (Eds.), Peri-Tethys Memoir 6: Peri Tethyan rift/wrench basins and passive margins, Mémoires du Muséum national d'histoire naturelle 186. Publications scientifi ques du Muséum, Paris, pp. 607–627.

Garfunkel, Z., Horowitz, A., 1966. The upper Tertiary and Quaternary morphology of the Negev, Israel. Isr. J. Earth Sci, 15(3), 101–117.

Gerson, R., Grossman, S., and Bowman, D., 1984. Stages in the creation of a large rift valley - geomorphic evolution along the southern Dead Sea Rift. In M. Morisawa, J. T. Hack (eds.), Tectonic Geomorphology. pp. 53-73.

Gerson, R., Grossman, S., Amit, R. and Greenbaum, N., 1993. Indicators of faulting events and periods of quiescence in desert alluvial fans. Earth Surface Proc. and Landforms, 18, 181-202.

Gibowicz, S. J., 1973. Variation of the frequency-magnitude relation during earthquake

sequences in New Zealand. Bulletin of the Seismological Society of America, 63(2), 517-528.

Gibowicz, S.J., 1974. Frequency-magnitude, depth, and time relations for earthquakes in island arc: North Island, New Zealand. Tectonophysics, 23(3), 283-297.

Ginat, H., 1997. Paleogeography and the landscape evolution of the Nahal Hiyyon and Nahal Zihor basins. Geological Survey of Israel Report No. GSI/19/97. Ph.D. thesis, Hebrew University of Jerusalem, 206 pp. (In Hebrew, English abstract).

Ginat, H., Eyal, Y., Bartov, Y., Zilberman, E., 1994. Mapping of young faults in alluvial funs in Elat. Isr. Geol. Surv. Rep., TR-GSI /14/94 (in Hebrew).

Goebel, T. H., Kwiatek, G., Becker, T. W., Brodsky, E. E., Dresen, G., 2017. What allows seismic events to grow big?: Insights from b-value and fault roughness analysis in laboratory stick-slip experiments. Geology, 45(9), 815-818.

Gomez, F., Meghraoui, M., Darkal A. B., Hijazi, F., Mouty, M., Suleiman, Y., Sbeinati, R., Darawcheh, R., Al-Ghazzi, R., Barazabgi, M., 2003. Holocene faulting and earthquake recurrence along the Serghaya branch of the Dead Sea Fault system in Syria and Lebanon. Geophys. J. Int., 153, 658-674.

Gomez, F., Karam, G., Khawlie, M., McClusky, S., Vernant, P., Reilinger, R., R., Jaafar, R., Tabet, C., Khair, K., Barazangi, M., 2007. Global Positioning System measurements of strain accumulation and slip transfer through the restraining bend along the Dead Sea fault system in Lebanon. Geophysical Journal International, 168 (3), 1021–1028.

Gulia, L., Wiemer, S., 2010. The influence of tectonic regimes on the earthquake size distribution: a case study for Italy. Geophysical Research Letters, 37, L10305, doi:10.1029/2010GL043066.

Guralnik, B., Matmon, A., Avni, Y., Fink, D., 2010. 10Be exposure ages of ancient desert pavements reveal Quaternary evolution of the Dead Sea drainage basin and rift margin tilting. Earth and Planetary Science Letters, 290(1-2), 132-141.

Gutenberg, B., Richter, C. F., 1944. Frequency of earthquakes in California. Bulletin of the Seismological Society of America, 34(4), 185-188.

Hamdache, M., 1998. Seismic hazard assessment for the main seismogenic zones in North Algeria. Pure and Applied Geophysics, 152, 281-314.

Hamiel, Y., Amit, R., Begin, Z. B., Marco, S., Katz, O., Salamon, A., Zilberman, E., Porat, N., 2009. The seismicity along the Dead Sea fault during the last 60,000 years. Bulletin of the Seismological Society of America, 99(3), 2020-2026.

Hamiel, Y., Piatibratova, O., Mizrahi, Y., 2016. Creep along the northern Jordan Valley section of the Dead Sea Fault. Geophysical Research Letters, 43(6), 2494-2501.

Hamiel, Y., Masson, F., Piatibratova, O., Mizrahi, Y., 2018a. GPS measurements of crustal deformation across the southern Arava Valley section of the Dead Sea Fault and implications to regional seismic hazard assessment. Tectonophysics, 724-725, 171-178.

Hamiel, Y., Piatibratova, O., Mizrahi, Y., Nahmias, Y., Sagy, A., 2018b. Crustal deformation across the Jericho Valley section of the Dead Sea Fault as resolved by detailed field and geodetic observations. Geophysical Research Letters, 45, 3043-3050. https://doi.org/10.1002/2018GL077547

Harris, R. A., 1998. Introduction to special section: Stress triggers, stress shadows, and implications for seismic hazard. Journal of Geophysical Research: Solid Earth, 103(B10), 24347-24358.

Harrison, R. W., Newell, W. I., Batihanli, H., Panayides, I., McGeehin, J. P., Mahan, S. A., Özhűr, A., Tsiolakis, E., Necdet, M., 2004. Tectonic framework and Late Cenozoic tectonic history of the northern part of Cyprus: implications for earthquake hazards and regional tectonics. Journal of Asian Earth Sciences, 32(2), 191–210.

Hartman, G., Niemi, T. M., Tibor, G., Ben-Avraham, Z., Al-Zoubi, A., Makovsky, Y., Akawwi, E., Abueladas, A.-R., Al-Ruzouq, R., 2014. Quaternary tectonic evolution of the Northern Gulf of Elat/Aqaba along the Dead Sea Transform. J. Geophys. Res. Solid Earth, 119, 9183–9205, doi:10.1002/2013JB010879.

Hashimoto, C., Noda, A., Sagiya, T., Matsu'ura, M., 2009. Interplate seismogenic zones along the Kuril–Japan trench inferred from GPS data inversion. Nature Geoscience, 2, 141-144.

Heimann, A., 2002. Active faulting in Israel. Isr. Geol. Surv. Rep. GSI/07/02., 33 p. (in Hebrew).

Helmstetter, A., Kagan, Y. Y., Jackson, D. D., 2006. Comparison of short-term and time-independent earthquake forecast models for southern California. Bulletin of the Seismological Society of America, 96(1), 90 – 106.

Helmstetter, A., Kagan, Y. Y., Jackson, D. D., 2007. High-resolution time-dependent grid-based forecast for M ≥ 5 Earthquakes in California. Seismological Research Letters, 78(1), 78 – 86.

Henderson, J., Main, I., 1992. A simple fracture-mechanical model for the evolution of seismicity. Geophysical Research Letters, 19, 365-368.

Heuret, A., Lallemand, S., Funiciello, F., Piromallo, C., Faccenna, C., 2011. Physical characteristics of subduction interface type seismogenic zones revisited. Geochem. Geophys. Geosyst., 12, Q01004, doi:10.1029/2010GC003230.

Hofstetter, A., 2003. Seismic observations of the 22/11/1995 Gulf of Aqaba earthquake sequence. Tectonophysics, 369(1), 21-36.

Hofstetter, A., van Eck, T., Shapira, A., 1996. Seismic activity along fault branches of the Dead Sea-Jordan transform system: the Carmel – Tirza fault system. Tectonophysics, 267, 317-330.

Hofstetter, A., Thio, H. K., Shamir, G., 2003. Source mechanism of the 22/11/1995 Gulf of Aqaba earthquake and its aftershock sequence. Journal of Seismology, 7, 99-114.

Hofstetter, R., Klinger, Y., Amrat, A.-Q., Rivera, L., Dorbath, L., 2007. Stress tensor and

focal mechanisms along the Dead Sea fault and related structural elements based on seismological data. Tectonophysics, 429, 165–181.

Hofstetter, R., Gitterman, Y., Pinsky, V., Kraeva, N., Feldman, L., 2008. Seismological observations of the northern Dead Sea basin earthquake on 11 February 2004 and its associated activity. Isr. J. Earth Sci., 57, 101–124.

Hofstetter, A., Dorbath, C., Dorbath, L., 2014. Instrumental data on the seismic activity along the Dead Sea transfrom. In Z. Garfunkel, Z. Ben-Avraham, E. J. Kagan (Eds.), The Dead Sea Transform Fault System: Reviews. Springer, Dordrecht, the Netherlands, pp. 263-278.

Hull, J., 1988. Thickness-displacement relationship for deformation zones. Journal of Structural Geology, 10(4), 431-435.

Hurwitz, S., Garfunkel, Z., Ben-Gai, Y., Reznikov, M., Rotstein, Y., & Gvirtzman, H., 2002. The tectonic framework of a complex pull-apart basin: seismic reflection observations in the Sea of Galilee, Dead Sea transform. Tectonophysics, 359(3-4), 289-306

Israeli, A., Harash, A., 1990. Shachmon site, Geotech. Rep. 04/90/10, Tahal, Israel, (in Hebrew).

Israel Electric Corporation (IEC), and William Lettis & Associates, Inc., 2002. Shivta-Rogem Site Report. IEC Rep. Rev. 0, 12/23/02.

Joffe, S., Garfunkel, Z., 1987. Plate kinematics of the circum Red Sea – a re-evaluation. In Z. Ben-Avraham (Ed.), Sedimentary Basins within the Dead Sea and Other Rift Zones. Tectonophysics, 141, 5-22.

Kafri, U., Ecker, A., 1964. Neogene and Quaternary subsurface geology and hydrogeology of the Zevulun plain. Geological Survey of Israel Bull No. 37, 11 pp.

Kaila, K. L., Narain, H., 1971. A new approach for preparation of quantitative seismicity maps as applied to Alpide belt-Sunda arc and adjoining areas. Bulletin of the seismological society of America, 61(5), 1275-1291.

Kaila, K. L. Madhava Rao, N., Narain, H., 1974. Seismotectonic maps of Southwest Asia region comprising eastern Turkey, Caucasus, Persian plateau, Afghanistan and Hindukush. Bulletin of the seismological society of America, 64(3), 657-669.

Katz, O., Amit, R., Yagoda-Biran, G., Hatzor, Y.H., Porat, N., Medvedev, B. 2009. Quaternary earthquakes and landslides in the Sea of Galilee area, the Dead Sea Transform: paleoseismic analysis and implication to the current hazard. Isr. J. Earth Sci., 58, 275–294.

Kagan, E., Stein, M., Agnon, A., Neumann, F., 2011. Intrabasin paleoearthquake and quiescence correlation of the late Holocene Dead Sea. J. Geophys. Res., 116, B04311, doi:10.1029/2010JB007452.

Kanari, M., Ben Avraham, Z., Tibor, G., Bookman, R., Goodman-Tchernov, B. N., Niemi, T. M., Wechsler, N., Ash, A., Nimer, T., Marco, S., 2015. On-land and Offshore evidence for Holocene earthquakes in the Northern Gulf of Aqaba-Elat, Israel/Jordan. 6th

International INQUA Meeting on Paleoseismology, Active Tectonics and Archaeoseismology, Italy.

Kanamori, H., Hauksson, E., Heaton, T., 1997. Real-time seismology and earthquake hazard mitigation. Nature, 390(6659), 461.

Kempler, D., Garfunkel, Z., 1994. Structures and kinematics in the northeastern Mediterranean: A study of an irregular plate boundary. Tectonophysics, 234, 19-32.

King, G., 1983. The accommodation of large strains in the upper lithosphere of the earth and other solids by self-similar fault systems: the geometrical origin of b-value. Pure and Applied Geophysics, 121(5-6), 761-815.

Klinger, Y., Rivera, L., Haessler, H., Maurin, J.-C., 1999. Active faulting in the Gulf of Aqaba: knowledge from the Mw = 7.3 earthquake of 22 November 1995. Bull. Seismol. Soc. Am, 89, 1025–1036.

Klinger, Y., Avouac, J .P., Abou Karaki, N., Dorbath, L., Bourles, D. Reyss, J. L., 2000. Slip rate on the Dead Sea transform fault in northern Araba valley (Jordan). Geophysical Journal International, 142(3), 755–768.

Le Béon, M., Klinger, Y., Al-Qaryouti, M., Mériaux, A. S., Finkel, R. C., Elias, A., Mayyas, O., Ryerson, F. J., Tapponnier,, P., 2010. Early Holocene and Late Pleistocene slip rates of the southern Dead Sea Fault determined from 10Be cosmogenic dating of offset alluvial deposits. Journal of Geophysical Research: Solid Earth, 115(B11).

Le Béon, M., Klinger, Y., Mériaux, A.-S., Al-Qaryouti, M., Finkel, R. C., Mayyas, O., Tapponnier, P., 2012. Quaternary morphotectonic mapping of the Wadi Araba and implications for the tectonic activity of the southern Dead Sea fault. Tectonics, 31, TC5003, doi:10.1029/2012TC003112.

Le Pichon, X., Gaulier, J.-M., 1988. The rotation of Arabia and the Levant fault system. In: X. Le Pichon and J. R. Cochran (Eds.), The Gulf of Suez and Red Sea Rifting. Tectonophysics, 153. 271-294.

Lefevre, M., Klinger, Y., Al-Qaryouti, M., Le Béon, M., Moumani, K., 2018. Slip deficit and time clustering along the Dead Sea fault from paleoseismological investigations. Sci. Rep. 8(1), 4511. http://dx.doi.org/10.1038/s41598-018-22627-9. (n.d.).

Machette, M. N., 1978. Dating Quaternary faults in the southeastern United States by using buried calcic paleosols. Jour. Research U.S. Geol. Survey, 6(3), 369–381.

Machette, M. N., 2000. Active, capable, and potentially active faults – a paleoseismic perspective. Journal of Geodymanics, 29, 387–392.

Mai, M., Beroza, G. C., 2000. Source scaling properties from finite-fault-rupture models. Bulletin of the Seismological Society of America, 90(3), 604–615.

Makovsky, Y., Wunch, A., Ariely, R., Shaked, Y., Rivlin, A., Shemesh, A., Agnon, A., 2008. Quaternary transform kinematics constrained by sequence stratigraphy and submerged coastline features: the gulf of Aqaba. Earth and Planetary Science Letters, 271(1), 109-122.

Marco, S., Agnon, A., 1995. Prehistoric earthquake deformations near Masada, Dead Sea graben. Geology, 23(8), 695-698.

Marco, S., Stein, M., Agnon, A., Ron, H., 1996. Long-term earthquake clustering: A 50,000-year paleoseismic record in the Dead Sea Graben. Journal of Geophysicsl Research, 101(B3), 6179–6191.

Marco, S., Hartal, M., Hazan, N., Lev, L. Stein, M., 2003. archaeology, history and Geology of the A.D. 749 earthquake, Dead Sea transform. Geology, 31, 665- 668.

Marco, S., 2007. Temporal variation in the geometry of a strike–slip fault zone: Examples from the Dead Sea Transform. Tectonophysics, 445(3-4), 186-199.

Marco, S., Klinger, Y., 2014. Review of on-fault palaeoseismic studies along the Dead Sea fault. In Z. Garfunkel, Z. Ben-Avraham, E. J. Kagan (Eds.), The Dead Sea Transform Fault System: Reviews. Springer, Dordrecht, the Netherlands, pp. 183-205.

Masson, F., Hamiel, Y., Agnon, A., Klinger, Y., Deprez, A., 2015. Variable behavior of the Dead Sea Fault along the southern Arava segment from GPS measurements. C. R. Geoscience, 347, 161-169.

Markušić, S., Herak, M., 1999. Seismic zoning of Croatia. Natural Hazards, 18, 269–285.

Marzocchi, W., Sandri, L., 2003. A review and new insights on the estimation of the b-value and its uncertainty. ANNALS OF GEOPHYSICS, 46(6), 1271–1281.

McKenzie, D. P., 1970. Plate tectonics of the Mediterranean Region. Nature, 226, 239-243.

McKenzie, D. P., 1972. Active tectonics of the Mediterranean Region. Geophysical Journal of the Royal Astronomical Society, 30, 109-185.

Migowski, C., Agnon, A., Bookman, R., Negendank, J. F., Stein, M., 2004. Recurrence pattern of Holocene earthquakes along the Dead Sea transform revealed by varve-counting and radiocarbon dating of lacustrine sediments. Earth and Planetary Science Letters, 222(1), 301-314.

Mitchell, S. G., Matmon, A., Bierman, P. R., Enzel, Y., Caffee, M., Rizzo, D., 2001. Displacement history of a limestone normal fault scarp, northern Israel, from cosmogenic ^{36}Cl. Journal of Geophysical Research, 106(B3), 4247–4264.

Meirova, T., Hofstetter, A., 2013. Observations of seismic activity in Southern Lebanon. Journal of Seismology, 17(2), 629–644.

Meirova, T., Hofstetter, A., 2017. Source parameters of regional earthquakes recorded by Israel Seismic Network: implications for earthquake scaling. Bull. Earthquake. Eng., 15, 3417–3436. DOI 10.1007/s10518-017-0111-0

Meghraoui, M., Gomez, F., Sbeinati, R., Van der Woerd, J., Mouty, M., Darkal, A. N., Radwan, Y., Layyous, I., Al Najjar, H., Darawcheh, R., Hijazi, F., Al-Ghazzi, R., Barazangi, M., 2003. Evidence for 830 years of seismic quiescence from palaeoseismology, archaeoseismology and historical seismicity along the Dead Sea fault in Syria. Earth and Planetary Science Letters, 210, 35-52.

Meletti, C., Patacca, E., Scandone, P., 2000. Construction of a seismotectonic model: the case of Italy. Pure and applied Geophysics, 157(1-2), 11-35.

Mori, J., Abercrombie, R. E., 1997. Depth dependence of earthquake frequency-magnitude distributions in California: implications for rupture initiation. Journal of Geophysical Research, 102(B7), 15081-15090.

Moustafa, A. R., 2013. Fold-related faults in the Syrian Arc belt of northern Egypt. Marine and Petroleum Geology, 48, 441-454.

Nahmias, Y., Sagy, A., 2013. Young faulting in the Dead Sea basin - Jericho fault. In G. Baer (ed.), Infrastructure instability along the Dead Sea shorelines: Final Report: 2011-2012. Isr. Geol. Surv. Rep. GSI/05/2013, pp. 6-12 (in Hebrew).

Navon, H., 2012. Mircroseismic characterization of Lake Kinneret basin. M.Sc. Thesis, Tel Aviv University, 113 pp.

Neev, D., Almagor, G., Arad, A., Ginzburg, A., Hall, J. K., 1976. The geology of the southeastern Mediterranean Sea. Geo. Surv. Isr. Bull. 68, 1-51.

Nemer, T., Meghraoui, M., 2006. Evidence of coseismic ruptures along the Roum fault (Lebanon): a possible source for the AD 1837 earthquake. Journal of Structural Geology, 28, 1483–1495.

Nielsen, S.B. Knopoff, L., 1998. The equivalent strength of geometrical barriers to earthquakes. Journal of Geophysical Research: Solid Earth, 103(B5), 9953–9965.

Niemi, T. M., Zhang, H., Atallah, M. Harrison, J. B. J., 2001. Late Pleistocene and Holocene slip rate of the northern Wadi Araba fault, Dead Sea transform, Jordan. Journal of Seismology, 5(3), 449–474.

Nur, A., Ben-Avraham, Z., 1978. The eastern Mediterranean and the Levant: Tectonics of continental collision. Tectonophysics, 46, 297-311.

Nuriel, P., Weinberger, R., Kylander-Clark, A. R. C., Hacker, B. R., Craddock, J. P., 2017. The onset of the Dead Sea transform based on calcite age-strain analyses. Geology, 45(7), 587–590, doi:10.1130/G38903.1.

Oryan, B., 2016. Heat flow values obtained by the ICDP cores and their implications. M.Sc. thesis, Tel Aviv University, 57 p.

Otsuki, K., 1978. On the relationship between the width of shear zone and the displacement along fault. Journal of the geological society of Japan, 84(11), 661-669.

Palano, M., Imprescia, P., Gresta, S., 2013. Current stress and strain-rate fields across the Dead Sea Fault System: Constraints from seismological data and GPS observations. Earth and planetary science letters, 369, 305-316.

Papazachos, B. C., 1975. Foreshocks and earthquake prediction. Tectonophysics, 28(4), 213-226.

Pecker, A., Faccioli, E., Gurpinar, A., Martin, C., Renault, P., 2017. An overview of the SIGMA research project. Springer, Berlin. doi:10.1007/978-3-319-58154-5

Porat, N., Wintle, A.G., Amit, R., Enzel, Y., 1996. Late Quaternary earthquake chronology from luminescence dating of colluvial and alluvial deposits of the Arava valley, Israel. Quaternary Research, 46, 107-117.

Porat, N., Amit, R., Enzel, Y., Zilberman, E., Avni, Y., Ginat, H., Gluck, D., 2010. Abandonment ages of alluvial landforms in the hyperarid Negev determined by luminescence dating. J. Arid Environ., 74, 861-869.

Quennell, A. M., 1959. Tectonics of the Dead Sea rift. Int. Geol. Congr., 20th, Mexico: Assoc. Serv. Geol. Afr., pp. 385-405.

Radulian, M., Mandrescu, N., Panza, G. F., 1996a. Seismogenic zones of Romania. ICTP Preprint IC/96/255.

Radulian, M., Mandrescu, N., Popescu, E., Utale, A., Panza, G. F., 1996b. Seismic activity and stress field characteristics for the seismogenic zones of Romania. ICTP Preprint IC/96/256.

Radulian, M., Mandrescu, N., Panza, G. F., Popescu, E., Utale, A., 2000. Characterization of seismogenic zones in Romania. Pure and Applied Geophysics, 157, 57-77.

Reasenberg, P. A., Jones, L. M., 1989. Earthquake hazard after a mainshock in California. Science, 243(4895), 1173-1176.

Reches, Z., Hoexter., D. F., 1981. Holocene seismic and tectonic activity in the Dead Sea area. In R. Freund, Z. Garfunkel (Eds.), The Dead Sea Rift. Tectonophysics, 80(1-4), 235-254.

Reches, Z., Hoexter, D. F., Hirsch, F., 1981. The structure of a monocline in the Syrian Arc system, Middle East – surface and subsurface analysis. Journal of petroleum geology, 3(4), 413 – 425.

Reches, Z., Erez, J., Garfunkel, Z., 1987. Sedimentary and tectonic features in the northwestern Gulf of Elat, Israel. Tectonophysics, 141, 169–180.

Reilinger, R., McClusky, S., Vernant, P., Lawrence, S., Ergintav, S., Cakmak, R., Ozener, H., Kadirov, F., Guliev, I., Stepanyan, R., Nadariya, M., Habubia, G., Mahmoud, S., Sakr, K., ArRajehi A., Paradissis, D., Al-Aydrus, A., Prilepin, M., Guseva T., Evren, E., Dmitrotsa, A., Filikov, S. V., Gomez, F., Al-Ghazzi, R., Karam, G., 2006. GPS constraints on continental deformation in the Africa-Arabia-Eurasia continental collision zone and implications for the dynamics of plate interactions. Journal of Geophysical Resarch: Solid Earth, 111(B5).

Reznikov, M., Ben-Avraham, Z., Garfunkel, Z., Gvirtzman, H., Rotstein, Y., 2004. Structural and stratigraphic framework of Lake Kinneret. Isr. J. Earth Sci, 53, 131–149.

Rotstein, Y., 1987. Gaussian probability estimates for large earthquake occurrence in the Jordan Valley, Dead Sea rift. Tectonophysics, 141, 95-105.

Sadeh, M., Hamiel, Y., Ziv, A., Bock, Y., Fang, P., Wdowinski, S., 2012. Crustal deformation along the Dead Sea Transform and the Carmel Fault inferred from 12 years of GPS measurements, J. Geophys. Res., 117, B08410, doi:10.1029/2012JB009241.

Sagy, A., Reches, Z., Agnon, A., 2003. Hierarchic three-dimensional structure and slip partitioning in the western Dead Sea pull-apart. Tectonics, 22(1), 1004, doi:10.1029/2001TC001323

Sagy, A., Brodsky, E. E., Axen, G. J., 2007. Evolution of fault-surface roughness with slip. Geology, 35(3), 283-286.

Sagy, A., Nahmias, Y., 2011. Characterizing active faulting zone. In G. Baer (ed.), Infrastructure instability along the Dead Sea: Final Report: 2008-2010. Isr. Geol. Surv. Rep. GSI/02/2011, pp. 7-17 (in Hebrew).

Sagy, A., Bartov, Y., Sneh, A., and Rosensaft, M., 2012. Map of 'Active' and 'Potentially Active' Faults that Rupture the Surface in Israel, updates 2012: Proposal of The Geological Survey of Israel for Israel Standard 413. Isr. Geol. Surv., Rep. GSI/12/2012, 22 p. (In Hebrew, English abstract).

Sagy, A., Sneh, A., Rosensaft, M., Bartov, Y., 2013. Map of 'Active' and 'Potentially Active' Faults that Rupture the Surface in Israel. Updates 2013 for Israel Standard 413: Definitions, comments and clarifications, Isr. Geol. Surv. Rep., GSI/02/2013, 18 p. (in Hebrew, English abstract).

Sagy, A., Sagy, Y., Rochlin, I,. 2014a. The structure of the Jericho Fault in the subsurface of Beit Haarava region, north Dead Sea basin area. In G. Baer (ed.), Infrastructure instability along the Dead Sea: Final Report: 2008-2010. Isr. Geol. Surv. Rep. GSI/06/2014, pp. 22-29 (in Hebrew).

Sagy, A., Wetzler, N., Sagy, Y., Nahmias, Y., Lyakhovsky, V., 2014b. The subsurface structure of the Jericho Fault and the associated deformation: geophysical observations and mechanical model. Isr. Geol. Surv. Rep. GSI/23/2014.

Sagy, A., Rosensaft, M., Bartov, Y., Sneh, A., 2016. Map of 'Active' and 'Potentially Active' Faults that Rupture the Surface in Israel: Update 2016 for Israel Standard 413. Geol. Surv. Isr. Report No., 54 p. (in Hebrew, English abstract). GSI/17/2016.

Sagy, A., Weiler, N., Avni, Y., Rosensaft, M., Amit, R., 2017. Map of Active and Potentially Active Faults and that Rupture the Surface in Israel. Updates 2017 for Israel Standard 413., Geol. Surv. Isr. Report No. GSI/13/2017, 18 p. (in Hebrew, English abstract).

Sagy, Y., Gvirtzman, Z., 2009. Subsurface mapping of the Zevulun valley. The Geophysical Institute of Israel, Report 648/454/09, p. 21 (in Hebrew).

Segev, A., Rybakov., M., 2010. Effects of Cretaceous plume and convergence, and Early Tertiary tectonomagmatic quiescence on the central and southern Levant continental margin. Journal of the Geological Society, 167(4), 731-749.

Segev, A., Rybakov, M., 2011. History of faulting and magmatism in the Galilee (Israel) and across the Levant continental margin inferred from potential field data. Journal of Geodynamics, 51(4), 264-284.

Segev, A., Lyakhovsky, V., Weinberger, R., 2014. Continental transform–rift interaction adjacent to a continental margin: The Levant case study. Earth-Science Reviews, 139,

83-103.

Salamon, A., 1987. The monoclines in the northern Negev: a model of tilted blocks and shortening. MS.c thesis., Hebrew University of Jerusalem, 101 pp. (in Hebrew, English abstract).

Salamon, A., Hofstetter, A., Garfunkel, Z., Ron, H., 1996. Seismicity of the eastern Mediterranean region: perspective from the Sinai subplate. Tectonophysics, 263, 293-305.

Salamon, A., Hofstetter, A., Garfunkel, Z., Ron, H., 2003. Seismotectonics of the Sinai subplate – the eastern Mediterranean region. Geophysical Journal International, 155, 149-173.

Schattner, U., Ben-Avraham, Z., 2007. Transform margin of the northern Levant, eastern Mediterranean: From formation to reactivation. TECTONICS, VOL. 26, TC5020, doi:10.1029/2007TC002112.

Schattner, U., Weinberger, R., 2008. A mid-Pleistocene deformation transition in the Hula basin, northern Israel: Implications for the tectonic evolution of the Dead Sea Fault. Geochem. Geophys. Geosyst., 9, Q07009, doi:10.1029/2007GC001937.

Scholz, C. H., 1968. The frequency-magnitude relation of microfracturing in rock and its relation to earthquakes. Bull of the Seismological Society of America, 58, 399–415.

Schorlemmer, D., Wiemer, S., Wyss, M., 2005. Variations in earthquake-size distribution across different stress regimes. Nature, 437, 539–542.

Schorlemmer, D., Wiemer, S., 2005. Microseismicity data forecast rupture area. Nature, 434, 1086.

Schwartz, D. P., Coppersmith, K. J., 1984. Fault behavior and characteristic earthquakes: Examples from the Wasatch and San Andreas fault zones. Journal of Geophysical Research: Solid Earth, 89(B7), 5681–5698.

Shalev, E., Lyakhovsky, V., Yechieli, Y., 2007. Is advective heat transport significant at the Dead Sea basin? Geofluids, 7, 292-300.

Shalev, E., Lyakhovsky, V., Weinstein, Y., Ben-Avraham, Z., 2013. The thermal structure of Israel and the Dead Sea Fault. Tectonophysics, 602, 69-77.

SI-413, 1995. Design Provisions for Earthquake Resistance of Structures. The Standards Institution of Israel, Tel-Aviv, Israel.

Sibson, R. H., 1986. Earthquakes and rock deformation in crustal fault zones. Ann. Rev. Earth Planet. Sci., 14, 149-175.

Sivan, D., 1996. Paleogeography of the Galilee coastal plain during the Quaternary. Geological Survey of Israel Report No. GSI/18/96. Ph.D. thesis, Hebrew University of Jerusalem (In Hebrew, English abstract), 214 pp.

Shaked, Y., Agnon, A., Lazar, B., Marco, S., Avner, U., Stein, M., 2004. Large earthquakes kill coral reefs at the north-west Gulf of Aqaba. Terra Nova 16, 133–138. doi:10.1111/

j.1365- 3121.2004.00541.

Shamir, G., Bartov, Y., Sneh, A., Fleischer, L., Arad, V., Rosensaft, M., 2001. Preliminary seismic zonation in Israel. GSI Report No. GSI/12/2001; GII Report No. 550/95/01.

Shapira, A., 1979. Redetermined magnitudes of earthquakes in the Afro-Eurasian junction. Israel Journal of Earth Sciences, 28, 107–109.

Shapira, A., 1983. Potential earthquake risk estimation by application of a simulation process. Tectonophysics, 95, 75-89.

Shapira, A. 1991. Detectability of regional seismic networks: analysis of the Israel Seismic Networks. Israel Journal of Earth Science, 41, f21-25.

Shapira, A., Feldman, L., 1987. Microseismicity of three locations along the Jordan Rift. In: Z. Ben-Avraham (Ed.), Sedimentary Basins within the Dead Sea and Other Rift Zones. Tectonophysics, 141: 89-94.

Shapira, A., van Eck, T., 1993. Synthetic Uniform-Hazard Site Specific Response Spectrum. Natural Hazards, 8, 201–215.

Shapira, A., Hofstetter, A., 1993. Source parameters and scaling relationships of earthquakes in Israel. Tectonophysics, 217, 217-226.

Shapira, A., Shamir, G., 1994. Seismicity parameters of seismogenic zones in and around Israel. Inst. Petrol. Res. Geophys., Report No. Z1/567/79(109).

Shapira, A., Hofstetter, A., 2002. Seismicity parameters of seismogenic zones. Geophysical Institute of Israel report No. 592/230/02.

Sharon, M., Kurzon, I., Sagy, A., Rosensaft, M., 2016. Updated analysis of seismogenic zones in Israel and adjacent areas: main approach and preliminary results. Geol. Surv. Isr. Report No. GSI/33/2016.

Sharon, M., Sagy, A., Kurzon, I., Marco, S., Ben-Avraham, Z., Rosensaft, M., 2018. Quaternary fault map of Israel. Jerusalem. ISR. GEOL. SURV., 1 MAP.

Shaw, B. E., 1993. Generalized Omori law for aftershocks and foreshocks from a simple dynamics. Geophysical research letters, 20(10), 907-910.

Sneh, A., Bartov, Y., Weissbord, T., Rosensaft, M., 1998. Geological Map of Israel, 1:200,000. Isr. Geo. Surv. (4 sheets).

Sneh, A., Weinberger, R., 2014. Major geological structures of Israel and Environs. Jerusalem: Geological Survey of Israel.

Shtivelman, V., Frieslander, U., Zilberman, E., Amit, R., 1998. Mapping shallow faults at the Evrona playa site using high-resolution reflection method. Geophysics, 63, 1257-1264.

Steckler, M. S., ten-Brink, U. S., 1986. Lithospheric strength as a control on new plate boundaries: examples from the northern Red Sea region. Earth and Planetary Science Letters, 79, 120-132.

Steckler, M. S., Berthelot, F., Lyberis, N., Le Pichon, X., 1988. Subsidence in the Gulf of

Suez: implications for rifting and plate kinematics. Tectonophysics, 153, 249-270.

Stein, S., Liu, M., 2009. Long aftershock sequences within continents and implications for earthquake hazard assessment. Nature, 462(7269), 87.

Stevens, V. L., Avouac, J. P., 2017. Determination of Mmax from background seismicity and Moment conservation. Bulletin of the Seismological Society of America, 107(6), 2578-2596.

Stirling, M., Rhoades, D., Berryman, K., 2002. Comparison of Earthquake Scaling Relations Derived from Data of the Instrumental and Preinstrumental Era. Bulletin of the Seismological Society of America, 92(2), 812-830.

Suyehiro, S., 1966. Difference between aftershocks and foreshocks in the relationship of magnitude to frequency of occurrence for the great Chilean earthquake of 1960. Bulletin of the Seismological Society of America, 56(1), 185-200.

Suyehiro, S., Sekiya, H., 1972. Foreshocks and earthquake prediction. Tectonophysics, 14(3-4), 219-225.

ten Brink, U. S., Flores, C. H., 2012. Geometry and subsidence history of the Dead Sea basin: a case for fluid induced mid-crustal shear zone? J. Geophys. Res., 117, B01406, doi:10.1029/2011JB008711.

Torfstein, A., Haase-Schramm, A., Waldmann, N., Kolodny, Y., & Stein, M., 2009. U-series and oxygen isotope chronology of the mid-Pleistocene Lake Amora (Dead Sea basin). Geochimica et Cosmochimica Acta, 73(9), 2603-2630.

Turkelli, N., Sandvol, E., Zor, E., Gok, R., Bekler, T., Al-Lazki, A., Karabulut, H., Kuleli, S., Eken, T., Gurbuz, C., Bayraktutan, S., Seber, D., Barazangi, M., 2003. Seismogenic zones in Eastern Turkey. Geophysical Research Letters, 30(24), 8039.

Utsu, T., 1966. A statistical signficance test of the difference in b-value between two earthquake groups. J. Phys. Earth, 14, 34-40.

von Seggern, D., Alexander, S. S., Baag, C. E., 1981. Seismicity parameters preceding moderate to major earthquakes. Journal of Geophysical Research: Solid Earth, 86(B10), 9325-9351.

Vroman, A. J., 1956. Strike-slip movements, their associated features and their ocourrenoe in Israe1. XXth Int. Geo1. Congress, Mexico, Seocion V, pp 399-408.

Walley, C.D., 1988. A braided strike-slip model for the northern continuation of the Dead Sea Fault and its implications for Levantine tectonics. Tectonophysics, 145, 63-72.

Wdowinski, S., Ben-Avraham, Z., Arvidsson, R., Ekström, G., 2006. Seismotectonics of the Cyprian Arc. Geophysical Journal International, 164, 176-181.

Wechsler, N., Rockwell, T. K., Klinger, Y., 2018. Variable slip-rate and slip-per-event on a plate boundary fault: The Dead Sea fault in northern Israel. Tectonophysics, 722, 210–226.

Wegener, A., 1966. The origin of Continents and Oceans (4th, J. Bi ed.). London: Dover, 263 pp.

Weinberger, R., Begin, Z. B., Waldmann, N., Gardosh, M., Baer, G., Frumkin, A., Wdowinski, S., 2006. Quaternary rise of the Sedom diapir, Dead Sea basin. In Y. Enzel, A. Agnon, M. Stein (eds.), New Frontiers in Dead Sea Paleoenvironmental Research. Geol. Soc. Am. Special Paper, 401, 33-51.

Weinberger, R., Bar-Matthews, M., Levi, T., Begin, Z. B., 2007. Late-Pleistocene rise of the Sedom diapir on the backdrop of water-level fluctuations of Lake Lisan, Dead Sea basin. Quaternary International, 175, 53-61.

Weinberger, R., Gross, M. R., Sneh, A., 2009. Evolving deformation along a transform plate boundary: Example from the Dead Sea Fault in northern Israel. Tectonics, 28, TC5005, doi:10.1029/2008TC002316.

Wells, D. L., Coppersmith, K. J., 1994. New empirical relationships among magnitude, rupture length, rupture width, rupture area, and surface displacement. Bulletin of the Seismological Society of America, 84(4), 974-1002.

Wieler, N., Avni, A., Ginat, H., Rosensaft, M., 2017. Quaternary map of the Eilat region on a scale of 10:000 with explanatory notes. Geol. Surv. Isr. Report No. GSI/37/2016 (in Hebrew, English abstract).

Wetzler, N., Sagy, A., Sagy, Y., Nahmias, Y., Lyakhovsky, V., 2015. Active transform fault zone at the fringe of the Dead Sea Basin. Tectonics, 34(7), 1475-1493.

Wetzler, N., Kurzon, I., 2016. The earthquake activity in Israel: Revisiting 30 years of local and regional seismic records along the Dead Sea transform. Seismological Research Letters, 87(1), 47-58.

Wiemer, S., Wyss, M., 1997. Mapping the frequency-magnitude distribution in asperities: an improved technique to calculate ceurrence times? Journal of Geophysical Research, 102(B7), 15115-15128.

Wyss, M., 2001. Locked and creeping patches along the Hayward fault, California. Geophysical Research Letters, 28(18) ,3537‑3,540

Wyss, M., Schorlemmer, D., Wiemer, S., 2000. Mapping asperities by minima of local recurrence time: The San Jacinto-Elsinore fault zones. Journal of Geophysical Research, 105(B4), 7829‑7844.

Wyss, M., Sammis, C. G., Nadeau, R. M., Wiemer, S., 2004. Fractal dimension and b-value on creeping and locked patches of the San Andreas fault near Parkfield, California. Bulletin of the Seismological Society of America, 94(2), 410-421.

Yamanaka, Y., Kikuchi, M.,(2004. Asperity map along the subduction zone in northeastern Japan inferred from regional seismic data. Journal of Geophysical Research, 109, B07307, doi:10.1029/2003JB002683.

Yeats, R. S., Sieh, K. E., Allen, C. R., 1997. The geology of earthquakes. USA: Oxford

University Press.

Zak, I., 1967. The geology of Mount Sedom. Ph.D. thesis, Hebrew University of Jerusalem, 208 pp. (in Hebrew, Englisg abstract).

Zaslavsky, Y., Shapira, A., Gorstein, M., Perelman, N., Ataev, G., Aksinenko, T., 2012. Questioning the applicability of soil amplification factors as defined by NEHRP (USA) in the Israel building standards. Natural Science, 4, 631–639.

Zilberman, E., 1981. The geology of the central Sinai-Negev shear zone, central Negev. Part A: the Sa'ad-Nafha Lineament. Geol. Surv. Isr. Rep. Hydro 1/81, 60 p.

Zilberman, E., 1983. The geology of the central Sinai-Negev shear zone, central Negev. Part B: the 'Arif-Batur Lineament. Geol. Surv. Isr. Rep. EG/6/83, 58 p.

Zilberman, E., 1985. The geology of the central Sinai-Negev shear zone, central Negev. Part C: the Paran Lineament. Geol. Surv. Isr. Rep. GSI/38/85, 53 p.

Zilberman, E., Baer, G., Avni, Y., Feigin, D. 1996. Pliocene fluvial systems and tectonics in the central Negev, southern Israel. Isr. J. Earth Sci. 45, 113-126.

Zilberman, E., Amit, R., Heimann, A., Porat, N., 2000. Changes in Holocene paleoseismic activity in the Hula pull-apart basin, Dead Sea Rift, northern Israel. Tectonophysics, 321(2), 237-252.

Zilberman, E., Greenbaum, N., Nahmias, Y., Porat, N., Ashqar, L., 2006. Middle Pleistocene to Holocene tectonic activity along the Carmel Fault – preliminary results of a paleoseismic study. Geological Survey of Israel Report No. GSI/02/2007.

Zilberman, E., Greenbaum, N., Nahmias, Y., Porat, N., Ashkar, L., 2008. Late Pleistocene to Holocene tectonic activity along the Nesher fault, Mount Carmel, Israel. Israel Journal of Earth Sciences, 57, 87-100.

Zilberman, E., Ron, H., Sa'ar, R., 2011a. Evaluating the potential seismic hazards of the Ahihud Ridge fault system by paleomagnetic and morphological analyses of calcretes. Geological Survey of Israel Report No. GSI/15/2011.

Zilberman, E., Greenbaum, N., Nahmias, Y., Porat, N., 2011b. The evolution of the northern shutter ridge, Mt. Carmel, and its implications on the tectonic activity along the Yagur fault. Geological Survey of Israel Report No. GSI/14/2011.

Zilberman, E., 2016. Summary of paleo-seismological researches on the tectonic activity along Nahal Schoret alluvial fan fault. Isr. Geol. Surv. Rep., TR-GSI\01\2016 (in Hebrew).

8. Appendices

Appendix 1: Details related to Chapter 3

1.1. Geological map data

1.1.1 List of 1:50,000 used geological map sheets (see locations in Appendix 1.2)

Sheet 1-IV: Nahariyya - Sneh Amihai, 2004;

Sheet 2-II: Metulla - Sneh Amihai, Weinberger Ram, 2003.

Sheet 2-II-E: Merom Golan – Mor Doron, 1987 (Digital editing, 2006)

Sheet 2-III: Zefat – Levitte Dov, Sneh Amihai, 2014

Sheet 2-IV: Rosh Pinna - Sneh Amihai, Weinberger Ram, 2006 (Partly revised, 2013)

Sheet 2-IV-E: En Zivan – Mor Doron, 1987 (Digital editing, 2006)

Sheet 3-I: Hefa (Haifa) – Karcz Ia'aqov, Sneh Amihai, 2011.

Sheet 3-II: Shefar'am - Sneh Amihai, 2008 (Partly revised, 2013)

Sheet 3-III: Atlit - Segev Amit, Sass Eitan, 2009.

Sheet 4-I: Arbel - Bogoch Ron, Sneh Amihai, 2008 (Partly revised, 2014)

Sheet 4-II: Teverya - Sneh Amihai (Editor), 2008.

Sheet 4-II-E: Ramat Magshimim – Mor Doron, 2012.

Sheet 5-I: Hadera - Sneh Amihai, Sass Eitan, Bein Amos, Arad Arnon, Rosensaft Marcelo, 1996 (Partly revised, 2014).

Sheet 5-II: Umm El Fahm - Sass Eitan, Dekel Ami, Sneh Amihai, 2013.

Sheet 5-III: Netanya - Ilani Shimon, 2016.

Sheet 5-IV: Shekhem – Cook Philip, 2000.

Sheet 6-I, II: Bet She'an – Hatzor H. Yosef, 2000.

Sheet 6-III: Beqa'ot- Mimran Yaakov, Shaliv Gadi, Sakal Emanuel, Sneh Amihai, 2014.

Sheet 7-II: Tel Aviv - Sneh Amihai, Rosensaft Marcelo, 2008.

Sheet 7-IV: Rishon LeZion - Sneh Amihai, Rosensaft Marcelo, 2004.

Sheet 8-I: Kefar Sava – Hildebrand–Mittlefehldt Nurit, 2011

Sheet 8-II: Ariel - Sneh Amihai, Shaliv Gaby, 2012.

Sheet 8-III: Lod - Yechieli Yosef, 2008.

Sheet 8-IV: Ramallah – Shachnai Emanuel, 2000.

Sheet 9-III: Jericho - Ze'ev Binyamin Begin, 1974.

Sheet 10-I: Ashdod - Sneh Amihai, Rosensaft Marcelo, 2004.

Sheet 10-II: Gedera - Sneh Amihai, 2004.

Sheet 10-III: Ashqelon - Sneh Amihai, Rosensaft Marcelo, 2008.

Sheet 10-IV: Qiryat Gat - Sneh Amihai (Editor), 2008.

Sheet 11-I: Bet Shemesh - Sneh Amihai (Digital editing), 2009.

Sheet 11-II: Jerusalem - Sneh Amihai, Avni Yoav, 2011 (Partly revised, 2013)

Sheet 11-III: Bet Guvrin - Sneh Amihai, 2016.

Sheet 11-IV: Hevron - Sneh Amihai, Roth Israel, 2012.

Sheet 12-I, II: Qalya - Roth Israel, Burg Avihu, Sneh Amihai, 2008.

Sheet 12-III: Mizpe Shalem – Mor Uri, Burg Avihu, 2000.

Sheet 13-II: Nirim - Sneh Amihai, Rosensaft Marcelo, 2008.

Sheet 13-IV: Nir Yizhaq - Sneh Amihai, Rosensaft Marcelo, 2008.

Sheet 14-I: Netivot - Sneh Amihai, Rosensaft Marcelo, 2008.

Sheet 14-II: Mishmar HaNegev - Sneh Amihai, Avni Yoav, Zilberman Ezra, 2015.

Sheet 14-III: Ze'elim – Zilberman Ezra, 2004.

Sheet 15-I: Eshtemoa - Sneh Amihai, Avni Yoav, 2008.

Sheet 15-II: Har Hezron - Gilat Arie, 1983.

Sheet 15-III: Tel Malhata – Wdowinski Shimon, Sneh Amihai, Avni Yoav, 2012.

Sheet 15-IV: Arad - Hirsch Francis, Burg Avihu, Avni Yoav, 2008.

Sheet 16-I: En Gedi – Raz Eli, 1984.

Sheet 16-III: Neve Zohar – Agnon Amotz, Sagy Amir, 2011.

Sheet 17-II: Holot Agur – Zilberman Ezra, 2002.

Sheet 17-IV: Nizzana - Zilberman Ezra, Avni Yoav, Sneh Amihai, 2011.

Sheet 18-I: Rehovot BaNegev – Zilberman Ezra, 2002.

Sheet 18-II: Revivim - Starinsky Avraham, Zilberman Ezra, Braun Moshe, Sneh Amihai, 2010.

Sheet 18-III: Shivta - Sneh Amihai, Avni Yoav, Bartov Yosef, Zilberman Ezra, Braun Moshe, Lasman Noah, Weinberger Ram, 2011.

Sheet 18-IV: Sede Boqer - Avni Yoav, Weiler Nimrod, 2013.

Sheet 19-I: Dimona – Roded Reuven, 1996.

Sheet 19-II: HaMakhtesh HaQatan – Hirsch Francis, 1995.

Sheet 19-III: Oron - Roded Reuven, 1982.

Sheet 19-IV, 20-III: Neot Hakikar - Yechieli Yosef, Elron Ehud, Sneh Amihai, 1994.

Sheet 20-I: Sedom - Agnon Amotz, Weinberger Ram, Zak Israel, Sneh Amihai, 2006.

Sheet 21-I: Har Hamran - Zilberman Ezra, Avni Yoav, 2004.

Sheet 21-II: Mizpe Ramon - Zilberman Ezra, Avni Yoav, 2004.

Sheet 21-III: Har Loz - Avni Yoav, 2001.

Sheet 21-IV: Be’erot Oded – Avni Yoav, 2017.

Sheet 22-I: Har Ardon - Avni Yoav, Bartov Yosef, Sneh Amihai, 2016.

Sheet 22-II: En Yahav - Sneh Amihai, Eyal Amir, Eidelman Amir, Bartov Yosef, 2014.

Sheet 22-III: Zofar – Baer Gideon, Soudry David, Bar Oded, Sneh Amihai, 2014.

Sheet 24-III, IV: Yahel - Ginat Hanan, Lifshitz Avi, 2008.

Sheet 25-I: Mizpe Sayyarim - Ginat Hanan, 2008.

Sheet 25-II: Yotvata - Ginat Hanan, 1994.

Sheet 25-III: Har Seguv – Segev Amit, Beyth Michael, 2000.

Sheet 25-IV: Be'er Ora – Beyth Michael, Segev Amit, Bartov Yosef, 2000.

Sheet 26: Elat – Beyth Michael, Eyal Yehuda, Garfunkel Zvi, 2000.

1.1.2: Locations of 1:50,000 geological map sheets used for the present map

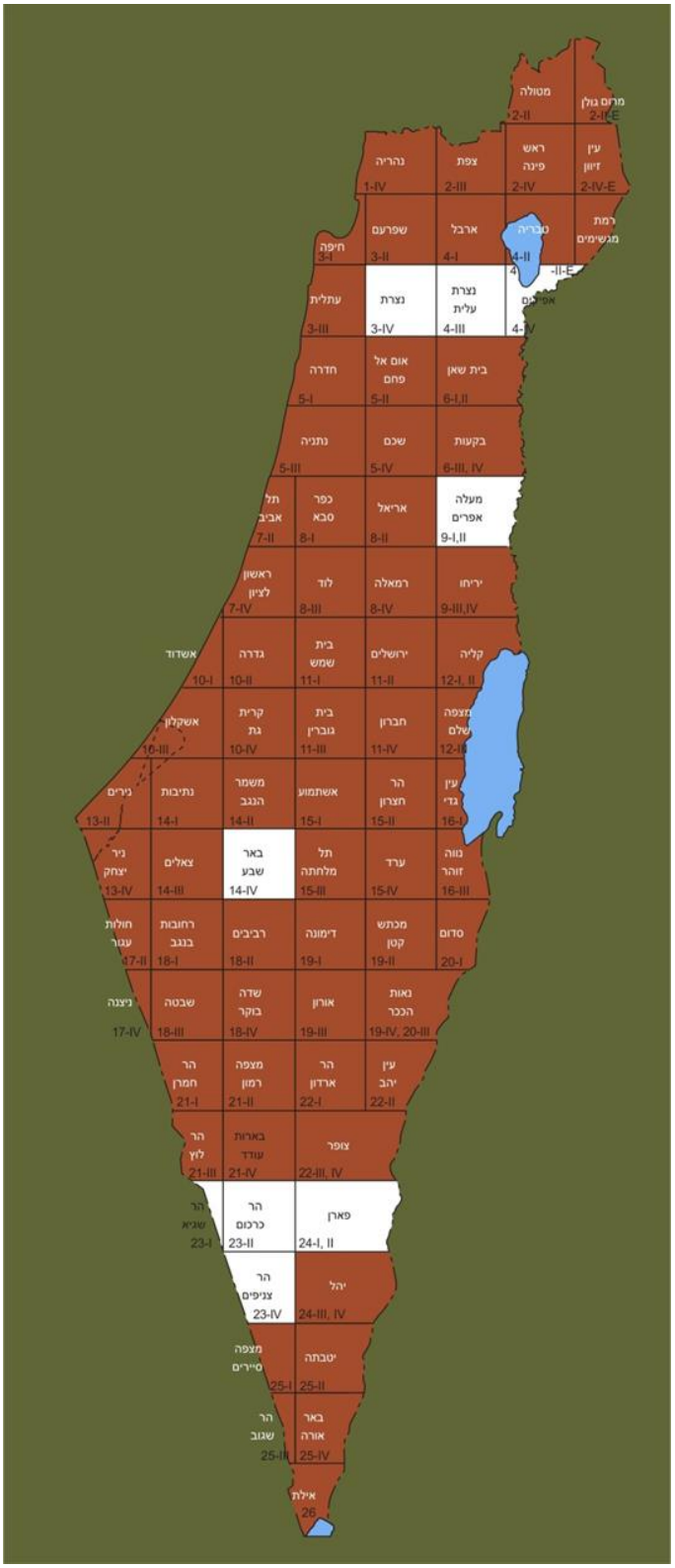

the map sheets that were not available for the current studies, so 1:200,000 data (Sneh et al., 1998) was used instead, where: Afikim, Be'er Sheva, Har Karkom, Har Sagy, Har Znifim, Ma'ale Efraim, Nazareth, Nazareth Ilit and Paran.

Brwon: locations of published 1:50,000 sheets.

White: locations of unpublished sheets.

1.2. Geological formations and mapping units of presumed Quaternary age

Formations	**Local sedimentary units**	**Local volcanic units**	**Other units***
Ahuzam Fm. (Cgl. **)	Amora salt	Avital tuff	Alluvium
Amora Fm.	Betlehem Cgl.	Bene Yehuda scoria	Beach rocks & reefs
Arava Fm.	Biq`at Uvda Cgl.	Berekhat Ram tuff	Calcareous sandstone (kurkar)
Ashmura Fm.	Edom facias	Dalton basalt	Colluvium
Elot Fm.	Egel Cgl.	Dalton scoria & tuff	Dune sand, Sand sheets, Red sands
Garof Fm.	En Awwazim Cgl.	Dalwe flows	Loess, fluvial & eolian
Gesher Benot Ya'aqov Fm.	En Feshha Cgl.	En Awwazim flow	Gypsum
Hazor & Gadot Fms.	Giv'at Oz Cgl.	En Zivan basalt flows	Lake sediments
Lisan Fm.	Karbolet caprock	Golan Basalt flows (Muweissa and En Zivan flows)	Loam (hamra)
Malaha Fm.	Lot caprock	Hazbani basalt flows	Neogene-Quaternary conglomerate units, Terrace Cgl.
Mazar Fm.	Mahanayim marl	Keramim basalt	Playa
Nevatim Fm.	Mearat Sedom caprock	Meshki basalt flows	Recent fan
Ortal Fm.	Nahshon Cgl.	Muweisse basalt flows	Soil
Pleshet Fm.	Ramat Gerofit Cgl.	Neogene basalts	Tufa, travertine
Samra Fm.	Ravid Cgl.	Raqad basalt	Unnamed clastic unit
Sede Zin Fm.	Ruhama Loess &	Sa'ar basalt flows	

	sand		
Seif Fm.	Sabkha soil	Shievan scoria	
Ye'elim Fm.	Si'on Cgl.	Yarda/Ruman basalt flows	
Ze'elim Fm.	Wadi Malih Cgl.	Yarmouk basalt	
Zehiha Fm.		Yehudiyya & Dalwe basalt flows	

*Geologic and geomorphic descriptions that appear in 1:50,000 geological maps for Quaternary deposits. **Cgl. means conglomerate

1.3. References for faults with explicit evidence for Quaternary faulting

Area	Name of fault / group of faults, or part of it	References
Southern Israel	Arif-Batur	Zilberman et al., 1996; Avni, 1998
	Evrona and Eilat	Amit et al., 1995; 1999; 2002; Ben-Avraham, 1985; Ehrhardt et al., 2005; Frieslander, 2000; Garfunkel, 1970; Garfunkel et al., 1981; Gerson et al., 1993; 1984; Ginat et al., 1994; Hartman et al., 2014; Heimann, 2002; Hofstetter, 2003; Israeli and Harash, 1990; Kanari et al., 2015; Klinger et al., 1999; Makovsky et al., 2008; Porat et al., 1996; 2010; Reches et al., 1987; Shaked et al., 2004; Shtivelman et al., 1998; Wieler et al., 2017; Zilberman, 2005; 2016
	Gerofit	Ginat, 1997
	Gevaot Ziya	Avni, 1998
	Halamish line	Avni, 1998
	Har Seguv	Avni, 1998
	Hiyyon	Ginat, 1997
	Katzra	Avni, 1998
	Milhan	Ginat, 1997
	Mitzpe Sayarim	Avni, 1998
	Noza	Ginat, 1997
	Ovda	Avni, 1998
	Paran	Zilberman, 1985; Avni, 1998; Calvo et al., 1998; Calvo, 2002
	Yotam	Wieler et al., 2017

	Zhiha	Avni, 1998
	Zin	Enzel et al., 1988; IEC and Lettis & Associates, 2002; Avni and Zilberman, 2007
	Znifim – Zihor – Barak	Ginat, 1997
	Zofar	Calvo, 2002
Central Israel and Dead Sea area	Jericho	Reches and Hoexter., 1981; Gardosh and Reches, 1990; Sagy and Nahmias, 2011; Nahmias and Sagy, 2013; Sagy et al., 2014a; 2014b; Wetzler et al., 2015
	Masada Plain	Bartov et al., 2006
	Modi'in	Buchbinder and Sneh, 1984
	Mt. Sedom	Bentor and Vroman, 1960; Zak, 1967; Weinberger et al., 2006; 2007
	Nahal Darga (east)	Enzel et al., 2000
	Nahal Kidron (east)	Sagy and Nahmias, 2011
Northern Israel	Ahihud	Kafri and Ecker, 1964; Sivan, 1996; Zilberman et al., 2011a
	Beit Qeshet (western part)	Zilberman et al., 2009
	Ha'on	Katz et al., 2009
	Hilazon	Kafri and Ecker, 1964; Zilberman, 2011a
	Kabul	Kafri and Ecker, 1964
	Nahef East Fault	Mitchell et al., 2001
	Nesher	Zilberman et al., 2006; 2008
	Tiberias	Marco et al., 2003
	Yagur	Zilberman et al., 2011b

Appendix 1.3: references for faults with explicit evidence of Quaternary activity. The names of faults are mainly according to the corresponding reference, but in some cases were given by the name of a nearby geographic feature.

1.4. References for faults located beyond Israel borders and/or subsurface interpretations

Geographic area	Reference
Gulf of Eilat	Hartman et al., 2014; Ben-Avraham, 1985
Arava valley	Le Béon et al., 2012; Calvo, 2002; Sneh and Weinberger, 2014
Sinai peninsula	Sneh and Weinberger, 2014
North-western Negev	Eyal et al., 1992
Dead Sea basin	Ben-Avraham and Schubert, 2006; Sneh and Weinberger, 2014
Jordan valley	Ferry et al., 2007; Sneh and Weinberger, 2014
Gilboa fault (western part)	Sneh and Weinberger, 2014
Carmel fault (eastern part)	Sneh and Weinberger, 2014
Sea of Galilee	Hurwitz et al., 2002; Reznikov et al., 2004; Eppelbaum et al., 2007; Sneh and Weinberger, 2014
Zvulun Valley	Sagy and Gvirtzman, 2009
Hula basin	Schattner and Weinberger, 2008
Lebanon and Syria	Weinberger et al., 2009; Garfunkel, 2014; Sneh and Weinberger, 2014
Mediterranean Sea	Schattner and Ben-Avraham, 2007

1.5. The earthquake density of values > $\sim 0.001\ events/Km^2/years$

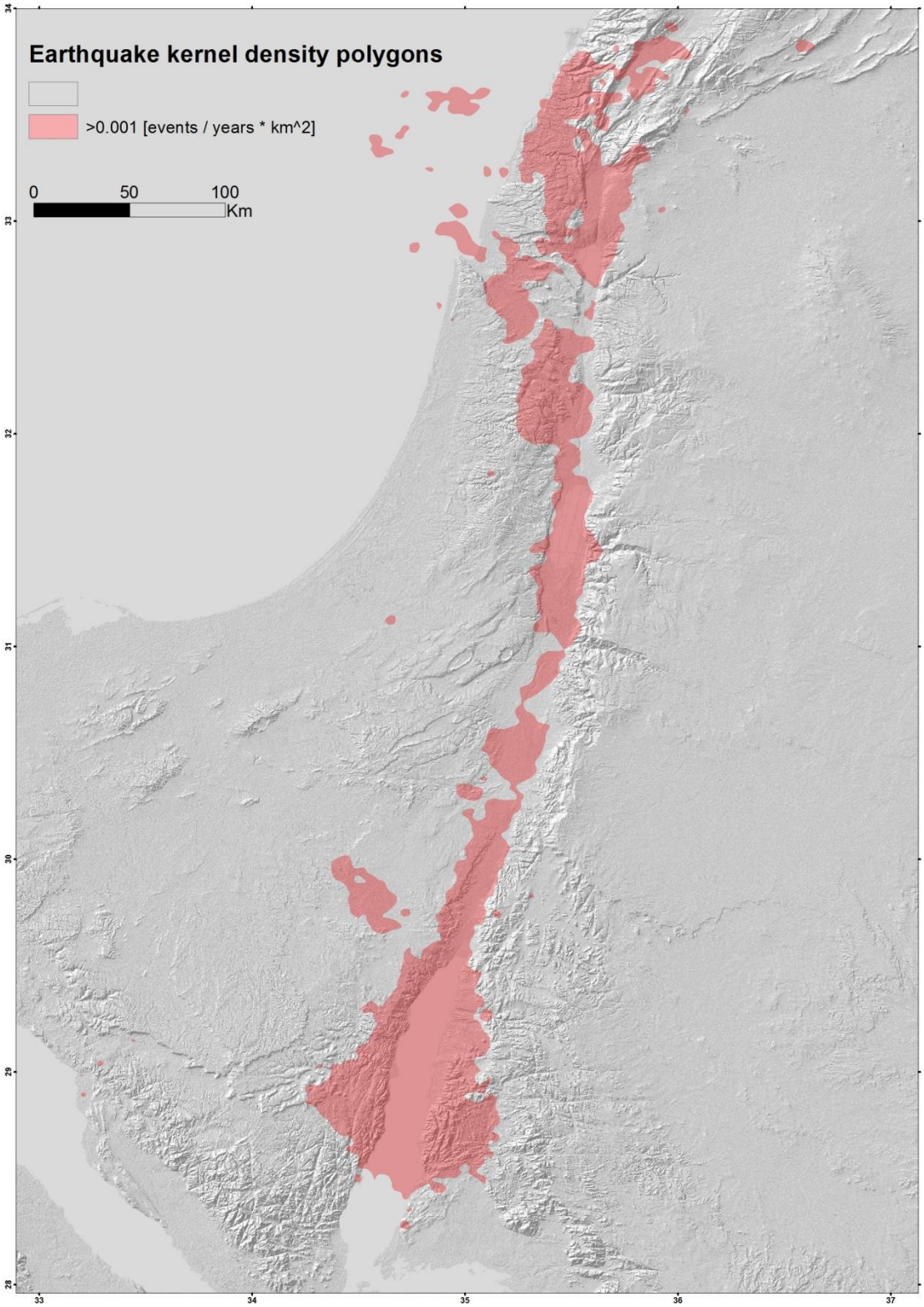

The *earthquake kernel density* of values > $\sim 0.001\ events/Km^2/years$, corresponding to at least the minimum level of this parameter, allowing it to be continuous along the DST.

1.6. The Mo density of values > ~$9.5\ log[joules/Km^2\ /years]$

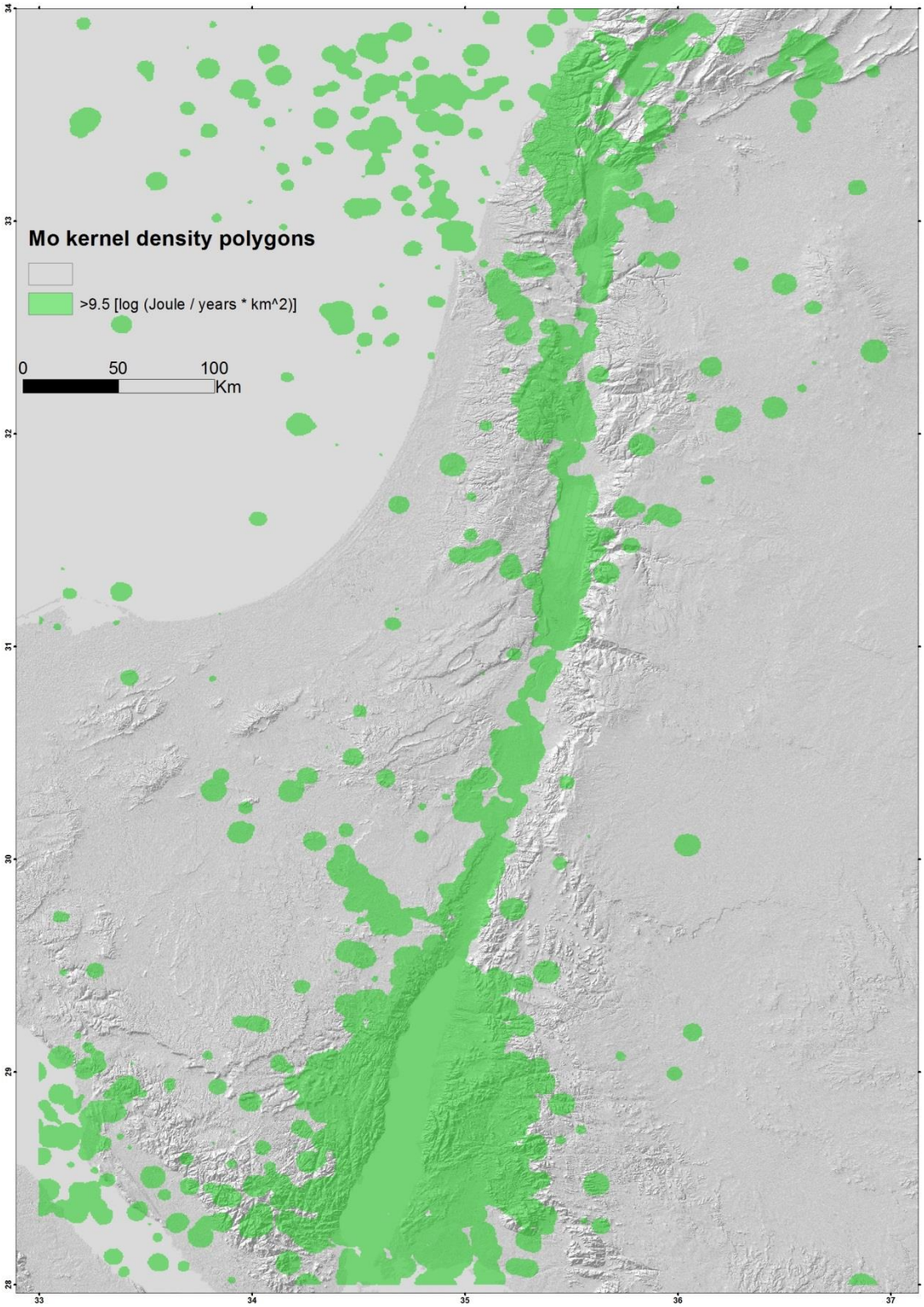

The *Mo density* of values > ~9.5 log[$joules/Km^2\ years$], corresponding to at least the minimum level of this parameter, allowing it be continuous along the DST.

1.7. Epicentres investigated in this study, recorded between the period of 1983–2017, superimposed on the overlap area of the two seismicity polygons

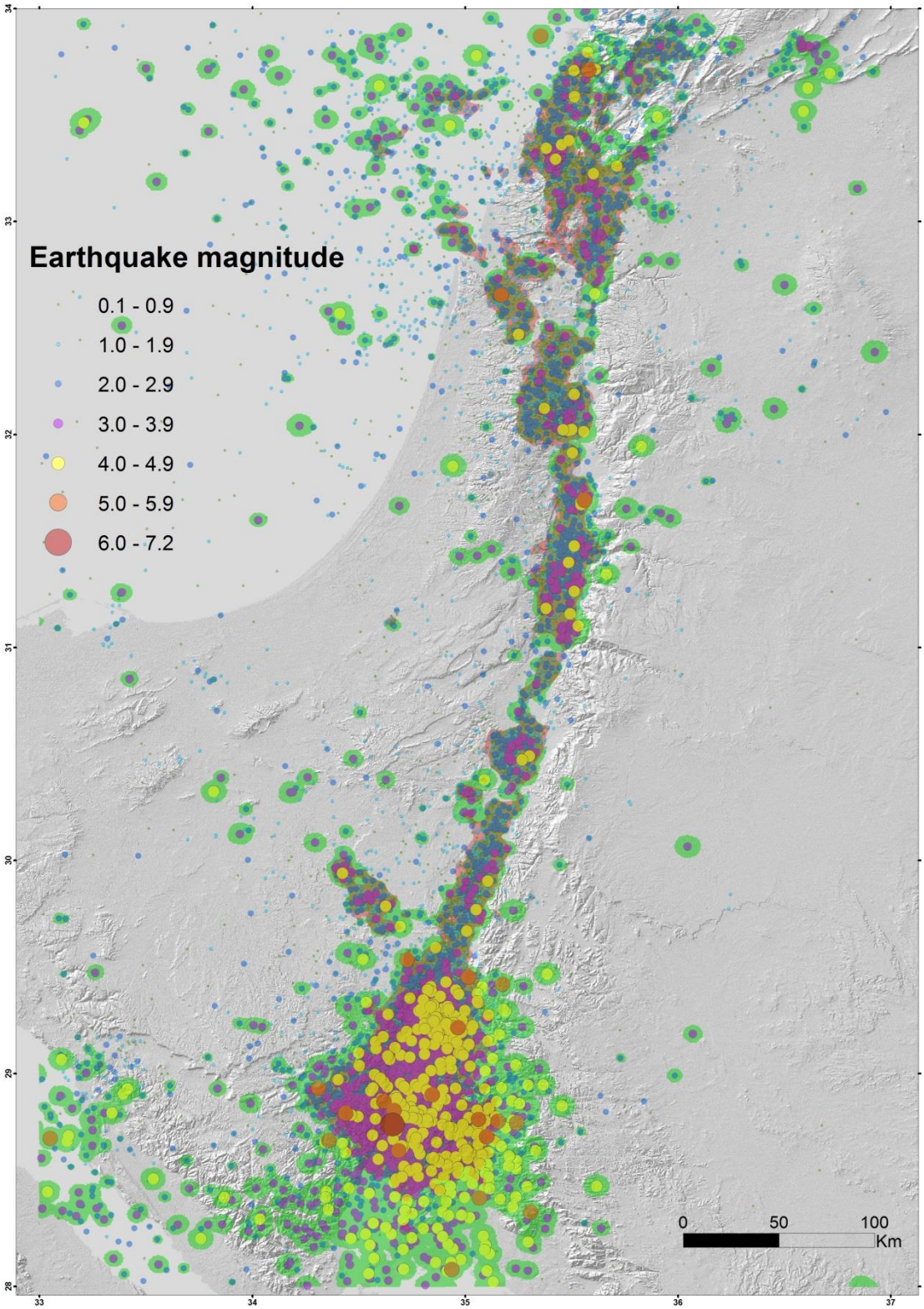

Epicentres investigated in this study, recorded between the period of 1983–2017, on top of the overlap area of the two seismicity polygons that appear separately in the above figures. As expected, most of the seismic activity is concentrated within these polygons.

1.8. The main seismic sources with associated slip rates of geodetic and geological sources

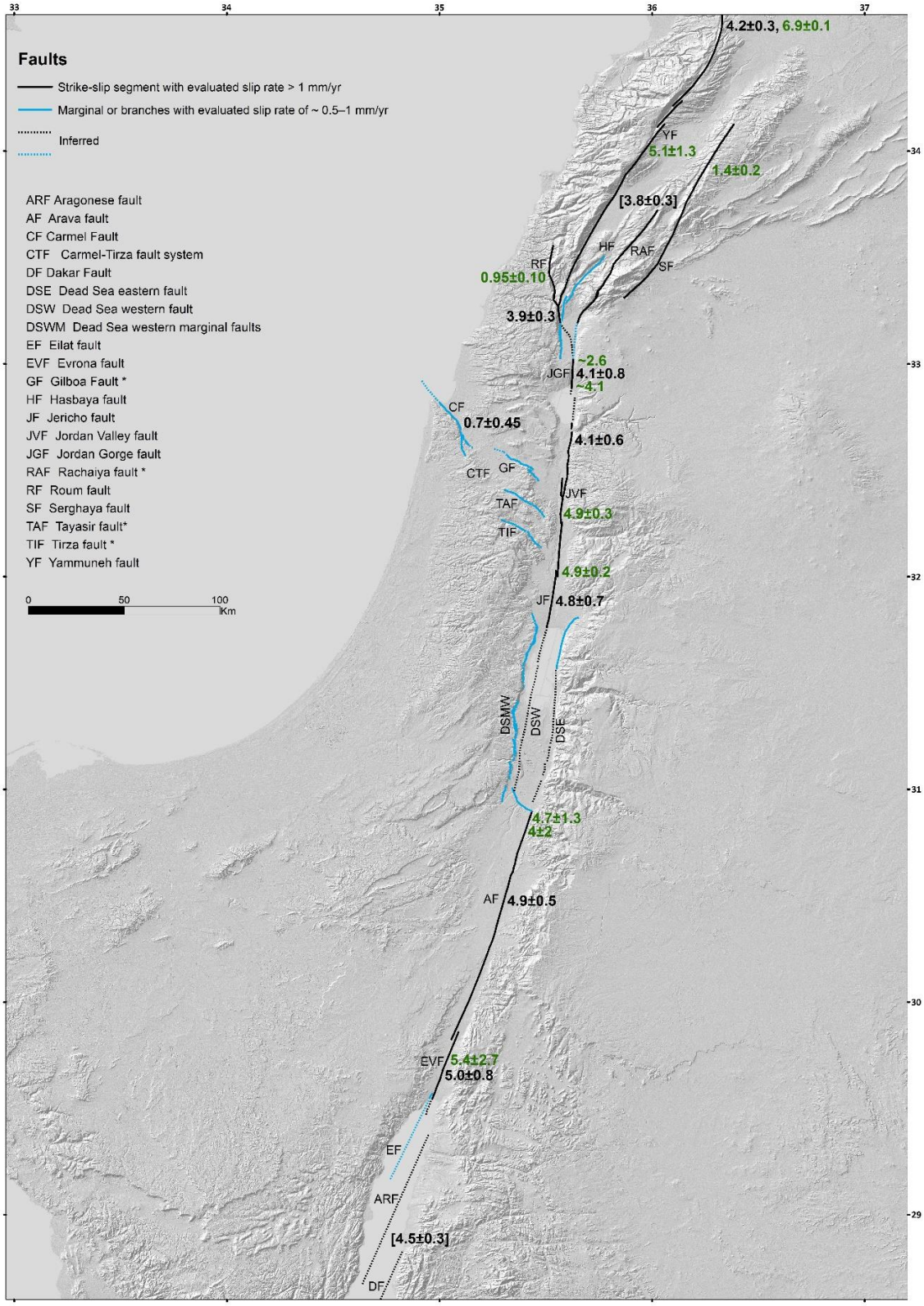

The main seismic sources in Israel and adjacent areas as in Fig. 3.3. Colours denote the two fault categories according to the criteria. Inferred subsurface faults are marked by dashed lines. Abbreviations are for the DST main strike-slip segments, its main branches and marginal faults. Numbers indicate lateral components of slip rates [mm/a] according to geodetic investigations (black) and field measurements of lateral offsets (green) based on recent studies (Tables 3.1; 3.2). Brackets indicate slip rates accommodated by an entire fault zone. Asterisk denote segments of unknown slip rates, where a fault splits to (sub-) parallel segments.

Appendix 2: The frequency-magnitude relation analysis for seismogenic zones

2.1. The Gulf of Eilat

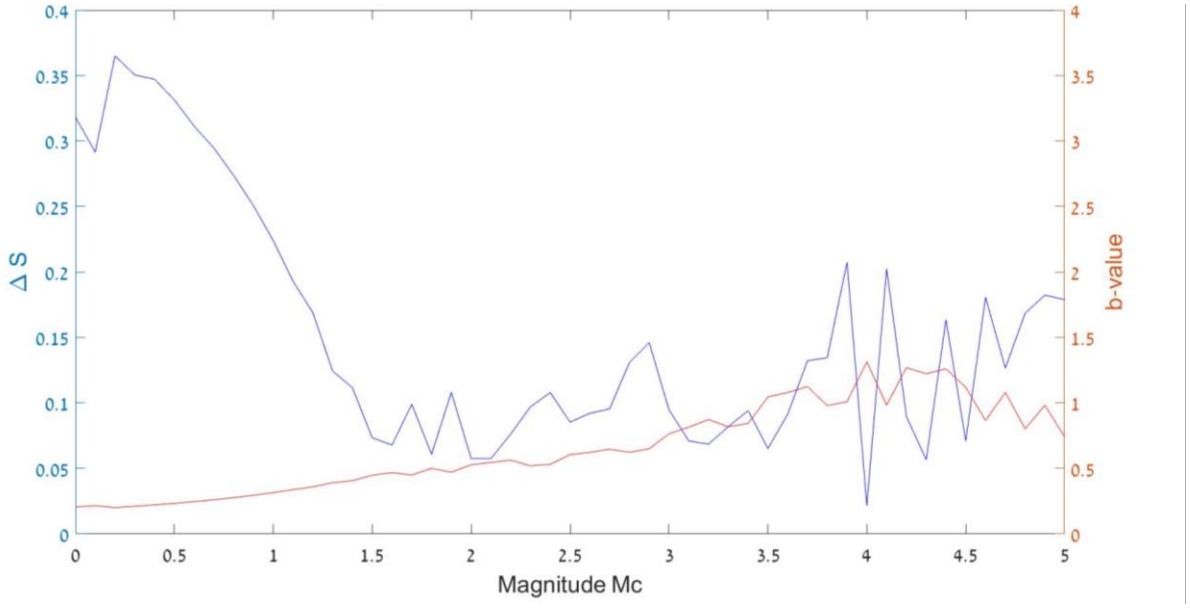

Appendix 2.1.1. The Kolmogorov-Smirnov test results for the 1983–2017 period within the Gulf of Eilat seismogenic zone. $M_c = 4.0$ is selected as the preferable option.

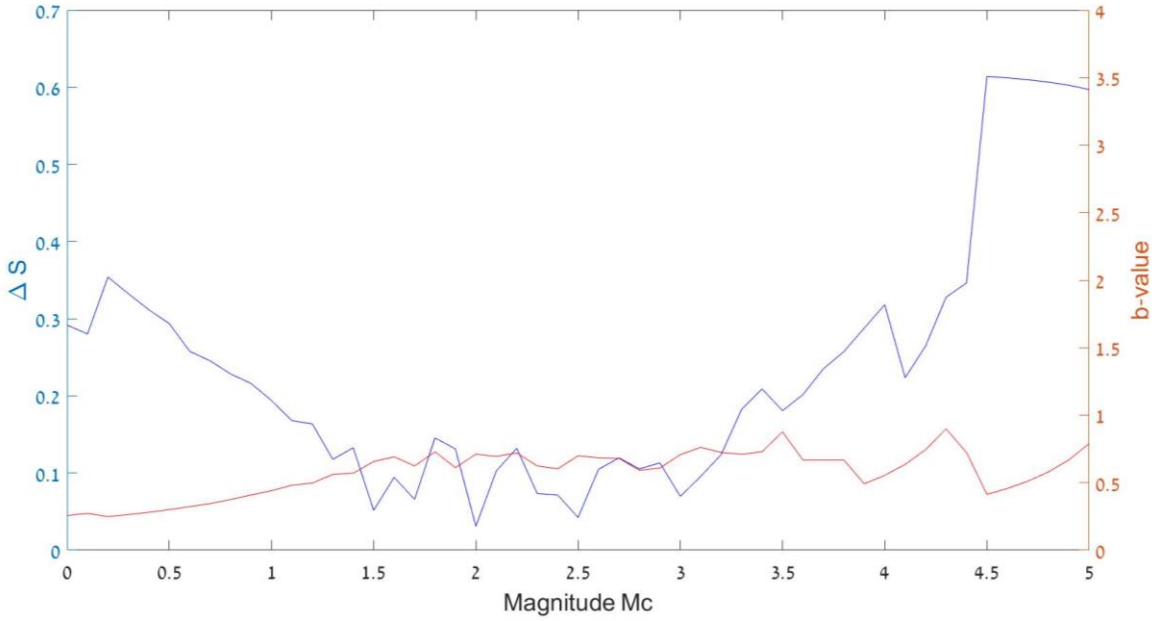

Appendix 2.1.2. The Kolmogorov-Smirnov test results for the 2007–2017 period within the Gulf of Eilat seismogenic zone. $M_c = 2.0$ is selected as the preferable option.

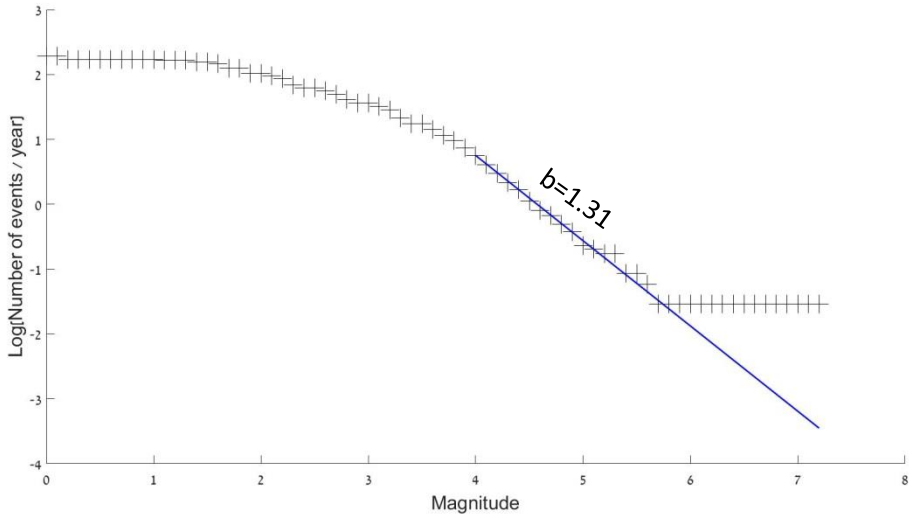

Appendix 2.1.3. The frequency-magnitude relation for the 1983–2017 period within the Gulf of Eilat seismogenic zone.

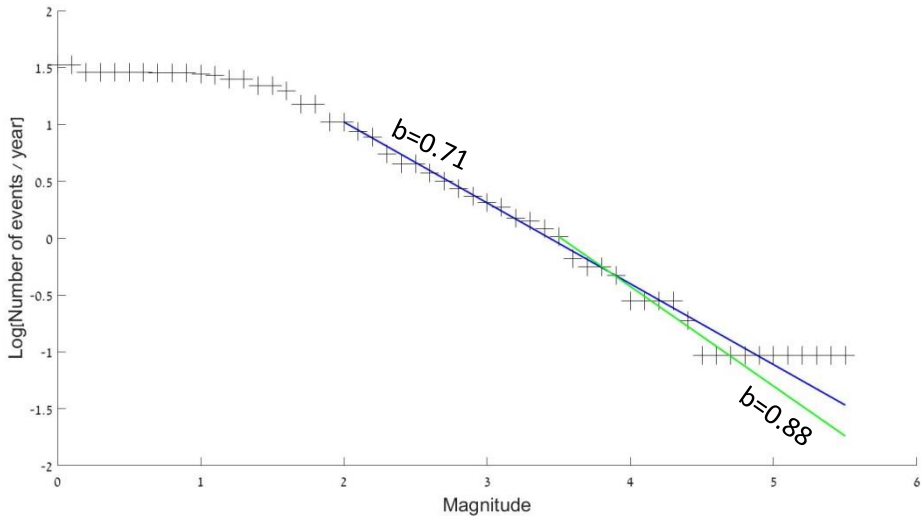

Appendix 2.1.4: The frequency-magnitude relation for the 2007–2017 period within the Gulf of Eilat seismogenic zone. Two options are suggested: the blue and green linear fits correspond to completeness magnitudes of 2.0 and 3.5, respectively. The Kolmogorov-Smirnov test suggests M_c of 2.0 or 2.5 (Appendix 2.1.2), but the ΔS is probably affected by the high magnitudes, so the lower M_c - *b-values* sets may be suggested by the test due to an artefact. $M_c = 3.5$ is preferred, also due to Pinsky and Shapira (2017) results, which indicate that some $M_d = 2.0$ may have not recorded during the years 2007–2014 (see further detectability issues in Chapter 2). However, only 23 $M \geq 3.5$ events were recorded (Table 4.1) so the corresponding *b-value* is very poorly constrained. Due to the unclarity, the two options of M_c − *b-value* sets are presented.

2.2. Eastern Sinai

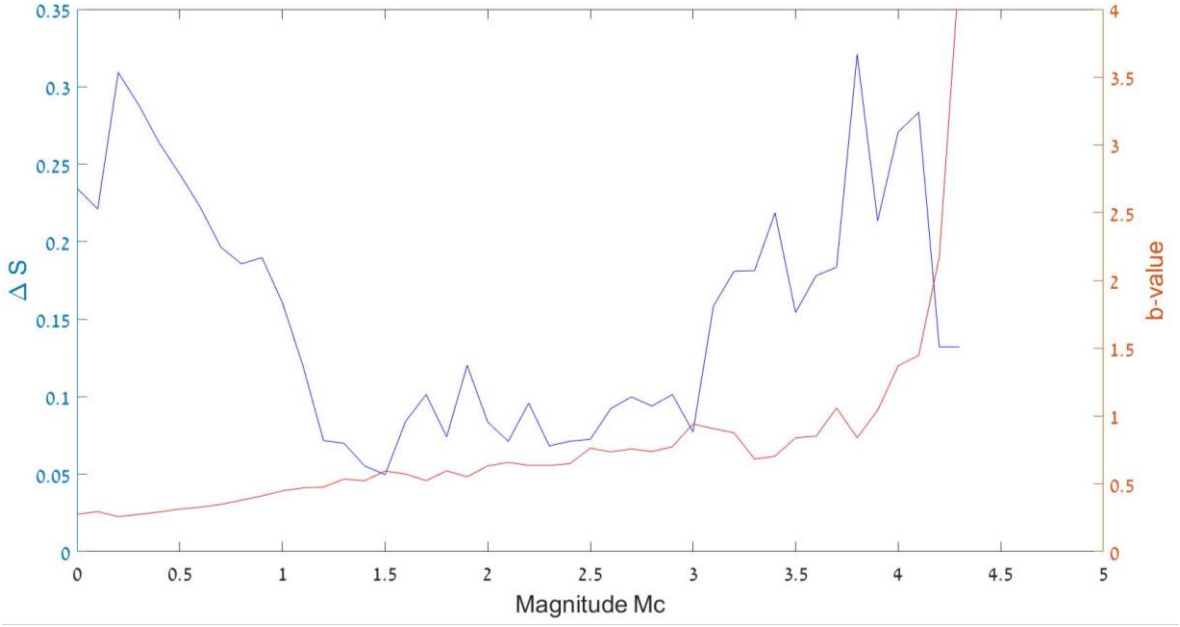

Appendix 2.2.1. The Kolmogorov-Smirnov test results for the 1983–2017 period within the Eastern Sinai seismogenic zone. $M_c = 1.5$ is selected as the preferable option.

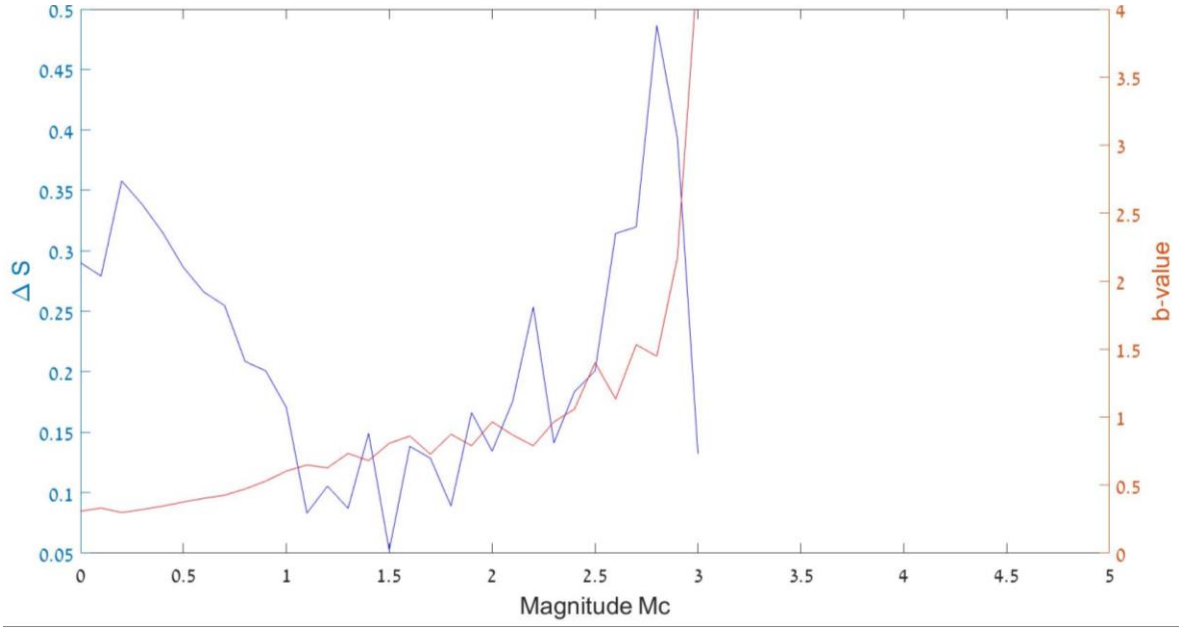

Appendix 2.2.2. The Kolmogorov-Smirnov test results for the 2007–2017 period within the Eastern Sinai seismogenic zone. The test suggests that $M_c = 1.5$ should be the preferable option, but the *b-value* calculation is very poorly constrained, with only 25 events of magnitudes $M \geq 1.5$, too poor to obtain reliable results.

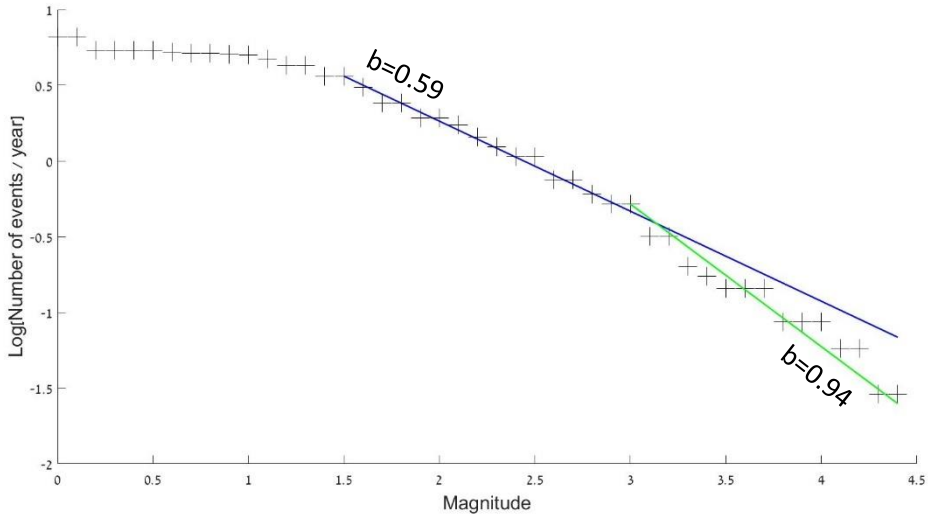

Appendix 2.2.3. The frequency-magnitude relation for the 1983–2017 period within the Eastern Sinai seismogenic zone**.** Two options are suggested: the blue and green linear fits correspond to M_c of 2.0 and 3.5, respectively. The Kolmogorov-Smirnov test suggests a completeness magnitude of 1.5 (Appendix 2.2.1), but a steeper slope (i.e. higher *b-value*) associated with a the ΔS peak at $M_c = 3.0$ fits better to the higher magnitudes. The latter *b-value* deduction is very poorly constrained (Fig. 4.1) but the two alternatives are suggested, since it is unclear whether the data is incomplete at $M_d < 3.0$ or at $M_d > 3.0$. The zone is outside the network coverage area but relatively close to the stations (Fig. 2.2), so a completeness magnitude of 1.5 is possible, although not very likely. Since the seismo-tectonics of this zone is not well understood (see sub-sections 4.3.1; 5.3.2; 5.3.1), a frequency-magnitude relation that does not obey the Gutenberg-Richter law is also plausible.

2.3. Arava Valley

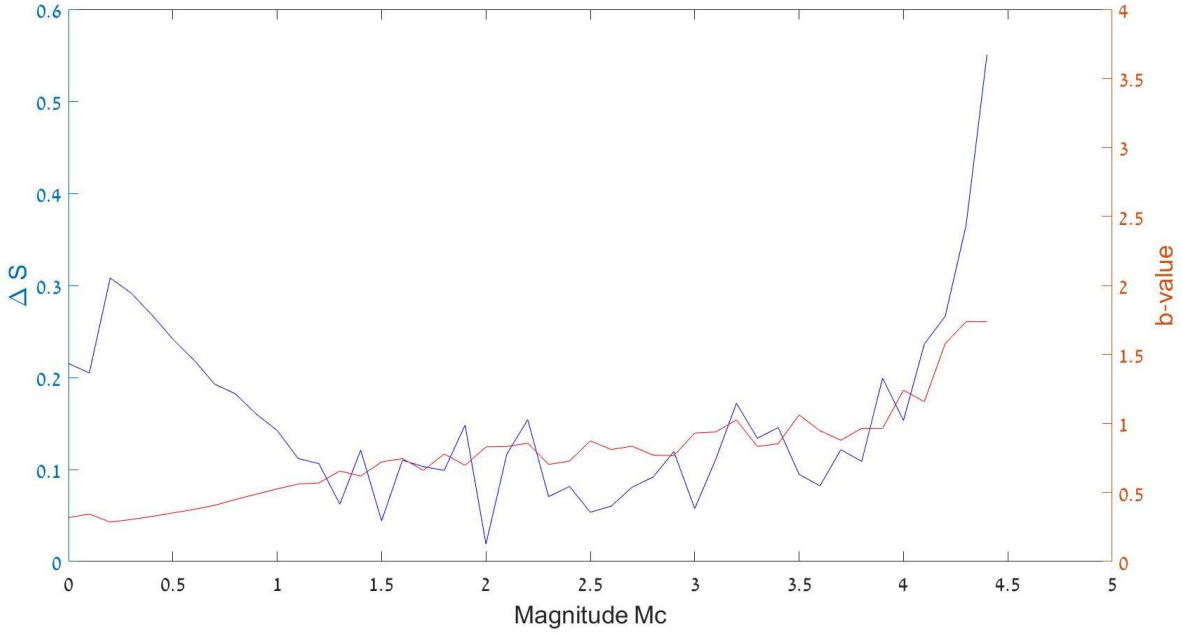

Appendix 2.3.1. The Kolmogorov-Smirnov test results for the 1983–2017 period within the Arava Valley seismogenic zone. $M_c = 2.0$ is selected as the preferable option.

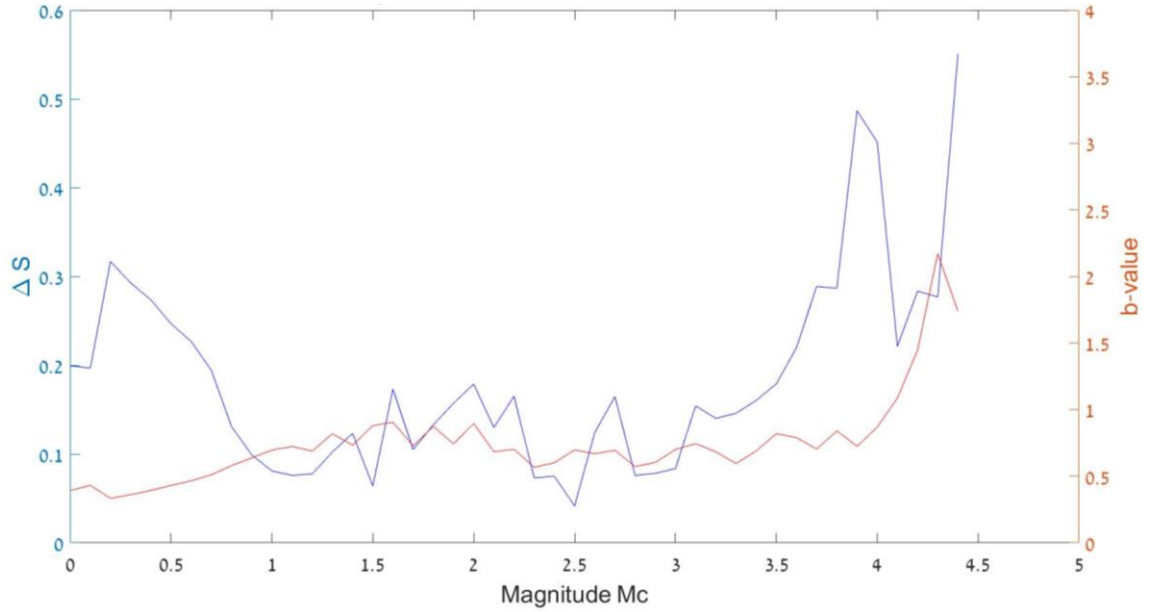

Appendix 2.3.2. The Kolmogorov-Smirnov test results for the 2007–2017 period within the Arava Valley seismogenic zone. $M_c = 1.5$, corresponding to the second-largest peak ($\Delta S = 0.064$), is selected as the preferable option, despite a better peak ($\Delta S = 0.0414$) at $M_c = 2.5$. The considerations are: a) the network performance improved over the years so a higher M_c than this of the whole period (1983–2017) is not plausible. The $\Delta S = 0.0414$ peak is interpreted as an artefact, probably resulted by a relatively high number of $M_d > 3.0$ events (Appendix. 2.3.4). b) The $1.5 \leq M_c \leq 3.0$ events (Appendix 2.3.4) are closer to the completeness level and thus are much larger in their amount than the higher magnitude range, probably represent the frequency-magnitude relation better.

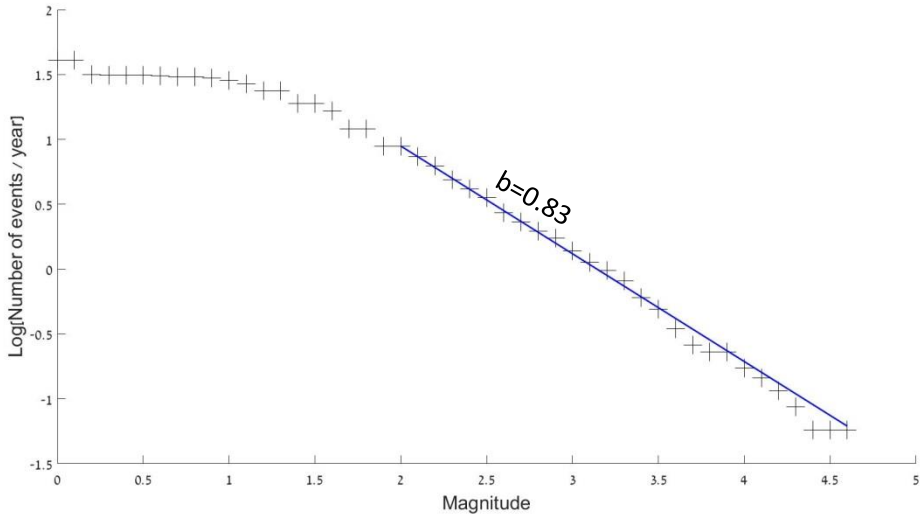

Appendix 2.3.3. The frequency-magnitude relation for the 1983–2017 period within the Arava Valley seismogenic zone.

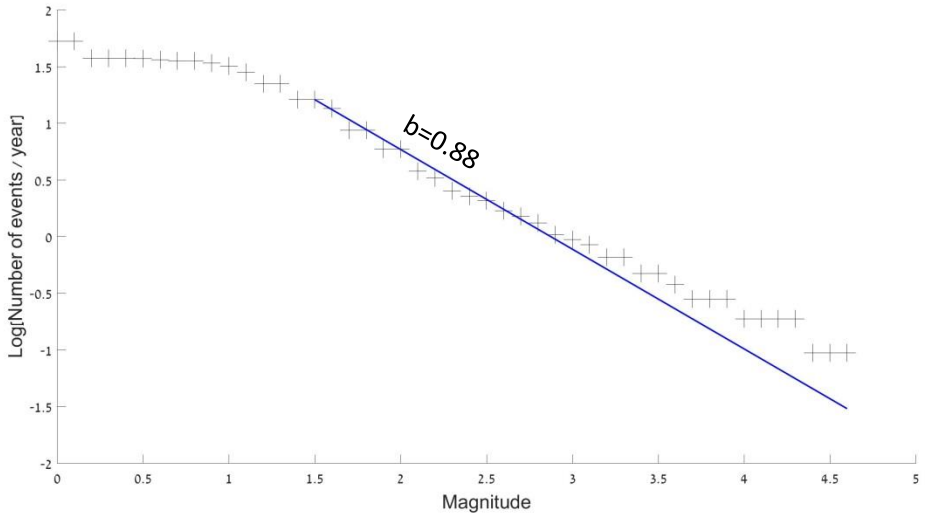

Appendix 2.3.4. The frequency-magnitude relation for the 2007–2017 period within the Arava Valley seismogenic zone.

2.4. Dead Sea Basin

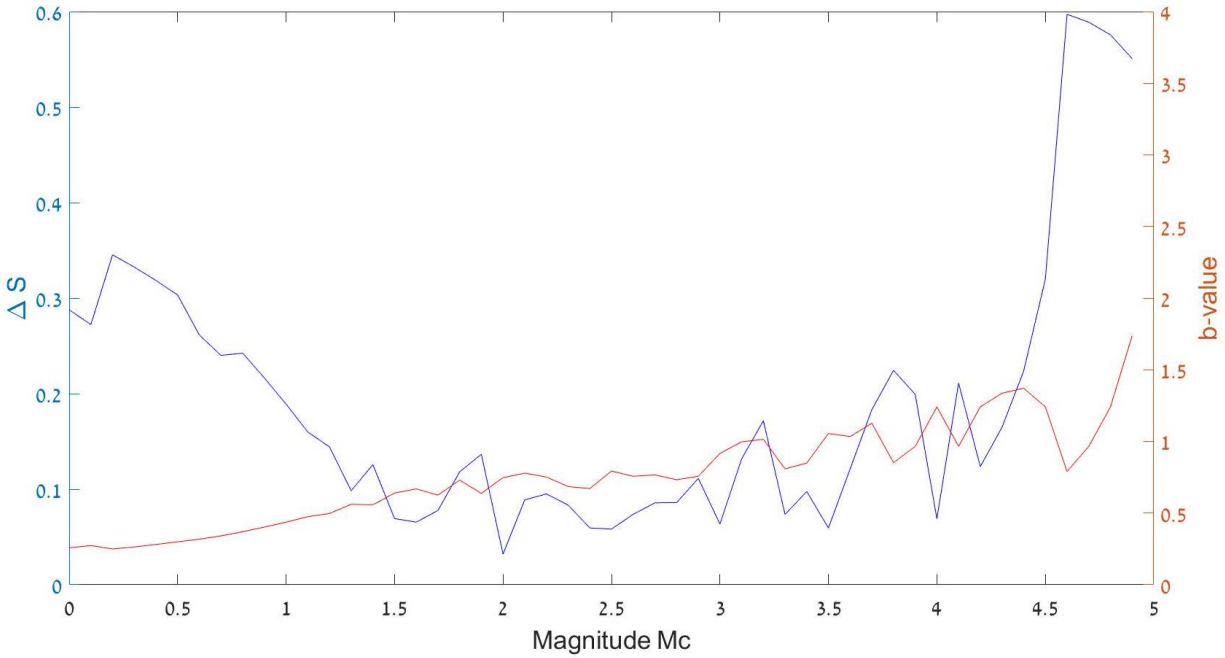

Appendix 2.4.1. The Kolmogorov-Smirnov test results for the 1983–2017 period within the Dead Sea Basin seismogenic zone. $M_c = 2.0$ is selected as the preferable option.

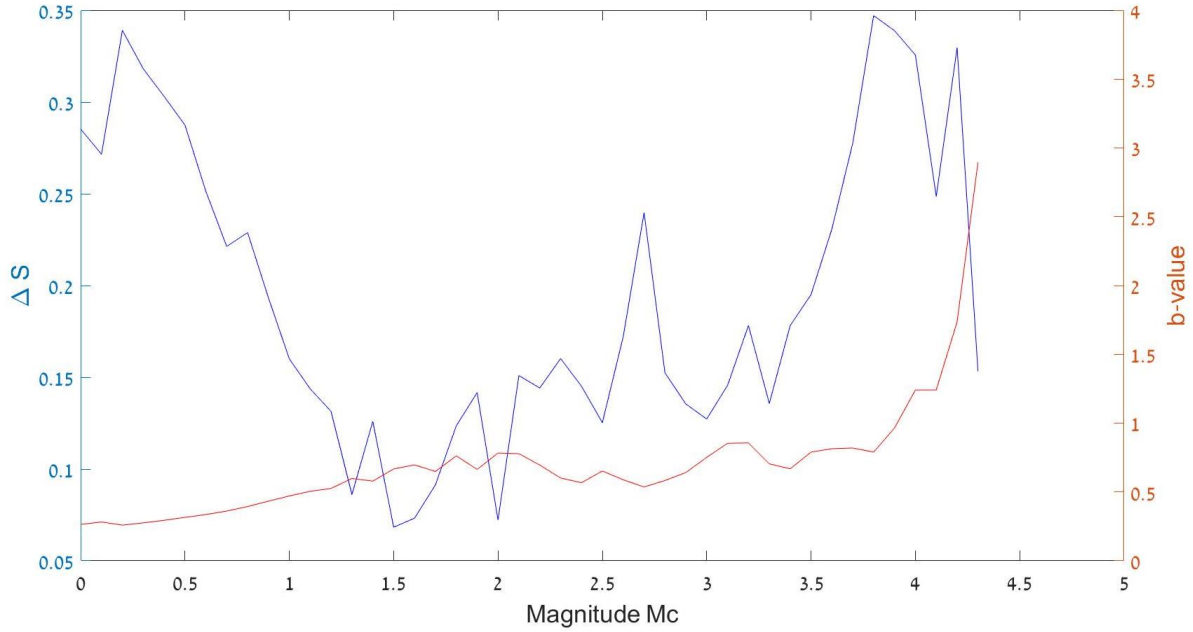

Appendix 2.4.2. The Kolmogorov-Smirnov test results for the 2007–2017 period within the Dead Sea Basin seismogenic zone. $M_c = 1.5$ is selected as the preferable option.

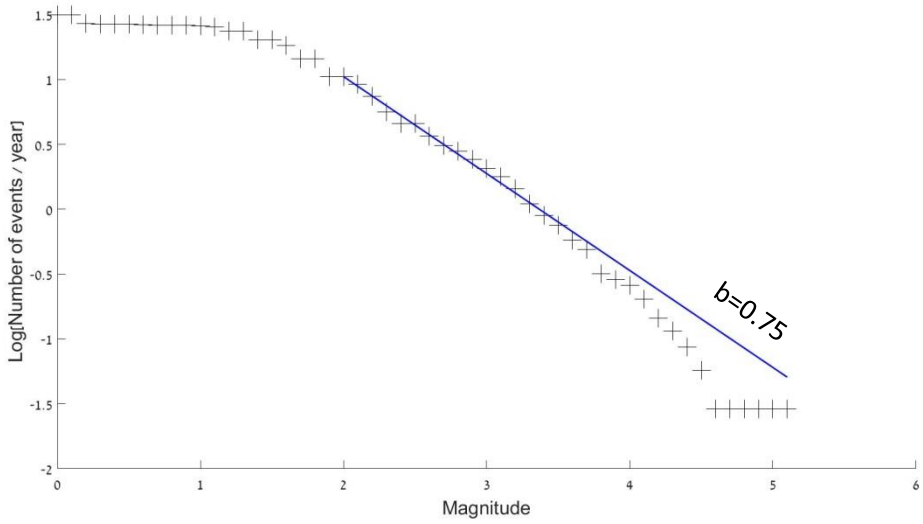

Appendix 2.4.3. The frequency-magnitude relation for the 1983–2017 period within the Dead Sea Basin seismogenic zone.

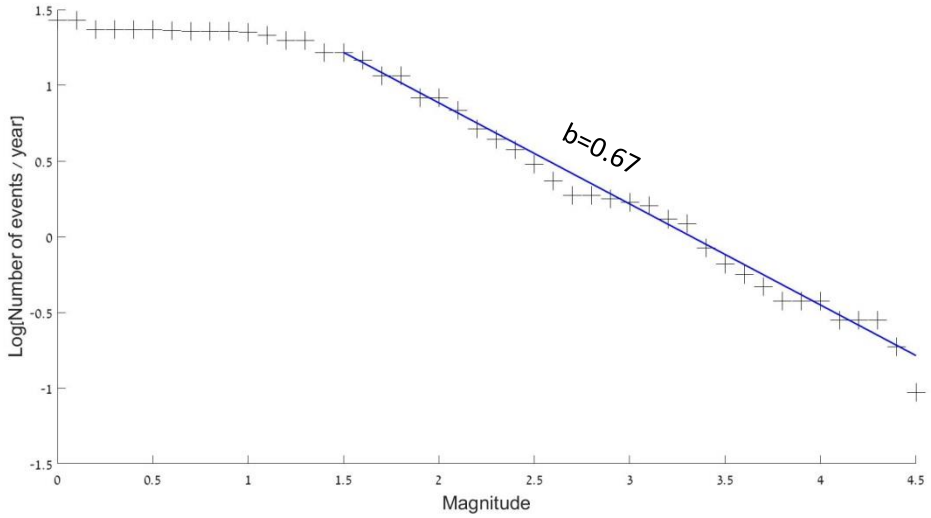

Appendix 2.4.4. The frequency-magnitude relation for the 2007–2017 period within the Dead Sea Basin seismogenic zone.

2.5. Carmel-Gilboa-Tirza

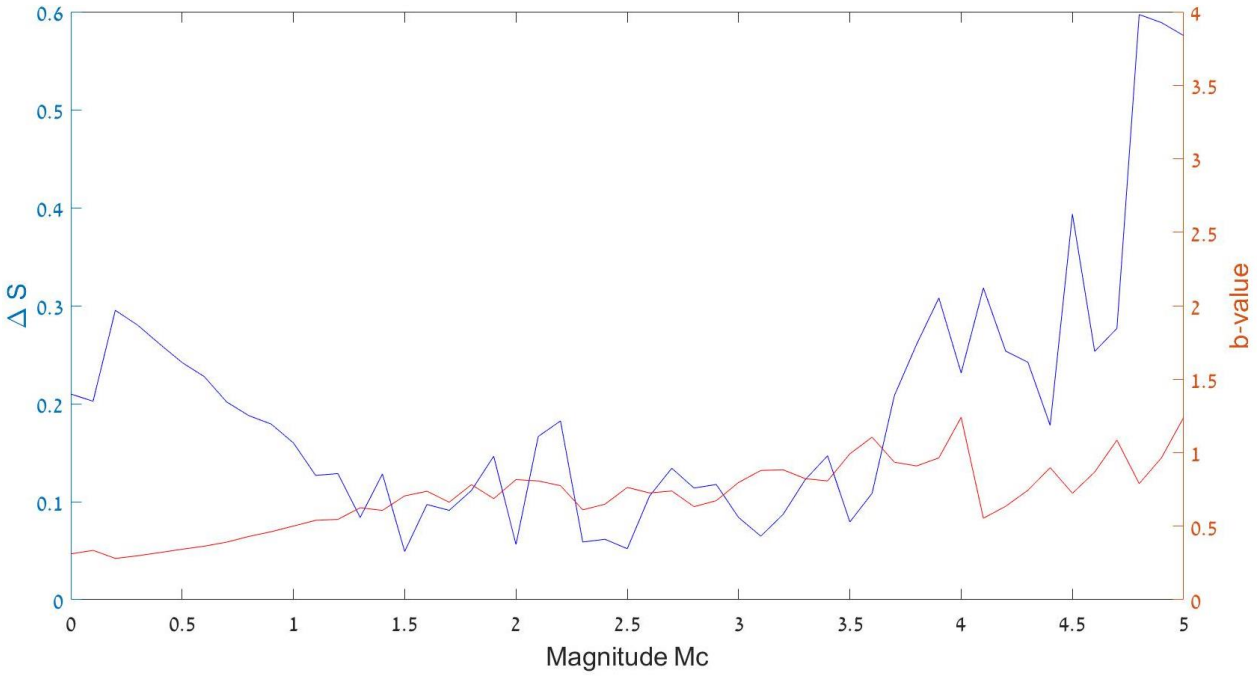

Appendix 2.5.1. The Kolmogorov-Smirnov test results for the 1983–2017 period within the Carmel-Gilboa-Tirza seismogenic zone. $M_c = 1.5$ is selected as the preferable option.

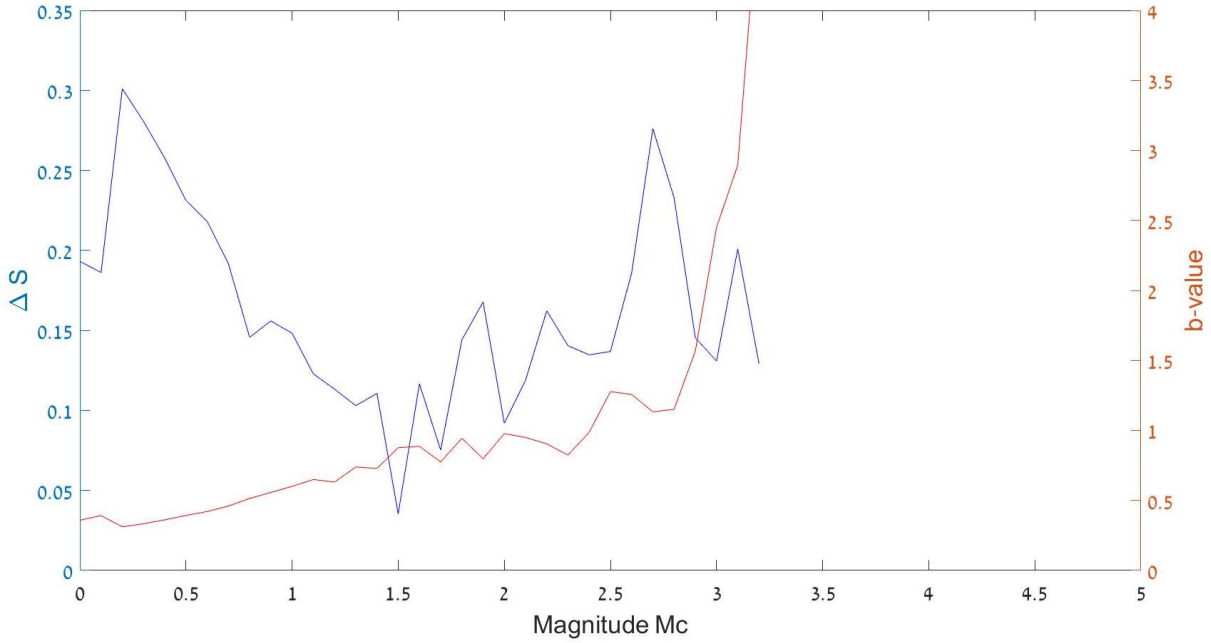

Appendix 2.5.2. The Kolmogorov-Smirnov test results for the 2007–2017 period within the Carmel-Gilboa-Tirza seismogenic zone. $M_c = 1.5$ is selected as the preferable option.

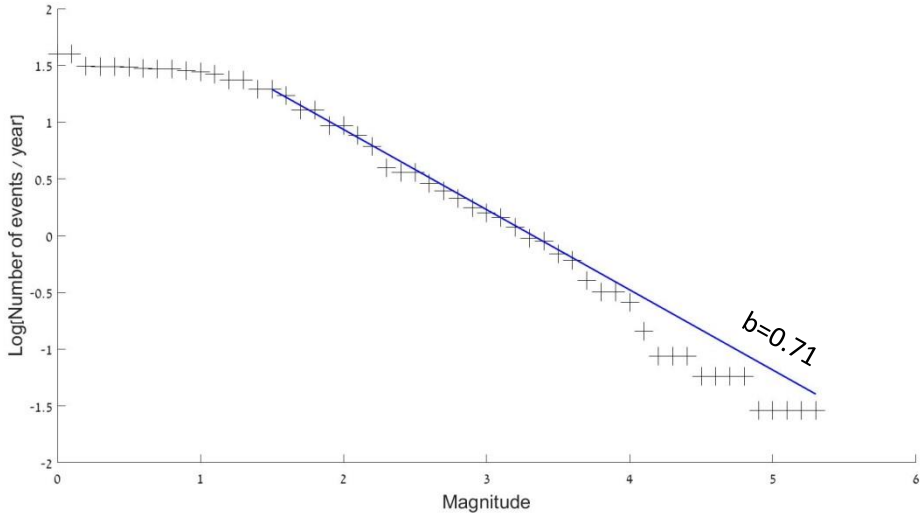

Appendix 2.5.3. The frequency-magnitude relation for the 1983–2017 period within the Carmel-Gilboa-Tirza seismogenic zone.

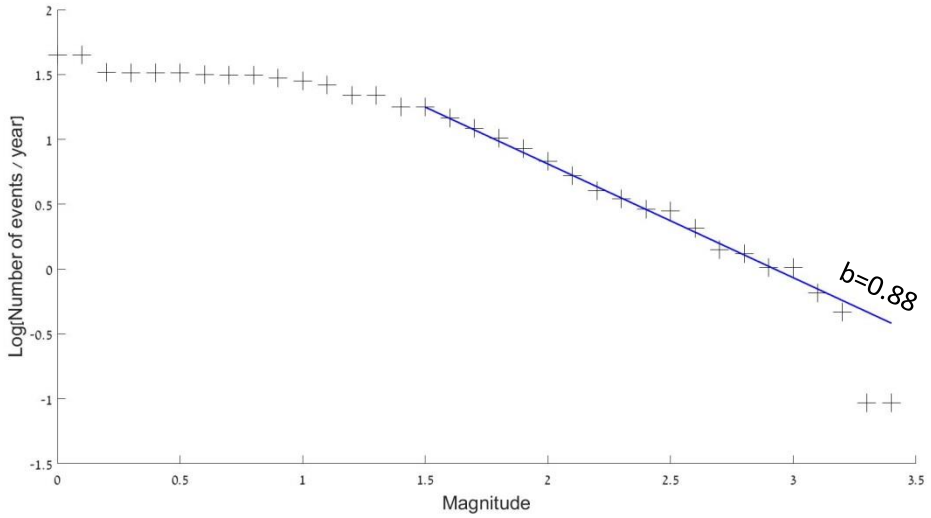

Appendix 2.5.4. The frequency-magnitude relation for the 2007–2017 period within the Carmel-Gilboa-Tirza seismogenic zone.

2.6. Kinnarot - Korazim - Hula

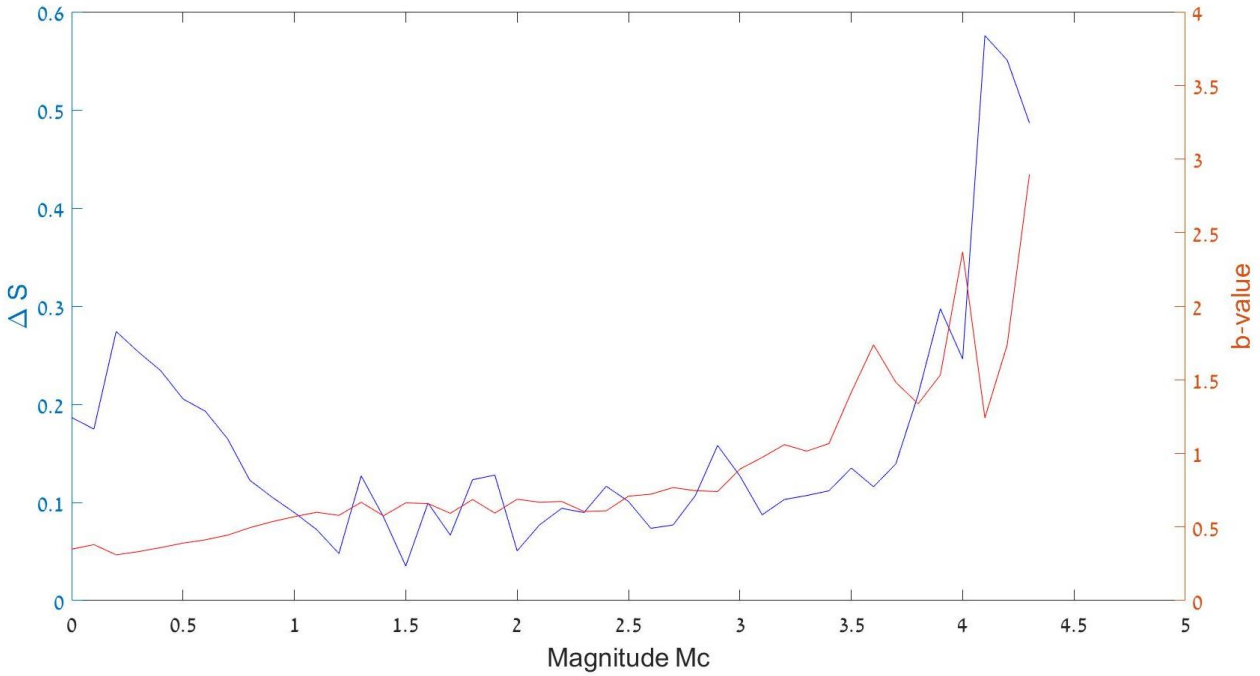

Appendix 2.6.1. The Kolmogorov-Smirnov test results for the 1983–2017 period within the Kinnarot - Korazim - Hula seismogenic zone. $M_c = 1.5$ is selected as the preferable option.

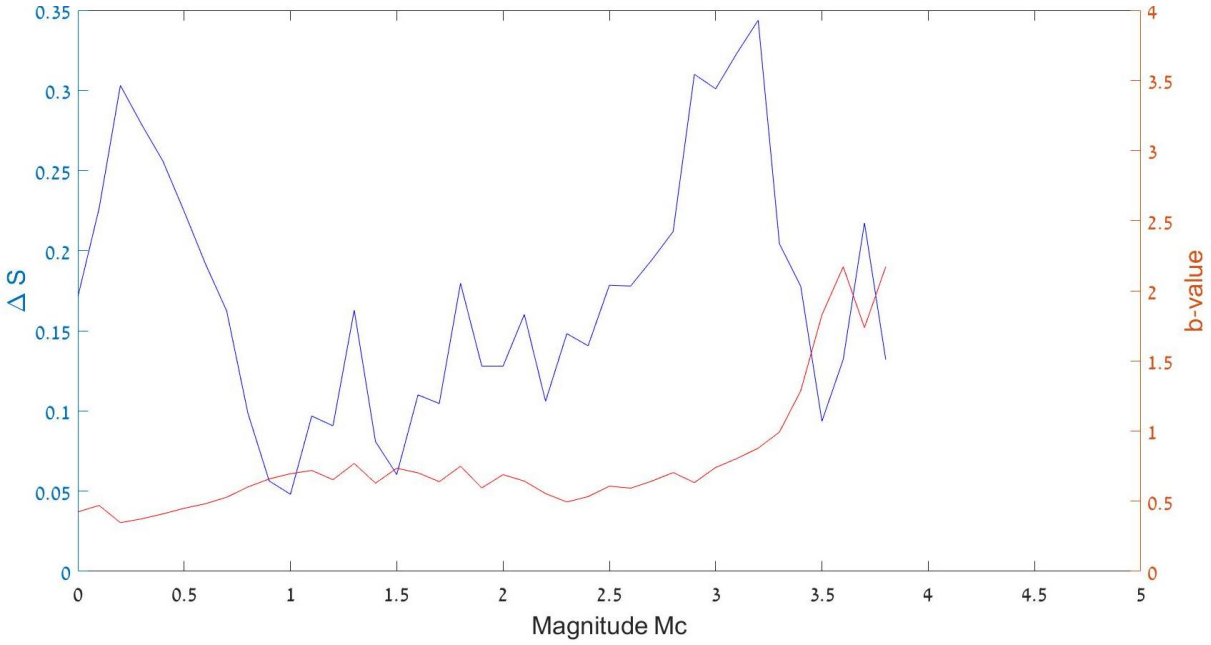

Appendix 2.6.2. The Kolmogorov-Smirnov test results for the 2007–2017 period within the Kinnarot - Korazim - Hula seismogenic zone. $M_c = 1.0$ is selected as the preferable option.

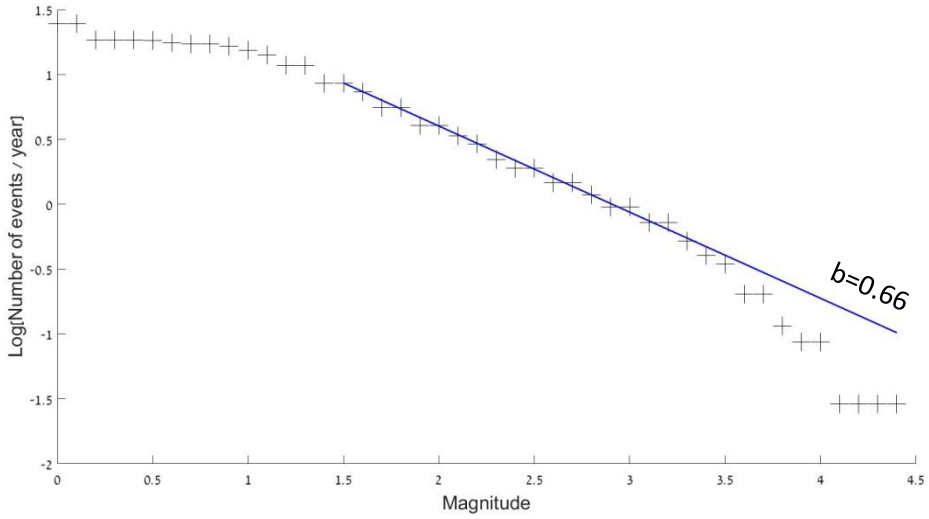

Appendix 2.6.3. The frequency-magnitude relation for the 1983–2017 period within the Kinnarot-Korazim-Hula seismogenic zone.

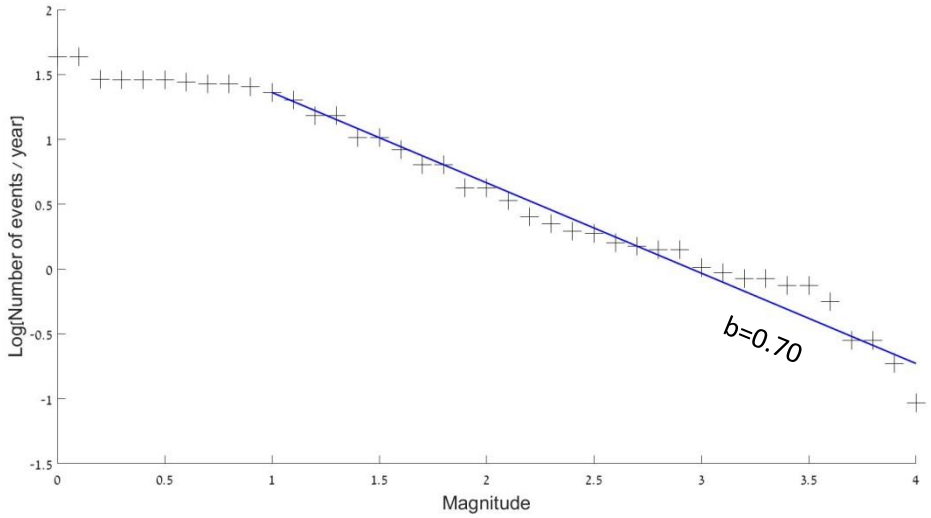

Appendix 2.6.4. The frequency-magnitude relation for the 2007–2017 period within the Kinnarot-Korazim-Hula seismogenic zone.

2.7. Upper Galilee – South Lebanon

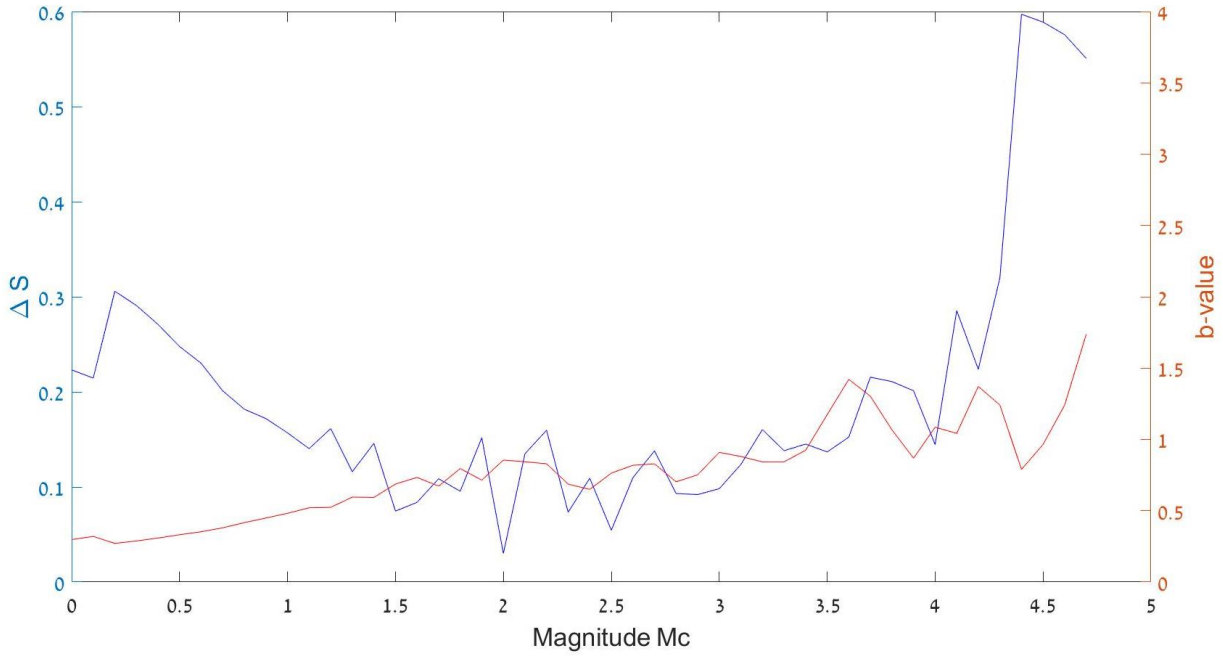

Appendix 2.7.1. The Kolmogorov-Smirnov test results for the 1983–2017 period within the Upper Galilee – South Lebanon seismogenic zone. $M_c = 2.0$ is selected as the preferable option.

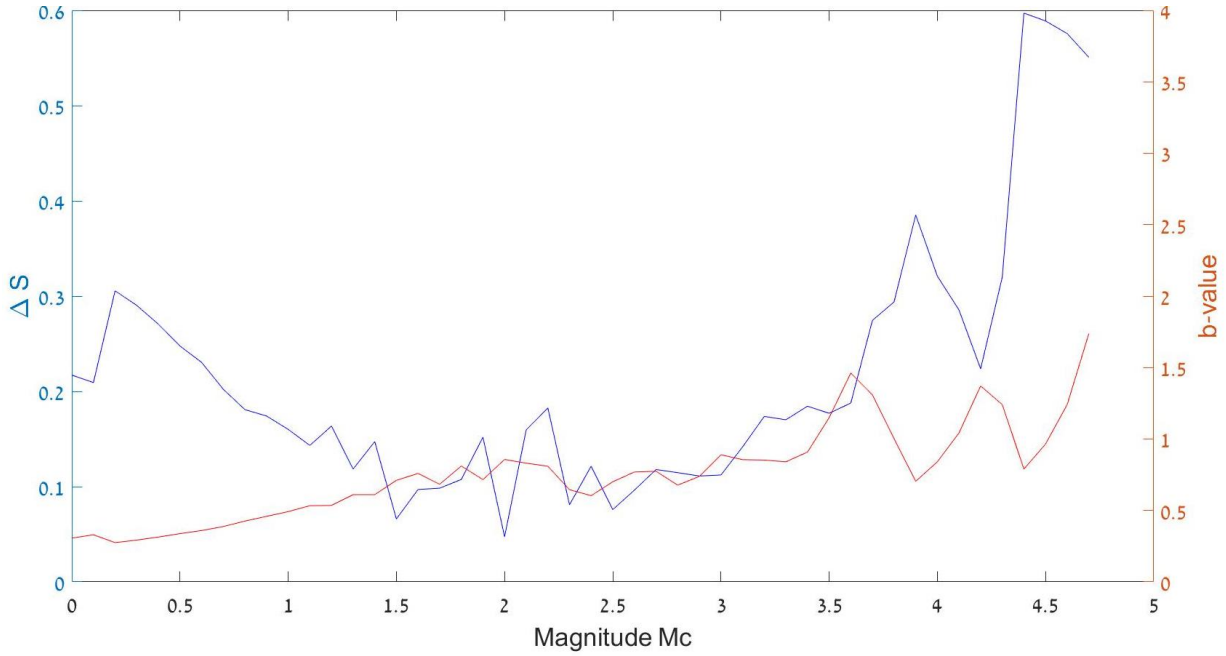

Appendix 2.7.2. The Kolmogorov-Smirnov test results for the 2007–2017 period within the Upper Galilee – South Lebanon seismogenic zone. $M_c = 2.0$ is selected as the preferable option.

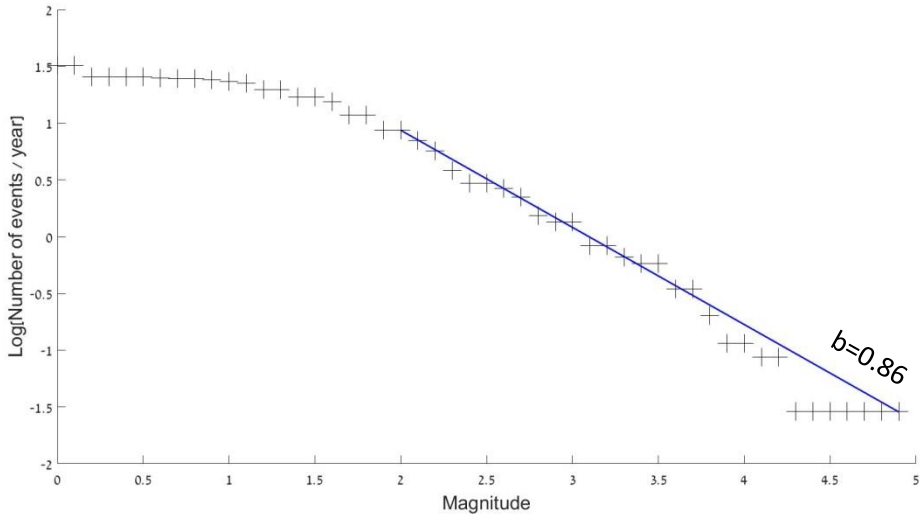

Appendix 2.7.3. The frequency-magnitude relation for the 1983–2017 period within the Upper Galilee – Southern Lebanon seismogenic zone.

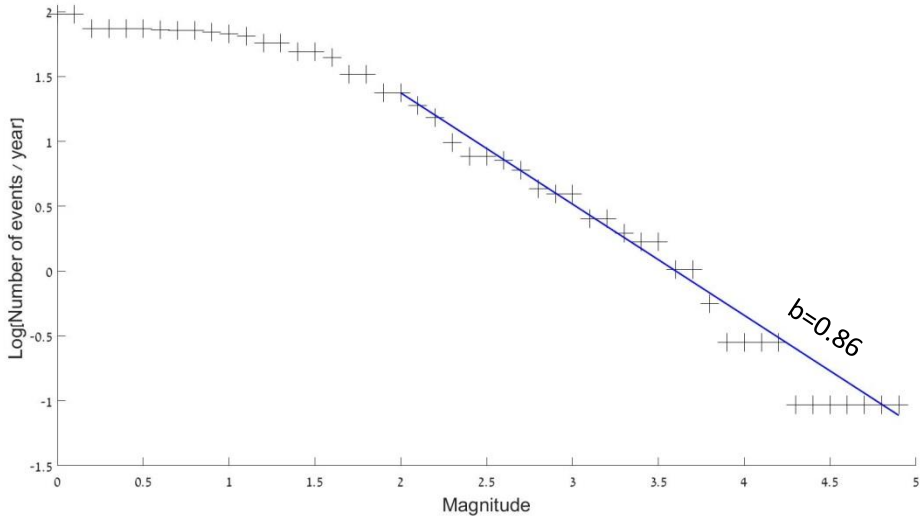

Appendix 2.7.4. The frequency-magnitude relation for the 2007–2017 period within the Upper Galilee – Southern Lebanon seismogenic zone.

2. 8. Roum Fault

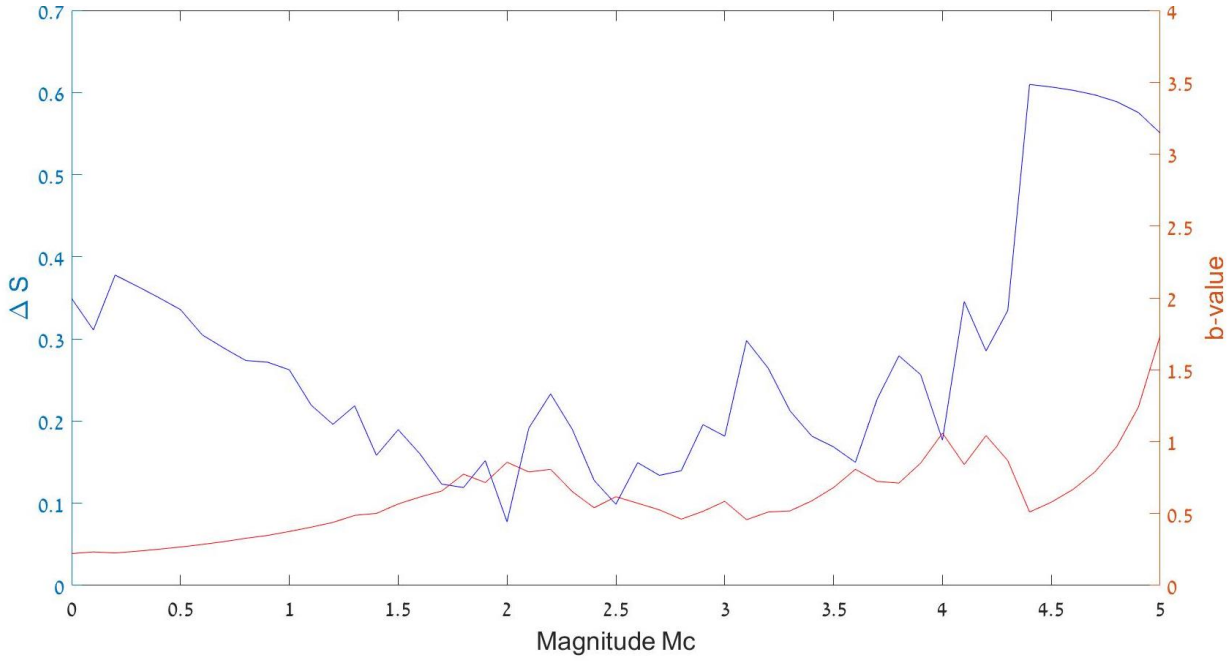

Appendix 2.8.1. The Kolmogorov-Smirnov test results for the 1983–2017 period within the Roum Fault seismogenic zone. $M_c = 2.0$ is selected as the preferable option.

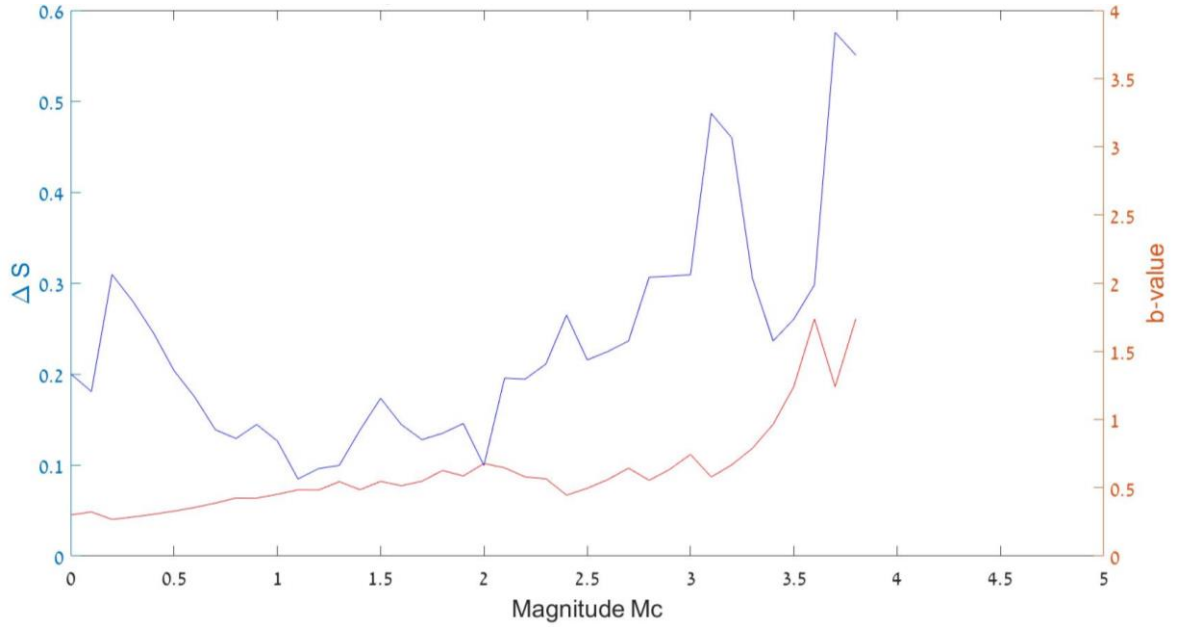

Appendix 2.8.2. The Kolmogorov-Smirnov test results for the 2007–2017 period within the Roum Fault seismogenic zone. The test suggests that $M_c = 1.1$, but the *b-value* deduction is too poorly constrained (only 26 $M \geq 1.1$ events) to obtain reliable results.

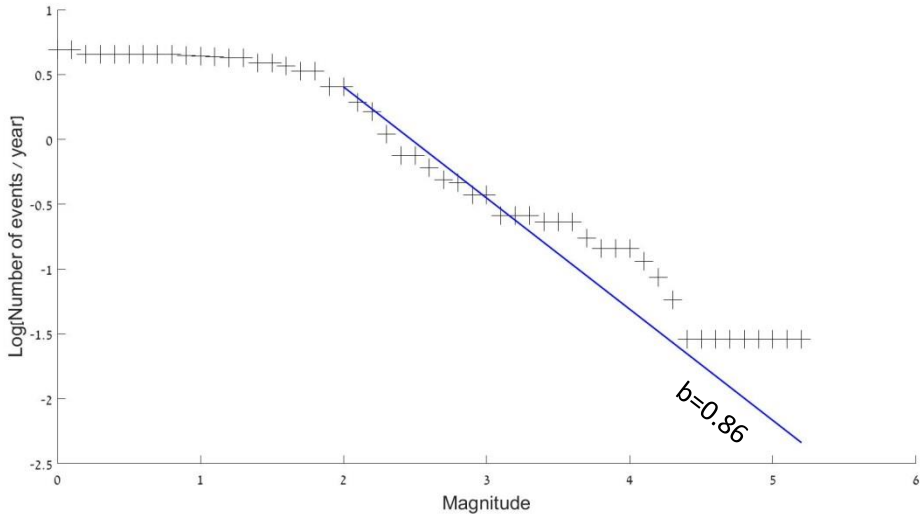

Appendix 2.8.3. The frequency-magnitude relation for the 1983–2017 period within the Roum Fault seismogenic zone.

2. 9. Lebanon restraining bend

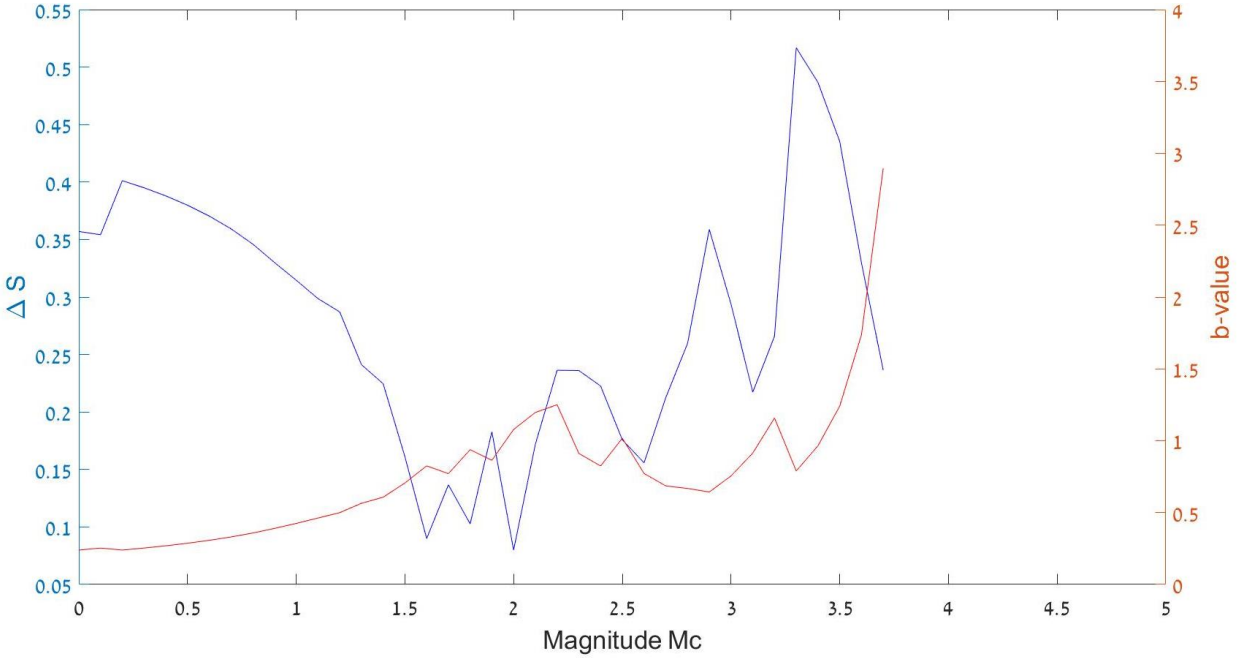

Appendix 2.9.1. The Kolmogorov-Smirnov test results for the 1983–2017 period within the Lebanon Restraining Bend seismogenic zone. $M_c = 2.0$ is selected as the preferable option.

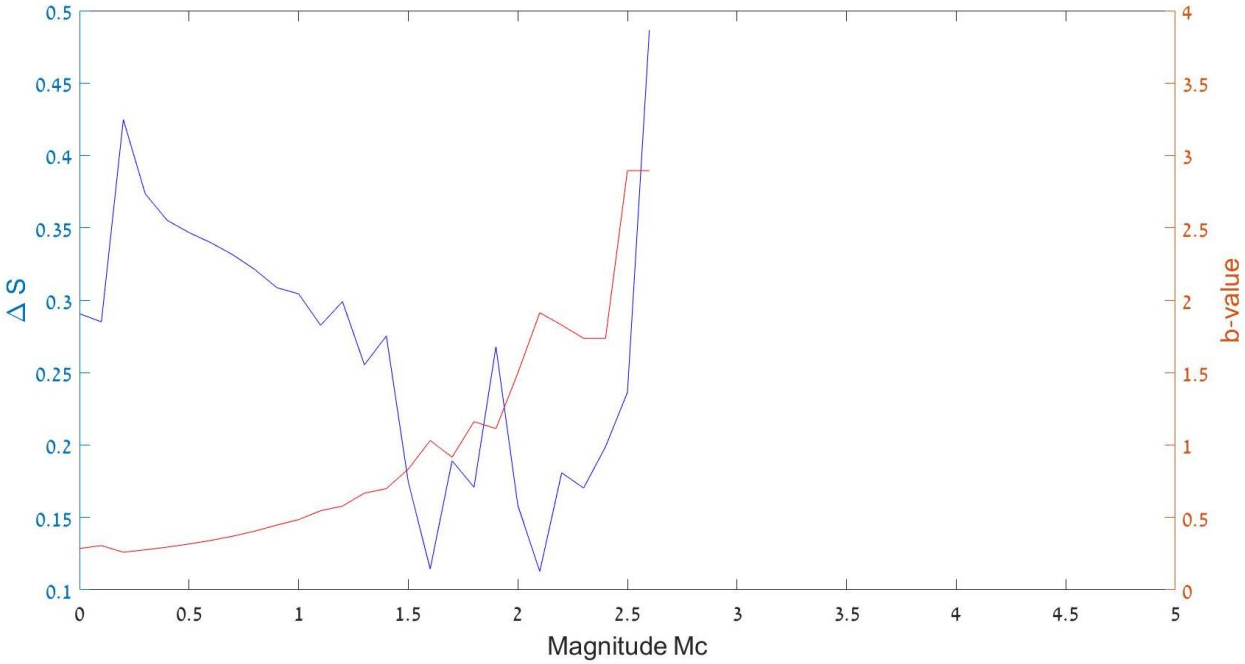

Appendix 2.9.2. The Kolmogorov-Smirnov test results for the 2007–2017 period within the Lebanon Restraining Bend seismogenic zone. The test suggests that $M_c = 1.6$, but the *b-value* deduction is too poorly constrained (only 31 $M \geq 1.6$ events) to obtain reliable results.

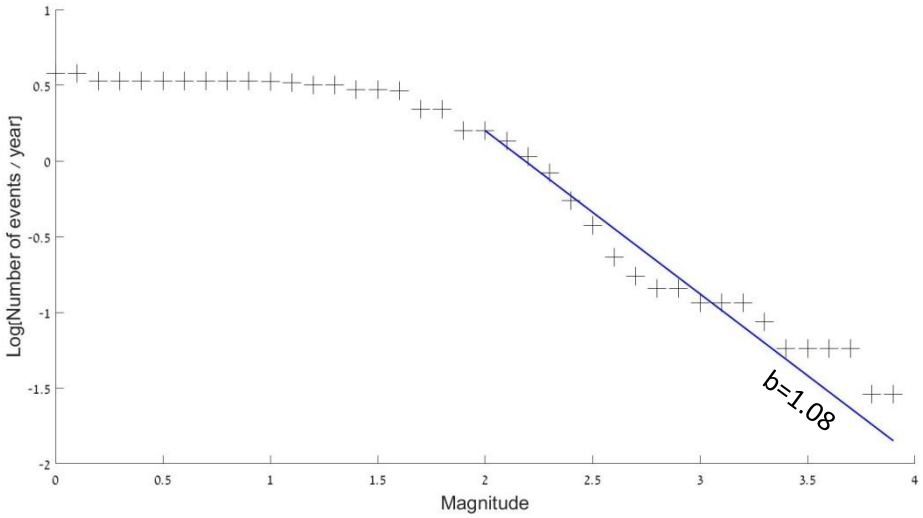

Appendix 2.9.3. The frequency-magnitude relation during the 1983–2017 period within the Lebanon Restraining Bend seismogenic zone.

מוקדש לחברי יונתן גורן ז"ל, שלמד עמי לתואר הראשון והשני, ושנהרג חודשים אחדים לאחר שהשלים את עבודת המאסטר במהלך טיפוס על הר געש בצ'ילה.

אנליזת זמן-מרחב מציעה שרעשי משנה (aftershocks) בקטלוג רעידות אדמה העני ברעשים מקדימים (foreshocks) כמו בקטלוג שנחקר בעבודה זו, משפיעים על הפרמטרים של הקשר תדירות–מגניטודה בכך שהם מעלים את ה-*b-value* וגם את ה-*a-value*, ומטים את מרווחי זמני החזרה הנובעים מהם למרווחים קצרים (ואחרת עבור המגניטודות הגבוהות ביותר). ה-*b-value* באזור המחקר המלא (1.19–0.99) מתפרש בעבודה זו כמוּטָה כתוצאה מרעשי משנה. בהתאמה, מרווחי זמני החזרה הנובעים ממנו קצרים מהמצופה, לפי מאה שנה של קטלוג רעידות בעידן המכשירים, וכאלפיים שנה של עדויות גיאולוגיות והיסטוריות. *b-value* יציב למדי של 0.8~ מתקבל באזור הכיסוי של הרשת הסיסמית, היכן שהאנליזה מבוססת על נתונים מדויקים יותר ורעשי משנה היו מועטים. מרווחי זמן החזרה הנובעים ממנו תואמים לרקורד של חלונות הזמן הארוכים יותר שצוינו. לכן, מוצע כאן ש-*b-value* של 0.8~ מייצג את הפעילות הסיסמית ב-35~ השנים האחרונות, ואולי גם בתקופות ארוכות יותר. *b-value* זה נמוך בהשוואה לאזורי שבירה אופקית אחרים, ייתכן שכתוצאה מלוקאליזציה של ההעתקה לאורך טרנספורם ים המלח. מרווחי זמני החזרה המוצעים הם 10~, 70~ ו-450~ שנה לרעידות במגניטודות $5.0 \leq M < 6.0$, $6.0 \leq M < 7.0$ ו-$7.0 \leq M < 8.0$, בהתאמה, בחלקו הדרומי של טרנספורם ים המלח (ללא מפרץ אילת).

ההעתקים הרביעוניים, המוגדרים בעבודה זו כ-'capable', מסווגים לפי קריטריונים היררכיים: א) העתקי התנועה האופקית הראשיים של טרנספורם ים המלח; ב) העתקים בעלי עדות ישירה לפעילות רביעונית; ג) הענפים הראשיים של העתקים בקטגוריות שלעיל, והעתקי שוליים של אגני הטרנספורם; ד) העתקים שניתן לקשרם לפעילות סיסמית בעידן המכשירים; ה) העתקים בתת-הקרקע. המפה מכסה את כל שטח ישראל, עם המשך של העתקים משמעותיים מעבר לגבולותיה ובים. התפרוסת ההומוגנית למדי של ההעתקים בקטגוריות השונות מציעה שהקריטריונים משלימים זה את זה, ולכן תומכים בעיצוב שלהם. כמה מערכות העתקים מובחנות: א) העתקי התנועה האופקית של טרנספורם ים המלח, הענפים העיקריים שלהם, והעתקי השוליים של האגנים המרכזיים; ב) מערכת העתקי הכרמל-גלבוע-תירצה; ג) העתקים המקבילים או תת-מקבילים להעתק הערבה בנגב; ד) חלק מחגורת הגזירה של הנגב וסיני; ה) העתקים בכיוון צפון-צפון-מערב בנגב; ו) העתקים בכיוון מערב עד צפון-מערב בגליל התחתון. המקורות הסיסמיים העיקריים מסווגים לפי הקריטריונים: א) עדות לקצב הסטה אופקית של לפחות 1 מ"מ בשנה; ב) קצבי הסטה מוערכים של כ- 0.5–1 מ"מ בשנה.

רוב האזורים הסיסמוגניים ממוקמים לאורך טרנספורם ים המלח, אולם אחרים מופו כאן ממערב ונראים כמסתעפים מאזור השבירה המרכזי. שינויים בזמן ובמרחב במאפיינים של האזורים, גם בתוך תתי-אזורים, שופכים אור נוסף על הבנת הפעילות הסיסמית. בתוך האזורים, ה-*b-value* ומרווחי זמני החזרה של רעידות חזקות הנובעים מהם, נחשבים כאן כבלתי-מייצגים עבור דפוס התרחשות הרעידות בחלונות זמן ארוכים, לאור המגבלות בזמן ובמרחב שהאנליזה בעבודה זו תלויה בהן. במגמה הפוכה למרווחי זמני החזרה של רעידות חזקות שהתקבלו בעבודה זו, הדפוס שמוצע כאן בפרקי זמן ארוכים מאופיין בפעילות סיסמית המתרכזת באגנים ופעילות מופחתת לאורך הסגמנטים הארוכים והישרים, שמשחררים מומנט סייסמי רב יותר ברעשים חזקים יותר. בהתאם לכך, הפעילות הסיסמית הקשורה להם דלילה יותר בתקופה הבין-סיסמית. לפיכך מוצעת כאן התנהגות (קוואזי - ?) 'טיפוסית' (characteristic) לסגמנטים אלו. המחסור היחסי ברעידות במגניטודות $5.0 \leq M < 6.0$ לאורכם, לאורך כמעט מאה שנה, מחזק את ההצעה הזו.

המפות של תפרוסת הפרמטרים הסיסמיים חושפות מגמה סיסמית בכיוון צפון-מערב ברצועות או ליניאמנטים אפשריים. הרצועה הבולטת ביותר מזוהה עם מערכת העתקי הכרמל-גלבוע-תירצה, והיא היחידה הקשורה לדפורמציית פני שטח משמעותית. הליניאמנט הבולט מבין השאר מכיל את האזור הסיסמוגני של מזרח סיני. הוא מוגדר כאן כליניאמנט אילת-בַּרְדַאוויל, ומוצע כענף תת-קרקעי של טרנספורם ים המלח. הליניאמנטים מקבילים או תת-מקבילים לאלמנטים טקטוניים מובהקים של מתיחה, ולכן מוצע כאן שהם משקפים מתיחה עדינה (בעיקרה) בכיוון דרום-מערב–צפון-מזרח. בהצעה זו תומכות כמה עדויות בלתי-תלויות. המחסור היחסי במעוות לאורך רצועת הגזירה של הנגב-סיני מאז הרביעון המוקדם מרמז על כך שמגניטודת ציר הלחיצה האופקי המקסימאלי (שבכיוון כללי דרום-מזרח–צפון-מערב) נחלשה או נעה לכיוון צפון.

תקציר

אסונות שנגרמו כתוצאה מרעידות אדמה בתקופה האחרונה מדגישים את הנחיצות במחקר הקשור בסיכונים סיסמיים, בייחוד היכן שמתקנים רגישים ממוקמים. תוצרים כגון גריד מרחבי של פרמטרים סיסמיים ומפות העתקים בעלי יכולת וסבירות לייצר רעידות אדמה משמעותיות חיוניים להערכת סיכוני קריעת פני שטח ותנודות קרקע, לשם קביעת מיקום ותכנון של מבנים. אנליזות עדכניות לסיכונים סיסמיים בישראל עדיין מבוססות על חלוקה מקדמית לאזורים סיסמוגניים, ועד לעבודה זו, לא היו בנמצא מפות העתקים המכסות את כל שטחה של מדינת ישראל, שנצמדות לסטנדארטים בינלאומיים של סיכונים עבור תחנות כוח גרעיניות. במחקר זה נעשה מאמץ לשפר את ההבנה הסיסמו-טקטונית האזורית, כשהמטרה היא הפקת תוצרים החיוניים להערכות סיכונים, על ידי: א) אפיון של הפעילות הסיסמית; ב) ייצור מאגר מידע של העתקים מְמופים שהיו פעילים בעבר הגיאולוגי האחרון (capable faults), בייחוד עבור מתקנים רגישים כגון סכרים ותחנות כוח גרעיניות; ג) הגדרה ואפיון של אזורים סיסמוגניים; ד) פיתוח מתודולוגיה המשלבת נתונים גיאולוגיים וסיסמולוגיים לשם המטרות שלעיל, ושתוכל להיות מיושמת גם באזורים אחרים. לצורך המחקר, אני מתבסס בעיקר על נתוני רעידות אדמה שהוקלטו בין 1983 ל-2017 ושאוכנו מחדש, ועל מפות גיאולוגיות המכסות את כל שטח ישראל (70 מתוך 79 גיליונות מפות זמינים בקנה-מידה של 1:50,000). מידע משלים מגיע מעבודות המלמדות על הפעילות הצעירה ביותר של העתקים, מתצלומי אוויר ומקצבי הסטה (slip rates) לפי מדידות גיאודטיות וגיאולוגיות.

תוצר מובהק של עבודה זו היא מתודולוגיה מדורגת (cascaded) המאגדת את המידע הגיאולוגי והסיסמולוגי בשלושה שלבים: תחילה, האזור מאופיין בגריד מרחבי של הפרמטרים הסיסמיים *צפיפות רעידות אדמה*, *צפיפות מומנט סיסמי* ו*עומק רעידות ממוצע*. אפיונים אלה מושגים על ידי עיבוד נתונים מבוסס-סטטיסטיקה, המאפשר להשתמש במידע רב של רעידות אדמה המכיל שגיאות מרחביות במיקומן, ולנצל את כמות הנתונים הגדולה כדי להתגבר על השגיאות. הפרמטרים של הקשר תדירות-מגניטודה, האופייניים למרחב, מושגים ומשמשים לחישוב מרווחי זמני חזרה של רעידות אדמה בינוניות עד חזקות, לפי החוק האמפירי של גוטנברג-ריכטר. בשלב השני, נבנה מאגר של העתקים ממופים בעלי עדות ישירה או עקיפה לפעילות צעירה, על ידי ניתוח מפות גיאולוגיות ויישום קריטריונים סיסמו-טקטוניים, המעוצבים לפי הסטרטיגרפיה המקומית והקונפיגורציה הטקטונית. קריטריונים נוספים, המבוססים על קצבי הסטה, מופעלים על העתקים אלו לקבלת מפה אזורית של המקורות הסייסמיים הראשיים, שצפויים בסבירות רבה לאכלס את רעידות האדמה החזקות ביותר באזור. בשלב השלישי מותווים אזורים סייסמוגניים, בהתבסס על הפרמטרים הסיסמיים שהושגו קודם לכן ועל מערכת ההעתקים הקשורה, והם מאופיינים במאפיינים סיסמו-טקטוניים. כל שלב במתודולוגיה המוצעת כאן תורם לאנליזות של סיכוני קריעת פני שטח ו/או תנודות קרקע.

תוצרי הגריד של הפרמטרים הסיסמיים מוצגים כמפות תפרוסת בין קווי הרוחב 28°–34° צפון וקווי האורך 33°–37° מזרח (אזור המחקר המלא). הפרמטרים *צפיפות רעידות אדמה* ו*צפיפות מומנט סיסמי*, במידה רבה בלתי-תלויים, משלימים זה את זה למיפוי המקורות הטקטוניים הפעילים ביותר ואזורים בעלי סבירות רבה להכיל את רעידות האדמה החזקות ביותר. הפעילות הסיסמית מרוכזת בעיקר לאורך מערכת ההעתקים של טרנספורם ים המלח ולאורך הענפים שלה, בייחוד הענף של הכרמל-גלבוע-תירצה. הפעילות הסיסמית מגיעה לשיאים באגני מתיחה (pull-apart) ובצמתים עם מערכות העתקים אחרות, אך לעיתים מתרכזת בקרבת פני שטח שאינם מזוהים לעת עתה עם טקטוניקה צעירה. הפרמטר *עומק רעידות ממוצע* תורם להבנה של דפוס הפעילות הסיסמית. הוא משתנה בין עומקים רדודים של קילומטרים אחדים ועד לכ-25 ק"מ או אף עמוק יותר, ותואם למחקרים קודמים.

המכון הגיאולוגי
משרד האנרגיה

מיפוי ואפיון של
מקורות טקטוניים פעילים
בישראל ובאזורים סמוכים

מתי שרון

חיבור זה הוגש כחלק מהדרישות לקבל התואר מוסמך אוניברסיטה (.M.Sc**)** בחוג לגיאופיזיקה ולמדעים פלנטריים, בית הספר לסביבה ולמדעי כדור הארץ על שם פורטר, הפקולטה למדעים מדויקים על שם ריימונד ובברלי סאקלר, אוניברסיטת תל אביב

העבודה הוכנה בהדרכתם של:

ד"ר איתי קורזון, ד"ר אמיר שגיא (המכון הגיאולוגי לישראל)

פרופ' שמואל מרקו, פרופ' צבי בן-אברהם (אוניברסיטת תל אביב)

דוח מס' GSI/19/2020 ירושלים, אוגוסט 2020